Triboelectric energy harvesting for ocean and harsh environments: characterization, performance and applications

Cátia Rodrigues
Doutoramento em Física
Departamento de Física e Astronomia
2023

Orientador
Prof. Dr. João Oliveira Ventura, IFIMUP e FCUP

Coorientador
Prof. Dr. André Trindade Pereira, IFIMUP e FCUP

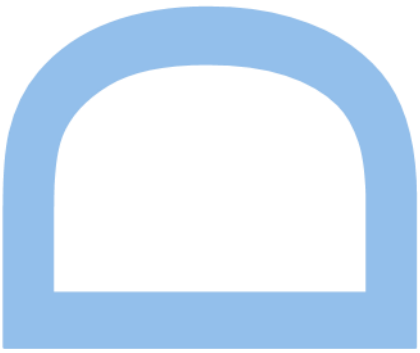




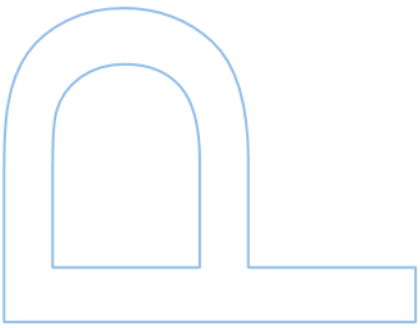
Universidade do Minho

U.PORTO

FACULDADE DE CIÊNCIAS
UNIVERSIDADE DO PORTO







Aos meus pais Manuela e José Luís,
ao meu marido Vítor e
à minha filha Alice

Declaração de Honra

Eu, Cátia Raquel da Silva Rodrigues, inscrita no Programa Doutoral em Física da Faculdade de Ciências da Universidade do Porto declaro, nos termos do disposto na alínea a) do artigo 14.º do Código Ético de Conduta Académica da U.Porto, que o conteúdo da presente tese reflete as perspetivas, o trabalho de investigação e as minhas interpretações no momento da sua entrega.

Ao entregar esta tese, declaro, ainda, que a mesma é resultado do meu próprio trabalho de investigação e contém contributos que não foram utilizados previamente noutros trabalhos apresentados a esta ou outra instituição.

Mais declaro que todas as referências a outros autores respeitam escrupulosamente as regras da atribuição, encontrando-se devidamente citadas no corpo do texto e identificadas na secção de referências bibliográficas. Não são divulgados na presente tese quaisquer conteúdos cuja reprodução esteja vedada por direitos de autor.

Tenho consciência de que a prática de plágio e auto-plágio constitui um ilícito académico.

Porto, 16 de maio de 2023

Acknowledgements

Over this work I had the pleasure and lucky to work with people who helped me in so many ways and makes this thesis possible. I am extremely grateful for the excellent education I received during this time.

First and foremost, I would like to express my deepest gratitude to everyone who supported me during this thesis, to all of those without whom it wouldn´t have been possible. I am truly thankful for all the personal and professional support I've had over these years because without a doubt I've been surrounded by excellent professionals and wonderful human beings.

I would like to sincerely thank my supervisor, Professor João Oliveira Ventura, for all his motivation, support, help and everything he taught me during all these years that made this work possible. Thank you so much for the friendship, dedication, enthusiasm, advice and trust deposited in my work along this challenging journey. Likewise, many thanks for his always intensive and fast review of all the manuscripts. My gratitude goes beyond words.

I am also thankful to my co-supervisors. To Professor André Pereira for his support and all the positivism transmitted since day one. Thank you so much for the opportunity and dedication towards the goal of this work. To Professor Carlos Baleizão for his professionalism, scientific integrity and being available to help.

I would like to thank to inanoEnergy team, namely to Manish Kumar, Diego Nunes, José Correia, Ricardo Esteves and João Magalhães, for their great dedication, cooperation, support and help to this work. Thank you for always welcoming me so well and making me feel part of the team.

I must express my gratitude to the INEGI, SHRHA- and the CIIMAR-FEUP team, especially to Daniel Clemente, Sr. Miguel and Professor Paulo Rosa for their support, availability, kindness, sympathy, and above all, I am very thankful for always welcoming me so well during the experimental tests carried out with the wave basin.

To Repsol Technology Lab, in particular to Ricardo Melo and Jose Gutierrez for their availability, kindness, patience, dedication and technical support during the experimental tests with equipment’s at Repsol.

To Eng. Francisco for his patience, help, dedication in working with me all these years and for all the important knowledge that always transmitted each time that I had to bother him. To Fernando for the help and technical support he gave me whenever I needed it. To Isabel Alves for her enormous dedication, friendship and promptitude in

solving each problem even when it was not her matter. To Dra. Armanda for her kindness, help and professionalism with bureaucracy problems. To Dra. Florbela, Dona Armanda, Dona Filomena, Dona Cristina, Dona Sandra and cleaning staff, and all the FCUP collaborators who support me and so kindly helped me over these years.

To Pedro Cruz for all time, help and patience every time I had to bother him with electronic issues. I am truly thankful for his genuine friendship, support and all the advice. Thanks to Hernani Marques and Gaspar Pacheco for their friendship and good vibes. Thank you guys for brightening my days so many times!

To all my dear IFIMUP colleagues for their friendship, help, support, collaboration, and good moments: Ana Pires, Ana Silva, Ana Sousa, Arlete Apolinário, Bogdan, Catarina Dias, Daniel Silva, Gonçalo Oliveira, Henrique Teixeira, Joana Silva, João Horta, Margarida Maia, Mariana Proença, Miguel Canhota, Pedro Rodrigues, Rui Vilarinho. To Rita Veloso for being such a good and genuine friend. I must thank her for all our conversations, all the support, help and all the work collaborations we have had together over these years.

To Mariana Rocha and Rui Costa for their truly friendship and support. I am truly grateful for all the comfort words, advice and for always being there to help whenever I needed it. I am so grateful that you and little Tomás are part of my life.

I am also thankful to former members Leandro Martins, Ana Gomes, Inês Figueiredo, Carla Alves, José Cardoso, Joel Puga, Filipe Falcão, Francisca Gomes, Bernardo Bordalo, Sílvio Menezes, Alvita, Pedro Resende, Tiago Leal, Rui M. Costa, Suellen Moraes and Vivian Andrade for their help, support, friendship and kindness. A special thanks to Paula Quitério for being such a good friend, always so kind, for being there for me, for all the comforting and motivation words. To my friend Mónica Cerquido for everything we lived together, for the tears and smiles shared over the years since nursery school. Thank you for being part of all the important moments of my life.

I am thankful to Fundação para a Ciência e a Tecnologia (FCT) and International Consortium of Nanotechnologies (ICON) funded by Lloyd's Register Foundation for the funding to this work, both through the PhD grant and the group projects. I also thank all the teaching and research staff of the MAP-fis program.

I am deeply grateful to my family. To my dear parents, Manuela and José Luis for being the great pillars of my life, for the sacrifices, unconditional love, friendship and always being by my side. My infinity thanks for everything you did and do for me. To my husband Vítor for always being by my side and supporting me unconditionally. Thanks for all your care, love, dedication, for being my pillar and never letting me go down. I will be eternally grateful to you. To my little daughter Alice, for her loving company throughout the writing of this thesis, which began with you still inside my belly and ended in my arms.

Thank you for turning my life upside down in such a wonderful way. Special thanks to my tiny kitten Kiko for coming into my life, for filling me with smiles and genuine affection.

Resumo

O mundo enfrenta o desafio de encontrar novas fontes de energia renovável e limpa para reduzir as emissões de carbono devido ao aquecimento global e à atual crise energética. Os nanogeradores triboelétricos (TENGs) têm demostrado ser, nos últimos anos, uma fonte de energia alternativa emergente, nomeadamente para alimentar sensores que fornecem dados ambientais e de segurança em tempo real em ambientes hostis e/ou remotos. O tamanho e peso reduzido, a elevada flexibilidade e o design adaptável destes micro/nanogeradores, permitem que sejam facilmente adaptados a diferentes superfícies e aplicados em locais remotos.

Neste trabalho, focámo-nos principalmente no estudo da geração de energia triboelétrica para ambientes oceânicos e hostis devido ao aumento da procura de novas fontes de energia para alimentar sistemas de monitorização em tempo real nessas condições para aplicações da Internet das Coisas (IoT). Para a captação de energia das ondas oceânicas, desenvolvemos três diferentes TENGs baseados em esferas para entender e obter correlações entre a dependência da geração de energia e a resposta hidrodinâmica da estrutura flutuante na qual estão integrados sob estados do mar relevantes. Testes num sistema de teste de bancada usando períodos e amplitudes de onda típicos de estados de mar reais demonstraram que a energia elétrica gerada pelos TENGs aumenta com a amplitude de pitch e decresce com o período de onda devido ao aumento da velocidade das esferas. O TENG lateral unidirecional gerou uma tensão, corrente e potência máxima de 14,6 V, 2,8 μA e 230 μW, respetivamente. Ao incorporar estes TENGs numa bóia de navegação e testá-los num tanque de ondas de grande escala sob condições de mar realistas, demonstramos que a tensão gerada aumenta com a frequência e amplitude das ondas, atingindo valores máximos para os períodos próximos do período natural da bóia (~0,920 s). Estes testes no tanque de ondas demonstraram claramente uma dependência da tensão elétrica com o grau de liberdade pitch e a necessidade de se ter em conta toda a dinâmica da bóia. Considerando a frequência de ocorrência dos estados do mar, foi então determinado que o TENG lateral unidirecional é o mais eficiente na captação de energia das ondas tendo em conta os seis graus de liberdade da bóia. Além disso, a influência das geometrias das plataformas flutuantes no desempenho de um duplo TENG lateral unidirecional também foi testada em condições de ondas regulares e irregulares. Neste estudo foi demonstrado que o dispositivo gerou maiores saídas elétricas quando implementado dentro de uma plataforma flutuante de casco semicilíndrico, gerando uma tensão, corrente e potência

máxima de ~ 70 V, 0,6 μA e 11 μW, respetivamente. Embora não haja uma correlação clara entre os graus de liberdade das plataformas flutuantes e as saídas elétricas do dispositivo triboelétrico, também foi demonstrado que é crucial levar em consideração a geometria do casco das plataformas flutuantes onde os TENGs são incorporados.

A captação de energia triboelétrica em condições adversas também foi estudada nesta tese, com o objetivo de demonstrar que esta tecnologia pode suportar e gerar energia em condições extremas. Neste trabalho conseguimos ampliar a gama de operação dos TENGs realizando estudos em metano e petróleo em amplas gamas de temperatura (até 120 ºC) e pressão (até 830 bar). Mostrámos que a temperatura é o parâmetro crítico para o desempenho do TENG ao variar independentemente a temperatura (T) e a pressão (P) em metano. Um pequeno aumento de V_{OC} e P_{max} foi observado entre 28 e 119 bar, a uma temperatura fixa de 90 ºC. No entanto, o desempenho do TENG diminuiu consideravelmente com o aumento da temperatura de 25 para 80 ºC, a uma pressão constante de 120 bar. A geração de energia triboelétrica em contato direto com petróleo também foi estudada para diferentes pressões (45 a 830 bar) aumentando constantemente a temperatura do petróleo. Foi demonstrado que a tensão gerada e a densidade de potência máxima diminuem gradualmente com o aumento da temperatura e da pressão. No entanto, o dispositivo triboelétrico continuou a gerar energia elétrica até P=830 bar e T=120 ºC. A geração de energia triboelétrica também foi estudada usando fluxos de óleo a altas pressões, obtendo-se uma densidade de potência máxima de 5,8 μW/m^2 abaixo dos 10 bar.

Por fim, desenvolvemos um dispositivo híbrido triboelétrico/termomagnético pioneiro capaz de recolher uma das fontes de energia mais omnipresentes que nos rodeia: o calor. Sob pequenas diferenças de temperatura, próximas da temperatura ambiente, o efeito termomagnético foi capaz de induzir o movimento periódico e sustentado de um material ferromagnético de segunda ordem em gradientes de temperatura abaixo dos 30 °C. Um TENG foi então usado para converter esse movimento mecânico em energia elétrica. Além de demonstrar que este dispositivo híbrido pode trabalhar numa ampla gama de temperaturas, tanto no lado frio (15 a 37 °C) como no lado quente (60 a 90 °C), também demonstrámos que a energia gerada por este TENG híbrido é 35× maior do que a obtida por um gerador termomagnético convencional acionado por indução magnética.

Esta tese abre novos horizontes e demonstra abordagens inovadoras sobre a adequação de dispositivos triboelétricos para coletar energia no oceano e em ambientes hostis, abrindo uma ampla gama de novas aplicações possíveis para monitorização remota em tempo real na Internet das Coisas.

Palavras-chave: Colheita de energia, Ondas oceânicas, Energia das ondas, Ambientes adversos, Petróleo e gás, Colheita térmica, Micro/nanogeradores triboelétricos.

Abstract

The world faces the challenge of finding new sources of renewable and clean energy to reduce carbon emissions to counteract global warming and the current energy crisis. Triboelectric nanogenerators (TENGs) have shown to be an emergent energy technology that can act as an alternative power source, namely to feed sensors that provide real-time environmental and safety data in harsh and/or remote environments. The implementation of these micro/nano-generators with small sizes, small weights, high flexibility and easily adaptable design, allows them to be tailored to different surfaces and placed in remote locations.

In this thesis, we focused on the study of triboelectric energy generation for ocean and harsh environments due to the increasing demand for autonomous real-time monitoring systems towards Internet of Things (IoT) applications. For ocean wave energy harvesting, we develop three different rolling-sphere-based TENGs to provide a better understanding of the dependence of their energy generation profile on the hydrodynamic response of the floating structure into which they are integrated under relevant sea state conditions. Tests in a “dry” bench system under typical periods and wave amplitudes of real sea states demonstrated that the TENGs electrical outputs increase with pitch amplitudes and decreasing period due to the increase of the spheres velocity. Maximum voltage, current and power of 14.6 V, 2.8 μA and 230 μW, respectively, were achieved by a unidirectional lateral-based TENG. By incorporating these TENGs into a navigational buoy and testing them in a large-scale wave basin under realistic sea-states, we demonstrated that the generated voltage increases with increasing wave frequency and amplitude, achieving maximum values for periods close to the natural period of the buoy (~0.920 s). These wave basin tests clearly demonstrated a dependency of the electrical outputs on the pitch degree of freedom and the need to take into account the full dynamics of the buoy. Considering the sea state occurrence frequency, it was then determined that the unidirectional lateral-based TENG is the most efficient in harvesting wave energy considering the six degrees of freedom of the floating buoy. Furthermore, the influence of floating platform geometries on the performance of a coupled unidirectional lateral-based TENG was also tested under regular and irregular wave conditions. In this study, it was demonstrated that the TENG device generated the highest electrical outputs when implemented inside the half-cylinder hull floating platform, reaching a maximum voltage, current and power of ~ 70 V, 0.6 μA and 11 μW, respectively. Although there was no clear correlation between the degrees of freedom of

the floating platforms and the electrical outputs of the triboelectric device, it was also demonstrated that it is crucial to take into account the hull geometry of the floating platforms where TENGs are incorporated.

Triboelectric energy harvesting under harsh conditions was also studied in this thesis, with the goal of showing that this technology can withstand and generate energy in extreme conditions. We were then able to expand the operating range of TENGs by carrying out extensive studies in methane and crude oil over wide ranges of temperature (T; up to 120 ºC) and pressure (P; up to 830 bar). We showed that temperature is the relevant parameter for TENG performance when independently varying temperature and pressure in a methane environment. A slight rise of V_{OC} and P_{max} was observed between 28 and 119 bar at a fixed methane temperature of 90 ºC. However, the TENG performance considerably decreased with increasing temperature from 25 to 80 ºC at a constant pressure of 120 bar. The triboelectric energy generation in direct contact with crude oil was also studied under different pressures (45 to 830 bar) by steadily rising the crude temperature. It was demonstrated that the generated voltage and maximum power density gradually decrease with increasing temperature and pressure. Nevertheless, the assembled triboelectric device continued to generate electrical energy up to P=830 bar and T=120 ºC. Furthermore, the triboelectric energy generation was also studied under oil flows at high pressures achieving a maximum power density of 5.8 μW/m^2 under 10 bar.

Finally, we developed a pioneering hybrid triboelectric/thermomagnetic device able to harvest one of the most ubiquitous energy sources that surrounds us: heat. Under small temperature differences near room temperature, the thermomagnetic effect was able to induce the periodic and sustained motion of a second-order ferromagnetic material in temperature gradients below 30 °C. A TENG was then used to harvest this mechanical motion into electrical power. In addition to demonstrating that this hybrid device can work under a broad range of operating temperatures in both the cold (15 to 37 °C) and hot (60 to 90 °C) sides, it was also shown that the power generated by this hybrid TENG is more than 35× higher than that obtained by a conventional thermomagnetic generator driven by magnetic induction.

This thesis then opens new horizons and shows innovative approaches concerning the suitability of triboelectric devices to harvest energy in ocean and harsh environments opening a wide new range of possible applications for real-time Internet of Things remote monitoring.

Keywords: Energy Harvesting, Ocean waves, Wave energy, Harsh environments, Oil & gas, Thermal harvesting, Triboelectric micro/nano-generators

Table of Contents

Acknowledgements xi
Resumo xv
Abstract xix
Table of Contents xxi
List of Figures xxv
List of Tables xxxiii
Nomenclature xxxv
Thesis Outline 1
Scientific Achievements 2
Chapter 1 – Triboelectric Micro/Nano-Generators: An Overview 5
1.1. Motivation 7
1.2. From tribology to triboelectric nanogenerators 9
1.3. Triboelectric nanogenerators: an overview 12
1.3.1. Triboelectric materials and optimization strategies 13
1.3.2. Basic modes of operation 15
1.3.2.1. Vertical contact-separation mode (VCTENG) 16
1.3.2.2. Lateral sliding mode (LSTENG) 18
1.3.2.3. Single-electrode mode (SETENG) 19
1.3.2.4. Freestanding triboelectric layer mode (FTENG) 20
1.3.3. Applications of TENGs 22
Chapter 2 – Experimental Techniques 27
2.1. Electrodes fabrication 29
2.1.1. Direct current (DC) magnetron sputtering deposition 29
2.1.2. Screen printing 30
2.2. Systematic characterization setups 31
2.2.1. Linear pneumatic system 34
2.2.2. 1-axis rotating frame system 34
2.2.3. Data analysis software 35
Chapter 3 – Harvesting Blue Energy using Triboelectric Nanogenerators 37
3.1. Introduction 39
3.2. Maritime applications of TENG technology 41
3.2.1. Ocean wave energy harvesting using TENG 42
3.3. An overview on TENG technologies for marine applications 44

3.3.1. TENGs based on rolling spheres 44
3.3.2. Other concepts 48
3.4. Integrated study of rolling spheres based on TENGs in realistic sea conditions 51
3.4.1. Structure design and fabrication of TENGs structures 52
3.4.2. Fabrication of floating buoy-based TENGs 53
3.4.3. Working mechanism of TENGs 54
3.4.4. Output performance using “dry” bench testing system 55
3.4.5. Wave basin demonstration 58
3.5. Influence of floating platforms geometries on the TENG’ performance 65
3.5.1. Structure design and fabrication of the floating platforms 66
3.5.2. Working mechanism of TENGs 67
3.5.3. Electrical outputs performance of the coupled lateral TENG 68
3.5.3.1. Regular water wave conditions 68
3.5.3.2. Irregular water wave conditions 71
3.6. Conclusions 73
Chapter 4 – Triboelectric Energy Harvesting in Harsh Conditions 75
4.1. Introduction 78
4.2. Environmental effects on TENGS performance: An overview 80
4.2.1. Temperature effect 80
4.2.2. Pressure effect 81
4.2.3. Gas atmosphere 83
4.3. Triboelectric energy harvesting in harsh conditions: Temperature and pressure effects 85
4.3.1. Structure design and fabrication of the triboelectric device 86
4.3.2. Working mechanism of the energy harvesting device 89
4.3.3. Experimental results 90
4.3.3.1. Energy generation in gaseous environment 90
4.3.3.2. Energy generation in crude environment 94
4.3.4. TENGs energy generation under closed-loop oil flux: a proof-of-concept 96
4.3.4.1. Triboelectric prototype and working mechanism 96
4.3.4.2. Closed loop oil flux test systems 98
4.3.5. Experimental results 99
4.3.6. Conclusions 101
4.4. Triboelectric and thermomagnetic effects: a novel low-grade thermal energy harvesting technology 102
4.4.1. Structural design of thermo-magnetic TENG demonstrator 103
4.4.2. Working mechanism of the TM-TENG and electrical signal generation 104
4.4.3. Optimization of the triboelectric device structure 108

4.4.4. TM-TENG electrical performance 110
4.4.5. Conclusions 113
Chapter 5 – Conclusions and Outlook 115
5.1. Main conclusions 117
5.2. Future perspectives 118
Bibliography 127
Appendix 151

List of Figures

Figure 1.1 – Trend on the global number (in billions) of connected IoT devices in the 2015 – 2027 period (adapted from Ref. [2]). 8

Figure 1.2 – Number of publications per year from 2012 until 2022 using the keywords "Triboelectric AND Nanogenerator OR Generator" (source www.scopus.com). 9

Figure 1.3 – Schematic diagram of the mechanism of charge transfer process in CE for (a) metal-dielectric and (b) dielectric-dielectric cases (adapted from Refs. [25,29]). 10

Figure 1.4 – Schematic diagram of the interatomic interaction model for general contact electrification cases (Reproduced with permission from Ref. [29], Copyright 2018, John Wiley and Sons)..... 12

Figure 1.5 – Structure of a basic TENG composed by two materials with opposite tribo-polarities and two metallic electrodes..... 12

Figure 1.6 – Triboelectric series for the most promising series of materials (adapted from Refs. [41,47]). 13

Figure 1.7 – Strategies to improve TENG performance. 14

Figure 1.8 – Basic vertical contact-separation working of a TENG (adapted from Refs. [41,64,65]): (a) dielectric/dielectric; (b) conductor/dielectric. 17

Figure 1.9 – Basic lateral sliding working mode of TENG (adapted from Refs. [41,64]): (a) dielectric/dielectric; (b) conductor/dielectric..... 18

Figure 1.10 – Basic single-electrode working mode of TENG (adapted from Ref. [64]): (a) conductor/dielectric contact mode; (b) conductor/dielectric sliding mode. 19

Figure 1.11 – Sliding-mode freestanding working mode of TENGs (adapted from Refs. [41,64]): (a) dielectric and (b) metal freestanding layer sliding TENG. 21

Figure 1.12 – Schematic diagram showing major application fields of TENGs as micro-/nano-energy source, blue energy and self-powered sensors. Reproduced with permission from Ref. [74], Copyright 2017, Elsevier. 22

Figure 1.13 – (a) Schematic diagram and (b) photograph of the I-TENG. (c) Voltage signal generated by the I-TENG in an animal preclinical test during the daytime. (d) Performance of a capacitor charging over a one day with the I-TENG implemented in the back of a mongrel. Reprinted with permission from ref. [83], Copyright 2021, Springer Nature. Schematic diagram of (e) the triboelectric auditory system for robotics and (f) the TAS. (i) Response of the TAS under various sound pressure levels. (j) TAS application for music recording . From [84]. Reprinted with permission from AAAS. (k) Schematic diagram of the all-fiber-structured TENG. (l) Performance of the TENG to charge different

commercial capacitors. (m) Demonstration of TENG to light up LEDs using arm movements. (n) Current generated by the all-fiber-structured TENG when harvesting energy from clapping hands, moving of arms, and walking. Reprinted (adapted) with permission from [85]. Copyright 2021 American Chemical Society. (o) Schematic diagram of the msTENG smart sensor glasses. (p) Comparation between the output voltage of the msTENG and the electro-oculogram. (q) Demonstration of a hands-free typing system. Modified from [82]. © The Authors, some rights reserved; exclusive licensee AAAS. Distributed under a CC BY-NC 4.0 License (http://creativecommons.org/licenses/by-nc/4.0/). 24

Figure 2.1 – (a) Schematic diagram of mechanism a typical magnetron sputtering system. (b)Magnetron Sputtering system available at IFIMUP facilities……..……29

Figure 2.2 – (a) Schematic of the screen-printing technique. (b) Screen-printing system available at the IFIMUP facilities. 31

Figure 2.3 – (a) Schematic diagram and (b) photograph of the characterization setup of TENGs using the linear pneumatic system: (I) linear pneumatic motor; (II) moving (left) and fixed (right) plates where the two tribo-pairs of a TENG are assembled; (III) resistances box; (IV) Keithley..... 32

Figure 2.4 – Schematic diagram of the electrical circuit to measure (a) voltage and (b) current generated by a TENG. 32

Figure 2.5 – Typical electrical peaks generated by a TENG under the action of the linear pneumatic system: (a) voltage; (b) current and (c) transferred charge. (d) Generated output voltage, current and power of a TENG for different load resistance values. 33

Figure 2.6 – (a) The pitch movement of a floating platform when subject to a water waves. (b) 1-axis rotating frame system with the equivalent motion parametrized by the period and pitch. 35

Figure 2.7 – Threshold lines and selected peaks for the output voltage of a TENG connected to a resistance of 470 MΩ. 36

Figure 3.1 – (a) Dynamics of ocean buoy under wave action. (b) Six degrees of freedom of a floating body. Reproduced from Ref. [225] with permission from the Royal Society of Chemistry. ……..……43

Figure 3.2 – Wave energy harvesting by TENGs: A holistic perspective. Reproduced from Ref. [225] with permission from the Royal Society of Chemistry. 44

Figure 3.3 – (a) Schematic and photograph of single TENG. (b) Photograph of a TENG-NW unit. (c) Open-circuit voltage and (d) short-circuit current generated by a ball collision at 10 m/s^2 with a displacement of 9 cm. Reprinted with permission from Ref. [126], Copyright 2015, American Chemical Society. (e) Schematic of spherical TENG with 6 spring-assisted TENGs. (f) Output voltage generated by each TENG unit. (g) Dependence of output current under various water waves frequencies. (h) Output power

generated by the spherical TENG under different orientation angles. Reprinted with permission from Ref. [124], Copyright 2020, The Royal Society of Chemistry. 47

Figure 3.4 – (a) Schematic of the SS-TENG. (b) Array of SS-TENGs to develop an ocean energy farm. (c) Photograph of the developed SS-TENG composed by a single segment. (d) Dependence of output voltage using various number of segments. Reprinted with permission from Ref. [136], Copyright 2018, Elsevier. (e) Schematic of the multiple T-TENG units and the basic structure of a T-TENG unit. (f) The short-circuit current generated in a water wave tank during 14h. (g) Dependence of power density generated using various numbers of TENG units in the tower. Reprinted with permission from Ref. [139], Copyright 2019, American Chemical Society. 48

Figure 3.5 – (a) Schematic and (b) photograph of the fabricated TENG. (c) Output voltage of a TENG unit. (d) Dependence of peak power and average power at various frequencies using a matched load of 13.8 MΩ. Reprinted with permission from Ref. [141], Copyright 2019, The Royal Society of Chemistry. (e) Schematic of the developed hybrid nanogenerator. (f) Photograph of the hybrid device floating in water and lighting up 108 LEDs. (g) Transferred charge and V_{OC} of the TENG for various displacements. (h) The short-circuit current and V_{OC} of EMG unit for various displacements. Reproduced with permission from Ref. [149], Copyright 2018, Elsevier. (i) Schematic and (j) photograph of the developed flexible TENG. Output (k) current and (l) voltage of the flexible TENG. Reproduced with permission from Ref. [143], Copyright 2017, AIP Publishing LLC. ... 49

Figure 3.6 – (a) Design of the navigation floating buoy-based on unidirectional and anisotropic triboelectric nanogenerators: (a_1) AC-TENG, (a_2) UF-TENG and (a_3) UL-TENG. b) Six-degrees of freedom motions of the buoy. Photographs of the (c) AC-, (d) UF and (e) UL-TENGs. 52

Figure 3.7 – The working mechanism of the (a) anisotropic circular-based TENG (AC-TENG) and unidirectional lateral-based TENG (UL-TENG). 55

Figure 3.8 – The generated output voltage, current and power of the (a) AC-TENG, (b) UF-TENG and (c) UL-TENG at a fixed period of 1.486 s and a pitch amplitude of 26º. 56

Figure 3.9 – Maximum voltage, current, charge and power generated using different pitch amplitudes and periods by (a)-(d) AC-TENG, (e)-(h) UF-TENG and (i)-(l) UL-TENG. 57

Figure 3.10 – Schematic diagram of the wave basin equipment and facilities. 59

Figure 3.11 – (a) Navigational buoy tested in the wave basin under realistic wave conditions. Inset of the buoy re-dimensioned in a 1:8 scale. (b) Bluetooth datalogger developed to measure and send the voltage generated by TENGs in real-time. (c) Simplified representation of the properties of the regular waves generated in the wave basin. 59

Figure 3.12 – Wave energy resource matrices for two sites near Figueira da Foz, Portugal: significant wave height (H_{m0}) versus peak wave period (T_p) (based on Ref. [226]). 60

Figure 3.13 – Maximum open-circuit voltage, time average of the integrated area of the voltage peaks generated by (a) AC-, (b) UF- and (c) UL-TENGs, under various wave conditions (wave periods and wave amplitudes) selected to represent the most frequently occurring sea states at the case study site. 62

Figure 3.14 – Response Amplitude Operator for configurations AC-TENG and UL-/UF-TENG, regarding: (a) surge, (b) heave and (c) pitch DoFs (physical model values). ... 63

Figure 3.15 – Periodicity correlation between the generated waves and the physical model's hydrodynamic response for configurations AC-TENG and UL-/UF-TENG, regarding the (a) surge, (b) heave and (c) pitch DoFs (physical model results). 64

Figure 3.16 – Time series profiles of the motions of the physical model, for all 6 DoFs. The profiles regard the results with combined configuration UL-/UF-TENG, for wave condition H = 0.125 m, T = 0.920 s. 64

Figure 3.17 – Sum of the energy generated by each TENG for the different wave combinations, considering the occurrence frequency of each wave combination (amplitude/period). 65

Figure 3.18 - Schematic of the (a) half-sphere, (b) half-cylinder and (c) trapezoidal prism floating platforms. (d) Two lateral-based TENGs connected electrically in parallel and (e) detailed configuration of individual structural design of lateral triboelectric device..... 67

Figure 3.19 – (a) Output current for a TENG inside the half-sphere floating platform under different waves periods at a fixed wave height of 0.100 m. (b) V_{OC} generated by the lateral based-TENG within the three floating platforms under different waves periods at a fixed wave height of 0.100 m..... 69

Figure 3.20 – Maximum voltage, current and power generated using different wave periods by (a) half-sphere, (b) half-cylinder and (c) trapezoidal prism floating platforms. Hydrodynamic response of the (d) half-sphere, (e) half-cylinder and (f) trapezoidal prism floating platforms, regarding: pitch, heave and surge DoFs (physical model values)… 70

Figure 3.21 – (a) Open-circuit voltage generated by the lateral based TENG inside the half-cylinder hull under irregular sea-states. (b) Mean voltage and power density generated by the TENG implemented inside the half-cylinder hull. 72

Figure 4.1 – (a) Schematic of the experimental setup and TENG. (b) Electrical signal curves of the open-circuit voltage at different temperatures. (c) Short-circuit current generated in a temperature range between -20 and 150 ºC. Reprinted with permission from Ref. [175], Copyright 2017, John Wiley & Sons. (d) Device schematic of the FD-TENG to harvest wind energy and sense wind speed at high temperature. (e) Current generated by FD-TENG using different triboelectric materials at 50, 100 and 200 ºC. (f) Current of FD-TENG at 6 m/s hot airflow using 1% BaTiO3-doped 6FDA–TFDB flap. Reprinted with permission from Ref. [194], Copyright 2021, John Wiley & Sons. ….80

Figure 4.2 – (a) Schematic of TENG with the coupling of surface and dielectric polarization. (b) Charge density generated by TENG in atmosphere and high vacuum. (c) Output current and power densities of optimized TENG with different resistive loads at vacuum. Reprinted with permission from Ref. [195], Copyright 2017, Springer Nature. (d) Schematic diagram of experiment setup to work at high-pressure gas environment. (e) Charge generated by TENG under contact-separation working mode. (f) Power density of TENG with different resistive loads at 1 and 7.8 bar. Reprinted with permission from Ref. [196], Copyright 2020, John Wiley and Sons. 82

Figure 4.3 – (a) Schematic of the DC-TENG in the measurement setup. (b) Illustration of the rotary mode DC-TENG. (c) Charges and (d) open-circuit voltage generated by DC-TENG at various atmosphere pressures. Reprinted with permission from Ref. [193], Copyright 2020, John Wiley and Sons. 83

Figure 4.4 – (a) Structure design of the integrated triboelectric self-powered respiration sensor. (b) Voltage generated by Ce-ZnO-2 based TSRS under dry NH_3. (c) Response of Ce-ZnO-2 based TSRS using different interfering gases under moist and dry atmospheres. Reprinted with permission from Ref. [182], Copyright 2019, Elsevier. (d) Schematic and (e) photograph of the gas-enhanced enclosed cubic-TENG. (f) Voltage and current generated by the cubic-TENG under different gas atmospheres of He, Ar, air, N_2, CO_2, CHF_2Cl and SF_6. (g) Charging curves using a 3.3 µF capacitor under various gas atmospheres. Reprinted with permission from Ref. [197], Copyright 2019, Elsevier. 84

Figure 4.5 – (a) Design of the setup structure used to test the triboelectric materials at high pressures and temperatures. (b) Schematic structure of the tested triboelectric pair. (c) Photography of the two Nylon 6,6/PTFE structures assembled at each end of the box and metallic spheres. (d) Photography of the assembled setup to be placed inside the high pressure container. (e) Photography of the assembled device inside the high pressure container with crude oil. (f) Photography of the special trolley used to support the high pressure container and to allow the rotation motions. (g) Schematic illustration of the rotation motion of the assembled device. 86

Figure 4.6 – Electrical outputs generated by the triboelectric device when the spheres are in contact with gold films using three different single-electrode configurations and our triboelectric device. ..... …88

Figure 4.7 – Dependence of pressure with the temperature inside the special high pressure/temperature container. 89

Figure 4.8 – Working mechanism of the assembled triboelectric nanogenerator based on the contact-separation mode. 90

Figure 4.9 – Energy harvesting results obtained in methane as a function of pressure at constant temperature (T = 90 ºC): (a) open-circuit voltage, and (b) maximum voltage, current and power density. Energy harvesting results obtained in methane as a function of temperature at constant pressure (P = 120 bar): (c) Open-circuit voltage, and (d) maximum voltage, current and power density. 91

Figure 4.10 – (a) Open-circuit voltage of the TENG as a function of pressure in crude. (b) Output voltage, maximum power density generated in crude by the assembled triboelectric device up to 830 bar and 120 ºC. 95

Figure 4.11 – Charging voltage over time for a 10 μF capacitor, using the assembled triboelectric device in crude environment for different temperatures and pressures. ... 95

Figure 4.12 – Photographs of the triboelectric prototype: (a) top and (b) lateral perspectives. 97

Figure 4.13 – Working mechanism of the triboelectric prototype based on the contact-separation mode. 97

Figure 4.14 – (a) Schematic of the oil flux testing bench developed and available at inanoEnergy. (b) Photograph of the continuous oil flux test chamber. 98

Figure 4.15 – (a) Photograph of the high pressure pipe with the triboelectric prototype assembled inside. (b) Photograph of the high pressure control system responsible for the closed circuit of the oil flow. 99

Figure 4.16 – (a) Open-circuit voltage and (b) short-circuit current under constant oil flow. (c) Dependence of the voltage, current and power density output on the external load resistance using the oil flux testing bench. 100

Figure 4.17 – (a) Open-circuit voltage and (b) short-circuit current of the TENG as a function of pressure. (c) Power density generated by the triboelectric device with inset showing its exponential decrease trend under different pressures. 100

Figure 4.18 – Schematic diagram of (a) an active and (b) a passive thermomagnetic generator (adapted from Refs. [217,227]). 103

Figure 4.19 – (a) Detailed schematic illustration and (b) photograph of the fabricated TM-TENG with heat sink module. 104

Figure 4.20 – Temperature dependence of the magnetization curve for Gd under a magnetic field of 100 Oe under heating (orange) and cooling temperature (blue). Inset: Temperature derivative of magnetization curve..... 105

Figure 4.21 – Schematic representation of the working mechanism of TM-TENG.... 106

Figure 4.22 – (a) Measured temperature on the surfaces of cold-side and hot-side during TENG operation under a thermal gradient of ~50 ºC and the consecutive Gd FM↔PM phase transitions evidenced by the temperature behavior of the hot- and cold-surfaces. (b) Open-circuit voltage generated by arc-shaped TENG at frequency of ~11 mHz, and extended output voltage during heating and cooling with the different positions of Gd and Cu plate. (c) Voltage peak generated by TENG correlated with Spatial temperature of the Gd block obtained with the numerical simulations: I, initial state, II, before falling, III, after falling, and IV, before jumping. (d) Finite-element simulation of the electrical potential distribution in the device in a contact cycle. 107

Figure 4.23 - Illustration (left) and photography (right) of the three different structures: (a) arc- (b) zigzag- and (c) parallel-shaped TENG. (d) Maximum open-circuit voltage, current and power density generated by the three different structures under a thermal gradient of ~41 ºC and frequency of ~10 mHz. (e) Electrical characterization of the arc-shaped TENG under a thermal gradient of ~41 ºC and ~10 mHz. 109

Figure 4.24 - Output voltage, current and power of the EMG fixed on surface of (a) Peltier coolers and (b) Peltier heater. 110

Figure 4.25 – Dependence of electrical outputs generated by the arc-shaped TENG when assembled on the cold-side surface under a range of: (a) cold-side temperatures from 15 to 37 ºC and fixed hot-side temperature of ~65 ºC; (b) hot-side temperature from ~60 to 90 ºC and fixed cold-side temperature of ~20º C. (c) Voltage, current and power density as function of the weight of the Gd/Cu set at fixed cold- and hot-side temperatures of ~20 and 60 ºC. (d) Performance-dependence of TENG assembled on hot-side surface under various hot-side temperatures..... 111

List of Tables

Table 1.1 – Summary of the main theoretical relations for the different working modes of triboelectric nanogenerators. In the table, σ is the static charges density, Q is the transferred charges, S the metal area, $\varepsilon 0$ the permittivity of free space, $d0$ is the effective dielectric thickness given by $d1/\varepsilon r1 + d2/\varepsilon r2$ (with $d1,2$ and $\varepsilon r1,r2$ the thicknesses and relative dielectric constants of dielectrics 1 and 2, $x(t)$ the time dependent distance between the two tribo-material, w the transversal width, l the length in the longitudinal direction, Ci are the equivalent capacitances formed between electrical nodes and g the gap between reference and primary electrodes. 16

Table 3.1 – Prototypes developed for wave energy harvesting in buoys and corresponding generation properties. Reproduced from Ref. [91] with permission from the Royal Society of Chemistry. 45

Table 3.2 – Reproduced regular wave conditions both at full and model scale. 61

Table 3.3 – Physical models of the three geometries of floating platforms: shape, dimensions, and main physical properties..... 66

Table 3.4 – Matrix of the reproduced regular wave conditions both at full and model scale. 68

Table 3.5 – Matrix considered in the experimental study with irregular waves both at full and model scale..... 71

Table 4.1 – Prototypes developed to harvest energy under various temperatures, pressures, and gas atmospheres with their corresponding generation properties. 79

Table 4.2 – Results of the temperature (T) and pressure (P) tests performed in hydrocarbons. 87

Table 4.3 – Elements composition of crude used during the performance studies. ... 94

Nomenclature

Acronyms/Abbreviations and Symbols

∇T, average thermal gradient

ΔM, magnetization variation

3D, three-dimensional

AC, alternating current

AC-TENG, anisotropic circular-based triboelectric nanogenerator

AFM, atomic force microscopy

CE, contact electrification

DC, direct current

DoF, degree of freedom

IoT, internet of things

I_{SC}, short-circuit current

EMG, electromagnetic generator

FFF, fused filament fabrication

FM, ferromagnetic

F_m, magnetic force

FTENG, freestanding triboelectric layer mode

KPFM, kelvin probe force microscopy

LED, light-emitting diode

LSTENG, lateral sliding mode

MIE, minimum ignition energy

PM, paramagnetic

PPM, parts per million

RAO, response amplitudes operator

Q_{SC}, short-circuit transferred charges

SETENG, single-electrode mode

T_C, Curie temperature

TE, triboelectrification

TENG, triboelectric nanogenerator

TM, thermomagnetic

TM-TENG, thermomagnetic triboelectric nanogenerator

UF-TENG, unidirectional flat-based triboelectric nanogenerator

UL-TENG, unidirectional lateral-based triboelectric nanogenerator

VCTENG, vertical contact-separation mode

V_{OC}, *open-circuit voltage*

σ, *charge density*

d_0, effective dielectric thickness

ε_0, *permittivity of free space*

Materials

Al, aluminum

Ag, silver

Au, gold

CH_4, methane

Cu, copper

ITO, indium tin oxide

Fe_2O_3, iron(III) oxide

FEP, fluorinated ethylene propylene

Gd, gadolinium

PDMS, polydimethylsiloxane

PET, polyethylene terephthalate

PLA, polylactic acid

PMMA, poly(methyl methacrylate)

PS, polystyrene

PTFE, polytetrafluoroethylene

PVC, polyvinyl chloride

PVDF, polyvinylidene fluoride

$SrTiO_3$, strontium titanate

PDMS, polydimethylsiloxane

Thesis Outline

The main focus of this thesis is the development of triboelectric devices to harvest mechanical motions from wave energy and under harsh environments, to open new horizons for this type of technology to be applied in real applications. Two main promising areas were studied in this thesis due to the increased necessity for real-time monitoring: (remote) ocean and harsh environments.

This thesis was carried out in collaboration with multidisciplinary teams involving research institutes and international companies. The performed studies concerning blue energy harvesting was developed under the collaboration between the Institute of Physics for Advanced Materials, Nanotechnology and Photonics (IFIMUP), at the Faculty of Sciences of the University of Porto (FCUP), inanoEnergy, the Institute of Science and Innovation in Mechanical and Industrial Engineering (INEGI), the Hydraulics Laboratory of the Hydraulics, Water Resources and Environment Division (SHRHA) of the Faculty of Engineering of the University of Porto (FEUP) and the Interdisciplinary Centre of Marine and Environmental Research of the University of Porto (CIIMAR) of FEUP. The studies performed under harsh environments were developed under collaborations between IFIMUP, inanoEnergy, Repsol Technology Lab (Spain) and Xrig AS (Norway).

This thesis is organized in five chapters, containing: an overview of triboelectric nanogenerators; the experimental setups used to evaluate the performance of materials and devices; two chapters focusing on the development and study of devices to harvest blue energy and under harsh environments; a chapter with main the conclusions and future perspectives.

A brief summary is here given:

-Chapter 1 introduces the phenomenon of triboelectrification with the focus on understanding this effect as an approach to enhance the performance of triboelectric micro/nano-generators. Then, based on the basic TENG structure, strategies are presented to modify the triboelectric materials in order to increase their electrical power. Finally, the basic modes of operations of this novel technology are presented, as well as its different applications areas.

-Chapter 2 describes the experimental setups used to perform standard systematic characterization of the triboelectric materials and devices developed during this thesis.

-Chapter 3 starts by describing the state-of-art of blue energy harvesting using triboelectric nanogenerators. Then, we present and discuss an integrated study of TENG performance in realistic sea conditions, considering the hydrodynamic response of the floating bodies and their different geometries into which TENGs are integrated.

-Chapter 4 starts with a brief state-of-art about triboelectric energy harvesting in harsh conditions, followed by an experimental study to understand the effect of temperature and pressure on the performance of triboelectric devices for application in oil extraction wells. A novel triboelectric device making use of the thermomagnetic effect was also demonstrated and studied to generate electrical power from small temperature gradients near room temperature.

-Finally, Chapter 5 summarizes the main conclusions of this thesis and future work.

Scientific Achievements

The research conducted in the framework of this thesis led to a number of novel scientific contributions, summarized as follows.

Ocean energy: For the first time, TENGs based on rolling spheres to harvest energy from multidirectional water wave were developed to:

- Provide a better understanding on the hydrodynamic response of the buoy/floating platforms under realistic sea-states, which can only be attained if the irregular and random nature of ocean waves are properly reproduced, due to the degrees of freedom of the spheres;
- Carry out a physical modelling study of a moored scaled navigational buoy/floating platforms with incorporated TENGs in a wave basin equipped with a multidirectional wavemaker, taking into full account the six degrees of freedom of the buoy/floating platforms [translatory (surge, sway, heave) and rotatory (roll, pitch, yaw)];
- Compare, at same time, the dependence of the TENGs performance with the hydrodynamic response of the scaled navigational buoy or floating platforms taking into full account its six degrees of freedom.

Harsh environments: In this thesis, an integrated study concerning the triboelectric energy generation under oil & gas environments in extreme conditions was also performed to:

- Show the performance of TENGs in harsh conditions (high temperature and pressure) like those found in extraction wells in direct contact with methane and crude oil;
- Demonstrate the superior versatility of TENGs both in terms of materials and device configurations so that they can be generalized in different structures that can take advantage of the static and linear flow of fluids;
- Show what is the limit of TENGs to work properly, which will promote a wide and practical application of TENGs, for example, in self-powered systems in sensing and infrastructure/environmental monitoring into the oil and gas sector.

The pioneering hybrid triboelectric/thermomagnetic device allowed to:

- Expand the applicability of triboelectricity into the realm of room temperature thermal harvesting;
- Attain interest from a broad community of scientists working on the energy field, including on triboelectric nanogenerators, magnetic and magnetocaloric materials, thermoelectrics, energy harvesting and heat management, among other.

Chapter 1

Triboelectric Micro/Nano-Generators:

An Overview

Chapter 1

Triboelectric Micro/Nano-Generators: An Overview

1.1. Motivation

Energy has been one of the major driving forces behind our societal development and economic growth. However, the resulting surge in energy demand has also led to the major environmental crisis we now face. We must thus urgently find new ways to replace fossil fuels by green technologies that can steer us towards a carbon-neutral world. The recent pledge of the United States to reduce greenhouse gas emissions by half by 2030 has only made this necessity even more urgent. This path toward sustainability can be pursued using the Internet of Things (IoT) to reduce electrical demand and improve efficiency and through the development of new technologies able to harvest energy from all the renewable sources that surround us.

In the Era of IoT, this emerging smart network composed by billions of sensors and devices interconnected has the potential to collect and analyzed massive amount of data in real-time [1]. This provides automated decision making in real-time and facilitating tools for efficient and sustainable energy management. The role of IoT is becoming more essential in industrial and commercial developments such as in the oil and gas industry (to allow operators to monitor systems and react safely and in real time to production issues as they arise) or in maritime buoy systems (to monitor the ocean or warn of natural disasters, for example).

Figure 1.1 shows the trend of the global number of IoT devices in the 2015-2027 period, with 16.7 billion expected by the end of 2023 [2]. Due this market's expansion, more energy-efficient options become necessary for powering IoT sensors and devices, since most of these are currently powered by batteries with limited lifetime, expensive maintenance and environmental hazards.

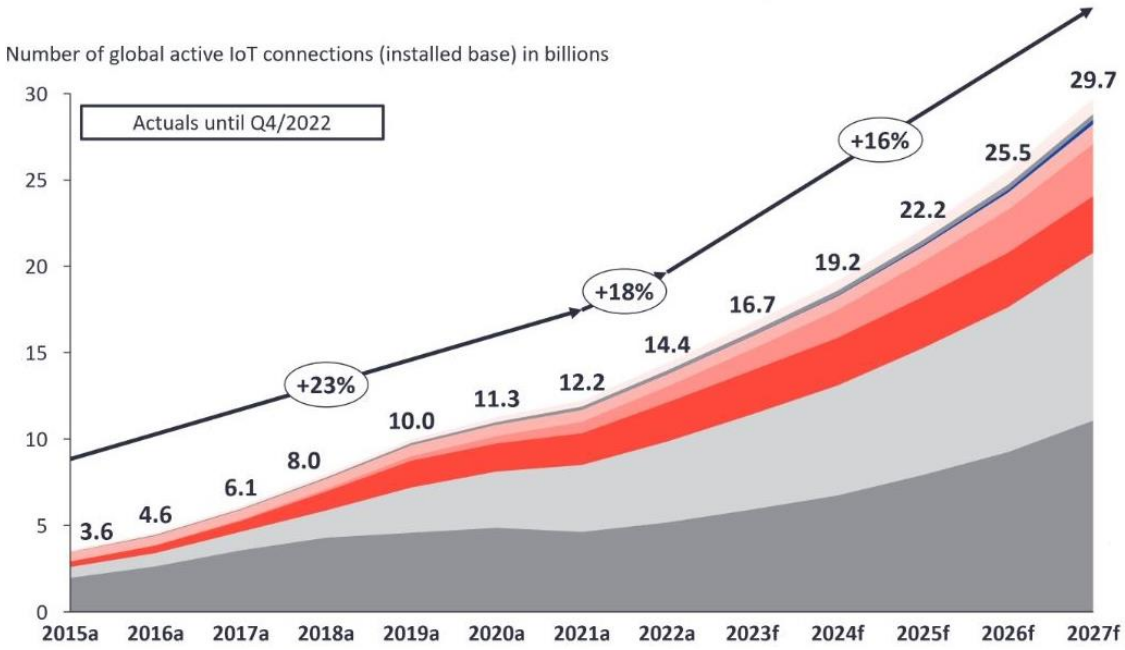


Figure 1.1 – Trend on the global number (in billions) of connected IoT devices in the 2015 – 2027 period (adapted from Ref. [2]).

In this regard, harvesting energy from renewable sources that are prevalent in our environment (such as thermal, mechanical and electromagnetic energies) can be an alternative solution to supply IoT devices and further increase their expansion. How can we them harness this energy that is all around us, but that it is being wasted?

Considering that most IoT devices are implemented in environmental or human monitoring applications where there is abundant mechanical energy, triboelectric nanogenerators (TENGs) have shown to be a promising energy harvesting technology [1,3]. Since its invention in 2012 by Prof. Wang and his team [4], TENGs have achieved significant attention over the years, as can be observed in Figure 1.2 showing the number of publications per year on TENGs. This novel type of nanogenerators takes advantage of the universally present contact electrification and operates on the basis of electrostatic induction. TENGs have been showing their capability to harvest different kinds of mechanical energies (random, regular, irregular, low or high frequency) [5–9], with a maximum power density of 500 W/m^2 [10] and a conversion efficiency of ~85% already reached [11]. They have outstanding characteristics such as low cost due to the immense quantity and diversity of materials that can be used, they have simple manufacture due to their versatile working mechanism and they do not depend on day/night cycles. As a new type of energy harvester, TENGs operate on a small scale and have a huge potential to be used in various applications such as micro/nano power sources [12–14], self-powered sensors [15–17], blue energy [5,18,19] and environmental

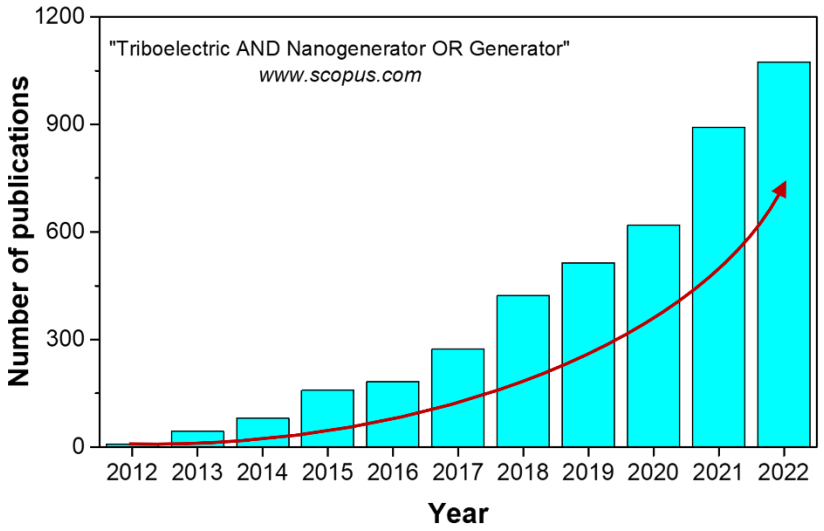


Figure 1.2 – Number of publications per year from 2012 until 2022 using the keywords "Triboelectric AND Nanogenerator OR Generator" (source www.scopus.com).

monitoring [20–22]. Therefore, this emerging technology is showing progresses to become an indispensable piece of the puzzle of the sustainable energy mix.

1.2. From tribology to triboelectric nanogenerators

The word tribology is derived from the Greek word *tribos*, meaning rubbing. Tribology is defined as the science and technology of interacting surfaces in relative motion and involves many local physical and chemical processes such as deformations, fracturing and heat generation [23].

Triboelectrification (TE) is one of the few effects that have been known for thousands of years and is also one of the most frequently experienced effects on our every daylife. Some common examples include the hair becoming charged after taking off an item of clothing or combing it. or the electrical shock we experience when touching the car or a door handle. Triboelectricity can cause discharges that damage several industrial processes, electronics and even cause wildfire in nature [24]. Although triboelectrification has been reported more than 2600 years ago [25], today there is still no consensus in the scientific community about the processes that lead to surface electrification due to the vast amount of materials (including metals, dielectrics, ceramics or semiconductors) where it occurs [25]. A most controversial topic in electrification is the identity of the involved charge carriers: electron transfer, ion transfer or even materials species transfer [26–28]. However, a growing interest has arisen in understanding the contact electrification (CE) mechanism due to the emergence of TENGs by Wang *et al.* in 2012 [4]. TENGs convert irregular and low-frequency external mechanical energy into electric

power by a conjunction of TE and electrostatic induction. Therefore, the output power of TENGs depends on the TE-magnitude, which proves to be increasingly important to understand this effect. There are several types of triboelectrification, although most of the published literature on TENGs is based on solid-solid triboelectrification. There is still no universal model that explains charge transfer in triboelectrification, although there are already several experimental and computational studies that show evidence of the dominant species in certain cases. Due to its importance, we will here focus on surface charging due to electron transfer [25,29,30], characterized by two models: the surface states model [31] and through a new approach centered on the overlapping of electron orbitals of the contacting atoms [29].

Electron transfer processes in CE between metal-dielectric and dielectric-dielectric pairs can be described by energy band diagrams (Figure 1.3). Studies have shown, through Kelvin probe force (KPFM) [32–35] and atomic force (AFM) microscopies [36], that electron transfer processes are the dominant mechanisms during CE in metal-dielectric cases. Assuming a 0 K temperature, the metal can be defined by its Fermi level, above which all the states are unoccupied and below which all the states are occupied. The surface of a dielectric material can be characterized by

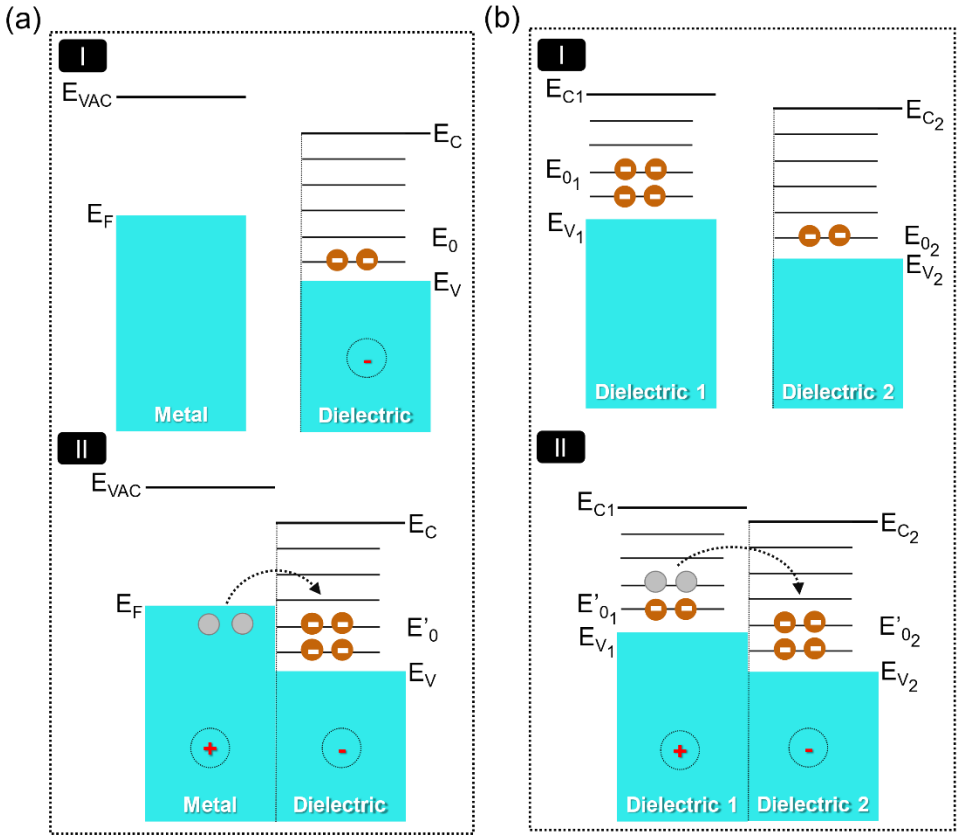


Figure 1.3 – Schematic diagram of the mechanism of charge transfer process in CE for (a) metal-dielectric and (b) dielectric-dielectric cases (adapted from Refs. [25,29]).

conduction and valence bands [Figure 1.3(a)-I]. In this case, the presence of surface/defects states in the band gap should be assumed, resulting in their occupation by electrons. After contact, and assuming that the Fermi level of the metal is above the valence band of the dielectric, electrons can be transferred from the metal into to the dielectric as there are surface states in the bandgap with energy below the Fermi energy [Figure 1.3(a)-II]. This leaves the dielectric surface negatively charged.

In the dielectric-dielectric case, an electron transfer process can also occur if the occupied surface states in dielectric 1 are higher than the unoccupied surface states of dielectric 2 [Figure 1.3(b)-I], for example. When the dielectric materials come into contact, some electrons can transfer from the surface of dielectric 1 to that of dielectric 2, resulting in CE. This process leads to net positive electrostatic charges in dielectric 1 and net negative electrostatic charges in dielectric 2 [Figure 1.3(b)-II]. Typically, the minimum thermodynamic energy needed to remove an electron from a solid to a point just outside the solid surface is in the order of eV [37]. After separation of the dielectric materials, on would expect these charges on the dielectrics to remain perpetually on their surfaces if not disturbed. However, the bound electrons can be released from the surface states to due thermal energy fluctuations, as predicted by the electron thermionic emission model.

However, there are materials without a well-defined molecular structure which cannot be characterized by a simple electronic structure model, such as wool, wood, animal fur, human hair, but still exhibit CE [25]. Recently, a new model based on KPFM experiments was proposed to explain CE in general materials, especially in those that do not have a well specified energy band structure [25,29,38]. It was experimentally shown the existence of CE between a KPFM platinum tip in tapping mode and insulators when the tip entered into the repulsive region of the insulator surface [38]. Then, an atomic-scale charge transfer mechanism for CE was proposed, as shown in Figure 1.4. When the two materials are separated, their electron clouds are also separated without overlap as illustrated in Figure 1.4(a). In nonconducting materials, the electrons are strongly bounded in specific orbitals due to the potential well, preventing them to easily escape. When materials A and B come into physical contact, electron clouds in the repulsive region will overlap between two atoms to form ionic or covalent bonds [Figure 1.4(b)]. Then, the initial single potential well becomes an asymmetric double-well potential, allowing electrons to transfer from the atom of material A to the atom of material B. After separation, the transferred electrons remain as static charges on material B due

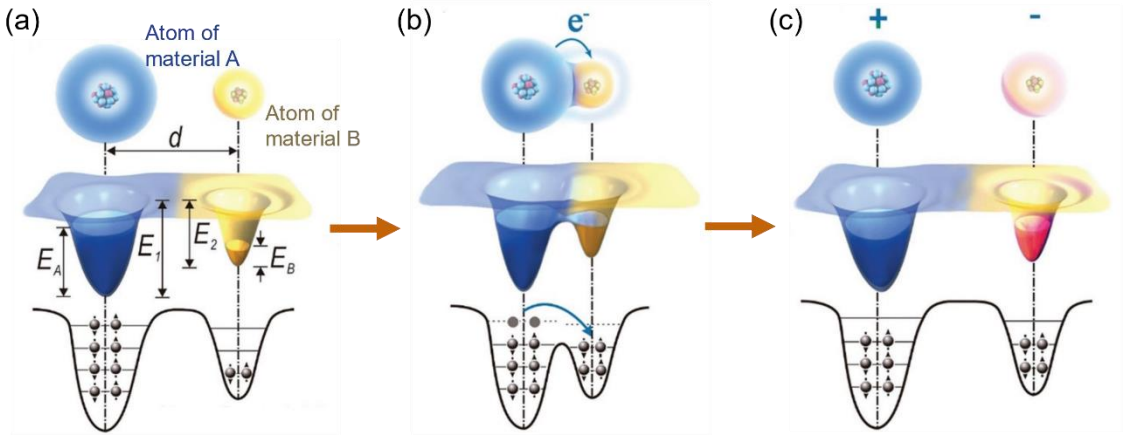


Figure 1.4 – Schematic diagram of the interatomic interaction model for general contact electrification cases (Reproduced with permission from Ref. [29], Copyright 2018, John Wiley and Sons).

to the energy barrier E_2, as showing in Figure 1.4(c). Although this model demonstrates that electron transfer is the dominant process during CE, ion transfer or material transfer can also occur in parallel, although they are minor processes due to the high energy required for them to occur [29].

1.3. Triboelectric nanogenerators: an overview

A triboelectric nanogenerator is an electrical energy generator that harvests and converts ambient mechanical motions into electric power with high efficiency and producing high output powers [39–43]. A basic TENG structure consists of two triboelectric layers with opposite tribo-polarities, an air gap between them and two metallic electrodes (Figure 1.5). The periodical contact-separation or sliding motion of the two tribo-materials then leads to the generation of electrical energy through a

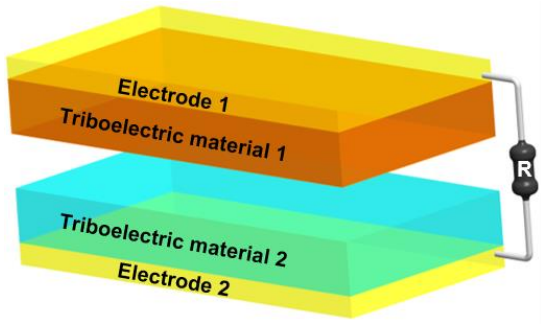


Figure 1.5 – Structure of a basic TENG composed by two materials with opposite tribo-polarities and two metallic electrodes.

combination of contact-induced electrification and electrostatic induction (see section 1.3.2 on the various working modes of TENGs). As we have seen, when the two tribo-materials come into contact, surface transference of electron or ions occurs between them (contact electrification), creating an electrical potential difference upon separation. By cyclically contacting and separating these charged surfaces, electrons will flow through an external load, generating a large electrical output [12,44–46].

1.3.1. Triboelectric materials and optimization strategies

The contact electrification performance depends significantly on the materials chosen as triboelectric layers, as these affect the amount of surface charges generated. The triboelectric polarity refers to the ability of a material for losing/gaining electrons [47]: materials with positive polarity [such as glass, wool, silica, aluminium or poly(methyl methacrylate) (PMMA)] tend to lose electrons when contacting materials of opposite tendency [such as PET (Polyethylene terephthalate), Kapton, PTFE (Polytetrafluoroethylene) or PDMS (Polydimethylsiloxane)], which tend to gain electrons during the contact electrification process. In general, most materials, including metals, polymers and wood, display triboelectrification effects. All these materials are potential candidates to fabricate new energy harvesting devices, but to maximize performance, materials selection for TENGs is based on the triboelectric series that orders them according to the polarity and the amount of charge that is transferred when coming in contact with another object (Figure 1.6). Typically, materials close to each other in the triboelectric series show small charge transfer, while the most distant materials in the

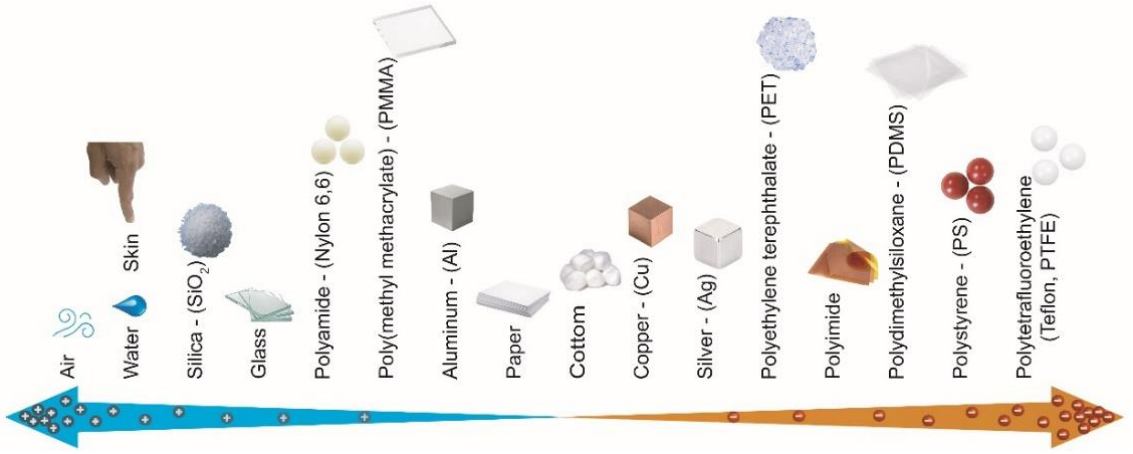


Figure 1.6 – Triboelectric series for the most promising series of materials (adapted from Refs. [41,47]).

series have the highest charge transfer between them [30,47,48]. It is from this latter category that TENG materials are usually chosen and properly modified [49,50].

Beside the choice of triboelectric materials based on triboelectric series, there are strategies and engineering protocols to improve the TENG performance, as shown in Figure 1.7. The enhancement of triboelectrification can be obtained by modifying surface morphologies by physical or chemical techniques. Examples of such nanopatterns include pyramid-, square-, micro- or hemisphere-based nanopatterns to enhance the effective contact area between the surfaces of the materials [41,47,51–53]. However, relatively bulky (micrometer scale) structures on the surfaces can lead to excessive and undesirable friction forces and consequently degrade the electrical outputs generated by the triboelectric nanogenerator [41]. On the other hand, nanoscale surface morphologies can restrict material selection, limit controllability and exhibit weak mechanical properties [54]. Therefore, it is important to note that there can be a reduction of the TENG performance when the structure created on the surface is irregular because it can increase the friction force [54]. Typically, the improvement of the efficiency of the nanogenerator with structured films can be related with:

- The sophisticated structures on films surface increasing the effective contact electrification and the tribo-charges generated on the surfaces during contact [55];

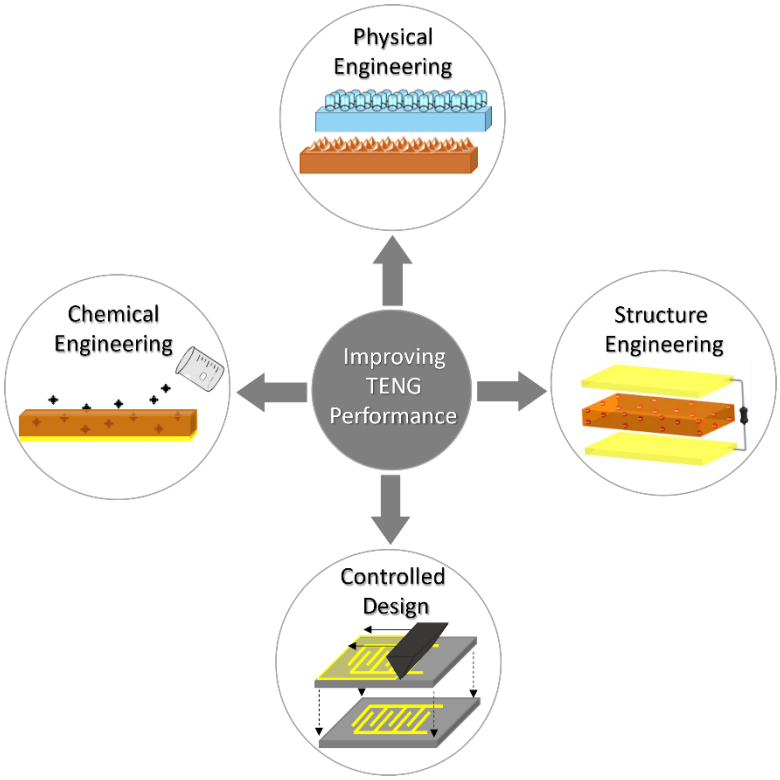


Figure 1.7 – Strategies to improve TENG performance.

- Micro air-voids in the films that can improve the capacitance change during pressing/bending processes and induce an additional dielectric constant enhancement [56];
- A larger dipole moment formed in the microstructured films between the electrodes because of an increased distance between the tribo-charges [57].

To further improve the output performance of TENGs, triboelectric films can be chemically modified using molecules, nanotubes, nanowires or nanoparticles, which enhance the surface charge density of tribo-materials, improving triboelectrification. Surface functionalization can lead to a change in the triboelectric sequence of a given material in the triboelectric series due to a change of the surface potential [49]. The doping of nanostructures/nanoparticles onto triboelectric materials and/or on its surfaces can change the effective permittivity and the triboelectric film thickness can be optimized using micro/nanomaterials. This will increase surface charge density and the relative permittivity of the tribo-materials to be effective for electrostatic induction. To increase the relative permittivity, the triboelectric films can also be doped with dielectric nanoparticles with high relative permittivity, such as iron(III) oxide (Fe_2O_3; $\varepsilon_r = 14$) or strontium titanate ($SrTiO_3$; $\varepsilon_r = 300$).

Polymer doping was shown to improve TENG performance by increasing the amount of surface charges and the relative permittivity of the tribo-materials. Graphite particles mixed into PDMS led to a rise of the power density by a factor of 3 [58]; integrating polystyrene (PS) and carbon nanotubes onto a polyvinylidene fluoride (PVDF) film increased the surface charge density by a factor of 11 [59]. Furthermore, the functional groups exposed on the surface of organic material can be changed to enhance the surface chemical potential [60–62]. For example, fluoro has the highest tendency to gain electrons. Thus, as perfluorinated materials (such as Teflon) are the most triboelectrically negative choices, and they are covered with the fluoro group, it is possible to tune the triboelectric charge density by surface functionalization with molecules of this head group (-F) [61].

1.3.2. Basic modes of operation

TENGs are classified by the different electrodes configurations and/or different relative motion of the triboelectric materials to perform their fundamental electrostatic induction. Four basic modes have so far been realized [40,41,63–66]: vertical contact-separation, lateral sliding, single-electrode, and freestanding triboelectric-layer. Each mode presents different theoretical frameworks that allow to evaluate the performance

of TENGs in terms of the expected short-circuit transferred charges (Q_{SC}), open-circuit voltage (V_{OC}) and general $V - Q - x$ (voltage-charge-position) relationship. Table 1.1 shows a summary of the main equations of the relevant quantities that characterize TENGs. These equations provide a general understanding and guidance to increase the electrical outputs of TENGs.

Table 1.1 – Summary of the main theoretical relations for the different working modes of triboelectric nanogenerators. In the table, σ is the static charges density, *Q* is the transferred charges, *S* the metal area, ε_0 the permittivity of free space, d_0 is the effective dielectric thickness given by $d_1/\varepsilon_{r1} + d_2/\varepsilon_{r2}$ (with $d_{1,2}$ and $\varepsilon_{r1,r2}$ the thicknesses and relative dielectric constants of dielectrics 1 and 2, $x(t)$ the time dependent distance between the two tribo-material, *w* the transversal width, *l* the length in the longitudinal direction, C_i are the equivalent capacitances formed between electrical nodes and *g* the gap between reference and primary electrodes.

Modes	Q_{SC}	V_{OC}	$V - Q - x$	Reference
Vertical Contact-Separation (VCTENG)	$\frac{S\sigma\, x(t)}{d_0 + x(t)}$	$\frac{\sigma\, x(t)}{\varepsilon_0}$	$V = -\frac{Q}{S\,\varepsilon_0}[d_0 + x(t)] + \frac{\sigma\, x(t)}{\varepsilon_0}$	[64]
Lateral Sliding (LSTENG)	$\sigma x w$	$\frac{\sigma x d_0}{\varepsilon_0(l - x)}$	$V = \frac{d_0}{\varepsilon_0 w(l - x)}Q + \frac{\sigma d_0 x}{\varepsilon_0(l - x)}$	[64,67]
Single-Electrode	$\frac{\sigma w l}{1 + \frac{C_1(x)}{C_2(x)}}$	$\frac{\sigma w l C_2}{C_1C_2 + C_2C_3 + C_1C_3}$	–	[64]
Freestanding Triboelectric-Layer	$\frac{2\sigma S x}{d_0 + g}$	$\frac{2\sigma x}{\varepsilon_0}$	$V = \frac{d_0 + g}{\varepsilon_0 S}Q + \frac{2\sigma x}{\varepsilon_0}$	[64,68]

1.3.2.1. Vertical contact-separation mode (VCTENG)

Triboelectric nanogenerators based on the vertical contact-separation mode work by an intermittent impact or shock and can harvest energy from water motion or walking, for example. This mode can be divided into two types: dielectric/dielectric and conductor/dielectric [Figure 1.8(a) and (b), respectively] [64,69].

Figure 1.8(a) shows an example of this working mechanism for a triboelectric nanogenerator in the dielectric/dielectric vertical contact-separation working mode, when using two similar dielectric films and two electrodes on the top and the bottom surfaces of the assembled device structure. Dielectrics 1 and 2 are defined as having thicknesses d_1 and d_2, respectively. In the initial state [Figure 1.8(a)-I], the two materials have no

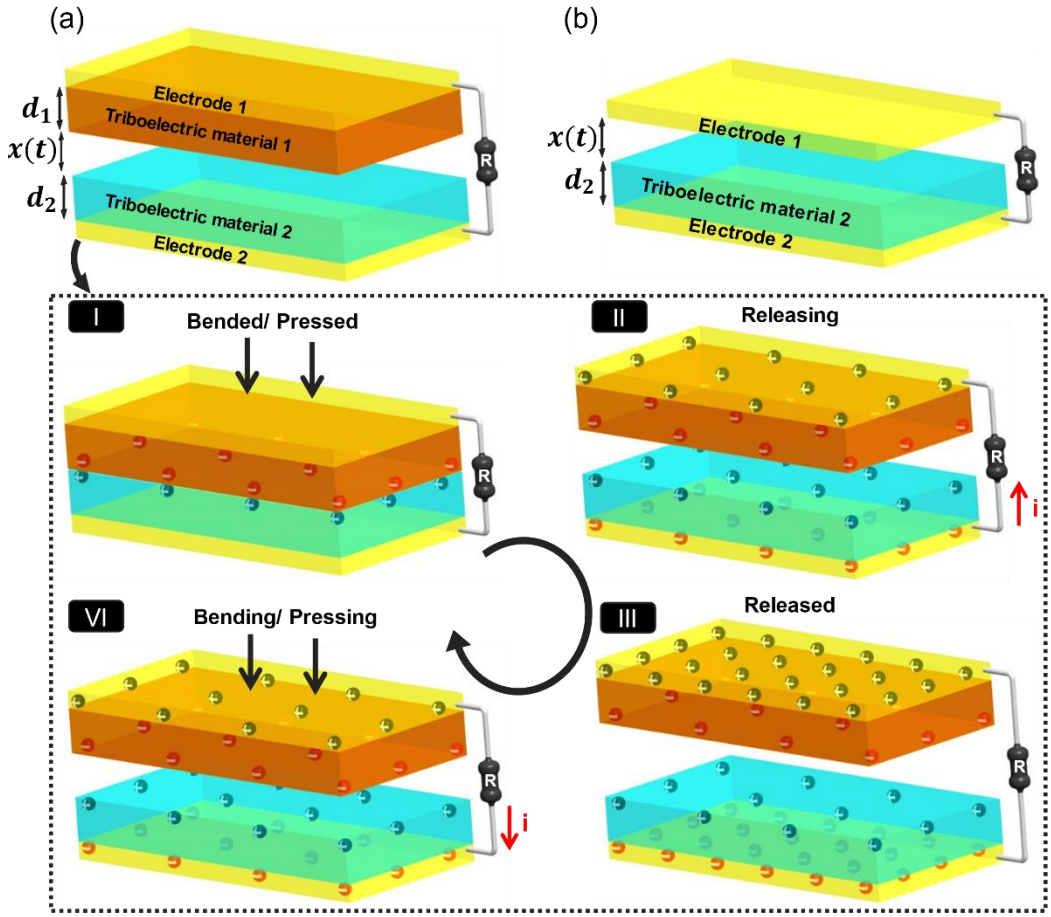


Figure 1.8 – Basic vertical contact-separation working of a TENG (adapted from Refs. [41,64,65]): (a) dielectric/dielectric; (b) conductor/dielectric.

triboelectric charges on their surfaces. Applying an external force (bending or pressing the device), the distance (x) between the two triboelectric materials will vary and they will come into contact with each other [Figure 1.8(a)-II]. At that time, charges transfer from one tribo-material to the other due to the triboelectric effect [41]. This way, one material will have negative static charges (density $-\sigma$) and the other positive static charges (density $+\sigma$), assuming that triboelectric charges are evenly distributed on the surfaces of both insulators. Removing the applied force [Figure 1.8(a)-III], the distance x starts to increase and the surfaces of the two insulators, now with opposite tribo-charges, are separated. Therefore, an electric potential difference is induced between the upper and lower electrodes and the total instantaneous charges on each electrode is $+Q$ and $-Q$ [64]. Electrons then flow between the electrodes through the external circuit, generating a positive current. Thus, the top and bottom electrodes accumulate induced charges with negative and positive sign, respectively [Figure 1.8(a)-IV]. Applying again an external force, the distance between the triboelectric surfaces decreases and, consequently, electrons flow from the top electrode back to the bottom electrode

(negative current) and there is a decrease of the amount of induced charges [Figure 1.8(a)-V]. When the two triboelectric materials return to the initial state, the power generation process restarts [Figure 1.8(a)-II] [24,41]. In Figure 1.8(b) the working mechanism is similar but dielectric 1 is replaced by metal 1, which plays the roles of both triboelectric layer and electrode [64].

Triboelectric nanogenerators working on the contact-separation mode are characterized by simple designs and high power densities [24] with several designs, such as arch-shaped, zigzag-structured or spring-supported, having been developed.

1.3.2.2. Lateral sliding mode (LSTENG)

The LSTENG has an identical structural design and types as the vertical contact-separation mode [Figure 1.9(a)] [64]. This working mode has the bottom part fixed but the top part slides along the longitudinal direction, so that two basic triboelectrification processes can occur: contact and lateral sliding [41]. When two triboelectric materials come in contact by a sliding motion parallel to the surfaces, opposite triboelectric charges are also created on their surfaces [$+\sigma$ at dielectric 1 and $-\sigma$ at dielectric 2; Figure 1.9(a)-I]. Applying a lateral external force, a tribo-polarization occurs along the sliding direction by an alternative change in the effective contact area, which creates an electric potential difference between electrodes. Consequently, a current flows from the top to the bottom electrode [Figure 1.9(a)-II] and continues until the two triboelectric materials are

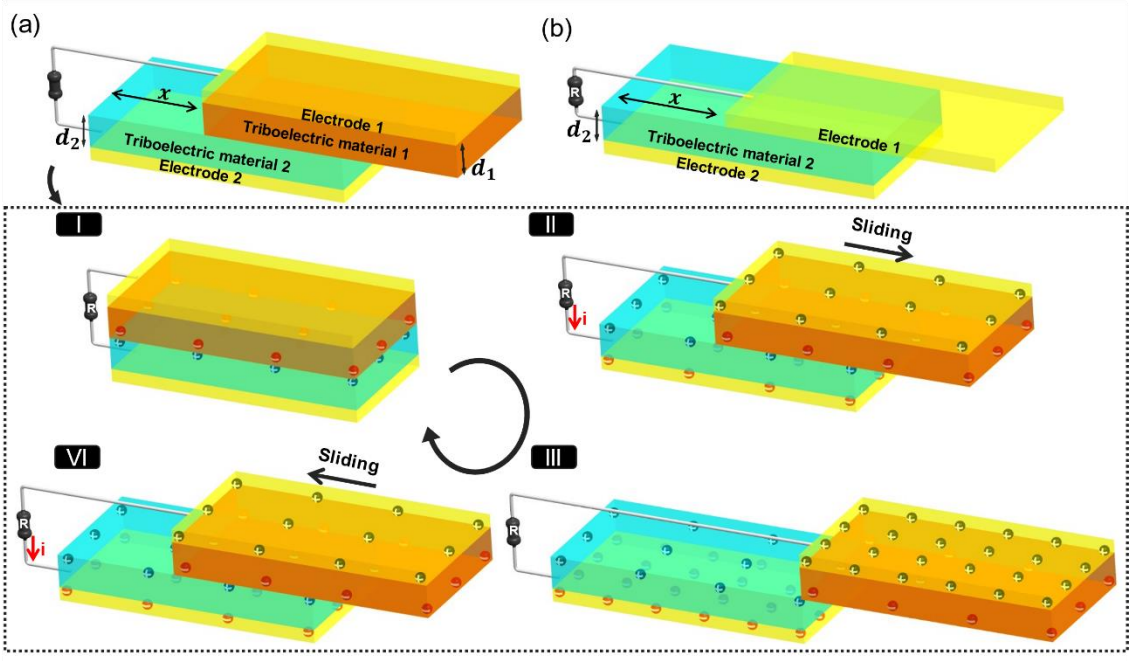


Figure 1.9 – Basic lateral sliding working mode of TENG (adapted from Refs. [41,64]): (a) dielectric/dielectric; (b) conductor/dielectric.

separated [Figure 1.9(a)-III] [41]. Afterwards, dielectric 1 moves inwards relative to dielectric 2, which results in a current flow in the external circuit with the opposite sign of that of the sliding out process [Figure 1.9(a)-IV]. When the two dielectrics return to the initial state, the charged triboelectric surfaces get in full contact, thereby again initiating the cycle [Figure 1.9(a)-I] [41]. For the conductor/dielectric TENG, the basic structural design is illustrated in Figure 1.9(b) and, in this case, electrode 1 is the triboelectric material and also one of the electrodes itself [64].

The sliding mode was already demonstrated to generate energy from harvesting wind, hydropower and gas flows. It can be achieved using planar motions, disc or cylindrical rotations. However, sliding-based TENGs can have a large frictional force between tribo-surfaces during the working process, which can limit the device durability and energy conversion efficiency [70]. Nevertheless, this mode has several advantages, as the relative lateral-sliding between triboelectric materials is more effective to generate tribo-charges than pure contact, and consequently there is an enhanced output power [24].

1.3.2.3. Single-electrode mode (SETENG)

TENGs based on a single-electrode can work using the vertical contact-separation and sliding modes [41,71]. The working principle is schematically shown in Figure 1.10, from which it is perceivable that one electrode (primary electrode; with thickness d_m, width w and length l) can work as the triboelectric material or be attached on the surface of a triboelectric material (with thicknesses d_0), while the other electrode is an electric potential reference (reference electrode) located at a gap g underneath the primary electrode [64]. In this working mechanism mode, only one electrode is attached to or

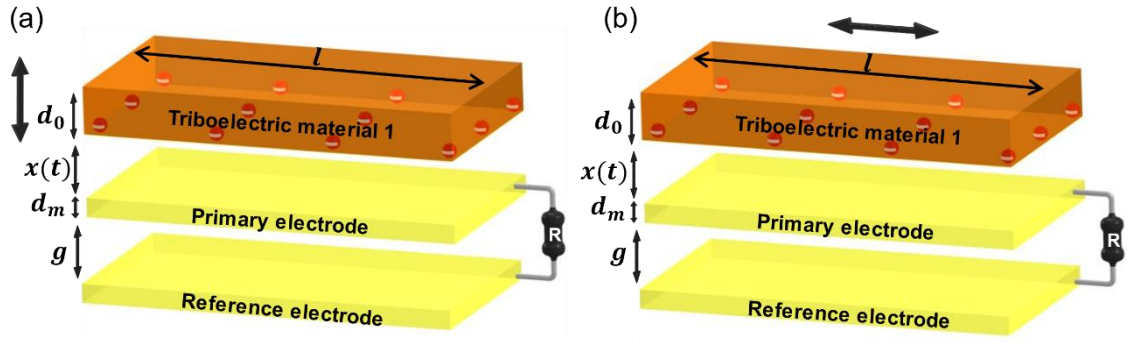


Figure 1.10 – Basic single-electrode working mode of TENG (adapted from Ref. [64]): (a) conductor/dielectric contact mode; (b) conductor/dielectric sliding mode.

acts as the triboelectric material and the reference electrode can be positioned anywhere in the space, even directly be the ground [72].

Considering the contact-mode type as reference [Figure 1.10(a)], when an external force is applied, dielectric 1 moves along the vertical direction and the distance x with the primary electrode varies, while the position of the two electrodes (primary and reference) is maintained (fixed). When the triboelectric 1 and the primary electrode are in contact, negative ($-\sigma$) and positive ($+\sigma$) tribo-charges are respectively induced on their surfaces. The total transferred charges from the primary to the reference electrode is Q and, under the minimum achievable charge reference state, the total amount of charges at the primary electrode is $\sigma wl - Q$ and at the reference electrode is Q [64].

The sliding mode [Figure 1.10(b)] is a hybridization between the lateral sliding mode described in the previous section and the single-electrode contact-mode. A TENG based on a single-electrode was reviewed as the most practical and feasible design because, contrarily to the previously discussed modes, there is no need for both triboelectric layers to be connected to an external circuit [24]. In fact, this energy harvesting strategy allows one of the triboelectric materials to move freely without connection to an external circuit [24,64]. Nevertheless, the maximum transferred charge efficiency can be only 50% due the electrostatic shielding of the primary electrode that limits the SETENGs performance.

1.3.2.4. Freestanding triboelectric layer mode (FTENG)

Another triboelectric mode, called freestanding-triboelectric-layer based TENGs (Figure 1.11) was created [24,40,64,68,73]. This mode, with two typical configurations (contact and sliding), is constituted by the triboelectric material alternatively approaching two fixed electrodes. Freestanding TENGs show improved energy conversion efficiency, minimized surface wear and long-term stability [24].

There are two typical subcategories for contact-mode freestanding TENGs with their working principles being very similar: dielectric and metal freestanding layer [Figure 1.11(a) and (b), respectively] [64]. The first configuration has a dielectric layer with thickness d_1 (relative dielectric constant ε_{r1}), two metal layers forming two triboelectric pairs (also serving as electrodes), and an air gap between these metallic layers (with spacing g). Applying an external force to the dielectric material, it is forced to come into alternating contact with the two metal layers, which induces tribo-charges on the top and bottom surfaces of the dielectric due to triboelectrification. The tribo-charge density of the top and bottom triboelectric surfaces is $-\sigma$ and, due to charge conservation, electrodes 1 and 2 will have the same amount of positive charges. Considering both

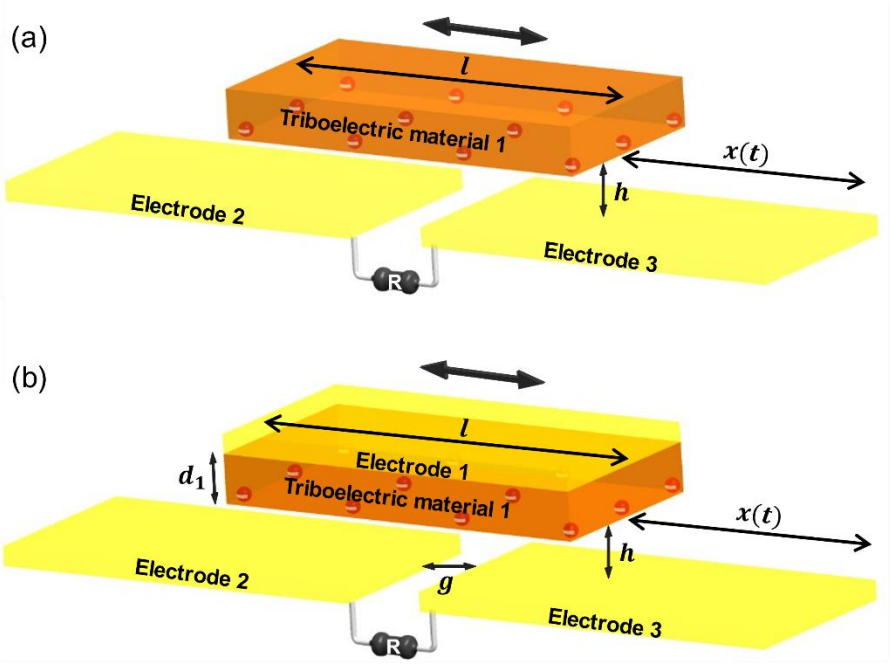


Figure 1.11 – Sliding-mode freestanding working mode of TENGs (adapted from Refs. [41,64]): (a) dielectric and (b) metal freestanding layer sliding TENG.

electrodes much larger than the air gap, all the electric potential on electrodes 1 and 2, the top and bottom surfaces of dielectric 1 are constant. The change of the position of triboelectric material 1 then induces an electron flow between electrode 1 and 2 through an external circuit. Figure 1.11(b) shows the metal freestanding layer TENG and corresponding working principle which is similar to the dielectric configuration previously analyzed. This new configuration allows to increase the TENGs' versatility and applicability to generate electric power from any external mechanical motion.

The same two subcategories (dielectric and metal freestanding layers) apply for the sliding-mode [64,68], as shown in Figure 1.11(a) and (b), respectively. In the dielectric case, the freestanding material only contains a dielectric, while in the metal case the dielectric freestanding material has a thin metal film deposited on top. These two structures are thus very similar, with the freestanding triboelectric material strongly influencing the electrical outputs of these nanogenerators. The sliding freestanding TENG has two electrodes placed as illustrated in Figure 1.11 and a freestanding triboelectric material on top at a distance h, called the freestanding height [64]. Otherwise, the main working principle of the contact and sliding freestanding TENGs are very similar.

The freestanding mode, compared to the lateral sliding-mode, can harvest energy without direct physical contact between the two tribo-surfaces and will decrease material wear and heat generation during the frictional process. This mode is characterized by its ultra-robustness and high-energy conversion efficiencies [24].

1.3.3. Applications of TENGs

Based on the four basic modes previously reviewed, several TENGs have been developed to harvest different types of energy, depending on specific applications (Figure 1.12) [74]. These nanogenerators can work, for example, as power sources to feed low-power electronic devices [75–78] or as self-powered sensors [39,41,63,79–81]. However, TENGs cannot feed directly commercial electronics because they are alternating current (AC) power sources. To feed commercial electronic devices, this current must be converted into a direct current (DC) using power management circuits to allow energy storage in a battery or a capacitor during electrical generation [82].

This thesis is focused on the study of triboelectric energy generation for ocean and harsh environments due to the increased energy need for real-time monitoring under these conditions towards applications for IoT. However, many authors have demonstrated the potential of TENGs for a wide range of applications, as shown in Figure 1.12. In the field of implantable medical devices, H. Ryu *et al.* an enclosed five-stacked inertia-driven TENG (I-TENG) to convert body motion and gravity into electricity to feed a cardiac pacemaker [Figure 1.13(a) and (b)] [83]. The I-TENG was composed by amine-

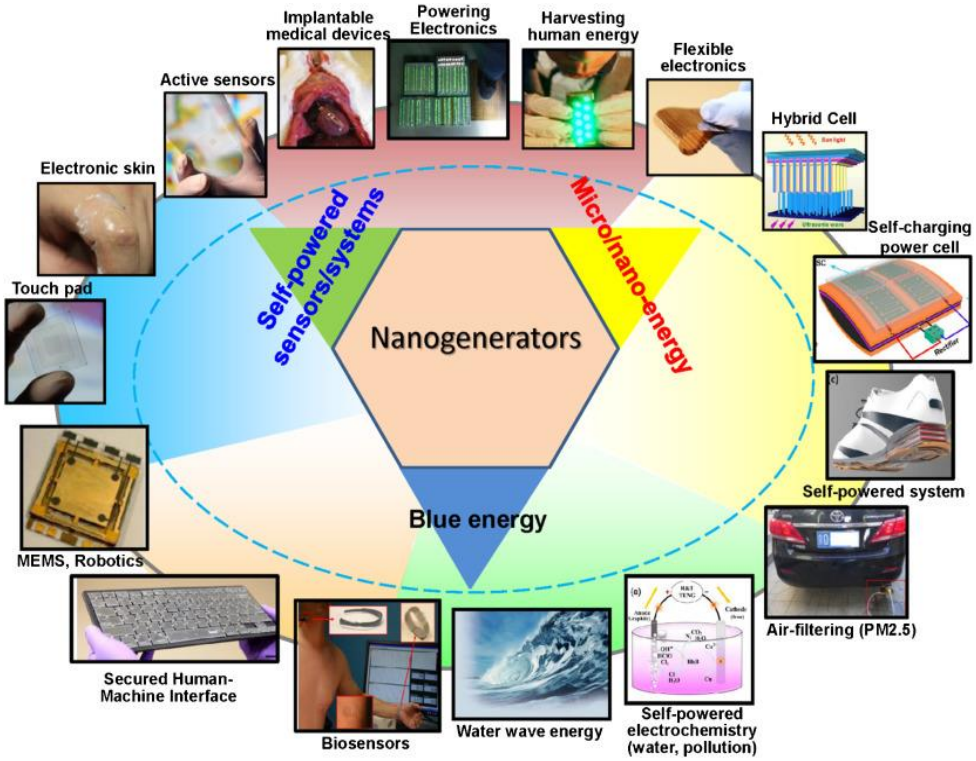


Figure 1.12 – Schematic diagram showing major application fields of TENGs as micro-/nano-energy source, blue energy and self-powered sensors. Reproduced with permission from Ref. [74], Copyright 2017, Elsevier.

functionalized poly(vinyl alcohol) (PVA-NH2) and perfluoroalkoxy (PFA) as triboelectric materials which come into contact due to oscillations occurring during body motions. In this work, the authors implemented an enclosed five-stacked I-TENG in the back of a mongrel to monitor device activity and estimate the amount of energy generated during 24 h [Figure 1.13(c)]. The results showed that there was more activity during the daytime than at night and the device generated ~ 144 mW. They also charged parallel-connected low-equivalent series inductance capacitors with a capacitance of 60 μF showing that device had sensibility to generated energy with small movements that occurred during sleep [Figure 1.13(d)]. Then, a cardiac pacemaker was also integrated with the I-TENG, which allowed demonstrating the applicability of the I-TENG to harvest in vivo energy for charging low-power implantable electric devices.

Figure 1.13(e) and (f) shows a self-powered triboelectric auditory sensor (TAS) which is an electronic hearing system for intelligent robotic applications [84]. This prototype is composed by fluorinated ethylene propylene (FEP)/gold (Au) and Au/Kapton membrane as triboelectric pairs. Under acoustic waves, the Kapton membrane will vibrate and induce a contact-separation motion between FEP and Au, generating electric signals. The authors tested the sensitivity and directional response of the TAS under sound pressure levels (SPL) from 50 and 110 dB. Figure 1.13(i) shows that the voltage generated by TAS exponentially increase with the sound intensity and even a weak sound was enough to be distinguished from the noise [inset of Figure 1.13(i)]. Finally, the TAS was incorporated with intelligent robots showing high-quality music recording [Figure 1.13(j)] and accurate voice detection.

The increasing demand for wearable devices has raised interest in textile-based TENGs. J. Huang *et al.* developed an all-fiber-structured TENG [Figure 1.13(k)] with ethyl cellulose/polyamide 6 nanofiber and MXene-based PVDF nanofiber triboelectric positive materials and MXene-based PVDF nanofiber mats as positive and negative triboelectric materials, respectively [85]. The durability and stability of the TENG to work as sensor was tested and it was obtained that voltage outputs remained constant for at least ~ 14000 cycles. Different capacitors were also charged to demonstrate the ability of TENG to work as an energy-harvesting power source, as shown in Figure 1.13(l). Furthermore, the all-fiber TENG was able to directly light up light-emitting diodes (LEDs) using arms motions and clapping of hands [Figure 1.13(m)]. Lastly, it was demonstrated that the current generated by the all-fiber TENG had different values for walking, clapping hands and moving arms which showed its potential to work as a self-powered wearable sensor [Figure 1.13(n)].

Triboelectric nanogenerators that allow hands-free interaction with machines have also been proposed. X. Pu *et al.* developed a mechnosensational TENG [msTENG;

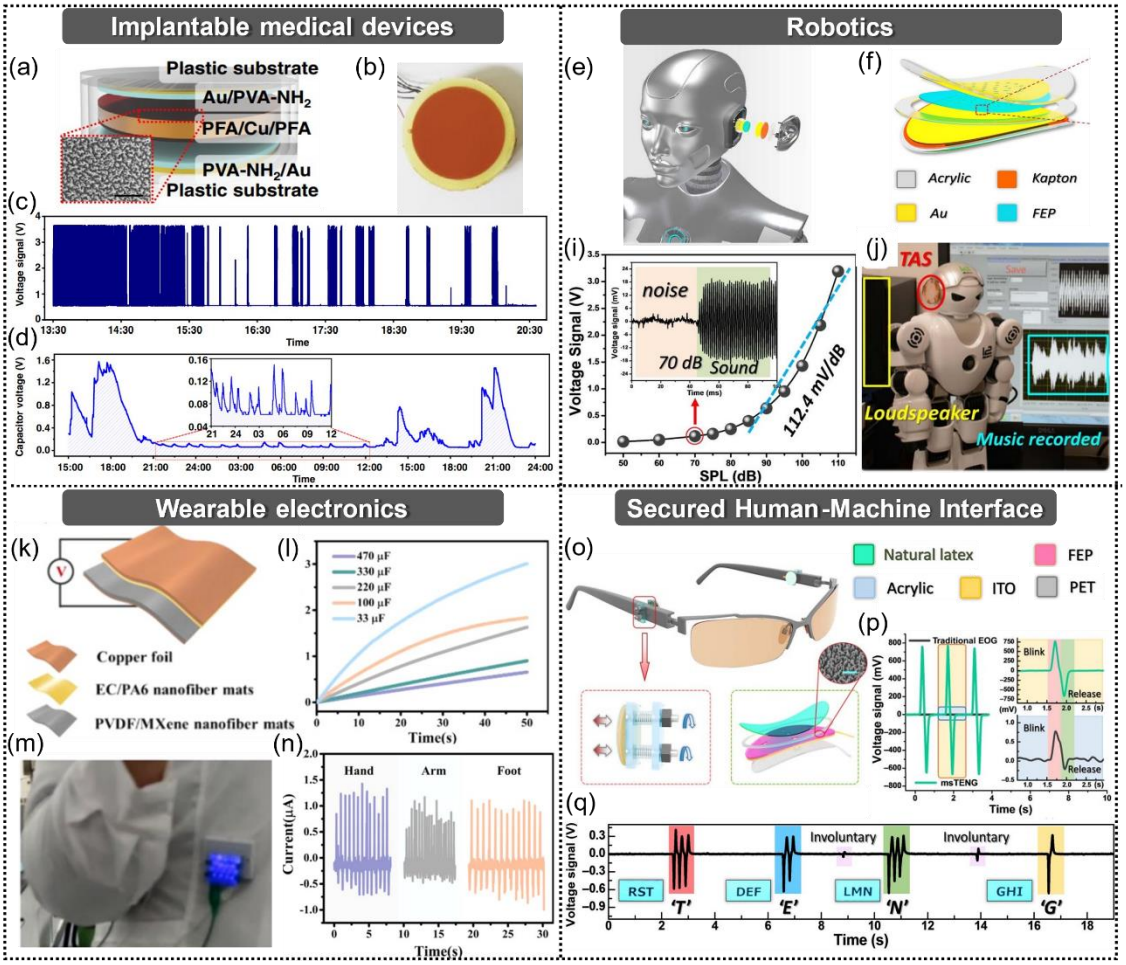


Figure 1.13 – (a) Schematic diagram and (b) photograph of the I-TENG. (c) Voltage signal generated by the I-TENG in an animal preclinical test during the daytime. (d) Performance of a capacitor charging over a one day with the I-TENG implemented in the back of a mongrel. Reprinted with permission from ref. [83], Copyright 2021, Springer Nature. Schematic diagram of (e) the triboelectric auditory system for robotics and (f) the TAS. (i) Response of the TAS under various sound pressure levels. (j) TAS application for music recording . From [84]. Reprinted with permission from AAAS. (k) Schematic diagram of the all-fiber-structured TENG. (l) Performance of the TENG to charge different commercial capacitors. (m) Demonstration of TENG to light up LEDs using arm movements. (n) Current generated by the all-fiber-structured TENG when harvesting energy from clapping hands, moving of arms, and walking. Reprinted (adapted) with permission from [85]. Copyright 2021 American Chemical Society. (o) Schematic diagram of the msTENG smart sensor glasses. (p) Comparation between the output voltage of the msTENG and the electro-oculogram. (q) Demonstration of a hands-free typing system. Modified from [82]. © The Authors, some rights reserved; exclusive licensee AAAS. Distributed under a CC BY-NC 4.0 License (http://creativecommons.org/licenses/by-nc/4.0/).

Figure 1.13(o)] that translates eye blink into control command to be applied in smart home control system and wireless hands-free typing system [86]. The msTENG works based on the single-electrode mode operation and was mounted on one of side arms of

glasses. The TENG is composed by FEP/indium tin oxide (ITO) as one tribo-pair and natural latex as the opposite tribo-material which will directly contact with the skin near the eye. In this work, it was demonstrated that the output voltage generated by msTENG is 750 times higher than that of the electro-oculogram [Figure 1.13(p)], which demonstrated its high sensitivity to detect micromotions of eye blinking. Then, the authors integrated a signal processing circuit with the msTENG smart sensor glasses to control household appliances such as lamp, fan, and the doorbell. Furthermore, a hands-free typing system using the eye blink was also developed to work as a virtual keyboard where each key could be selected based on the detected eye blink times during a specified period [Figure 1.13(q)].

Chapter 2

Experimental Techniques

Chapter 2

Experimental Techniques

In this chapter, a brief description of the fabrication techniques used to develop the electrodes for the triboelectric devices is present. In addition, we also present a brief description of the experimental setups used to systematically characterize the performance of the materials and triboelectric devices.

2.1. Electrodes fabrication

2.1.1. Direct current (DC) magnetron sputtering deposition

DC Magnetron Sputtering is a physical vapor deposition method performed in vacuum, where a magnetically confined plasma is created between the target and the substrate by introducing an inert gas (typically argon) in the chamber and applying a voltage to the target. The target material is bombarded with ionized gas molecules, causing atoms from the target to be sputtered out in the process. Then, the sputtered atoms have a certain kinetic energy and are deposited on the surface of the substrate.

Figure 2.1(a) shows a typical schematic diagram of a DC magnetron sputtering, where the target material works as cathode and a voltage of the order of hundreds of volts is applied between the cathode and anode. Then, a magnetic field is applied near

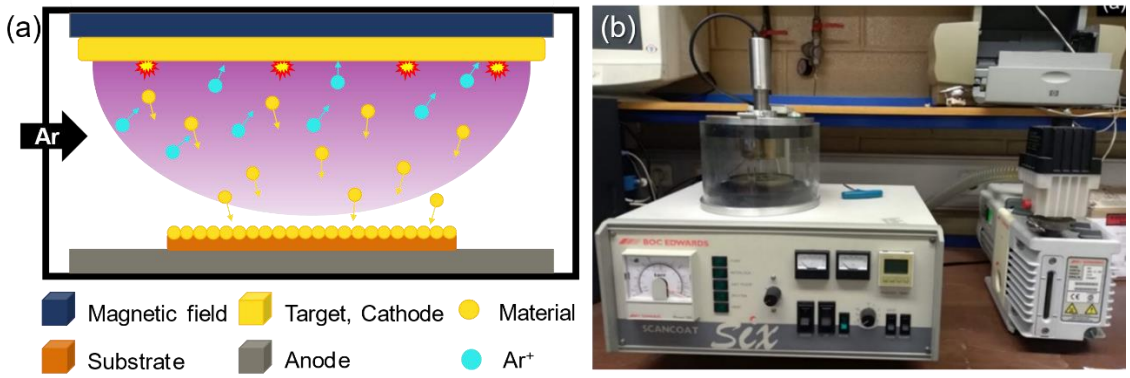


Figure 2.1 – (a) Schematic diagram of mechanism a typical magnetron sputtering system. (b)Magnetron Sputtering system available at IFIMUP facilities.

the cathode region which concentrate and intensifies the plasma in the space immediately above the target to trap electrons near the target surface. These electrons ionize the *Ar* atoms into Ar^+ cations which are then accelerated to collide with the target. After impact, target atoms are released and travel to the substrate, where they form layers of atoms in thin film form.

A Magnetron Sputtering by *BOC Edwards [Scancoart six*; Figure 2.1(b)] was used to deposit gold electrodes on one of the surfaces of PTFE and Nylon 6.6. In this work, gold depositions were performed at IFIMUP facilities, where two depositions on one surface of each triboelectric material were made using a pressure of ~ 1.5 mTorr, a current of 25 mA and a voltage of ~ 950 V during 300 s for each deposition.

2.1.2. Screen printing

The screen-printing technique has been considered one of the most cost-effective methods of depositing a variety of films on planar substrates and involves the direct contact transfer of ink from a stenciled mesh to a target substrate. This technique involves the use of a screen made of a fine mesh of silk or synthetic fibers that is initially completely porous across its entire surface and a squeegee to print the ink. The pore size of the screen is selected based on the rheological properties of the desired ink. The desired patterns on the mesh screen are performed by employing a photo emulsion that is photo-curable when exposed to ultraviolet (UV) light. Initially, the entire mesh screen is covered with the emulsion. After dry, a photolith of the desired pattern is attached on top of the mesh screen and exposed to UV light for 30 minutes. To reveal the pattern, the screen is rinsed with water and the exposed portion will remain on the screen, while the unexposed portion will peel away, leaving the screen porous. Thus, the ink only pass through the portion devoid of emulsion, printing only the desired pattern on the target substrate.

Figure 2.2(a) shows the schematic diagram of the screen-printing method. Initially, the clean substrate is fixed on the work bench using the vacuum system of the screen-printer to ensure it does not move during the printing process. With the vacuum switched on, the patterned screen is lowered and put on top of the desired substrate, and the ink is applied to the mesh at top of the pattern as shown in Figure 2.2(a)-I. The ink is distributed over the pattern using the squeegee and exerting light pressure to avoid contact between the mesh and the substrate. This allows for a more homogeneous print because there is an even layer covering the desired pattern. Passing the squeegee while

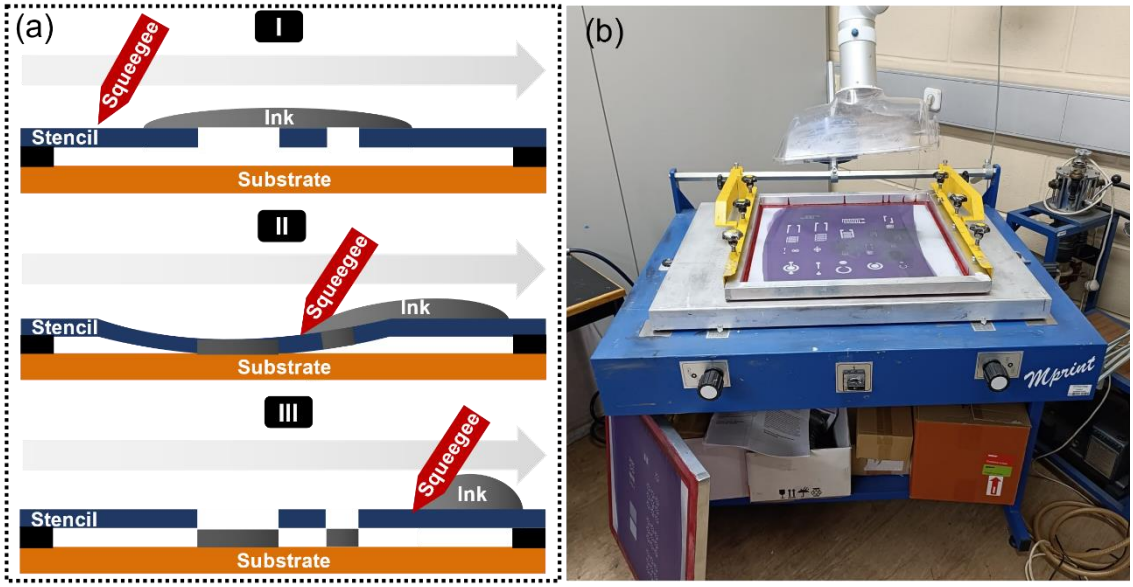


Figure 2.2 – (a) Schematic of the screen-printing technique. (b) Screen-printing system available at the IFIMUP facilities.

applying pressure, the ink is then transferred onto the substrate, printing the desired pattern on the substrate surface [Figure 2.2(a)-II and III].

Figure 2.2(b) shows the screen-printing system available at IFIMUP that was used to fabricate the flexible electrodes of silver (Ag) ink on the surface of the triboelectric materials used in this thesis. The chosen mesh used to print the Ag ink was PET 1500 90/48W, with a mesh-opening of 55 µm. It should be noted that the mesh opening was chosen based on the size of the material grains present in the commercial Ag ink datasheet, as suggested by the manufacturer. The silver ink used was by VFP Ink Technologies [87].

2.2. Systematic characterization setups

The typical characterization of a TENG requires the acquisition of voltage, current and charge during its operation. Figure 2.3 shows a typical setup for the full performance characterization of a TENG that was developed in this thesis. The voltage and current generated by a TENG were measured using a Keithley 6514 electrometer (IV) in parallel and serial connections with a load resistance, respectively, which allows obtaining the maximum generated output power (Figure 2.4). To perform each acquisition, the device is connected to a “resistances box” (III) with 11 different resistances (from 100 Ω to 470 MΩ) and relays controlled by an Arduino Nano. This Arduino is connected to the computer by a LabVIEW program (V) that allows to automatically scan the resistances range or to fix a desired resistance. The parallel and series connections are switched by

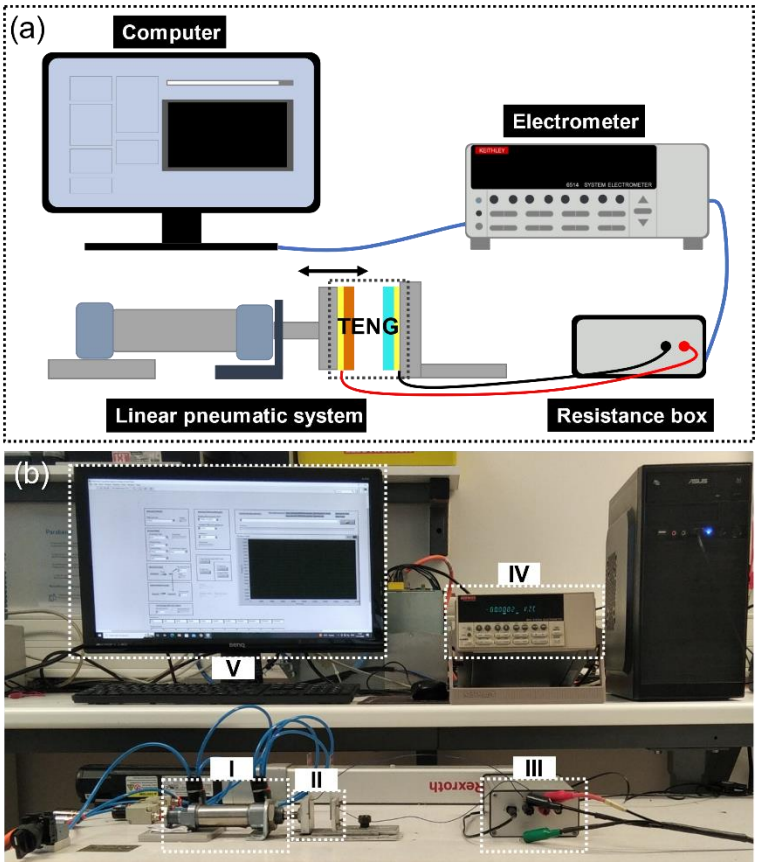


Figure 2.3 – (a) Schematic diagram and (b) photograph of the characterization setup of TENGs using the linear pneumatic system: (I) linear pneumatic motor; (II) moving (left) and fixed (right) plates where the two tribo-pairs of a TENG are assembled; (III) resistances box; (IV) Keithley

hand, but the resistances are scanned using a LabVIEW program that also allows viewing and saving the values of voltage and current measured by the electrometer. This LabVIEW control panel allows us to select and change the electrometer

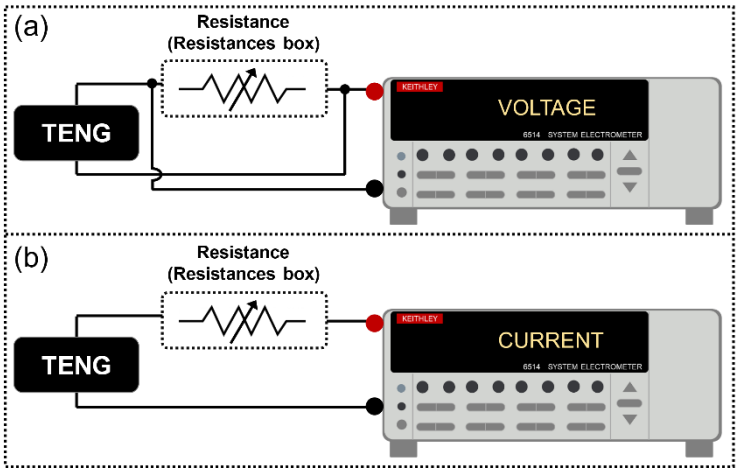


Figure 2.4 – Schematic diagram of the electrical circuit to measure (a) voltage and (b) current generated by a TENG.

acquisition configuration to measure the voltage, current, and charge generated by TENGs.

Figure 2.5(a)-(c) shows an example of the typical shape of voltage, current and charge peaks generated by a TENG using the linear pneumatic system (see section 2.2.1). To obtain the maximum peaks of voltage and current, in this case the TENG was connected to a resistance of 470 MΩ and 100 Ω, respectively [Figure 2.5(a) and (b)].

Regardless of the designed setup used to induce external mechanical motion, the standard characterization (Voltage, Current, Power; V-I-P) of TENGs [Figure 2.5(d)] is performed using the previous equipment and methodology [24]. The power generated by a TENG is calculated through the product of voltage and current achieved in each connected resistance. The V, I and P curves in Figure 2.5(d) are usually divided into three working-regions. Region I corresponds to low resistances, in which the electrical output characteristics are close to the short-circuit condition and there is a maximum transfer of charge between the materials (maximum current). On the other hand, for high resistance values (Region III), the output characteristics are close to the open-circuit condition, in which the maximum voltage saturates (and the current goes to zero). In Region II is achieved the maximum power point, where current drops dramatically but the voltage increases at a reverse trend. It should be noted that the optimum resistance varies with the TENG geometry, and the previous classification is not strict in terms of resistance delimitation [88].

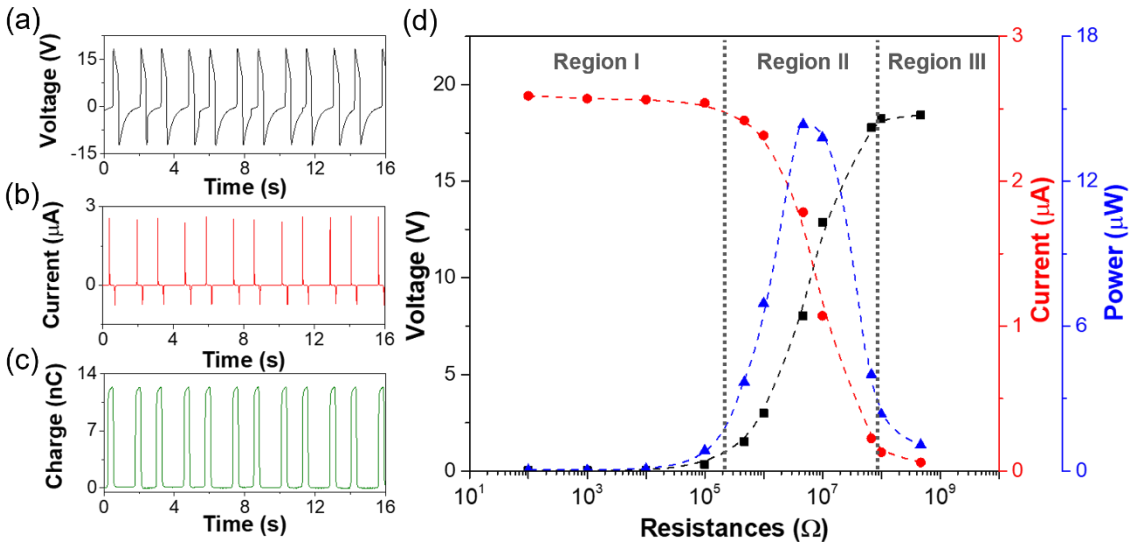


Figure 2.5 – Typical electrical peaks generated by a TENG under the action of the linear pneumatic system: (a) voltage; (b) current and (c) transferred charge. (d) Generated output voltage, current and power of a TENG for different load resistance values.

2.2.1. Linear pneumatic system

Testing the triboelectric performance of tribo-materials when incorporated on a TENG requires a systematic and controllable motion. To simulate the working principle of the contact-separation mode between two tribo-materials, a linear pneumatic motor was used (Figure 2.3; I). One triboelectric layer with the attached electrode is fixed on the moving plate on one end of the linear motor (II). The opposite triboelectric layer and corresponding electrode is assembled at a metallic plate fixed on the table (II), where the distance between the two tribo-materials can be varied up to a chosen distance.

Since the linear pneumatic system depends on compressed air, extra vibrations and pressure variations can affect the electrical measurements during the air compressing process that occurs periodically. Then, the electrical characterization of TENGs must be performed during the period without interferences, i.e., the measurement time must start after air compression and stop before the start of air compression.

2.2.2. 1-axis rotating frame system

To test the performance of TENGs for ocean applications, a rotating frame system that allows the replication of specific parameters of realistic water waves was developed in collaboration with inanoEnergy [89]. The system consists in a 1-axis rotating frame where TENGs are assembled and tilted using a servo motor DF15RMG controlled by an Arduino Uno. This mechanical system provides a support to the TENGs [Figure 2.6(a)], possessing a rotating frame where they are fixed (usually by gluing and attaching with ribbon, although holes for screwing exist).

Figure 2.6(a) shows the pitch movement that the 1-axis rotating frame can replicate by receiving the period of the motion T (in milliseconds) and the pitch A (in degrees) which is the maximum amplitude from the flat position (zero) to each side. It is the Arduino that communicates with the servo motor that allows to replicate the pitch movement that is one of the most relevant degrees of freedom of a floating body under wave actions [Figure 2.6(b)], as will be demonstrated in Chapter 3. The servomotor is able to rotate 180º, i.e. 90º for each side with steps as small as 1º. Concerning the period of rotation, 500 milliseconds is the minimum period that the microcontroller is able to achieve. The values of periods and pitch amplitudes to be tested are inserted directly on the Arduino code.

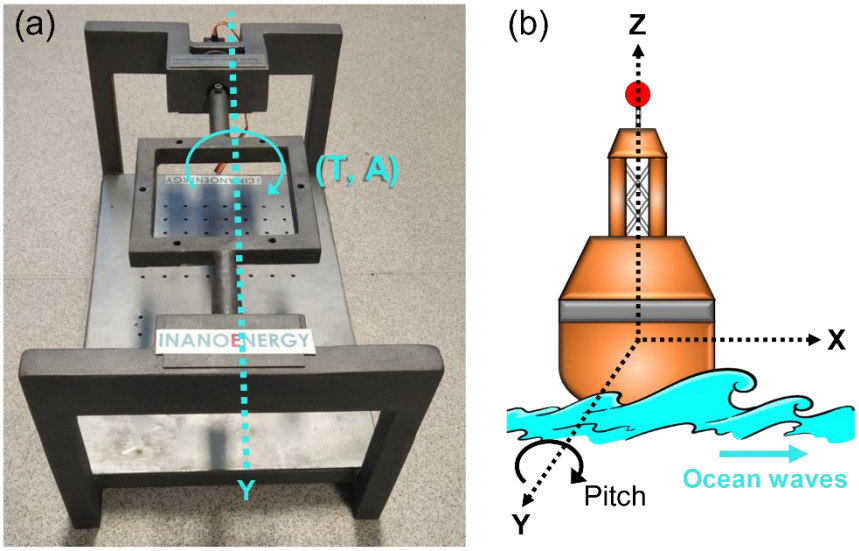


Figure 2.6 – (a) The pitch movement of a floating platform when subject to a water waves. (b) 1-axis rotating frame system with the equivalent motion parametrized by the period and pitch.

2.2.3. Data analysis software

Typically, a large amount of data is saved by the LabVIEW program when voltage and current time sequences are measured for several resistances and/or various pairs of periods and amplitudes. For a quick analysis, we used a Python routine developed by an MSc student that allows to achieve the automation of this data processing and displays a graph of the analyzed data in a few seconds [90].

The Phyton routine needs three parameters to realize the analyses: T (period of motion); N (number of maximum or minimum peak per period) and β (variable). This Python routine starts by identifying the number of maximum or minimum peaks per period of a specific data file. For example, if a TENG generates two peaks per period, the program will split the data file in half periods and search for one maximum and one minimum in each half period. The mean value of positive ($\overline{X_P}$) and negative ($\overline{X_N}$) peaks are calculated independently. In this step, the program can detect small peaks that do not correspond to the actual electrical output of the TENG. For instance, the Phyton routine can select noise peaks in half periods if the electrometer does not acquire one positive and/or negative peak in these half periods. To avoid this, the program will only select positive peaks above the threshold $\overline{X_P} - \beta\sigma_P$ and negative peaks under the threshold $\overline{X_N} + \beta\sigma_N$ (where σ_P and σ_N are the standard deviation of positive and negative peaks, respectively), as shown in Figure 2.7. The recommended value of β is 1 because it has shown close to perfect results in all developed TENGs. For the voltage and current of each test, this analysis software allows us to obtain the mean of the positive and

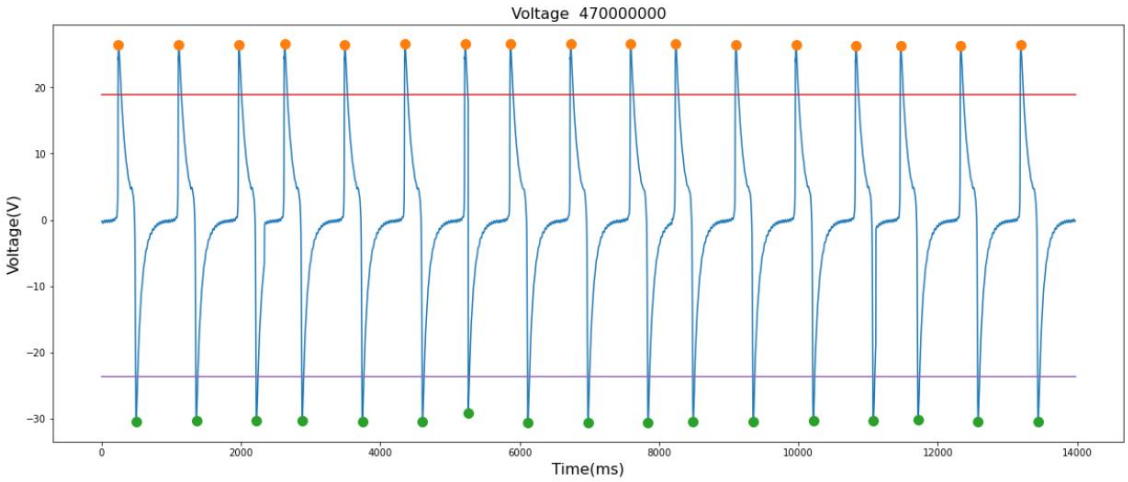
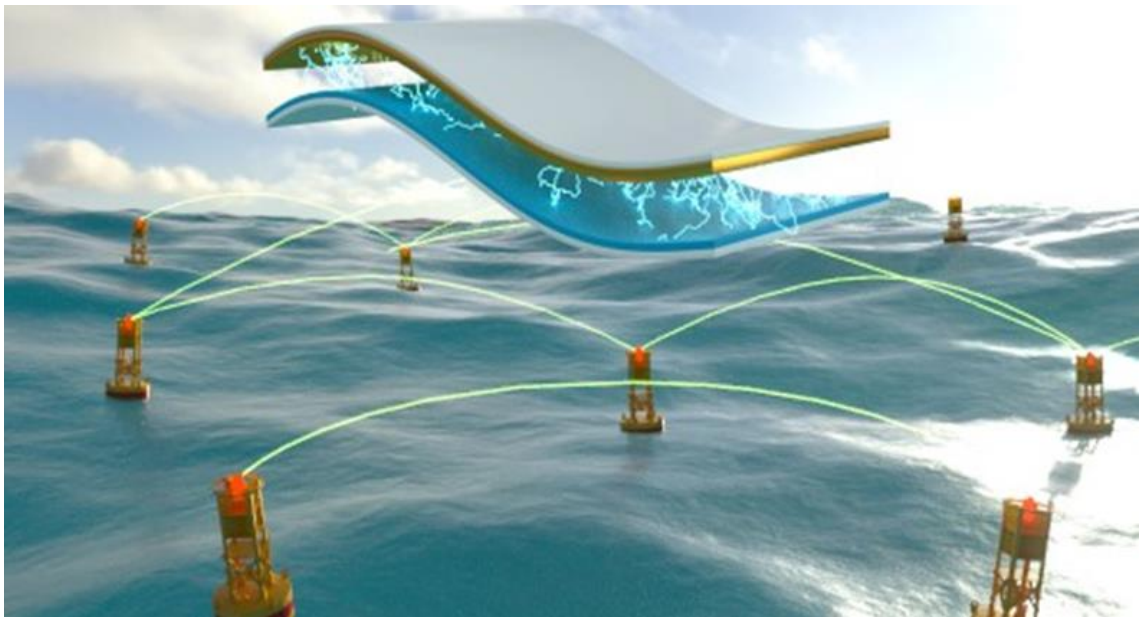


Figure 2.7 – Threshold lines and selected peaks for the output voltage of a TENG connected to a resistance of 470 MΩ.

negative peaks with the corresponding standard deviations. Finally, the output power generated during each test is also calculated by this data analysis software multiplying the voltage and current obtain for each resistance.

Chapter 3

Harvesting Blue Energy using Triboelectric Nanogenerators



Chapter 3

Harvesting Blue Energy using Triboelectric Nanogenerators

Ocean related activities are often supported by offshore equipment with particular power demands. These are usually deployed at remote locations and have limited space, thus small energy harvesting technologies, such as photovoltaic panels or wind turbines, are used to power their instruments. However, the inherent energy sources are intermittent and have lower density and predictability than an alternative source: wave energy.[1] In this thesis, we propose and critically assess TENGs as a promising technology for integration into wave buoys. Three TENGs based on rolling-spheres were developed and their performance compared in both a "dry" bench testing system under rotating motions, and in a large-scale wave basin under realistic sea-states installed within a scaled navigation buoy.[2] The influence of three different floating platforms' geometries on TENGs performance was also studied to obtain the correlation between the TENGs and floating platforms. This approach could be a strategy to improve TENGs sensitivity and conversion efficiency in moving water waves. The work here presented opens new horizons and strategies to apply TENGs in marine applications, considering realistic hydrodynamic behaviors of floating bodies.

3.1. Introduction

One of the key paradigms that has emerged in recent years when it comes to ocean technologies is energy demand for fluvial and (remote) offshore activities, namely for

---

[1] This part was adapted from C. Rodrigues, D. Nunes, D. Clemente, N. Mathias, J. M. Correia, P. Rosa-Santos, F. Taveira-Pinto, T. Morais, A. Pereira and J. Ventura – "Emerging triboelectric nanogenerators for ocean wave energy harvesting: state of the art and future perspectives" Energy & Environmental Science 2020, 13, 2657-2683. DOI: 10.1039/D0EE01258K [Reproduced from Ref. [91] with permission from the Royal Society of Chemistry]; (Review paper written and published during COVID-19 pandemic).

[2] This work was adapted from C. Rodrigues, M. Ramos, R. Esteves, J. Correia, D. Clemente, F. Gonçalves, N. Mathias, M. Gomes, J. Silva, C. Duarte, T. Morais, P. Rosa-Santos, F. Taveira-Pinto, A. Pereira, J. Ventura – "Integrated study of triboelectric nanogenerator for ocean wave energy harvesting: Performance assessment in realistic sea conditions" Nano Energy 2021, 84, 2657-2683. DOI: 10.1016/j.nanoen.2021.105890 [Reproduced from Ref. [5], Copyright 2021, Elsevier].

underwater and surface metocean monitoring [91–93] to support, e.g. weather forecasting [94], oceanography [95], aquaculture [96,97], maritime transportation and navigation [98], hydrodynamic studies [99], bathymetric surveying [100], monitoring of offshore structures [101], surveillance and security monitoring [102,103] and exploration of deep-sea resources [104,105]. Oceans and other inner water masses contain thousands of drifting and moored buoys, floaters and other platforms collecting data and supporting different activities, which need electrical power for the monitoring sensors, communication and telemetry equipment, control systems for ballast compensation and fishing feed, among many other functions. Nonetheless, that energy is difficult and more expensive to obtain in remote locations [106] and an increased demand is expected in the near future, especially due to the increase of activities carried in the sea [107,108].

The use of solar panels is nowadays a mature and relatively inexpensive option [109], although marine and fluvial applications may impose the use of non-standard and therefore more expensive solutions [110]. Moreover, their power production is intermittent since it depends on light conditions. On the other hand, due to the low energy density of solar energy (annual average of 170 W/m^2) [111], large areas, not available in buoys and small floating platforms, may be needed to provide the required power output. Small-scale wind energy harvesting technologies are also mature and can be used in autonomous offshore measurement stations and other platforms [112], but energy production is linked to the intermittency of the wind resource, which is, however, denser than the solar resource (around 500 W/m^2) [113].

Therefore, innovative energy harvesting technologies that are low cost, non-intrusive, scalable and do not depend on day/night cycles should be preferably used to create truly self-powered and autonomous systems, able to survive in the ocean or other remote aquatic environments during long periods of time, to enhance the operation and applicability of buoys and other offshore platforms.

Marine energy resources are abundant, presenting an annual theoretical potential of approximately 151,300 TWh [114]. Among these, ocean wave energy stands out with a global potential resource of nearly 18,500 TWh [115], being well distributed worldwide, persistent and presenting a high energy density of 2–3 kW/m^2 [113], and up to 6 kW/m^2 during storms.

Several technologies are available to harvest wave energy [116,117], but not all are suitable to provide energy to autonomous offshore stations or platforms. Moreover, some relevant challenges still exist to the viable deployment of wave energy conversion technologies, mostly linked to the irregular nature of waves and the distribution of energy in both direction and frequency, alongside the seasonal variability of the resource that greatly influences the amount of energy that can effectively be harnessed [118].

The use of wave energy converters in self-powered sensor buoys has already been tested, namely by applying the well-known oscillating water column principle [119] or other floating oscillating systems [120]. However, the quest for exploring and understanding the ocean and its resources requires other solutions, eventually less limited in terms of power output and with performances less dependent on the resource characteristics, to satisfy these novel and demanding applications. In this regard, the harvesting of wave energy using TENGs is a very promising and also disruptive solution [121,122], with the ability to harvest energy efficiently from low amplitude and frequency oscillations, which are typical of many ocean systems [123,124].

3.2. Maritime applications of TENG technology

As with any other technology, the application of TENGs to provide energy to marine activities involves both advantages and drawbacks. For instance, Wang *et al.* denotes the low amount of wave energy currently being exploited due to restrictions associated with solutions based on electromagnetic generators (EMGs) [125]. This is justified by the negative influence of the irregular nature of ocean waves and low frequency operation of the technologies (below 5 Hz) [123], an issue that is tackled by TENGs since they are capable of converting the irregular oscillatory wave energy into electricity, even considering slow motions of water wave particles [126]. Also, TENGs can, in theory, be applied in numerous marine applications, making them a versatile technology and particularly suitable for powering electronic components [75,127]. TENGs equally demonstrate a high energy conversion and storage efficiency [128], between 50% and over 90%, respectively, and a high area power density [40] with a maximum of about 1200 W/m^2 already achieved. The technology itself is also lightweight and has inherent low fabrication costs, giving it an important potential edge over alternative systems for wave energy conversion, as cost reduction is a vital challenge that needs to be addressed by the wave energy sector [113]. The underlying concepts and possibilities are well-known, at this stage, both from a theoretical [74,129] and practical [63] perspective. In fact, TENGs are also being considered for harvesting wind energy [130], a far more mature sector than that of wave energy, thus reinforcing the importance of considering them for marine applications as well [9]. Being a recent technology, TENGs are still maturing and hence require a considerable R&D effort before they can be fully deployed. This involves a thorough analysis of various optimization strategies and material selection, as described throughout this chapter that will require considerable investment in terms of both capital, knowledge and equipment. Furthermore, TENGs will

have to be protected adequately from the harsh sea environment, as both physical loads and biochemical agents may jeopardize their operational efficiency and, at worst, integrity.

3.2.1. Ocean wave energy harvesting using TENG

Ocean waves originate from the action of wind over a water mass and are therefore an indirect and concentrated form of solar energy. In deep waters, it can be considered that energy in a wave can be equally divided in two parts: the kinetic component, due to the motion of water particles in their circular orbits, and the potential component associated to the mechanical work performed when the flat ocean surface is deformed to a wavy (water lifted against the gravity force from wave troughs to wave crests). The averaged stored energy per unit area of ocean surface is given by:

$$E = \rho g \frac{H_{m0}^2}{16} = \rho g \int_0^\infty S(f) df, \quad (1)$$

where ρ represents the mass density of sea water, g the acceleration of gravity, H_{m0} the spectral significant wave height for the actual sea state and $S(f)$ the wave energy spectrum that defines quantitatively how the different wave frequencies f contribute to the wave energy.

A typical sea state characterized by a H_{m0} = 2.0 m presents an energy density of approximately 2.5 kW/m^2. TENGs can be used to convert the two components of wave energy and thus generate electricity. As described in Chapter 1, TENGs work based on two fundamental effects: contact induced electrification and electrostatic induction. This principle allows for the conversion of energy from various frequencies, including low frequency agitation or vibration.

Since the ocean is a harsh environment, it is primarily envisaged to install the TENG units sheltered inside a hull. Figure 3.1(a) shows, in a simplified form, the dynamics of a floating body (ocean buoy) in deep water, under the action of waves. As the wave passes by, the floating body has translatory (surge, sway, heave) and rotatory (roll, pitch, yaw) motions [Figure 3.1(b)] that can excite the TENG, installed within, in different ways. In fact, the four main operation modes of TENGs allow a wide variety of applications in the ocean environment. In a more holistic perspective, TENG technology could provide energy for a broad range and integrated systems and sensors in operation in the ocean

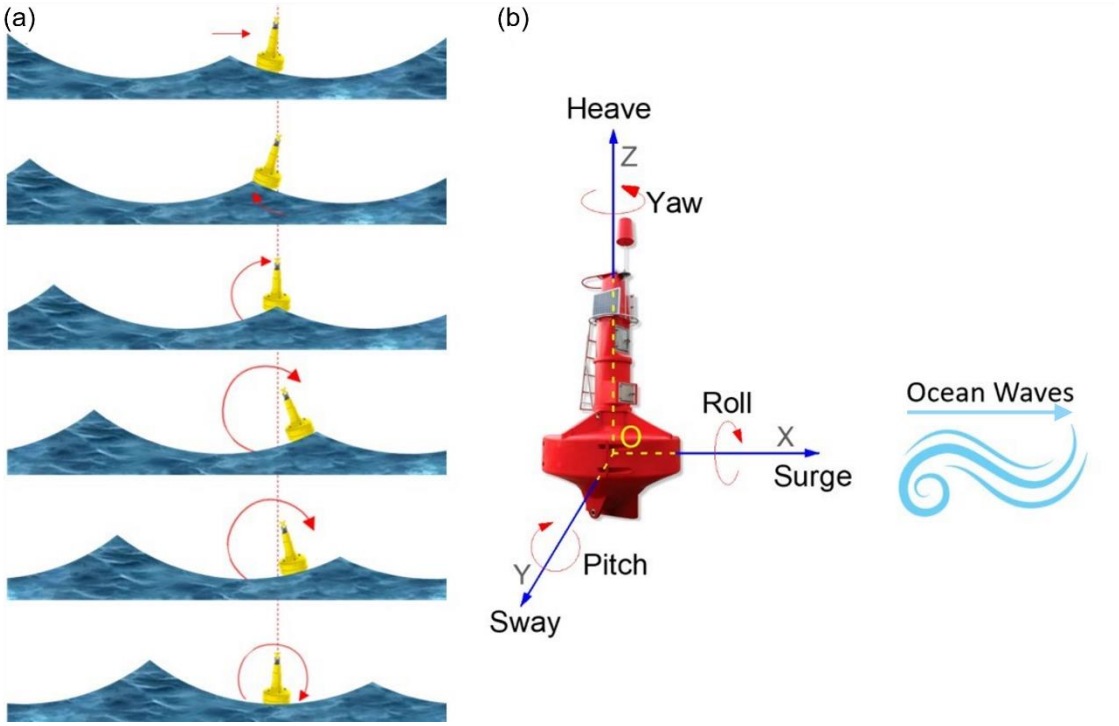


Figure 3.1 – (a) Dynamics of ocean buoy under wave action. (b) Six degrees of freedom of a floating body. Reproduced from Ref. [225] with permission from the Royal Society of Chemistry.

(Figure 3.2). The most common buoy designs for those applications are based on the use of spherical geometric shapes or small cylindrical towers on top high-volume cylinders [131–133]. The interior of the buoy could have different components, such as balance weights, batteries, sensors and other instrumentation. Besides all the gear needed for the operation of the buoy, there is also empty space that could be used for TENGs based on different operating methods. Furthermore, the prototypes developed so far can rely only on the triboelectric effect or be combined with EMGs, thus building a hybrid and possibly more efficient generator [134,135]. All these alternative options are described in section 3.3.

Table 3.1 summarizes some of the main results obtained in the harvesting of wave energy using triboelectric nanogenerators. Different triboelectric configurations have been presented in the literature, with the most common involving the use of rolling spheres and of the direct contact with water to generate electrical energy. Since our developed concept is based on rolling spheres, we will present here a more detailed state-of-the-art overview on the subject, and a smaller emphasis on other concepts.

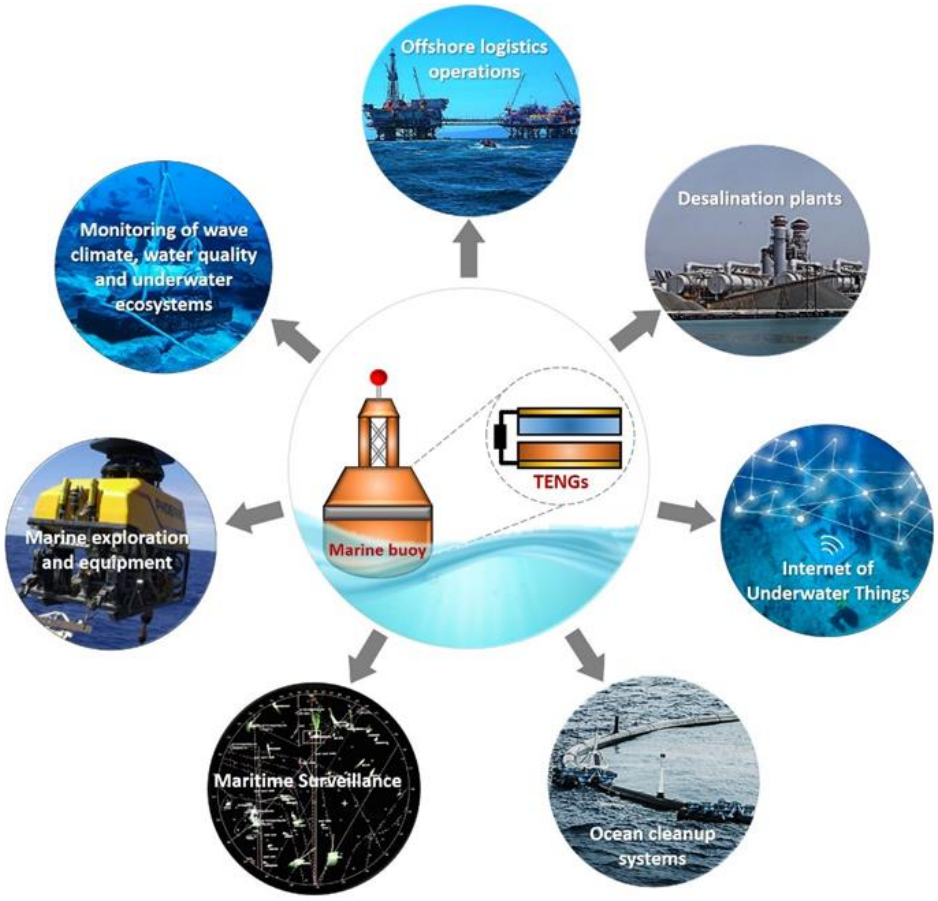


Figure 3.2 – Wave energy harvesting by TENGs: A holistic perspective. Reproduced from Ref. [225] with permission from the Royal Society of Chemistry.

3.3. An overview on TENG technologies for marine applications

3.3.1. TENGs based on rolling spheres

Given the versatility of TENGs in harvesting all kinds of mechanical motion, numerous different prototypes have been assembled and reported. One straightforward method to take advantage of the motion of a floating body in the ocean is to use rolling spheres freely moving on top of a triboelectric surface. One of the initial prototypes based in this concept and published in 2015 also proposed the implementation of a TENG network (TENG-NW) with a large number of units connected to harvest large-scale water

Table 3.1 – Prototypes developed for wave energy harvesting in buoys and corresponding generation properties. Reproduced from Ref. [91] with permission from the Royal Society of Chemistry.

Category	Ref.	Generation Method	V_{max} (V)	I_{max} (μA)	Freq. (Hz)	P_{max} (mW)	Power Density	Prototype Main Shape	Year
Rolling Spheres	[124]	TENG	280	120	1	8.5	4.81 W/m^3	Sphere with spring-assisted TENGs	2020
	[136]	TENG	250	0.5	NA	NA	NA	Ball slider	2018
	[137]	TENG	90	0.8	2	NA	NA	Sphere	2019
	[138]	TENG	160	2.60	1	22.45	NA	Torus	2019
	[139]	TENG	105	1.3	1.6	NA	7 W/m^3	Cylinder with Spheres	2019
	[126]	TENG	569.9	930	NA	NA	2.6 W/m^2	Rectangular	2015
Multilayered	[140]	TENG	450	85	1.4	6.5	12.4 W/m^3	Sphere with spiral TENG	2019
	[141]	TENG	NA	220	0.6	29.8	7.45 W/m^3	Open-book like shape	2019
	[18]	TENG	354	270	1	12.2	3.33 W/m^3	Sphere with inner springs	2019
	[142]	TENG	250	NA	2	NA	0.013 W/m^2	Cylinder with inner stacks	2019
Water Contact	[143]	TENG	200	10	NA	0.016	NA	Multi-wire cylinder shaped	2017
	[144]	TENG	13.5	0.38	NA	NA	NA	Spheres	2017

Other Architectures	[145]	TENG	600	12.5	NA	NA	NA	Single TENG unit	2017
	[146]	TENG	12	0.225	NA	0.0012	NA	Tower-like shape	2018
	[147]	TENG	360	3.4	2	0.196	NA	Sphere with pendulum	2019
	[148]	TENG	281	76	4	475	NA	Oblate spheroidal TENG	2019
Hybrids	[149]	TENG + EMG	550 + 3	1.5 + 4650	4	0.0217 + 0.00823	NA	Honey-comb-like	2018
	[6]	TENG + EMG	300 + 10	59 + 30000	3	NA	271.1 W/m^3 + 700 W/m^3	N = 12 (min 2, max 16)	2018
	[8]	TENG + EMG	180 + 13	7 + 50000	2	0.65 + 265	3.25 W/m^2 + 79.9 W/m^2	Cylinder with an axis	2019
	[19]	TENG + EMG	75 + 1.7	1 + 1000	NA	NA	NA	Sphere with inner rows	2019
	[150]	TENG + EMG	150 + 4.3	15 + 15000	2	0.850 + 9	NA	Ship-shaped	2019
	[151]	TENG + EMG	390 + 0.18	7.2 + 120000	2.5	NA	213 W/m^3 + 144 W/m^3	Duck-shaped	2017
	[152]	TENG + EMG	97 + 1.1	3 + 4000	0.8	0.015 + 1.23	NA	Chaotic pendulum	2020

wave energy from the sea [126]. The single TENG-NW unit consisted of four lateral triboelectric pair stacks within an acrylic box triggered by ball collisions driven by gravity [Figure 3.3(a)-(d)]. Under an acceleration of 10 m/s^2 and a displacement of 9 cm, the ball collision generated an V_{OC} and short-circuit current (I_{SC}) of 569.9 V and 0.93 mA, respectively, and a maximum power density of 0.26 mW/cm^2. Zhong Lin Wang and co-authors also developed a spherical TENG with 6 spring-assisted TENGs to collect multidirectional water energy [Figure 3.3(e)-(h)] [124]. Each TENG unit was supported by 4 springs and used a Kapton film in a zigzag structure as substrate, where copper electrodes and FEP films are assembled. To ensure contact-separation between the triboelectric materials, six copper ball roll due to the water motions and collide with the 6 spring-assisted zigzag TENGs. A maximum output voltage, current and transferred charge of 280 V, 120 µA and 1.0 µC were generated at 1 Hz and a fixed orientation angle of 90º (angle between the water wave triggering direction and the middle plane of the spherical TENG). They showed an increase of the electrical outputs with increasing wave frequency because of the increased velocity of the spheres. However, the electrical outputs decrease for frequencies above 1 Hz due to the unstable oscillation of the balls.

Figure 3.4(a)-(d) displays the so-called sea snake-like triboelectric nanogenerator (SS-TENG) [136]. This prototype has an external and an internal acrylic box with a spring attached in the bottom, with 6 rectangular columns of 5.1×6.4×2.54 cm^3 and 6 PTFE

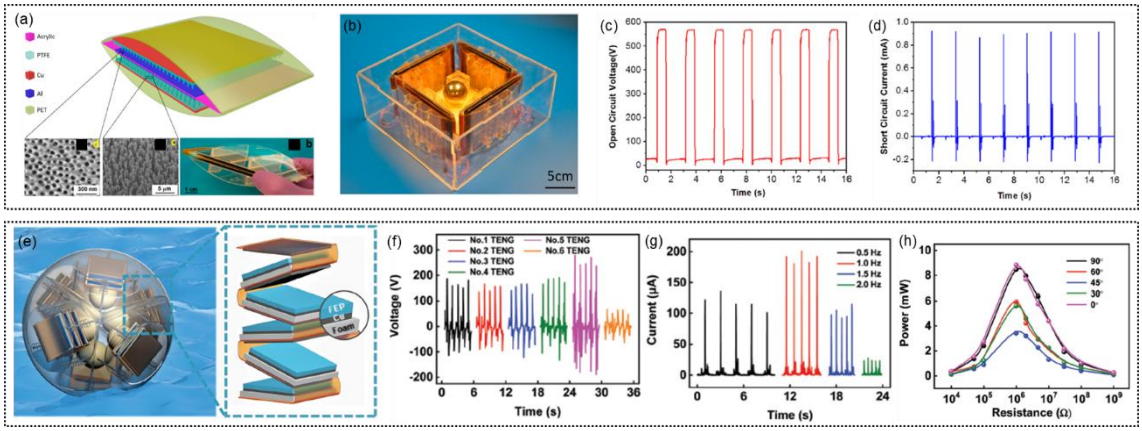


Figure 3.3 – (a) Schematic and photograph of single TENG. (b) Photograph of a TENG-NW unit. (c) Open-circuit voltage and (d) short-circuit current generated by a ball collision at 10 m/s^2 with a displacement of 9 cm. Reprinted with permission from Ref. [126], Copyright 2015, American Chemical Society. (e) Schematic of spherical TENG with 6 spring-assisted TENGs. (f) Output voltage generated by each TENG unit. (g) Dependence of output current under various water waves frequencies. (h) Output power generated by the spherical TENG under different orientation angles. Reprinted with permission from Ref. [124], Copyright 2020, The Royal Society of Chemistry.

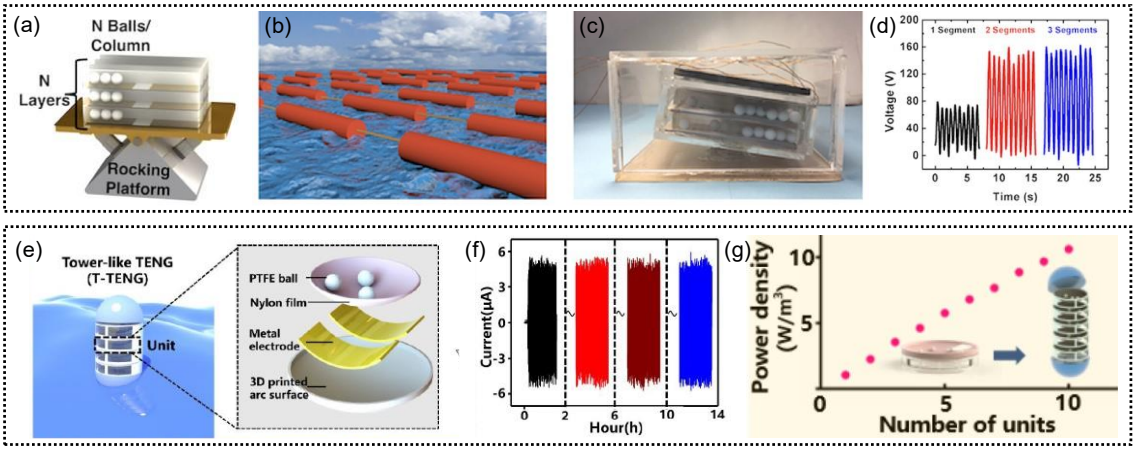


Figure 3.4 – (a) Schematic of the SS-TENG. (b) Array of SS-TENGs to develop an ocean energy farm. (c) Photograph of the developed SS-TENG composed by a single segment. (d) Dependence of output voltage using various number of segments. Reprinted with permission from Ref. [136], Copyright 2018, Elsevier. (e) Schematic of the multiple T-TENG units and the basic structure of a T-TENG unit. (f) The short-circuit current generated in a water wave tank during 14h. (g) Dependence of power density generated using various numbers of TENG units in the tower. Reprinted with permission from Ref. [139], Copyright 2019, American Chemical Society.

balls for each column acting as a dielectric layer. The spheres moved back and forth on a Nylon film with an interdigital copper (Cu) electrode that in turn is on top of a soft spring. With 3 units of the SS-TENG connected in series by springs, this prototype achieved a maximum output voltage of 160 V, charging 2 V of a 100 μF capacitor in 10 min and lightning 152 LEDs connected in series. Another prototype making use of the same basic concept is shown in Figure 3.4(e)-(g) [139]. This tower based triboelectric nanogenerator (T-TENG) is composed by an acrylic tubular block with a shell diameter of 94 mm, stacking 4 layers, each one combined with a Nylon film, a metal electrode and 5 PTFE spheres. Under the excitation of the external waves, generated in a water tank by a linear motor at 1.6 Hz with an amplitude of 150 mm, the PTFE spheres roll back and forth on the arc surface giving a V_{OC} of 105 V, a I_{SC} of 1.3 μA and a charge of 51 nC. When 10 T-TENGs units are used, the maximum generated power density is 10.6 W/m^3, being able to light 540 LEDs.

3.3.2. Other concepts

To improve the volume density of the triboelectric contact and to generate higher power densities, multilayered devices have been developed to incorporate several TENG units in small spaces for wave energy harvesting. Taking advantage of the pitch

motion of a buoy, a central weight swinging in a range of 180° was fabricated, pushing the layers of the triboelectric materials against each other in the contact-separation mode [Figure 3.5(a)-(d)] [141]. In the first tests, the movement was driven by a linear motor, followed by tests in a water tank with wave agitation. A device composed by 50 stacked TENG units generated a transferred charge and a rectified I_{SC} of 26 μC and 0.45 mA, respectively, at 1.15 Hz with an angle amplitude of 13.6°. This device generated a peak (average) power density of 7.45 Wm^{-3} (0.283 Wm^{-3}) in water at ~ 0.6 Hz.

Hybridizing TENGs with electromagnetic concepts has also become a recent trend to obtain higher output powers in wave energy harvesting. They are able to combine the large voltages and low-frequency efficiency of TENGs with the higher currents generated by EMGs. For example, to capture the kinetic and potential energy of water waves, Feng *et al.* developed a hybridized device, with the TENG operating in two working modes: vertical contact-separation and lateral sliding [Figure 3.5(e)-(h)] [149]. The TENG

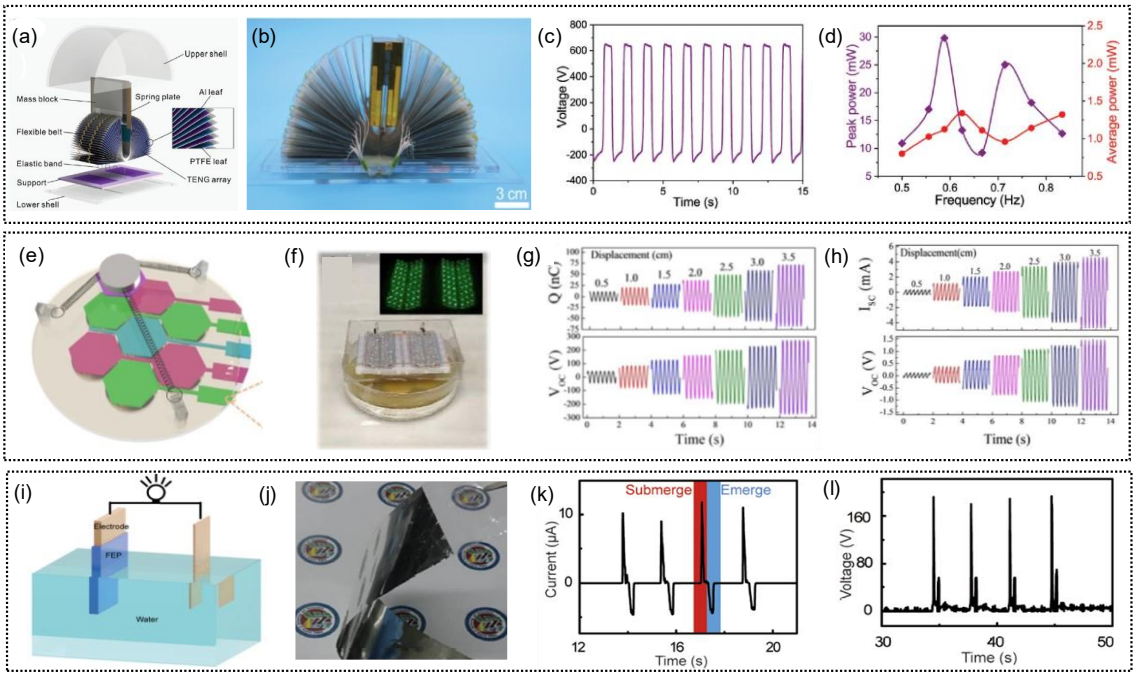


Figure 3.5 – (a) Schematic and (b) photograph of the fabricated TENG. (c) Output voltage of a TENG unit. (d) Dependence of peak power and average power at various frequencies using a matched load of 13.8 MΩ. Reprinted with permission from Ref. [141], Copyright 2019, The Royal Society of Chemistry. (e) Schematic of the developed hybrid nanogenerator. (f) Photograph of the hybrid device floating in water and lighting up 108 LEDs. (g) Transferred charge and V_{OC} of the TENG for various displacements. (h) The short-circuit current and V_{OC} of EMG unit for various displacements. Reproduced with permission from Ref. [149], Copyright 2018, Elsevier. (i) Schematic and (j) photograph of the developed flexible TENG. Output (k) current and (l) voltage of the flexible TENG. Reproduced with permission from Ref. [143], Copyright 2017, AIP Publishing LLC.

unit consists of an acrylic board with seven hexagonal electrodes covered (connected in three electrodes group) with PTFE film as triboelectric material, and a mobile magnet. In the magnet was fixed a hexagonal acrylic plate covered with an aluminum film as triboelectric material and electrode. The EMG unit was composed by seven Cu coils fixed on the backside of an acrylic substrate. Under waves oscillations, the hybridized device will move in a multi-angle range due to the free movement of the magnet. Increasing the sliding displacement from 0.5 to 3.5 cm at 4 Hz, the TENG unit generated an open-circuit voltage and charge that increased linearly, reaching a maximum of 550 V and 140 nC, respectively. A similar linear increase with sliding displacement was observed for I_{SC} (up to 4.65 mA) and V_{OC} (up to 3 V) of the EMG, for a maximum power of 8.23 μW. For frequencies varying from 1 to 5 Hz (and fixed displacements of 3.5 cm), the current generated by TENG showed a linear increase (up to 1.5 μA), while the transferred charge and open-circuit voltage values remained constant (140 nC and 550 V). The authors further demonstrated that a capacitor charged up to 2 V in 23 s and that 180 green LEDs can be simultaneously lit.

All the structures described previously depend on movable structures within an encapsulated floating body. This puts strict requirements on the packing of the whole structure, as any water leakage would result in device failure. To counter this issue, a new set of triboelectric devices operating in the single electrode mode was put forward based on the direct contact of water with a solid triboelectric material. Given the position of water on the triboelectric series (on the positive polarity side), negative triboelectric materials such as PTFE or FEP are typically chosen as the tribo-pair. As an example, Li *et al.* used a FEP nanowires based TENG with enhanced contact area with water and thus extra generated charges [Figure 3.5(i)-(l)] [143]. Submerging the FEP film in water leads to sharp positive peaks, while its removal leads to a smaller negative signal. The nanowire-based structure has a high output performance, generating an output current of 10 μA and a voltage of 200 V, with a maximum instantaneous power of 16 μW. In the demonstration, the prototype powered a system with a suitable capacitor and an infrared emitter.

3.4. Integrated study of rolling spheres based on TENGs in realistic sea conditions

As detailed in the previous sections, the vast majority of the developed TENGs for blue energy harvesting were implemented within a simple floating waterproof body and tested in simplified experimental setups. Although the reported studies have succeeded in showing the capability of TENGs to harvest low-frequency and small-amplitude mechanical energy, the methods used do not allow a realist assessment of their performance. In fact, this is only possible if the nature of ocean waves is properly reproduced, together with the actual motion profile of the whole floating body (TENG and buoy). Considering the body's dynamic, one must then study the dependence of the electrical energy generation of TENGs within a floating body at realistic frequencies and wave amplitudes. Therefore, it is critical to carry out complex experimental campaigns within fully equipped wave basin facilities capable of reproducing realistic sea-states. This type of experimental study, under controlled conditions, is common practice in the field of Wave Energy Converts (WEC) research and development, where devices are subjected to a wide range of wave conditions. These conditions include (i) regular waves, for a parametric analysis of the device's behaviour and power production within and far away from the resonance range and (ii) irregular waves, from which more realistic estimates on the energy output and data on the device's hydrodynamic response are attained [153–162]. Albeit more expensive and time consuming, tests within wave basin facilities allow for a far greater realism and reliability than tests carried out with simplified experimental setups [163].

Besides yielding crucial data to attain more robust power output estimates from the TENG, wave basin tests also provide a better understanding on the hydrostatic properties and hydrodynamic response of the floating structure into which it is integrated. This is of the utmost importance, as the performance of the TENG at sea is directly linked with the oscillatory behaviour of the floating structure when subjected to the wave action. In this section, we developed TENGs based on rolling spheres to harvest energy from multidirectional water waves, and provide a better understanding on the hydrodynamic response of the buoy, due to the degrees of freedom of the spheres. Therefore, we present and discuss the developing of three TENGs based on rolling-spheres and their performance compared in both a "dry" bench testing system under rotating motions, and in a large-scale wave basin under realistic sea-states installed within a scaled commercial navigation buoy.

3.4.1. Structure design and fabrication of TENGs structures

To study the most appropriate triboelectric structure to harvest kinetic and potential wave energy, three different rolling-sphere-based TENGs were implemented inside the model of a commercial navigational buoy in a 1:8 scale [Figure 3.6(a)]. The developed TENGs are based on the movement of stainless-steel spheres that promote the periodic contact-separation of the two triboelectric materials (PTFE and Nylon 6,6 films).

The three TENGs were developed using easy and fast fabrication techniques: screen-printing and 3D printing (Ultimaker 2+ extended 3D printer). The screen-printing technique was used to develop the electrodes by transferring flexible and commercial conductive silver ink onto PTFE (50 µm thick) and Nylon (17 µm) films. Then, the silver films were dried for 10 min at 150 ºC in a heating chamber. The structure of each TENG was fabricated using polylactic acid (PLA) in the form of filament by the Fused Filament Fabrication (FFF) method by 3D printing. The anisotropic circular-based TENG [AC-TENG; Figure 3.6(a_1)] is a circular PLA structure with 21.5 cm of diameter and a curvature radius of 4 m^{-1}. At the base of this structure the PTFE/silver (Ag) and Nylon/Ag films are fixed, and ten stainless steel spheres (each with a diameter of 12 mm and a weight of 7.2 g) are placed over these two tribo-pairs. The unidirectional flat-based TENG [UF-TENG; Figure 3.6(a_2)] is composed of a 21.5×21.5 cm^2 PLA structure with five

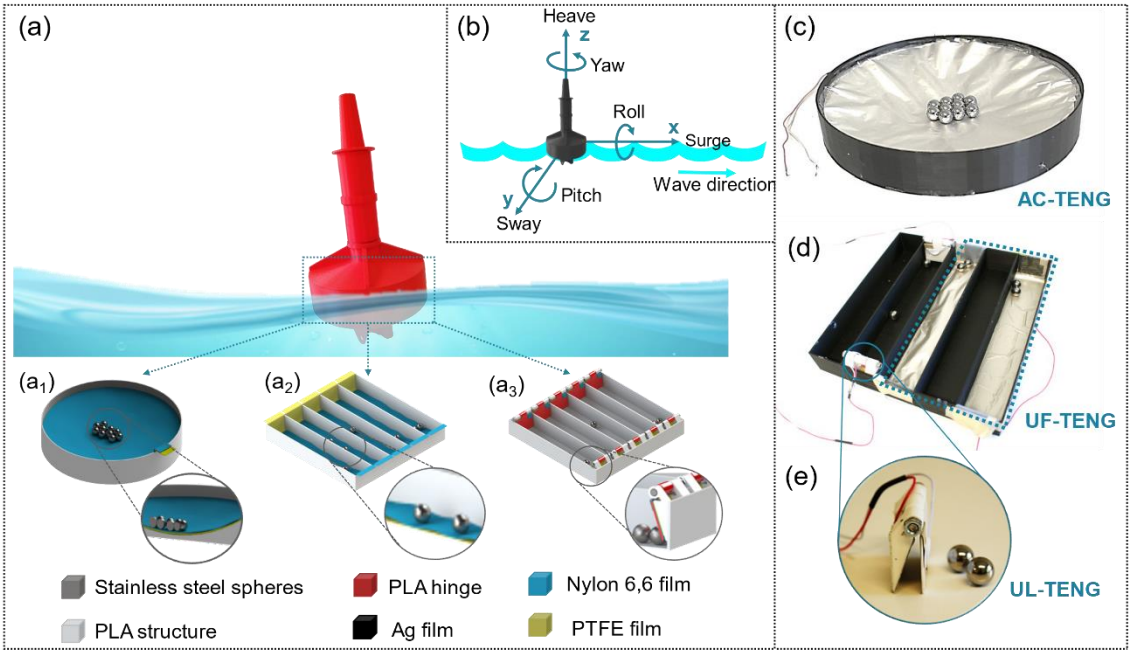


Figure 3.6 – (a) Design of the navigation floating buoy-based on unidirectional and anisotropic triboelectric nanogenerators: (a_1) AC-TENG, (a_2) UF-TENG and (a_3) UL-TENG. b) Six-degrees of freedom motions of the buoy. Photographs of the (c) AC-, (d) UF and (e) UL-TENGs.

troughs (each one with 4×21.5 cm^2), where PTFE and Nylon 6,6 films were assembled at the base of each PLA trough. Then, two stainless steel spheres per trough were placed over the triboelectric pairs. The unidirectional lateral-based TENG [UL-TENG; Figure 3.6(a_3)] has two PLA plates with 2.65×3.75 cm^2, where PTFE/Ag and Nylon 6,6/Ag films were attached with the same dimensions. Each trough has two UL-TENGs fixed at its ends and two stainless steel spheres. The density of spheres (number of spheres per area) of these three TENGs is kept constant (1/40 cm^{-2}) for a straightforward comparison.

3.4.2. Fabrication of floating buoy-based TENGs

The navigational floating buoy [Figure 3.6(a); Atlantic-2600 buoy [164] was designed and manufactured by Institute of Science and Innovation in Mechanical and Industrial Engineering (INEGI), based on a model currently operating on the Portuguese west coast, for which product information was supplied by Sealite. In order to replicate real wave conditions (sea states) and perform the detailed studies, the buoy was re-dimensioned to a 1:8 scale model considering the characteristics of the wave basin available at Hydraulics Laboratory of the Hydraulics, Water Resources and Environment Division (SHRHA), at the Faculty of Engineering of the University of Porto (FEUP). The preliminary model was designed with the software SolidWorks®, in accordance to the buoy manual supplied by Sealite. The scaled buoy (with height and diameter of 47.7 and 26 cm, respectively) was fabricated in several parts, to be assembled by means of threaded connections, using an additive manufacturing process. PLA filament was used to manufacture the model, given its mechanical properties and adequacy to the chosen manufacturing method. Due to the porosity of the layer-by-layer printing with extruded filament, the manufactured parts presented high level of permeability, so all the components that were expected to be in contact with water were sanded and coated with an epoxy resin. All threaded connections were assembled with rubber o-rings and Terostat sealing tape was applied on the connection with the bigger diameter. In order to ensure the significance of the experimental results and to guarantee a correct transposition to full scale scenarios, special attention was given to geometric and dynamic similarity laws. To ensure the dynamic similarity between the model and the full-scale equipment, the total mass of the buoy was reduced by a factor of 512 (8^3).

3.4.3. Working mechanism of TENGs

The first TENG configuration is the AC-TENG [Figure 3.6(a_1)]. This device is composed by a circular PLA structure where the triboelectric pairs (Nylon 6,6/Ag and PTFE/Ag films) are assembled, and by stainless steel spheres that can move anisotropically on top of the triboelectric materials, generating electrical energy. Considering the six degrees of freedom of a floating body, the spheres can move freely on top of the triboelectric materials in the AC-TENG. The curvature allows a symmetry in the mass distribution of the AC-TENG since the oscillation amplitudes of the floating buoy can be insufficient to modify the initial position of the spheres for waves with high periods. Under the excitation of waves, Nylon and PTFE will come into contact, becoming positive and negatively charged, respectively, due to contact electrification. While the spheres role, this will induce opposite charges on the two electrodes, which will result in an alternating current flowing between them [Figure 3.7(a)].

A similar structure and energy generation mechanism operate in the UF-TENG [Figure 3.6(a_2)]. However, in this case, the base where the triboelectric materials are assembled is composed by narrow and flat PLA troughs and thus the spheres can only move unidirectional in the plane of the device. This configuration can limit the spheres motion to harvest wave energy considering the six degrees of freedom of the floating buoy.

The UL-TENG [Figure 3.6(a_3)] was also developed to harvest energy from the shock of the linear and unidirectional movement of the spheres on the lateral ends of a PLA trough. This device is composed by a PLA structure with a triboelectric pair (PTFE/Ag films) fixed in the lateral trough. The opposite triboelectric pair (Nylon 6,6/Ag) is assembled in a free PLA plate articulated to work as a hinge. Wave oscillations induce the motion of the spheres and their shock with the lateral ends of the trough. This makes the free PLA plate come into contact with the fixed PLA plate. According to the TENG contact-separation mode, when the Nylon 6,6 film comes into physical contact with the PTFE film, triboelectric charges with opposite signal will be generated on the two contacted surfaces. Then, the free plate will move away from the fixed one and a potential difference will be induced when the two triboelectric surfaces are separated due to the oscillation of ocean waves, driving an electron flow between the two silver electrodes [Figure 3.7(b)].

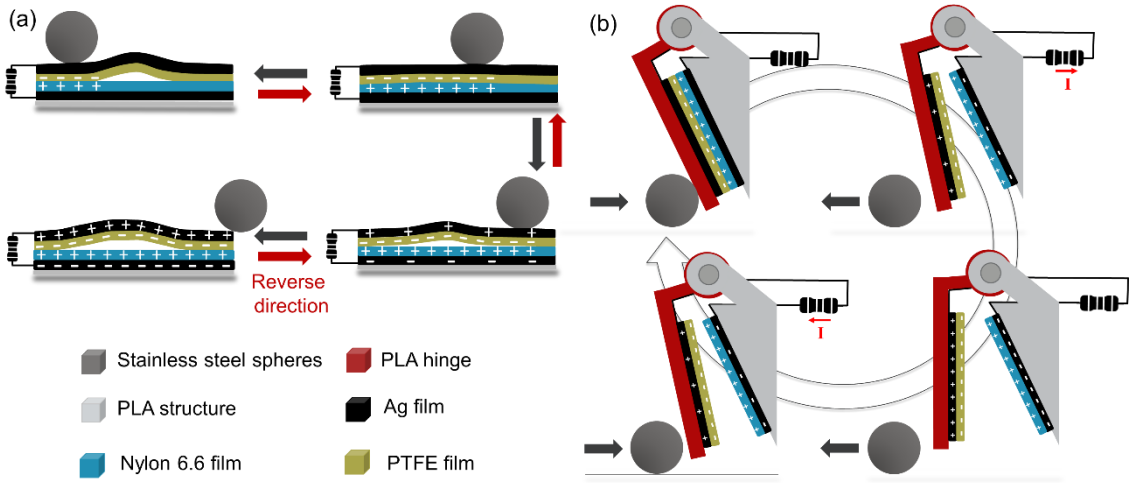


Figure 3.7 – The working mechanism of the (a) anisotropic circular-based TENG (AC-TENG) and unidirectional lateral-based TENG (UL-TENG).

3.4.4. Output performance using "dry" bench testing system

Aiming to optimize the harvesting of wave energy, the dependence of the electrical outputs of the developed TENGs under different pitch frequencies and amplitudes was systematically studied using the rotary-based testing system. To electrically characterize the developed TENGs, the generated voltage (V), current (I) and power (P) were first measured when connected to variable external load resistances from 100 Ω to 470 MΩ at a constant pitch period (1.486 s) and peak-to-peak amplitude [26º; Figure3.11(a)-(c)]. The electrical characterization of the AC-, UF- and UL-TENGs displays the typical three working-regions behavior [Figure3.11(a)-(c)]. Region 1 corresponds to the low resistance range, where the transfer of charge between materials is enhanced (short-circuit-like condition), giving maximum currents of ~ 2.4, 1.0 and 2.7 µA for the AC-, UF- and UL-TENGs, respectively. On the other hand, Region 3 relates to the high resistance range, where open-circuit-like conditions are reached. In this region, maximum output voltages of ~ 15, 10 and 18 V were generated by the AC-, UF- and UL-TENGs, respectively. In Region 2, one observes opposite trends, with the voltage increasing and the current decreasing with increasing load resistance. Analyzing the electrical outputs in this region, maximum powers of ~ 7.5, 6.2 and 29 µW were reached for the AC-, UF- and UL-TENGs, respectively, at a load resistance of ~10 MΩ.

Figure 3.9 shows the maximum outputs generated by the developed TENGs under pitch amplitudes from 8 to 26º and periods from 1.486 to 7.071 s. Maximum voltages (currents) of ~ 16.5 (~ 0.8 µA), 4.9 (~ 1.2 µA) and 17.6 V (~ 2.8 µA) were generated by

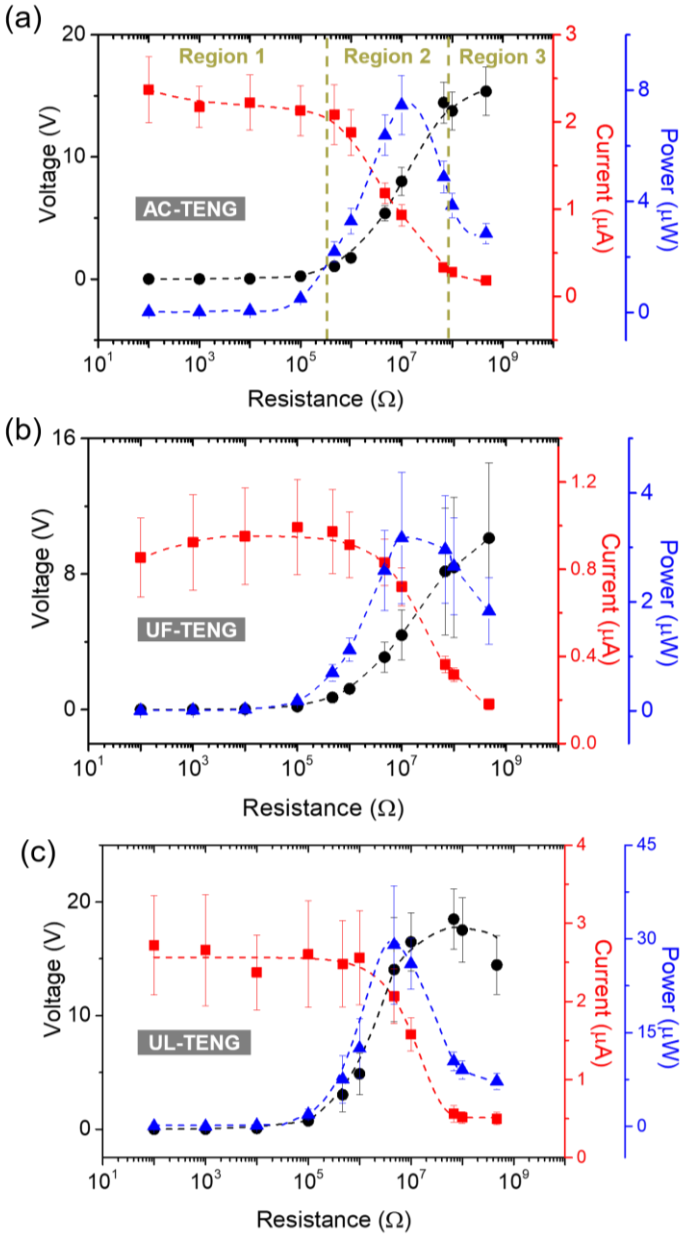


Figure 3.8 – The generated output voltage, current and power of the (a) AC-TENG, (b) UF-TENG and (c) UL-TENG at a fixed period of 1.486 s and a pitch amplitude of 26º.

the AC-, UF- and UL-TENGs, respectively. Determining the power obtained by the different configurations at a load resistance of ~ 10 MΩ shows that the UL-TENG has the highest electrical outputs, reaching a maximum power of 230 μW, for a period of 1.846 s and an amplitude of 26º. This is related with the higher effective contact area between the two tribo-pairs in the UL-TENG (single-area contact due the triboelectric

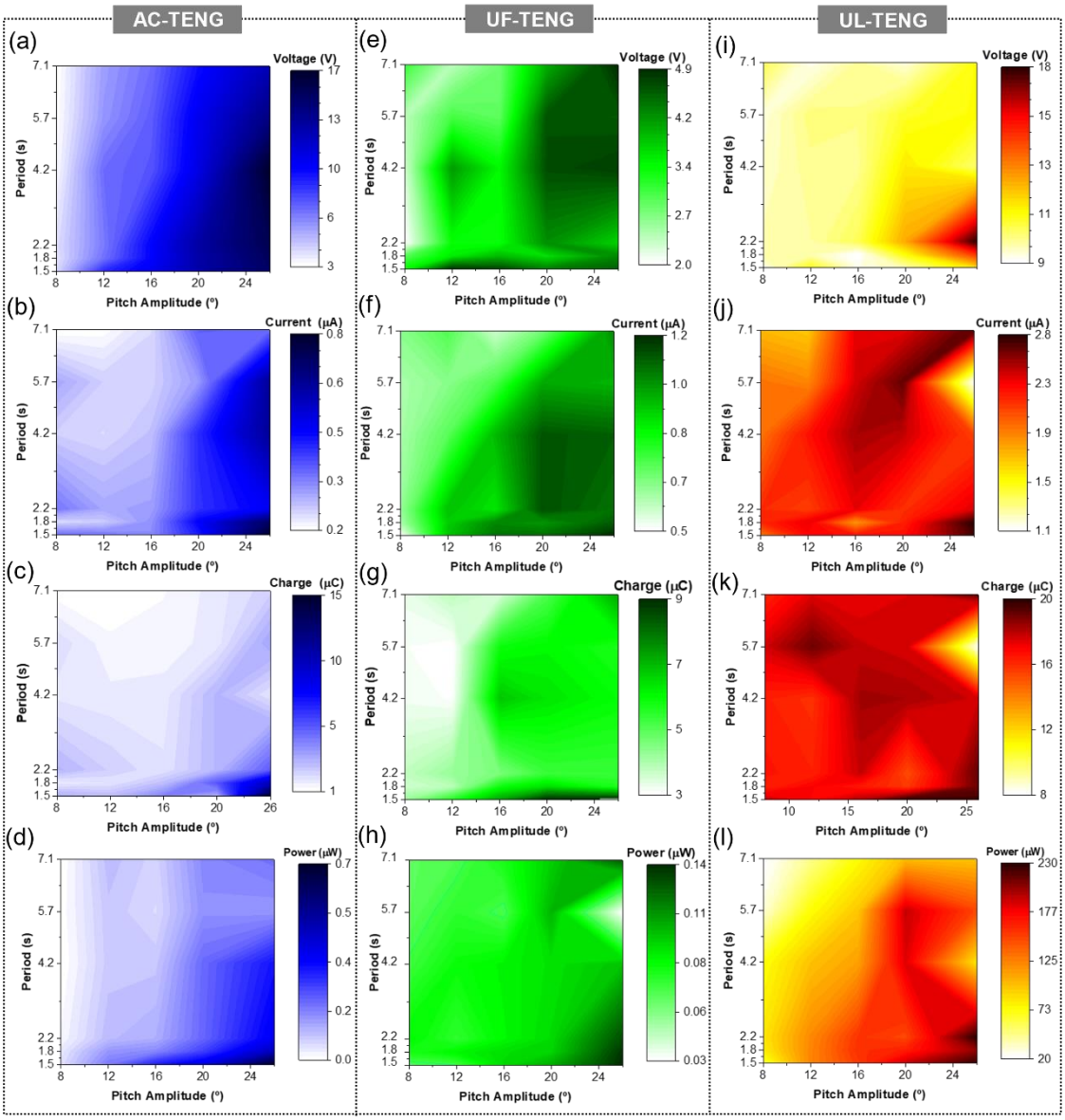


Figure 3.9 – Maximum voltage, current, charge and power generated using different pitch amplitudes and periods by (a)-(d) AC-TENG, (e)-(h) UF-TENG and (i)-(l) UL-TENG.

configuration) when compared with that of the UF- and the AC-TENGs (single-point contact due to the geometric shape of the spheres). This result is in line with the TENG theory reported by Z. L. Wang [64], and various reported articles [42,165–167] that shown that the performance of TENGs tends to increase with the effective contact area between the triboelectric materials. Furthermore, the unidirectional characteristic of the UF-TENG (P= 0.14 μW) limits its energy generation capability when compared with the AC-TENG (P= 0.68 μW), whose anisotropy also promotes collisions between spheres that increase the effective contact-separation mode between the tribo-pairs.

The power generated by the AC-, UL- and UF-TENGs is highly dependent on the pitch degree of freedom. In fact, and although the TENGs generated electrical energy in the whole range of studied motions, a general trend of increasing electrical outputs with

decreasing period and (more markedly) with increasing amplitude is observed (Figure 3.9). At low pitch amplitudes/high periods, the small displacements of the spheres (e.g., below a pitch amplitude of 8º no significant movement of the spheres was observed) results in a decrease of the effective contact between the opposite triboelectric pairs for the AC-, UF- and UL-TENGs. Under these motions the spheres tend to have limited movements and be positioned at one end (UF and UL-TENGs) or at the center (AC-TENG) of the prototype. As the pitch amplitude/frequency increases, the spheres increase their motion span, acquire larger momentum and enhance the contact between the Nylon and PTFE films (in the cases of the AC-, UF-TENG) or collide with a higher impact force on the free PLA plate (UL-TENG). Consequently, the electrical energy generation increases with increasing pitch amplitude, with the maximum performance achieved for the UL-TENG at an amplitude of 26º.

3.4.5. Wave basin demonstration

Systematic tests under “dry” conditions are first tests to understand and improve TENGs in order to maximize their energy generation. However, studies in a wave basin capable of reproducing realistic sea-states reveal the correlations between the hydrodynamic motions of floating bodies (typically buoys) and TENGs aiming at practical applications. This approach is highly representative, particularly in terms of wave-structure interaction. For instance, the induced excitation associated with wave action on the buoy model and, most importantly, on the actual TENG is better reproduced. The same goes for the hydrodynamic response of the physical model, which cannot be adequately studied under “dry” conditions, as presented above nor with the small wave tanks which are typically employed in the TENGs' field.

To demonstrate the actual capability of the AC-, UF- and UL-TENGs to harvest energy from wave motion, a navigational buoy was fabricated as stated previously. Its geometrical scale was selected taking into account the physical dimensions of the wave basin (28.0 m long, 12.0 m wide and 1.2 m depth) at FEUP’s Hydraulics Laboratory (Figure 3.10), the capability of its wavemaker to properly reproduce regular and irregular (long and short-crested) wave conditions [Figure 3.10 and Figure 3.11(a)] and the need to provide enough internal space for the installation of the TENG systems and all measuring equipment. To promote the dissipation of energy attributed to wave reflections

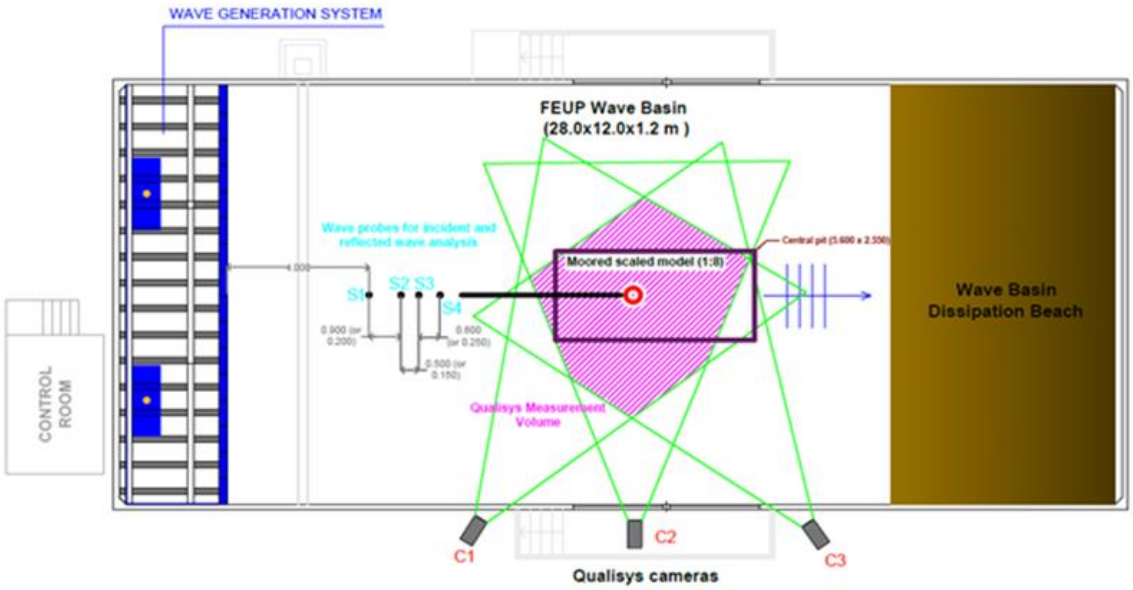


Figure 3.10 – Schematic diagram of the wave basin equipment and facilities.

off the boundaries of the wave basin, an 8 m long dissipating beach (~15 % inclination) was located at the opposite end of the wavemaker system, as shown in Figure 3.10.

The open-circuit voltage of the TENGs was acquired using a Bluetooth datalogger implemented inside the navigational buoy to measure and transmit data in real-time to a personal computer and monitor the generated energy for all wave conditions [Figure 3.11(b)].

Figure 3.11(c) shows the general properties of a periodic linear ocean wave, where the period is the time it takes a wave to complete one cycle and the amplitude is the distance between the still water level and the wave crest (or the wave trough), which is

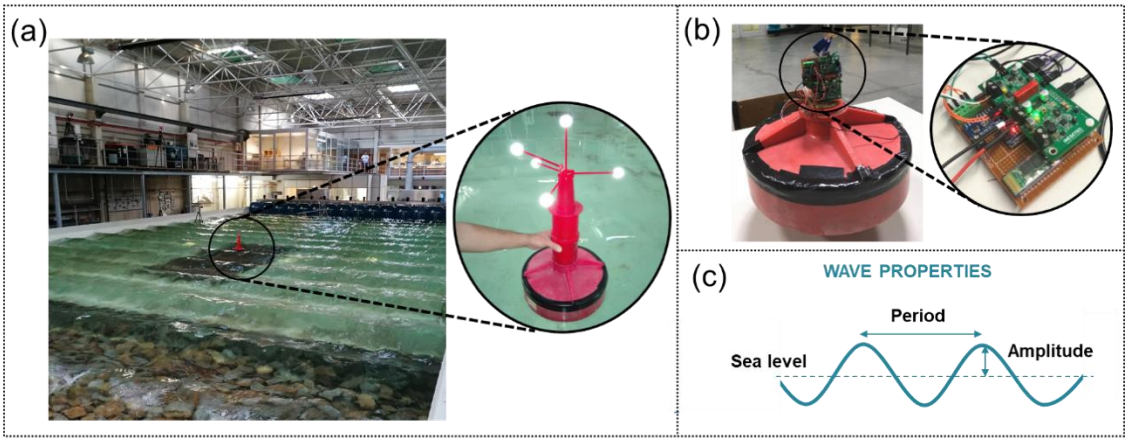


Figure 3.11 – (a) Navigational buoy tested in the wave basin under realistic wave conditions. Inset of the buoy re-dimensioned in a 1:8 scale. (b) Bluetooth datalogger developed to measure and send the voltage generated by TENGs in real-time. (c) Simplified representation of the properties of the regular waves generated in the wave basin.

linked to the amount of energy that is being transported by the wave. For linear waves, the wave height is equal to twice the wave amplitude.

The wave conditions to be tested in the experimental study were selection to encompass both the resonance conditions of the reference navigational buoy and the real sea states occurring at a possible deployment site. Therefore, we considered three combinations of wave amplitude and wave period within the pitching resonance range of the physical model (0.0625 m – 0.742 s and 0.125 m – 0.920 s, 1.097 s) and taken into account five combinations based on the most frequently occurring wave conditions for a deployment site of the real-scale product version of the physical model, at Figueira da Foz, Portugal (Figure 3.12).

Table 3.2 shows the characteristics (wave height and wave period) of the chosen wave conditions at the full-scale of the commercial navigational buoy (0.5 to 2 m; 2.1 to 10 s) and the same wave conditions converted to the 1:8 scaled model using the Froude similitude law (0.0625 to 0.250 m; 0.742 to 3.536 s). The selection of regular wave conditions was studied and proposed by D. Clemente *et al.* [168].

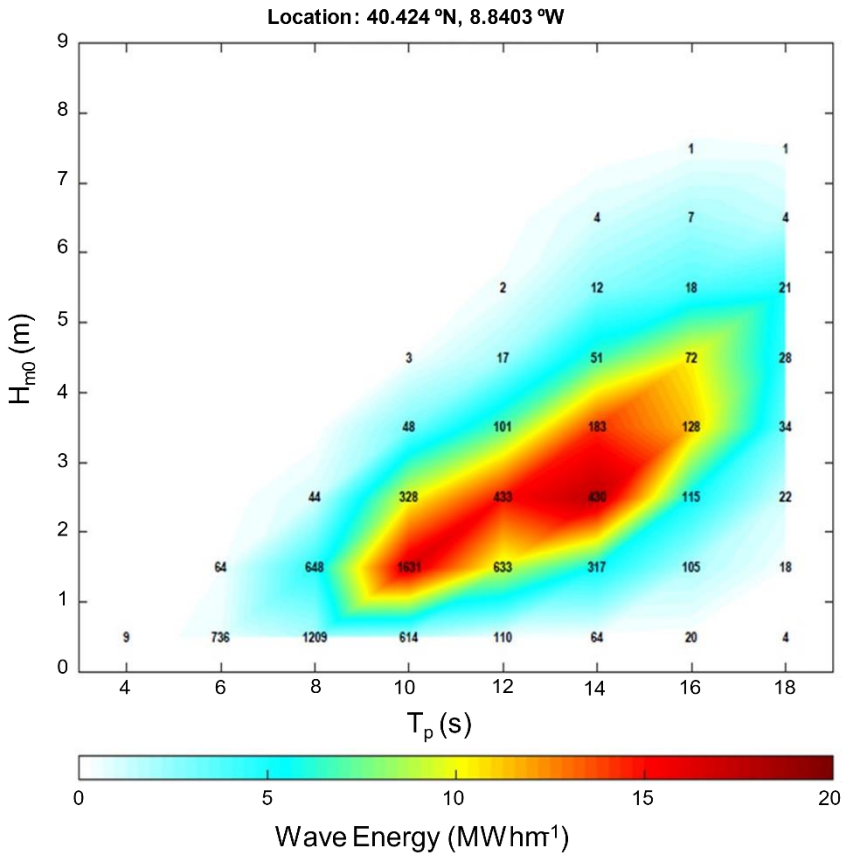


Figure 3.12 – Wave energy resource matrices for two sites near Figueira da Foz, Portugal: significant wave height (H_{m0}) versus peak wave period (T_p) (based on Ref. [226]).

Table 3.2 – Reproduced regular wave conditions both at full and model scale.

Full-scale (prototypes)		1:8 scale models		Wave Condition
H (m)	T (s)	H (m)	T (s)	
0.5	2.1	0.0625	0.742	1
1.0	2.6	1.0	0.920	2
	3.1		1.097	3
	6.0		2.121	4
	8.0		2.828	5
	10.0		3.536	6
2.0	8.0	2.0	2.828	7
	10.0		3.536	8

Figure 3.13(a)-(c) shows the electrical outputs generated by the UF-, UL- and AC-TENGs under different wave periods and amplitudes. Similarly to the dry bench tests, the generated voltage tends to increase with decreasing period and increasing wave amplitude for the different TENGs.

However, a sharp peak, that is not present in the “dry”-bench experiments, is also visible as one approaches the natural pitch period of the buoy (0.920 s). To understand this behavior, one must consider the full dynamics of the navigational buoy when subjected to the excitations of waves. Figure 3.14 shows the response amplitudes operators (RAOs) for the three most significant DoFs of the different TENGs. It should be noted that the RAOs are transfer functions used to determine the effect each sea state has on the buoy's motion, where each motion amplitude is normalized to the correspondent incident wave height. First one notes that the motion of the model buoy with different TENG configurations (Figure 3.14) is, overall, very similar. As such, the TENGs do not denote a significant influence on the hydrodynamics of the navigational buoy. This is further demonstrated by the linear correlation between the periods of the oscillatory cycles of the physical model and the corresponding wave periods of each test (Figure 3.15) which implies an almost perfect match between each pair of values (trend curve at 45º). From a physical perspective, the buoy model follows the passing waves,

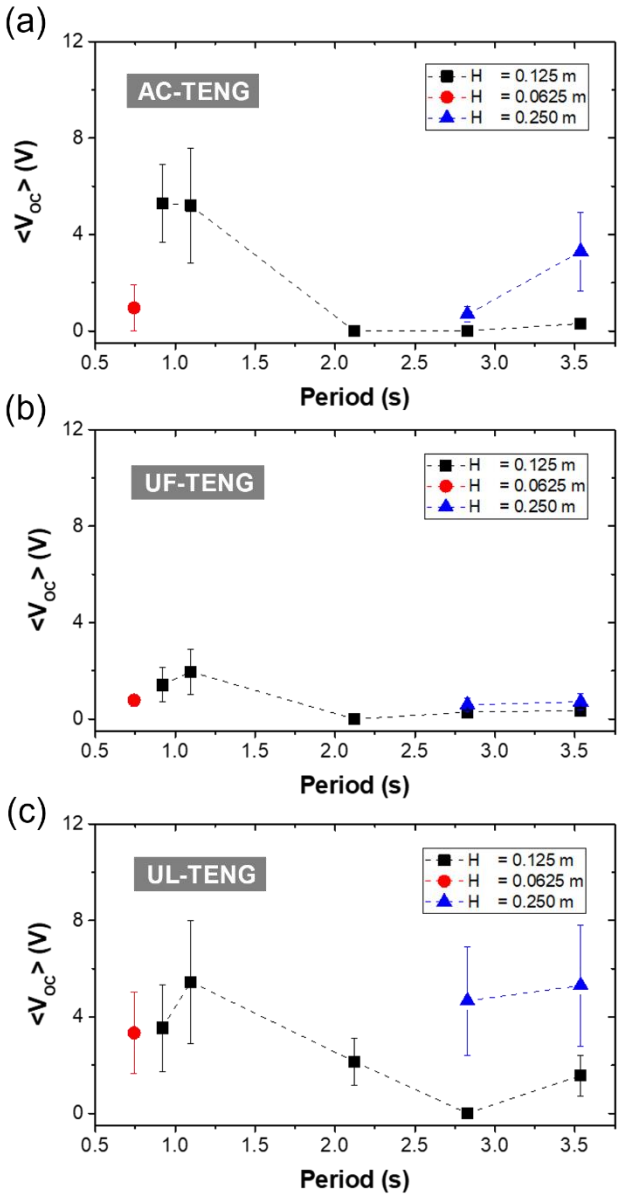


Figure 3.13 – Maximum open-circuit voltage, time average of the integrated area of the voltage peaks generated by (a) AC-, (b) UF- and (c) UL-TENGs, under various wave conditions (wave periods and wave amplitudes) selected to represent the most frequently occurring sea states at the case study site.

rather than oscillating for a fixed period. This is an expected occurrence when the length of the floating structure is much smaller than the wavelength, as is the case here [163].

Analyzing in detail the six degrees of freedom (DoFs) of the floating body, one clearly sees that the surge, heave and pitch oscillations are the most relevant ones, as shown in Figure 3.14 and Figure 3.16.

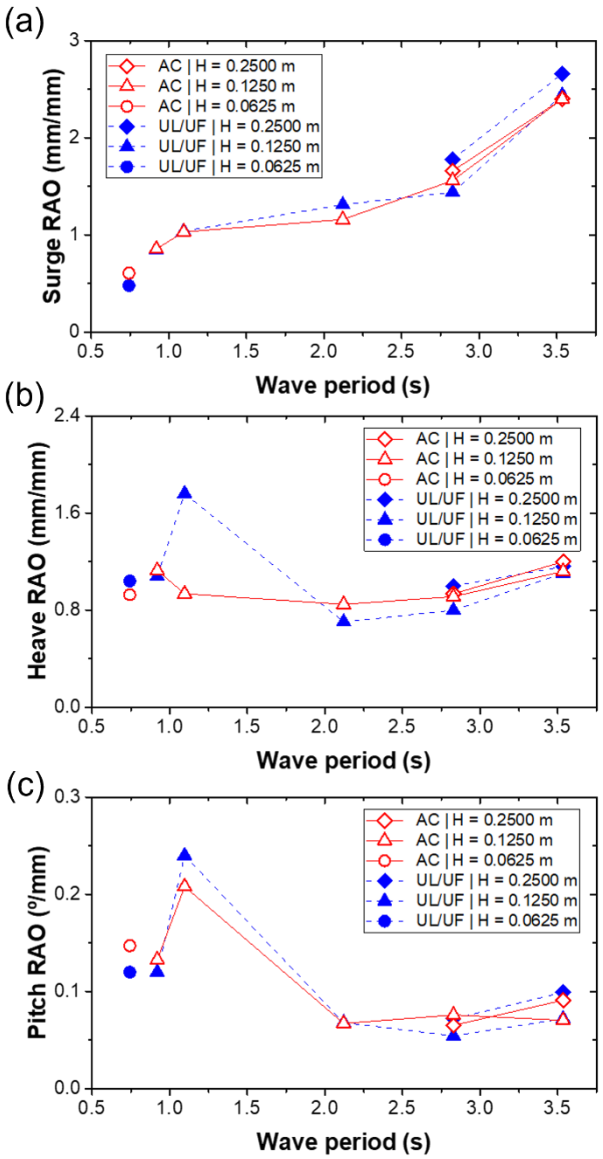


Figure 3.14 – Response Amplitude Operator for configurations AC-TENG and UL-/UF-TENG, regarding: (a) surge, (b) heave and (c) pitch DoFs (physical model values).

This relevance is in agreement with the wave direction and the orientation of the model buoy, as the reproduced waves advance in a single direction with a constant wave front along the transversal direction (unlike short-crested irregular waves, for instance). The surge, heave and pitch DoFs are the ones that are mainly excited, while the remaining DoFs denote negligible alterations. Nevertheless, the energy generation results show a pattern mostly in line with those of the physical model's response for the heave and pitch. In fact, looking at the dynamics of the navigational

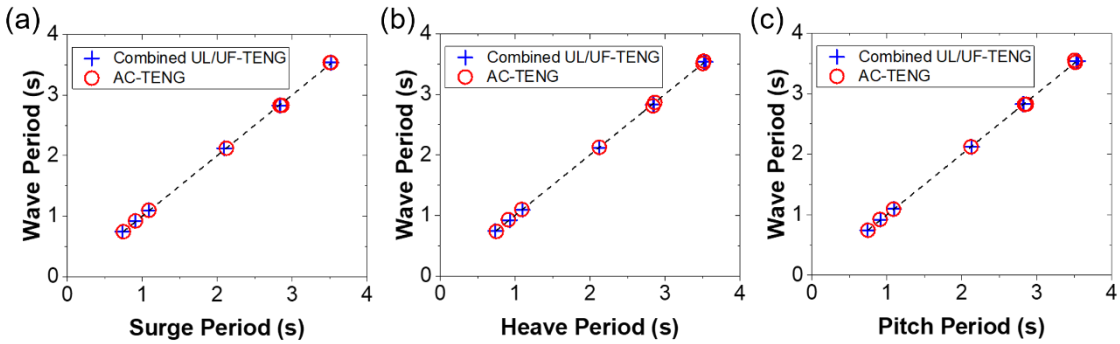


Figure 3.15 – Periodicity correlation between the generated waves and the physical model's hydrodynamic response for configurations AC-TENG and UL-/UF-TENG, regarding the (a) surge, (b) heave and (c) pitch DoFs (physical model results).

of the buoy, although the heave values remain relatively constant, a small increase is visible when comparing wave conditions with the same amplitude and increasing period. On the other hand, the pitch DoF shows a clear increment for the wave conditions near the physical model's natural pitch period (~ 0.920 s), together with a considerable decrease for wave periods above 1.097 s, where the values seem to stabilize within a very limited range. Therefore, there is a clear correlation between the electrical outputs

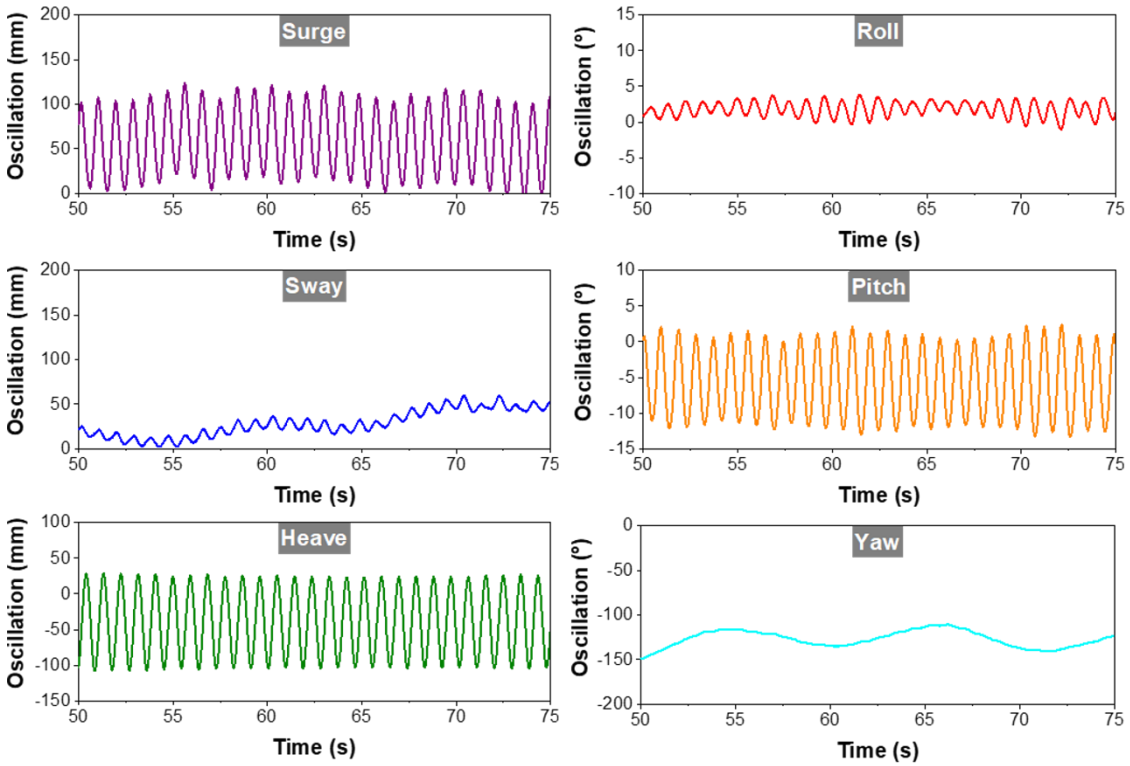


Figure 3.16 – Time series profiles of the motions of the physical model, for all 6 DoFs. The profiles regard the results with combined configuration UL-/UF-TENG, for wave condition H = 0.125 m, T = 0.920 s.

of the TENGs with the pitch response of the scaled commercial navigation buoy, for the different studied wave characteristics (periods and amplitudes).

Finally, by considering the energy generated by each TENG configuration under the different wave conditions tested pondered by the corresponding sea-state occurrence frequency (Figure 3.12), one finds that the UL-TENG achieves the highest electrical outputs, as shown in Figure 3.17.

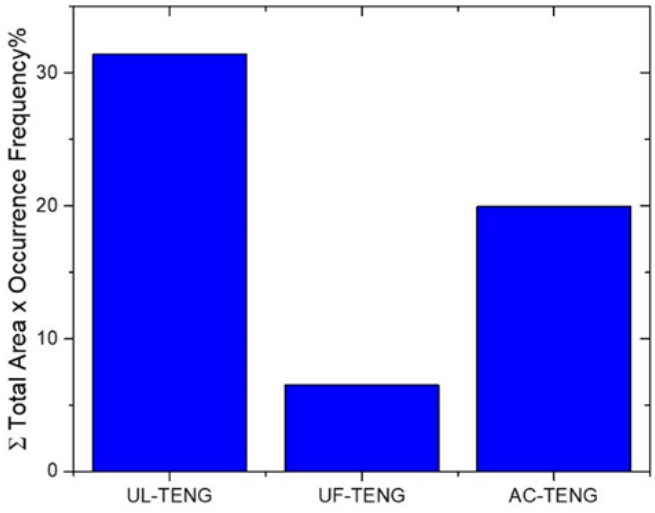


Figure 3.17 – Sum of the energy generated by each TENG for the different wave combinations, considering the occurrence frequency of each wave combination (amplitude/period).

3.5. Influence of floating platforms geometries on the TENG' performance

Despite all previous studies focusing on the design and optimization of TENGs structures for marine applications, the influence of the actual geometry of the floating platform on TENG performance has seldom been studied. Therefore, understanding the relationship between the floating platform and TENG could provide an innovative strategy to improve water waves conversion efficiency and energy harvesting sensitivity. In this study, we explore the hydrodynamic response of scaled floating structures incorporating TENGs under realist sea conditions. This is of the utmost importance, as the performance of TENG at sea depends of the oscillatory behavior of the floating platform geometry when subjected to wave action. As such, we incorporated TENGs in three different floating platform geometries, and tested their integrated performance in the large-scale wave basin equipped with a multidirectional wavemaker, taking into full

account the six degrees of freedom of the floating body. Considering our previous study in section 3.4 in which the UL-TENG achieved the highest electrical outputs under the different wave conditions tested, this configuration was chosen to study the effect of the wave-geometries interaction on the TENG performance.

3.5.1. Structure design and fabrication of the floating platforms

The floating platforms were designed and manufactured by the Interdisciplinary Centre of Marine and Environmental Research of the University of Porto (CIIMAR) of the Faculty of Engineering of the University of Porto (FEUP). The reduced scale physical models used in this study were reproduced at a 1:20 geometrical scale, based on the Froude criterion, to allow replication of equivalent wave-structure interactions and hydrodynamics at laboratory level, with regards to those expected at sea. Three floating platforms with different hull shapes were constructed: a half-cylinder, a half-sphere, and a trapezoidal prism. The hulls were constructed in methacrylate from molds of the required shapes, as were the respective lids. An exception was made for the half-sphere platform due to mass distribution adjustments (which affect the natural roll period), being the cylindrical lid cut out from a polyvinyl chloride (PVC) plaque. The dimensions of the floating platforms models are presented in Table 3.3.

Table 3.3 – Physical models of the three geometries of floating platforms: shape, dimensions, and main physical properties.

Model			
Dimensions	Outer radius: 0.345 m; Thickness: 5 mm.	Length: 1.000 m; Radius/height: 0.500 m; Thickness: 10 mm.	Length: 0.980 m; Lower width: 0.495 m; Upper width: 0.850 m; Height: 0.500 m; Thickness: 10 mm.
Metacentric height	0.103 m	0.146 m	0.114 m
Natural pitch period	1.91 s (unmoored)	2.04 s (unmoored)	2.15 s (unmoored)

3.5.2. Working mechanism of TENGs

The selection of three different floating platforms was based on the outcomes of a preceding numerical study by Clemente *et al.* [169]. Figure 3.18(a)-(c) shows the structural designs of the different floating platform hull shapes: half-sphere, half-cylinder, and trapezoidal prism. To provide a correlation between the hydrodynamic response of the floating platforms and the TENG' output, a triboelectric device based on rolling spheres was used.

Figure 3.18(d) illustrates the schematic design of the coupled lateral-based triboelectric device composed by an individual trough of PLA, where two stainless steel spheres can move linear and unidirectionally. These spheres can strike with two TENGs assembled in the lateral ends of a PLA trough. Each TENG has a triboelectric pair of PTFE/Ag films assembled on a PLA structure that is fixed in the lateral trough, while the opposite triboelectric pair (Nylon 6,6/Ag films) is assembled and attached onto a free PLA plate articulated to operate as a hinge, as shown in Figure 3.18(e). The working mechanism of the lateral based-triboelectric device is similar to that described previously in section 3.4.

Under the excitation of waves, the spheres can move freely along of directional PLA trough, and they collide with the PLA hinge, which is pressed against the PLA plate fixed

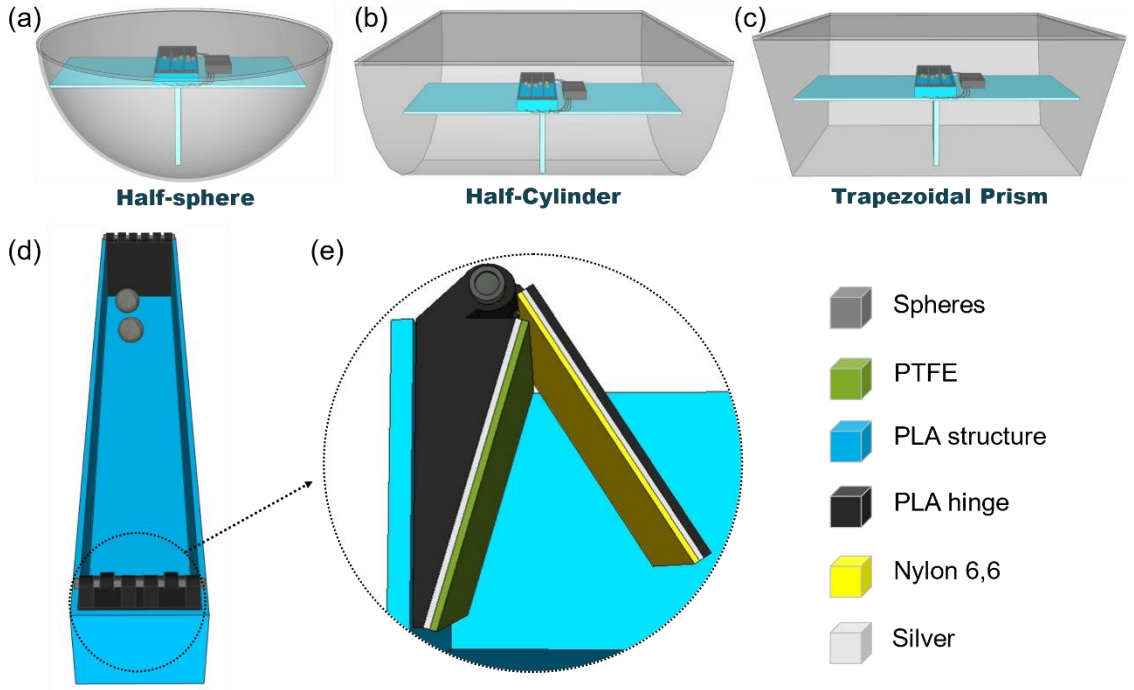


Figure 3.18 - Schematic of the (a) half-sphere, (b) half-cylinder and (c) trapezoidal prism floating platforms. (d) Two lateral-based TENGs connected electrically in parallel and (e) detailed configuration of individual structural design of lateral triboelectric device.

in the lateral trough. This makes Nylon 6.6 and PTFE films come into contact generating opposite charges on their surfaces. Then, the free plate will move away from the fixed one and a potential difference will be induced when the two triboelectric surfaces are separated due to the oscillation of ocean waves, driving an electron flow between the two silver electrodes.

3.5.3. Electrical outputs performance of the coupled lateral TENG

3.5.3.1. Regular water wave conditions

The dependency of the performance of the lateral-based triboelectric devices on the hydrodynamic response of the floating platforms was studied in a wave basin (28.0 m long, 12.0 m wide and 1.2 m depth) capable to properly reproduce regular and irregular wave conditions. Two UL-TENGs were connected electrically in parallel, and the electrical outputs were acquired using a Bluetooth datalogger implemented inside each floating platform, measuring and transmitting data in real-time to a personal computer. The matrix of wave periods was prepared encompassing seven wave periods, including the platforms' natural pitch period of about 2 s (resonant period, model value), at a fixed wave height of 0.100 m (2 m in prototype values). The matrix was based on the most frequently occurring wave conditions for two deployment sites: Aguçadoura and São Pedro de Moel in Portugal [170]. Table 3.4 shows the characteristics (wave height and wave period) of the chosen wave conditions at the full-scale of the floating platforms (2 m; 6 to 12 s) and the same wave conditions converted to the 1:20 scaled model using the Froude similitude law (0.100 m; 1.342 to 2.683 s). The selection of regular wave conditions was studied and proposed by D. Clemente of CIIMAR, FEUP.

Table 3.4 – Matrix of the reproduced regular wave conditions both at full and model scale.

Full-scale (prototypes)		1:20 scale models		Wave Condition	
H (m)	T (s)	H (m)	T (s)		
2.0		6.0	0.100	1.342	1
		7.5		1.677	2
		8.5		1.901	3
		9.0		2.012	4
		9.5		2.124	5
		10.5		2.348	6
		12.0		2.683	7

Figure 3.19(a) shows the short-circuit current generated by the lateral based TENG implemented inside the half-sphere floating platform under different waves periods at a fixed wave height of 0.100 m. As the wave periods rises from 1.342 to 2.683 s, I_{SC} gradually decreases from a maximum of 2.2 µA down to zero. The open-circuit voltage generated by the lateral-based triboelectric device within the three floating platforms under different waves periods (ranging from 1.342 to 2.683 s) is shown in Figure 3.19(b). A dependency of V_{OC} with the wave period is observed, where the triboelectric outputs decrease with increasing wave period (i.e., decreasing wave frequency) reaching zero for longer waves periods. By increasing the waves' frequency, the spheres increase their motion speed and acquire larger momentum upon colliding with higher impact force on the free PLA plate of the two TENG units. Thus, V_{OC} increases with increasing wave frequency. This trend was observed using the three floating platforms; however, the highest V_{OC} was achieved using the half-cylinder floating platform, reaching a maximum of ~ 247 V for a wave period of 1.677 s.

The maximum V_{OC}, I_{SC} and P of the coupled lateral-based triboelectric device were characterized using the three floating platforms under different waves periods at a fixed

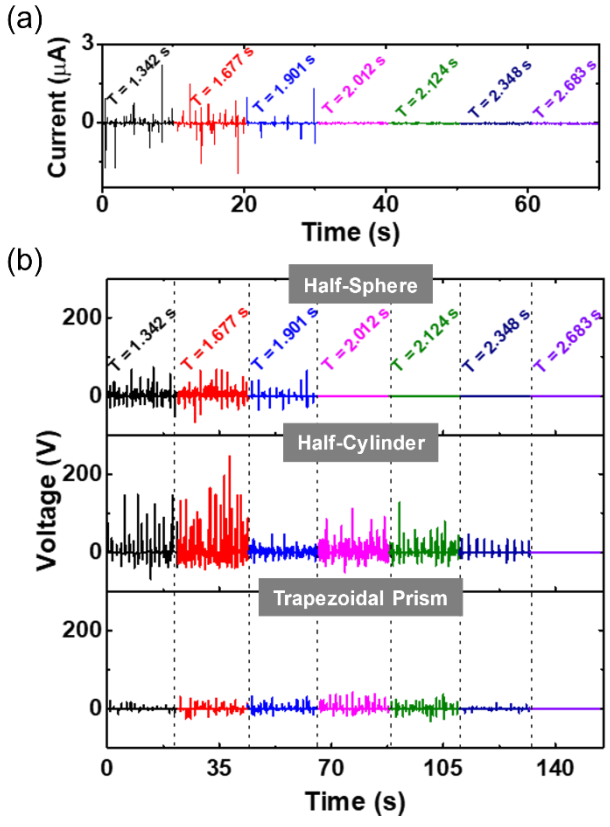


Figure 3.19 – (a) Output current for a TENG inside the half-sphere floating platform under different waves periods at a fixed wave height of 0.100 m. (b) V_{OC} generated by the lateral based-TENG within the three floating platforms under different waves periods at a fixed wave height of 0.100 m.

wave height of 0.100 m, as shown in Figure 3.20. Considering the range of tested wave periods, there is a trend and dependence on the electrical outputs generated by triboelectric device with the structural geometry of the different floating platforms. Figure 3.20(a) shows that the electrical outputs of the TENG inside the half-sphere structure tend to decrease with increasing wave period up to 1.901 s, which is close to the natural period of the half-sphere floating platform (1.91 s). Then, the electrical outputs continue to decrease and reach zero for wave periods above 2.012 s. The triboelectric device assembled inside the half-cylinder floating platform generated electrical outputs over almost all of the range of the tested wave periods (with the exception of the longest period, 2.683 s). Then, maximum V_{OC}, I_{SC} and P of ~ 70 V, 0.6 μA and 11 μW, respectively, were reached for a wave period of 1.677 s [Figure 3.20(b)]. After that period, the electrical outputs tend to decrease. Studying the triboelectric performance within the trapezoidal prism floating platform, we obtained a V_{OC} increase from ~ 8 V to 22 V when the wave period increases from 1.342 to 2.012 s [Figure 3.20(c)]. Further increasing the wave period, the voltage tends to decrease and reaches zero for 2.683 s. The power (current) reveals similar tendency and a maximum power (current) of ~ 3 μW (~ 0.4 μA) was generated at 2.012 s. These results show that the coupled lateral-based triboelectric device generates the largest electrical outputs when implemented inside the half-cylinder floating platform under regular wave conditions.

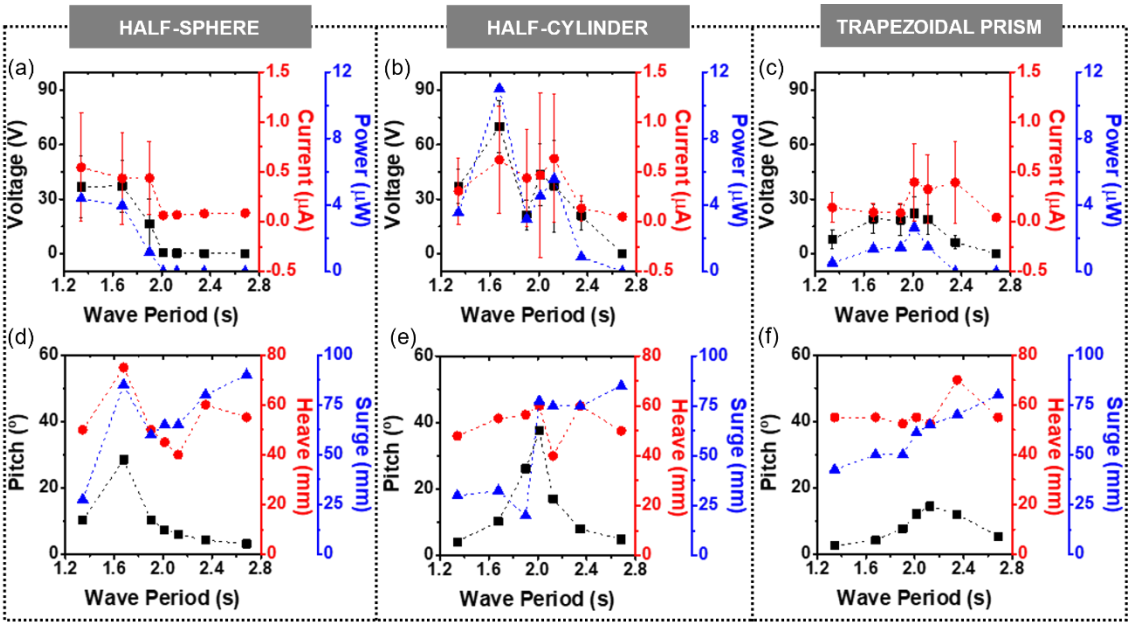


Figure 3.20 – Maximum voltage, current and power generated using different wave periods by (a) half-sphere, (b) half-cylinder and (c) trapezoidal prism floating platforms. Hydrodynamic response of the (d) half-sphere, (e) half-cylinder and (f) trapezoidal prism floating platforms, regarding: pitch, heave and surge DoFs (physical model values).

In summary, we were not able to observe a clear correlation between the electrical outputs generated by TENG inside the three different floating platforms and the corresponding degree of freedom. In particular, the maximum outputs do not always occur for the natural period of each of the geometric structures. However, the same was not observed in the experimental tests mentioned in section 3.4.5, where a clear correlation was achieved between the electrical outputs of the TENGs with the pitch response of the scaled commercial navigation buoy, for the different studied wave characteristics. In the case of the scaled commercial navigation buoy, the voltage generated by the TENGs increased with increasing wave frequency and amplitude, achieving maximum values for periods close to the natural period of the buoy.

3.5.3.2. Irregular water wave conditions

The sea rarely shows regular water waves, as it is characterized by a mixture of waves of different lengths and heights, i.e., irregular sea states. Therefore, it is crucial to obtain the electrical outputs of TENGs when subjected to irregular waves, as these are the closest to realistic sea conditions. Considering that the coupled lateral-based TENG achieved the highest output power when implemented inside the half-cylinder hull in regular sea states, we also performed studies in this structure under irregular wave conditions using the wave basin. Table 3.5 shows the total of eight reference sea-states selected for the tests with irregular long-crested waves. This selection was studied and proposed by D. Clemente *et al.* [171] from the resource matrices associated with the case studies of Aguçadoura and São Pedro de Moel [170].

The open-circuit voltage under the eight sea-states considered in the experimental study with irregular waves is presented in Figure 3.21(a). An average open-circuit voltage and power density of ~ 85 V and 182 mW/m^2, respectively, was achieved for sea-state

Table 3.5 – Matrix considered in the experimental study with irregular waves both at full and model scale.

Full-scale (prototypes)		1:20 scale models		Wave
H (m)	T (s)	H (m)	T (s)	Condition
1.330	8.960	0.067	2.004	1
2.309	10.412	0.115	2.328	2
2.358	11.464	0.118	2.564	3
3.203	11.554	0.160	2.584	4
3.321	12.550	0.166	2.806	5
3.701	12.654	0.185	2.830	6
3.827	13.627	0.191	3.047	7
4.249	13.730	0.212	3.070	8

1, which corresponds to a wave period closer to the resonant period of the floating platform (2.040 s in model values, or approximately 9.123 s in prototype values). A significant decrease of V_{OC} is observed when the wave period deviates from the resonant period. However, an increase of the electrical outputs was obtained with increasing wave height and wave period, as shown in Figure 3.21. This trend may be related to the increase in the wave excitation and the inherent transported energy. On the other hand, the surge DoF increases with increasing height and period of waves, which can also lead to an increase in the generated electrical outputs. Thus, the larger wave excitation and surge excursions cause the spheres to increase their motion span, acquiring larger momentum and colliding with a higher impact force on each tribo-device fixed on the lateral ends of the PLA trough.

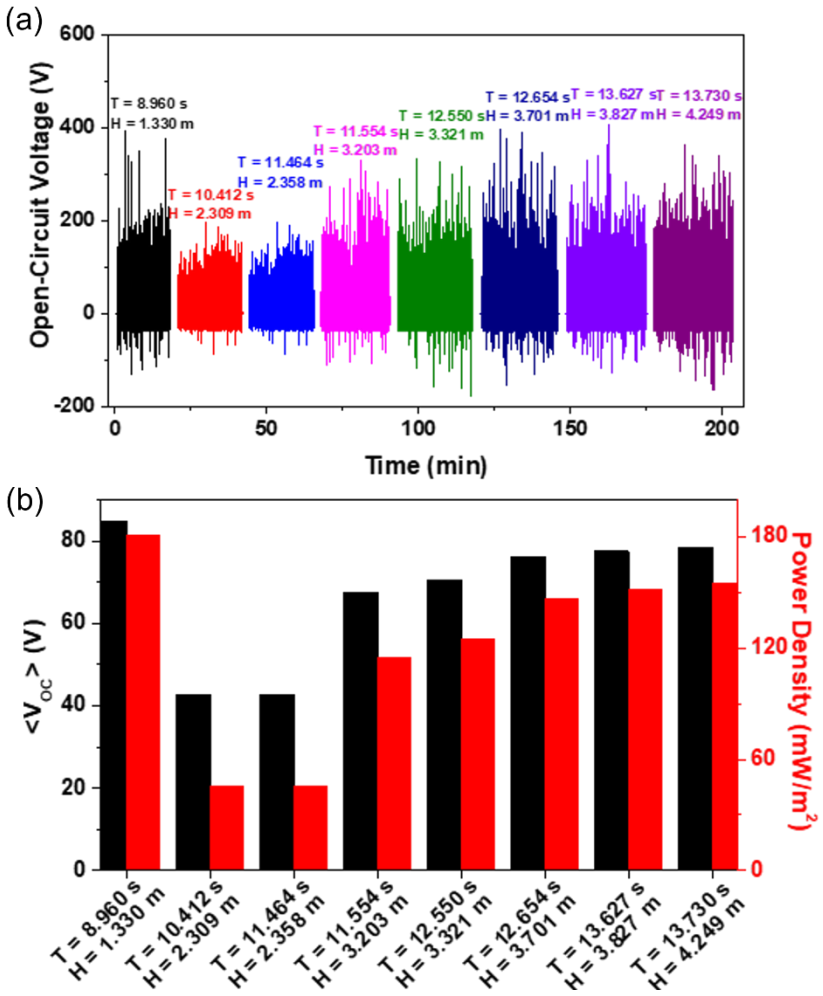


Figure 3.21 – (a) Open-circuit voltage generated by the lateral based TENG inside the half-cylinder hull under irregular sea-states. (b) Mean voltage and power density generated by the TENG implemented inside the half-cylinder hull.

3.6. Conclusions

The main objective of this work was to understand the dependence of TENGs energy generation on the hydrodynamic response of the floating structure inside which they are integrated under relevant sea state conditions. We started by developing three different rolling-sphere-based TENGs and implementing them inside the scaled model of a commercial navigational buoy to harvest kinetic wave energy. The most appropriated structure was determined based on systematic studies spanning typical periods and wave amplitudes of real sea states. The TENGs electrical outputs tend to rise with increasing pitch amplitudes and decreasing period due to the increase of the spheres' velocity. The UL-TENG generated the highest electrical outputs, reaching a maximum voltage, current and power of 14.6 V, 2.8 μA and 230 μW, respectively. The capability of these TENGs to harvest energy from ocean waves when incorporated into a navegational buoy was shown under realistic sea states. The voltage generated by the TENGs increases with increasing wave frequency and amplitude, achieving maximum values for periods close to the natural period of the buoy (~ 0.920 s). Based on the sea state occurrence frequency, it was determined that the UL-TENG is the most efficient in harvesting wave energy considering the DoFs of a floating body under realistic conditions. This integrated study provided new horizons to integrate TENGs within buoys to harvest low-frequency and small-amplitude wave energy and shows the importance of the DoFs of the movement of the floating bodies under the wave action on the excitation of the installed TENGs.

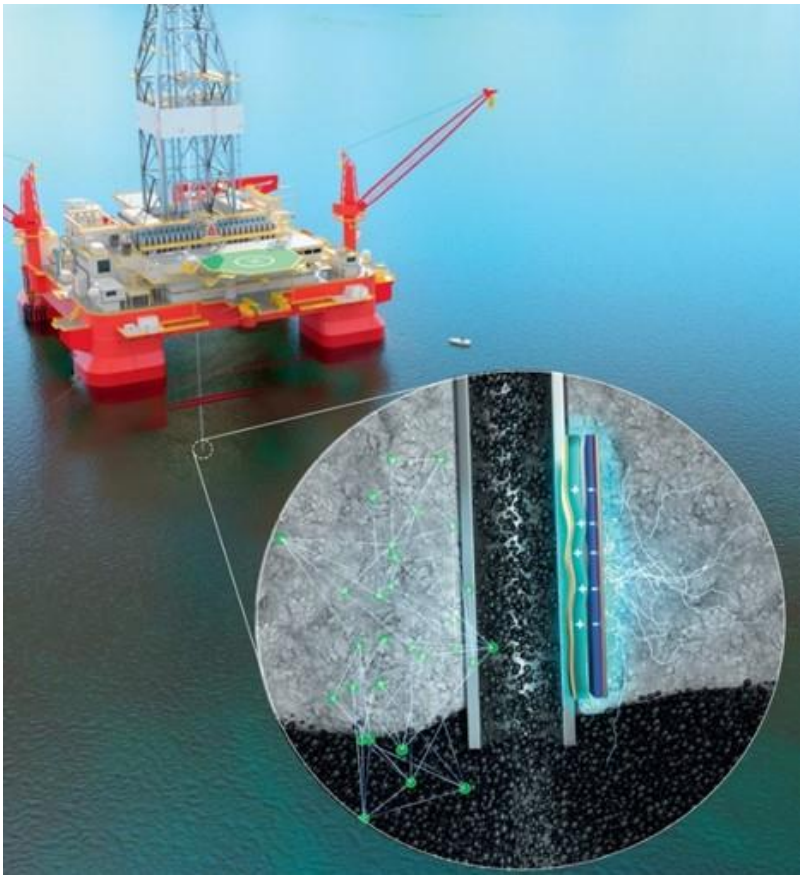
Furthermore, three different floating platforms' geometries within a couple lateral-based triboelectric device were also developed to study and understand the effect of the wave-geometry interaction on the performance of the coupled lateral-based TENG. The influence of the buoys' geometries on the TENGs' performance was carried out using wave periods and amplitudes of realist sea states simulated in a wave basin. There is a dependence of the electrical outputs generated by the triboelectric device with the structural geometry of the different floating platforms. In general, the electrical outputs generated by the triboelectric device tend to be higher for periods close to the natural pitch period for the three hull geometries and go to zero for high wave periods (~ 2.683 s). The couple lateral-based TENG generated the highest electrical outputs when implemented inside the floating platform with the half-cylinder hull, reaching a maximum voltage, current and power of ~ 70 V, 0.6 μA and 11 μW, respectively. The capability of the triboelectric device to harvest energy from ocean waves when incorporated into the half-cylinder floating platform was also studied under irregular sea states as those found in the ocean. In addition to being important to take into account the degrees of freedom

of floating bodies in the TENGs performance, it was also demonstrated that is crucial to take into account the hull geometry of the floating platforms where these triboelectric devices are incorporated. A maximum voltage and power density of ~ 85 V and 182 mW/m^2, respectively, was achieved for a wave period close to the resonant period of the half-cylinder floating platform (2.040 s in model values). This study suggests new perspectives on the performance of TENGs under irregular waves when incorporated within different floating platforms and shows the importance of hull geometries to excite TENGs in order to improve their applicability in the oceans.

The advanced fabrication of buoys allows the integration of sensors and electronic systems to support the long-term operation of maritime sensors in remote oceanic or coastal locations. Then, the encapsulation of our TENGs within the hull of the floating buoy can be an effective approach to isolate the device from external environmental factors, providing a more stable and reliable output even in harsh working conditions. Finally, for real ocean applications, our developed TENGs must be optimized in order to generate power to feed the electronic systems and sensors integrated inside commercial buoys.

Chapter 4

Triboelectric Energy Harvesting in Harsh Conditions



Chapter 4

Triboelectric Energy Harvesting in Harsh Conditions

Environmental and safety sensing is becoming increasingly important in harsh environments. However, present solutions to feed theses sensors are expensive and dangerous and there is so far no technology able to generate electrical energy in harsh working environments, such as high/low temperatures and pressures. Here, we show that TENGs can withstand and harvest energy in harsh conditions. By conducting thorough experiments in methane and crude oil over large ranges of pressures and temperatures, we were able to extend the operation realm of TENGs. By independently varying temperature (25–80 ºC) and pressure (28–119 bar) in methane, we demonstrate that temperature is the most critical parameter for TENGs operating in harsh environments. Furthermore, energy harvesting experiments performed in crude oil reveal a decrease of the electric outputs with increasing crude temperature and pressure. Nevertheless, the assembled device continued to generate electrical energy up to pressures of 830 bar and temperatures of 120 ºC.[3] *On the other hand, there are also economical sectors, such as industries or transportation, where released waste heat can be effectively used to alleviate the pressure on energy demand. Therefore, we also developed a TENG able to harvest one of the most ubiquitous energy sources that surrounds us: heat. Here, we demonstrate that TENGs, when combined with the thermomagnetic effect, can generate considerable electrical power by harvesting small temperature differences near room temperature. The thermomagnetic effect allows to induce the periodic and sustained motion when a magnetic second-order transition (ferromagnetic to paramagnetic) occurs in temperature gradients below 30 °C. This mechanical motion is then converted into electrical energy using a low-cost TENG. The applicability of this concept is demonstrated in a broad range of operating temperatures in both the cold (15 to 37 °C) and hot (60 to 90 °C) sides. It is further shown that the*

[3] *This work was adapted from C. Rodrigues, M. Kumar, M. P. Proença, J. Gutierrez, R. Melo, A. Pereira and J. Ventura – "Triboelectric energy harvesting in harsh conditions: Temperature and pressure effects in methane and crude oil environments" Nano Energy 2020, 72, 2657-2683. DOI: 10.1016/j.nanoen.2020.104682 [Reproduced from Ref. [45], Copyright 2021, Elsevier].*

electrical power generated by the hybrid TENG is more than 35 times higher than that obtained by a conventional thermomagnetic generator driven by magnetic induction.[4]

4.1. Introduction

Energy has been one the major driving forces behind our societal development and economic growth. However, the resulting surge in energy demand has also led to the major environmental crisis we now face. We must thus urgently find new ways to replace fossil fuels by green technologies that can steer us towards a carbon neutral world. This path towards sustainability can only be pursuit if one is able to develop new technologies that harvest energy from all the renewable sources that surround us. The wide application potential of these new energy harvesting technologies also brings new challenges. Critical devices work at harsh and remote environments, and the operation condition of a device might change over its life span. Thus, it is important to know the effect of environmental parameters on the performance of nanogenerators. In fact, working environmental parameters and operation conditions, such as temperature [29,172–178], pressure [172–174,179], humidity [172,179–183], atmosphere [17,172,181,182,184–186], gas flow [187–190] and gas concentration [186,188,191] are known to impact the behavior of triboelectric charging, as well as electrostatic induction processes, affecting the output performance of a TENG. However, it should be noted that most of these studies individually addressed each of the previously mentioned effects (temperature, pressure, and gas atmosphere) and considered only small ranges. In real applications, these effects cannot be separated, requiring their combination for actual applications in hash conditions.

Nevertheless, there are still a limited number of reports on the effects of harsh conditions (at extreme pressures and temperatures) on the characteristics and performance of TENGs. As the applications for TENGs expand, operations under extreme conditions may be required. Therefore, after a brief-state-of-the-art review, in this work we will mainly focus on the effect of temperature, pressure, and gas atmosphere on the triboelectric nanogenerators properties for applications under harsh and remote conditions.

Table 4.1 summarizes some of the main results obtained in the harvesting of mechanical energy in different environments using TENGs.

---

[4] *This part of work was adapted from C. Rodrigues ,A. Pires, I. Gonçalves, D. Silva, J. Oliveira, A. Pereira and J. Ventura – "Hybridizing Triboelectric and Thermomagnetic Effects: A Novel Low-Grade Thermal Energy Harvesting Technology" Nano Energy 2022, 32. DOI: 10.1002/adfm.202110288 [Reprinted with permission from Ref. [173], Copyright 2022, John Wiley & Sons].*

Table 4.1 – Prototypes developed to harvest energy under various temperatures, pressures, and gas atmospheres with their corresponding generation properties.

Parameter	Ref.	Temperature Range (ºC)	Pressure Range (bar)	Tribo-pair	V_{max} (V)	I_{max} (μA)	Q_{max} (nC)	Power Density	Year
Temperature	[175]	-20 – 150	NA	PTFE/Al	800 @ -20 ºC	1.4 @ -20 ºC	40 @ -20 ºC	0.4 W/m^2 @ -20 ºC	2017
	[176]	-196 – 227	NA	PTFE/Al	46@ -13 ºC	4 @-13 ºC	NA	NA	2014
	[177]	20 – 400	NA	Ti/SiO_2	300 @ 250 ºC	1.8 @ 250 ºC	80 @ 250 ºC	316 W/m^2 @ 250 ºC	2018
	[178]	-196 – 47	NA	PTFE/Al	23 @ -196 ºC	8 @ -196 ºC	NA	200 W/m^2 @ -20 ºC	2015
	[192]	140 – 260	NA	Al/Al_2O_3	NA	NA	12 @ 140 ºC	NA	2019
	[193]	20 – 200	5×10^{-10}	Fe/PTFE	500 @ 200 ºC	0.6 @ 200 ºC	525 @ 200 ºC	NA	2020
	[194]	50 – 200	NA	1 % BaTiO3-doped 6FDA–TFDB/Al	NA	2.3 @ 50 ºC	NA	NA	2021
Pressure	[179]	NA	0.07 – 0.87	PDMS/Al	NA	NA	12 @ 0.87 bar	NA	2013
	[193]	200	5×10^{-10}	Fe/PTFE	500 @5×10^{-10} bar	0.6 @5×10^{-10} bar	525 @ 5×10^{-10} bar	NA	2020
	[195]	NA	1 ;1.3×10^{-9}	BT-PTFE/Cu	180 @1.3×10^{-9} bar	513 @1.3×10^{-9} bar	903 @ 1.3×10^{-9} bar	50 W/m^2 @ 1.3×10^{-9} bar	2017
	[196]	NA	1 – 7.8	Kapton/Cu	NA	8 @ 7.8 bar	160 @ 7.8 bar	664 W/m^3 @ 7.8 bar	2019
Gas Atmosphere		**Type of Gases**							
	[182]	NH_3		PDMS/ Ce-doped ZnO	9	40.5	NA	210 mW/m^2	2019
	[186]	air, ethanol, ammonia, acetone, formaldehyde		HCl-doped PANI/Varnish	NA	0.015 @ ammonia	NA	NA	2018
	[188]	Air, CO, NH_3, NO		PDMS/Ppy–CSA	NA	0.115 @ NO	NA	NA	2019
	[197]	Air, He, Ar, N_2, CO_2, CHF_2Cl, SF_6		FEP/Conductive fabric	500 @ SF_6	11 @ SF_6	NA	NA	2018
	[198]	N_2, O_2, CO_2, Ar, He		Cu/PTFE Cu/PET	80 @ CO_2 60 @ CO_2	NA	40.29 @ CO_2 43.46 @ CO_2	NA	2018

4.2. Environmental effects on TENGS performance: An overview

4.2.1. Temperature effect

Temperature is one of the environmental parameters that can readily affect TENG performance due to heat transfer to or from the device. Thus, it has become important to verify the applicability of TENGs in a wide range of temperatures. Lu *et al.* studied the temperature effect on the electrical performance of a TENG composed by an Al foil and PTFE as triboelectric materials [Figure 4.1(a)-(c)] [175]. They showed that I_{SC} and power density decreased from 1.45 to 0.875 µA and from 0.3943 to 0.1157 W/m^2, respectively, when the temperature increased from -20 to 150 ºC. However, V_{OC} and I_{SC} exhibited only a residual increase between 20 and 100 ºC, which can be considered as stable electrical outputs in this temperature range, then dropping rapidly when the temperature continues to increase. To maintain effective electrical outputs of TENGs under high temperature

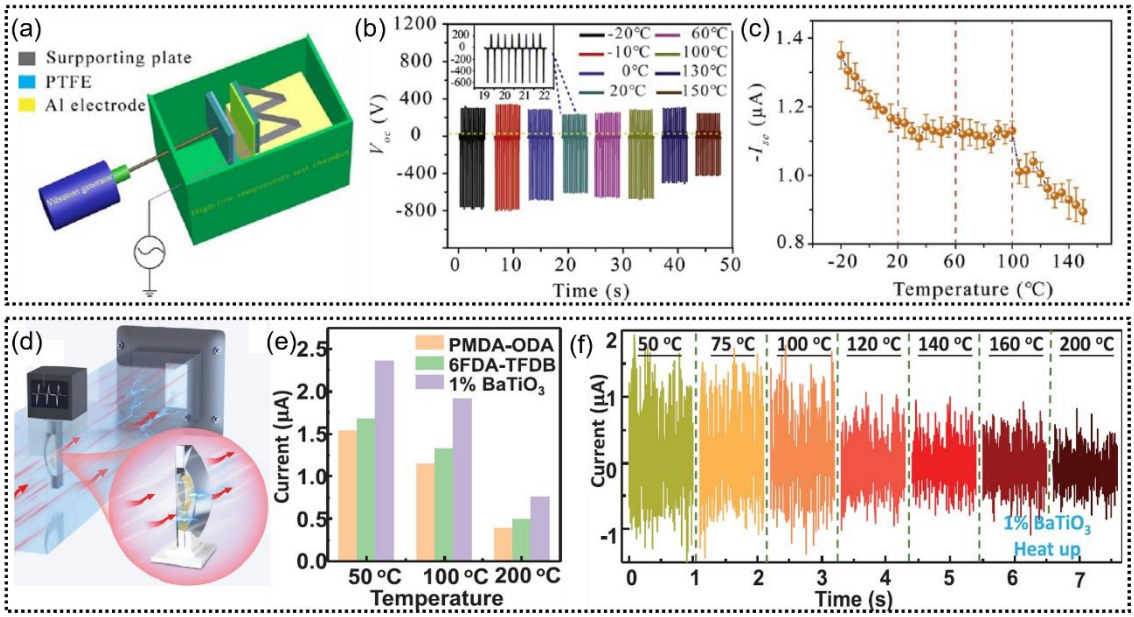


Figure 4.1 – (a) Schematic of the experimental setup and TENG. (b) Electrical signal curves of the open-circuit voltage at different temperatures. (c) Short-circuit current generated in a temperature range between -20 and 150 ºC. Reprinted with permission from Ref. [175], Copyright 2017, John Wiley & Sons. (d) Device schematic of the FD-TENG to harvest wind energy and sense wind speed at high temperature. (e) Current generated by FD-TENG using different triboelectric materials at 50, 100 and 200 ºC. (f) Current of FD-TENG at 6 m/s hot airflow using 1% BaTiO3-doped 6FDA–TFDB flap. Reprinted with permission from Ref. [194], Copyright 2021, John Wiley & Sons.

conditions, Tao *et al.* modified polyimide films [4,4′-(hexafluoroisopropylidene)phthalic anhydride–bis(3-aminophenyl) sulfone (6FDA–APS), 6FDA–2,2"-bis(trifluoromethyl)benzidine (TFDB), pyromellitic dianhydride-4,4"–oxydianiline (PMDA–ODA) and 1% barium titanate ($BaTiO_3$)-doped 6FDA–TFDB] by introducing strong electron withdrawing groups into the main chain [Figure 4.1(d)-(f)] [194]. The main goal was to further enhance charge density and thermal charge stability of these fluorinated polyimides. Since the 1% $BaTiO_3$ nanocomposite 6FDA–TFDB film demonstrated to have the highest enhance triboelectric performance and thermal charge stability, the authors developed a flutter-driven TENG (FD-TENG) to harvest wind energy and sense wind speed at high temperatures. The performance of FD-TENG was tested under a temperature range between 50 and 200 ºC, and it was obtained that its current decreased but can maintain 32% of its output performance at 200 ºC in comparison with room temperature values.

4.2.2. Pressure effect

The performance of TENGs can also be affect by pressure since the maximum charge density that can be accumulated on the surface of dielectric tribomaterials in air or in another gas is limited by the phenomenon of electrical air breakdown. There are already studies carried out on the effect of pressure on TENGs performance, opening horizons for applications under harsh conditions. One of the first studies was published in 2017 by Wang *et al.* [Figure 4.2(a)-(c)] [195]. In this work, the triboelectric charge density was increased by introducing built-in dielectric polarization using a ferroelectric material that has a residual polarization. Then, a TENG composed by a top copper electrode, a PTFE fil adhered to a ferroelectric material (barium titanate) and a back copper electrode at the bottom was fabricated [Figure 4.2(a)]. The authors demonstrated that the output charge density increased from 142 $\mu C/m^2$ in air to 1003 $\mu C/m^2$ in high vacuum (~ 1.3×10^{-9} bar), as shown in Figure 4.2(b). The V_{OC} , I_{SC} and power density also raised from 26 to 180 V, 80 to 570 mA/m^2 and 1.1 to 50 W/m^2, respectively [Figure 4.2(c)]. In this work, the charge density was clearly improved at 1.3×10^{-9} bar where the limitation of air breakdown is eliminated. This type of environment also spares TENGs from performance degradation caused by the natural accumulation of dust and air moisture.

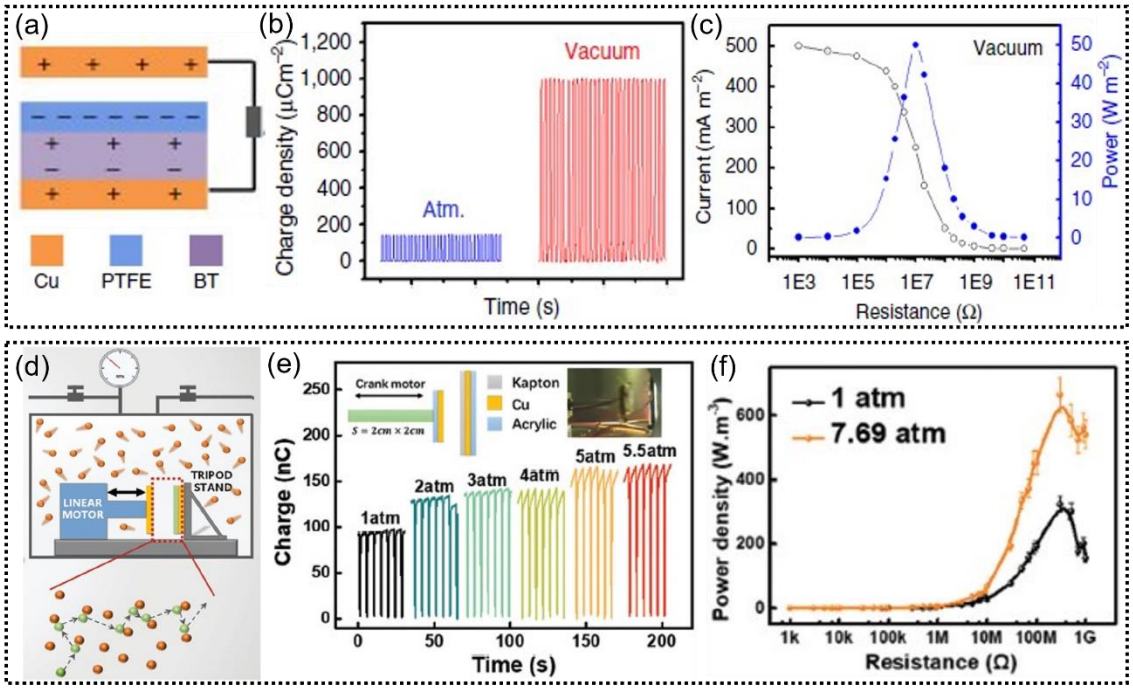


Figure 4.2 – (a) Schematic of TENG with the coupling of surface and dielectric polarization. (b) Charge density generated by TENG in atmosphere and high vacuum. (c) Output current and power densities of optimized TENG with different resistive loads at vacuum. Reprinted with permission from Ref. [195], Copyright 2017, Springer Nature. (d) Schematic diagram of experiment setup to work at high-pressure gas environment. (e) Charge generated by TENG under contact-separation working mode. (f) Power density of TENG with different resistive loads at 1 and 7.8 bar. Reprinted with permission from Ref. [196], Copyright 2020, John Wiley and Sons.

Figure 4.2(d) shows a method of suppressing the breakdown effects in the high-pressure gas environment in order to enhance TENGs performance [196]. In this work, Fu *et al.* showed that the charge density can be boosted with the increase of the gas pressure and they used a multiplier circuit to accumulate charge generation to push the limit of threshold charge density under high-pressure gas environments [Figure 4.2(e)]. A contact-separation mode TENG composed by Cu and Kapton/Cu as triboelectric pairs was developed to operate in high gas-pressure (7.69 atm) in order to suppress the gas breakdown effect due to air gaps between the two tribo-surfaces. Then, the peak I_{SC} and maximum power density increased from 4.6 to 8 μA and 324 to 664 W/m^3, respectively [Figure 4.2(f)].

Z. L. Wang and co-authors demonstrated an optimized direct-current TENG (DC-TENG) based on contact electrification and electrostatic breakdown [Figure 4.3] [193]. The DC-TENG is composed by a frictional electrode (FE), a charge collecting electrode (CCE) and a triboelectric material (PTFE film). The working mechanism of DC-TENG

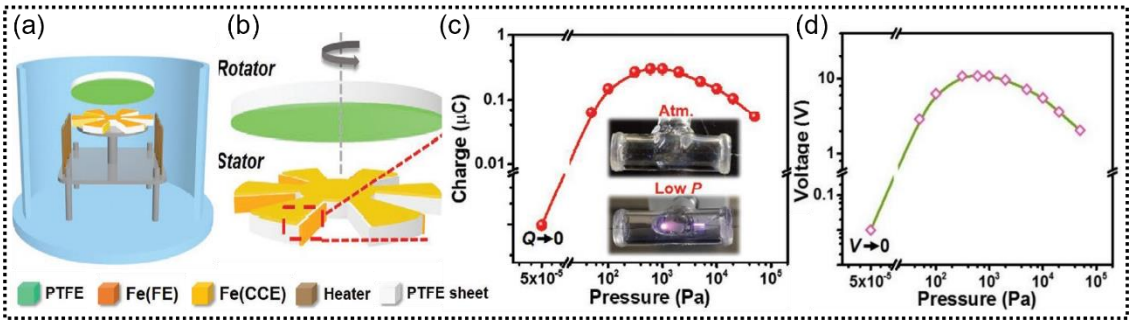


Figure 4.3 – (a) Schematic of the DC-TENG in the measurement setup. (b) Illustration of the rotary mode DC-TENG. (c) Charges and (d) open-circuit voltage generated by DC-TENG at various atmosphere pressures. Reprinted with permission from Ref. [193], Copyright 2020, John Wiley and Sons.

was based on the sliding mode and its performance was studied under various atmosphere pressures. The charge and V_{OC} generated by DC-TENG first increased then decreased with decreasing atmosphere pressure, as shown in Figure 4.3(c) and (d). The maximum electrical outputs were achieved at ~ 300 Pa, where the minimum air breakdown occurs. The authors also confirmed that a low pressure facilitated air breakdown by comparing a study of atmosphere electrostatic breakdown in atmosphere and low pressures, as observed in Figure 4.3(c). Then, it was demonstrated that the high vacuum environment can avoid the air breakdown.

4.2.3. Gas atmosphere

Contact electrification can be also influenced by adsorbed chemicals on the contact surface of triboelectric materials which will affect the TENGs performance. Thus, the electrical outputs generated by TENGs will depend on the amount and the chemical species of the gas atmosphere to which the devices are exposed. Some previous works have already shown the potential of TENGs for self-powered gas sensing/detection applications due to the screen effect of adsorbed target gas molecules on the electrostatic effect [182,186,188,197].

Figure 4.4(a)-(c) shows an integrated triboelectric self-powered respiration sensor (TSRS) that was developed to monitor human respiratory behaviors and NH_3 concentration of exhaled gases [182]. The triboelectric sensor is composed by two Au electrodes coated on flexible PET working as substrates and Ce-doped ZnO and modified PDMS films as triboelectric materials. In this sensor, Ce-doped ZnO sensitive film also worked as gas sensing material. S. Wang and co-authors studied and tested the TSRS under a simulated respiratory atmosphere, i.e., TSRS as subject to ammonia

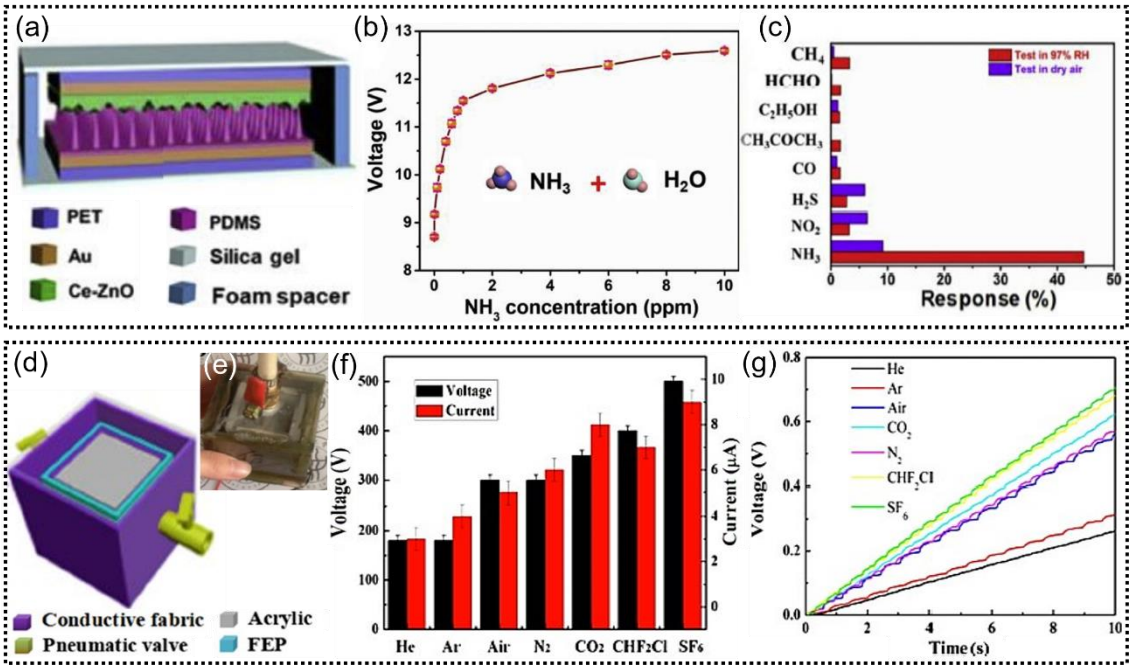


Figure 4.4 – (a) Structure design of the integrated triboelectric self-powered respiration sensor. (b) Voltage generated by Ce-ZnO-2 based TSRS under dry NH_3. (c) Response of Ce-ZnO-2 based TSRS using different interfering gases under moist and dry atmospheres. Reprinted with permission from Ref. [182], Copyright 2019, Elsevier. (d) Schematic and (e) photograph of the gas-enhanced enclosed cubic-TENG. (f) Voltage and current generated by the cubic-TENG under different gas atmospheres of He, Ar, air, N_2, CO_2, CHF_2Cl and SF_6. (g) Charging curves using a 3.3 μF capacitor under various gas atmospheres. Reprinted with permission from Ref. [197], Copyright 2019, Elsevier.

(NH_3) gas under a moisture of 97.5 % relative humidity (RH). It was observed that the generated voltage increased monotonously with increasing concentration [Figure 4.4(b)], which showed an opposite trend compared to the voltage generated under dry NH_3 and pure moisture environments. The authors also demonstrated that the sensing response of TSRS under NH_3 was ~12.5 times higher than when subject at other gases under moist atmosphere and ~1.5 times under dry atmosphere [Figure 4.4(c)]. These results showed that water molecules improved the selectivity due the specific reaction among ZnO, water and NH_3.

S. Lv *et al.* [197] studied the influence of different gases (He, Ar, air, N_2, CO_2, CHF_2Cl, and SF_6) on the performance of a gas-enhanced enclosed cubic-TENG [Figure 4.4(d)-(g)]. The cubic-TENG had an outer and an inner box made of acrylic, where the triboelectric materials are assembled. The two tribo-pairs were composed of FEP/conductive fabric and conductive fabric that come into contact via the shaking of the outer box. The authors showed that the cubic-TENG generated higher voltage when filled with N_2, CO_2, CHF_2Cl, and SF_6 than He, Ar and air [Figure 4.4(f)]. This TENG reached a

maximum voltage and current of 500 V and 11 μA under a SF_6 atmosphere, an increase of 67% and 120%, respectively, compared to the values obtained in air. The charging behavior of a capacitor of 3.3 μF also showed a similar trend of generated voltage and current, as shown in Figure 4.4(g). The authors explained these different trends with varying atmospheres conditions due to “gas discharge” since the gas molecules will collide with the charged triboelectric materials and carried the different charges in opposite direction. Then, the total charge accumulated on the triboelectric surfaces will be reduced due to this process of impact ionization.

4.3. Triboelectric energy harvesting in harsh conditions: Temperature and pressure effects

To reliably obtain data in harsh environments (defined as those in which human survival is difficult or impossible) is one of the most difficult achievements of the information age we live in. Although the Internet of Things (IoT) revolution is connecting billions of sensors that provide an unsurmountable amount of data, there is one thing all these devices still need: electrical power [199]. This is particularly critical in the oil and gas industry that needs to constantly monitor crucial safety and environmental parameters in extraction wells in order to prevent disasters such as oil spills, oil fires or, ultimately, explosions. However, electrical power in oil and gas wells is so far supplied downhole via tubing encapsulated cables (from the surface) or in-situ via batteries. Both scenarios come at high risks: long lengths of cable lead to reliability concerns due to possible ruptures, and battery replacement involves complicated and costly underwater operations. One then needs to locally generate the required electrical power by harvesting environmental energy available at the bottom of extraction wells, such as vibrations or fluid flow. However, present energy harvesting technologies do not cope well with the extreme conditions encountered in oil and gas wells that operate at high temperatures (T; up to 120 ºC), high pressures (P; up to 830 bar or ~ 12,000 psi) and involve a highly corrosive environment.

In this section, we demonstrate a triboelectric energy harvesting device able to generate electrical energy in harsh conditions similar to those found in extraction wells (pressures up to 830 bar and temperatures up to 120 ºC) in direct contact with gas and crude oil. Under the rotation movement of a high pressure/temperature trolley, flexible triboelectric materials come into contact by the motion of metallic spheres, leading to electrical power generation. The performance of the assembled device was studied over a wide range of pressures and temperatures in methane (CH_4) and crude oil

environments. Finally, the ability of a triboelectric device to generate energy under a continuous oil flux was performed using a closed loop oil flux system available at Xrig AS (Norway). Understanding the impact of hash environmental conditions on the performance of TENGs will ultimately broaden their applicability range into the realm of critical and extreme environments.

4.3.1. *Structure design and fabrication of the triboelectric device*

An energy harvesting device was developed to test energy generation in extreme conditions similar to those found in extraction wells. The assembled device consists in a box case of stainless steel (with internal dimensions of 24.9 × 3.4 × 1 cm^3 where the triboelectric materials are fixed and a set of five metallic spheres [with diameters of 0.8 cm and masses of 7.210 g; Figure 4.5(a)]. The box case was developed with specific material composition and dimensions to ensure the durability and to fit within the setup that simulates the harsh conditions.

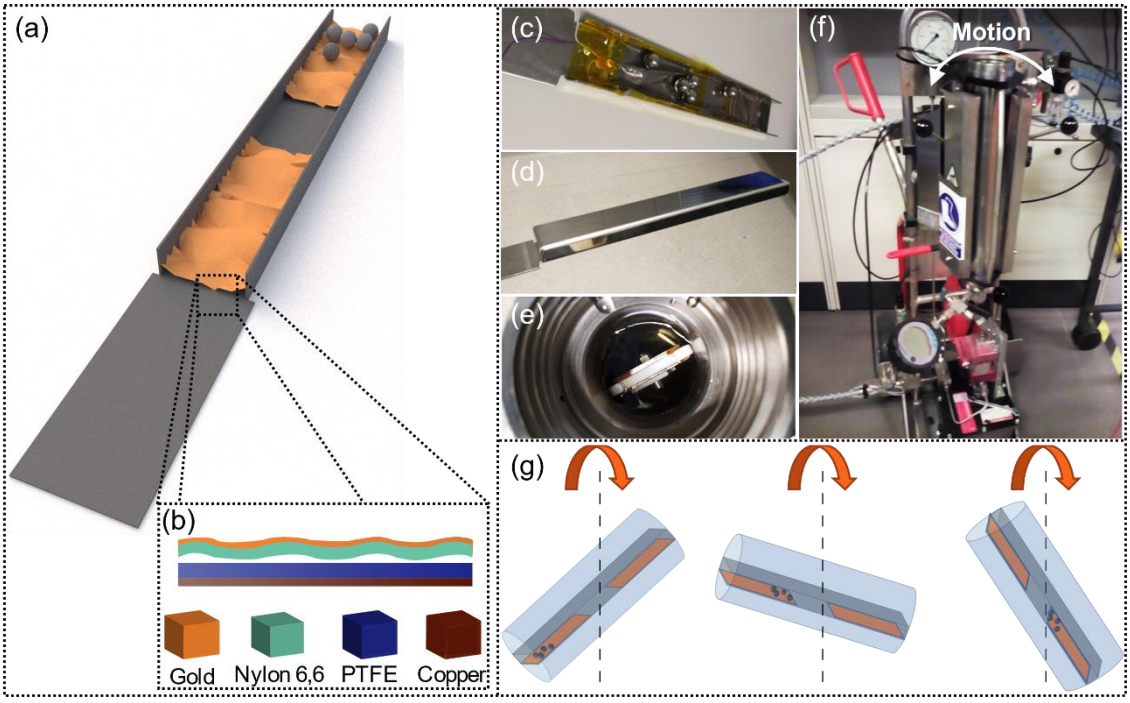
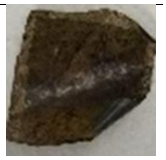
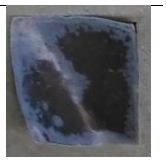


Figure 4.5 – (a) Design of the setup structure used to test the triboelectric materials at high pressures and temperatures. (b) Schematic structure of the tested triboelectric pair. (c) Photography of the two Nylon 6,6/PTFE structures assembled at each end of the box and metallic spheres. (d) Photography of the assembled setup to be placed inside the high pressure container. (e) Photography of the assembled device inside the high pressure container with crude oil. (f) Photography of the special trolley used to support the high pressure container and to allow the rotation motions. (g) Schematic illustration of the rotation motion of the assembled device.

The triboelectric nanogenerator was assembled using Nylon 6,6 and PTFE films (~ 25 µm and ~ 50 µm of thickness, respectively) as tribo-pair. Different electrodes (aluminium, copper and gold) were also tested at high temperatures in hydrocarbons environment to verify their durability in harsh conditions (Table 4.2). Durability tests of different electrodes were performed for high temperature and pressure using a closed high/temperature container filled with hydrocarbons. The temperature was slowly raised until reaching a pressure of around 689 bar. The system was then kept at such conditions during two hours and thirty minutes.

Table 4.2 – Results of the temperature (T) and pressure (P) tests performed in hydrocarbons.

Triboelectric material/ metallic electrode	T (°C)	P (bar)	Time (h)	Metallic Contact	
Nylon/Cu	110	689	2.5	Removed	
Nylon/Au	110	689	2.5	Maintained	
Nylon/Al	110	689	2.5	Maintained	
PTFE/Cu	110	689	2.5	Maintained	
PTFE/Au	110	689	2.5	Maintained	
PTFE/Al	110	689	2.5	Maintained	

Based on these results, gold was deposited on one side of the Nylon 6,6 film, while the PTFE electrode consisted in a copper foil tape [Figure 4.5(a) and (b)]. To improve the triboelectric generation, the Nylon film was assembled in a wrinkled structure, as shown in Figure 4.5(a) and (b). Two Nylon 6,6/PTFE structures were then prepared, one at each end of the box [Figure 4.5(b)]. The five spheres were then placed on top of the structures and the box closed with a cover. Both the assembled prototype casing and

the spheres are made of stainless steel to avoid the deterioration of the structure and thus ensure its durability when immersed in crude oil.

The influence of the triboelectric charges of the spheres was also studied using three different configurations based on the single-electrode mode with spheres in direct contact with Au thin films. In these structures, Nylon and glass work only as substrates, while the spheres are one of the triboelectric materials and the Au film acts as the other triboelectric material and as electrode. To performance a detailed study, two different electrode configurations were developed. In two of the studied structures, a continuous gold film (with 2.5 × 5 cm^2) was deposited on substrates of Nylon and glass with ~ 25 µm and 1 mm of thicknesses, respectively. The third structure also uses Nylon as substrate, but the Au film was deposited with a gap separation of ~ 5 mm. Figure 4.6 shows the electrical outputs generated by each one of these configurations and our triboelectric device. One can observe that there is a negligible generation of triboelectric charges occurring on the surface of the spheres, as there is no generated voltage when the device is tested using configurations based on the single-electrode mode (Figure 4.6). Thus, the spheres do not influence the electrical output of our triboelectric device.

The assembled device [Figure 4.5(c) and (d)] was placed inside a special high pressure/temperature container [Figure 4.5(e)], to be filled with gas or crude oil and withstand high temperatures (up to 120 °C) and pressures (up to 830 bar). Then, the performance of the triboelectric device was tested using a high pressure/temperature container available at Repsol Technology Lab (Madrid, Spain). Fixing the volume of gas

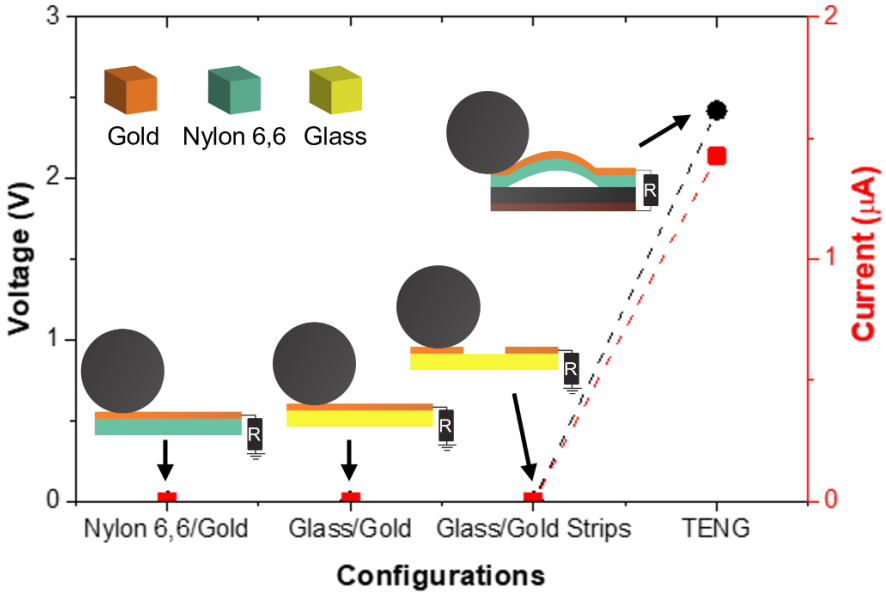


Figure 4.6 – Electrical outputs generated by the triboelectric device when the spheres are in contact with gold films using three different single-electrode configurations and our triboelectric device.

or crude oil inside of this container, the pressure increases due to the increase of the internal temperature of the container which is achieved using heaters attached to the outside of the container. Figure 4.7 shows the linear dependence between pressure and temperature for both increasing and decreasing cases. The experimental tests can only be performed after the stabilization of these two parameters at required values, as observed in the yellow region of Figure 4.7.

A special assembling was used so that mechanical motion could be induced inside the filled container and thus assess triboelectric performance. For this, the high pressure container was placed in a trolley [Figure 4.5(f)] that allows the manual imposition of rotation motions. These were performed at a frequency of 1.3 Hz, in 180 º rotations with an amplitude of ~ 25 cm. Therefore, when the whole apparatus was rotated, the spheres rolled on top of the two triboelectric materials, compressing them and generating energy [Figure 4.5(g)].

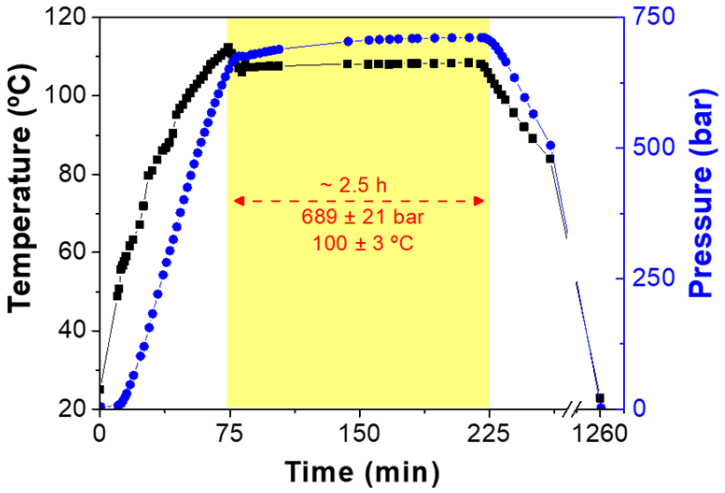


Figure 4.7 – Dependence of pressure with the temperature inside the special high pressure/temperature container.

4.3.2. Working mechanism of the energy harvesting device

The working mechanism for this triboelectric nanogenerator can be seen in more detail in Figure 4.8. Under an external triggering, such as the rotation motions of the special trolley, the assembled energy harvesting device will be tilted, causing the spheres to roll on top of the triboelectric materials. As this process occurs, the Nylon film will

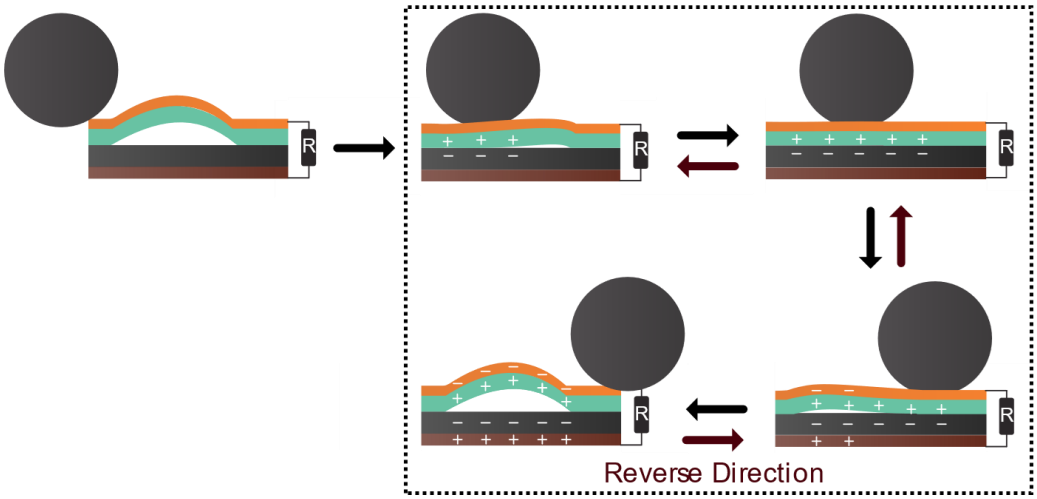


Figure 4.8 – Working mechanism of the assembled triboelectric nanogenerator based on the contact-separation mode.

contact the PTFE film, becoming positively charged. On the other hand, the PTFE film becomes negatively charge due to contact electrification. While the spheres are sliding, they will induce opposite charges on the two electrodes, which will result in a current flowing between them. After the spheres completely cross the triboelectric materials, the trolley will be tilted in the opposite direction, re-starting the energy generation cycle. Such contact-separation mode was chosen because of its simple design and capability of testing inside the high pressure container. It should be noted that this working mechanism is similar to the TENGs developed to study ocean energy generation presented in section 3.4 and 3.5.

4.3.3. Experimental results

4.3.3.1. Energy generation in gaseous environment

To demonstrate the potential of TENGs to harvest energy in harsh conditions and obtain the influence of pressure on the output properties of the assembled device, the special container was filled with methane gas and heated up to a constant temperature of 90 ºC. The pressure of the container was then decreased in steps from 119 to 28 bar. Figure 4.9(a) shows the open-circuit voltage generated by the assembled device for different pressures. The inset shows representative open-circuit voltage peaks with different magnitudes generated by the spheres when they induce various contacts between the two tribo-pairs. Figure 4.9(b) shows that the open-circuit voltage increases quasi-linearly as a function of pressure, with a maximum generated value of ~ 5.1 V at

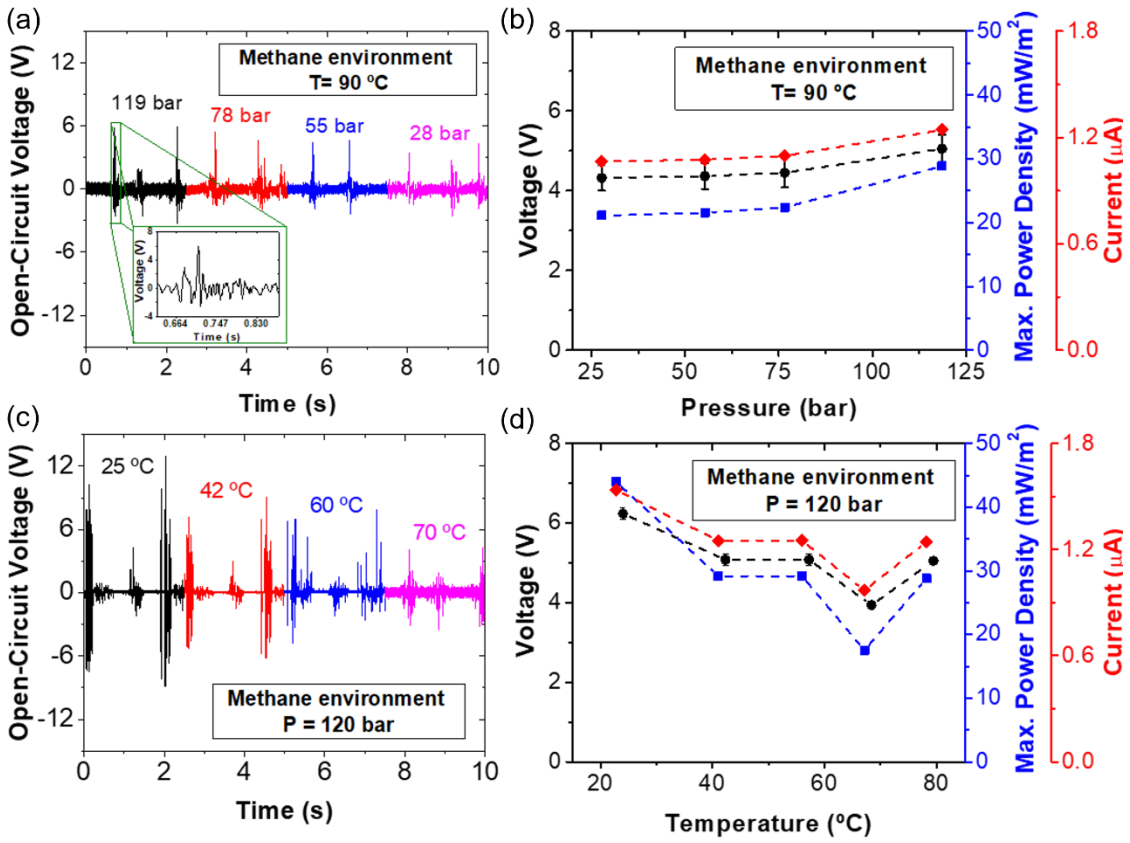


Figure 4.9 – Energy harvesting results obtained in methane as a function of pressure at constant temperature (T = 90 ºC): (a) open-circuit voltage, and (b) maximum voltage, current and power density. Energy harvesting results obtained in methane as a function of temperature at constant pressure (P = 120 bar): (c) Open-circuit voltage, and (d) maximum voltage, current and power density.

the highest achieved pressure (119 bar) and a small decrease of 14% for the lowest pressure (28 bar). The short-circuit current has a small increase with increasing pressure, achieving a maximum value of ~1.24 μA at 119 bar, as shown in Figure 4.9(b). Comparing the output voltage obtained in our study with those of several published works based on the same concept of rolling spheres [188,200–202] all reported similar electrical outputs. Particularly, Wang *et al.* [200] developed an encapsulated TENG composed by FEP pellets rolling between 3D copper electrodes which generated a short-circuit current smaller than ~ 2 μA at 2 Hz. Yong *et al.* [201] also developed a wind-rolling TENG to harvest energy from expanded polystyrene (EPS) rotating along a vortex whistle substrate. This TENG generated a maximum rectified open-circuit voltage of 11.2 V and short-circuit current 1.86 μA using 3 EPS spheres. Regarding the outputs recorded in these works, this performance is likely related to the smaller effective contact area between the triboelectric materials due to the spheres' motions.

The maximum power density data confirm the small increase of P_{max} with increasing pressure [Figure 4.9(b)]. We also observed that the assembled TENG generated higher electrical outputs when placed in a methane atmosphere than in air. This improvement of the TENG performance should be related with adsorbed molecular species of the methane gas that modify the triboelectric behavior of the contact surfaces, thus changing contact electrification [191,197]. The obtained pressure-dependence can be explained by a two-phase equilibrium model which describes the surface charge dependence with pressure in insulator–insulator triboelectrification [203]. In this model, the triboelectric surfaces are in equilibrium with its external environment because charge transfer occurs rapidly. One can then model the triboelectric surfaces as having localized states with a given adsorption energy in which CH_4 ions can be adsorbed (weak bonds) due to intermolecular forces while residing in vibrational energy states. Then, the total charge density (σ) of the triboelectric film resulting from adsorbed ions is given by [203]:

$$\sigma = \frac{q_e N}{S} \frac{P}{(k_B T)^{\frac{5}{2}} \left(\frac{m}{2\pi\hbar^2}\right)^{\frac{3}{2}} e^{-\frac{\xi_0}{k_B T}} + P}, \tag{2}$$

where q_e is the electronic charge, N is the total sites on the triboelectric surface that can be occupied by ions, S is the surface of the electrode, ξ_0 is the adsorption energy of the ion, k_B is Boltzmann's constant and $\hbar$ is the reduced Planck's constant. According to the previous equation, the total triboelectric charge density increases with increasing pressure. Consequently, V_{OC} and I_{SC} also increase, as confirmed by the corresponding ruling equations [68,88]:

$$V_{OC} = \frac{\sigma x(\mathrm{t})}{\varepsilon_0} \tag{3}$$

and

$$I_{SC} = \frac{\sigma S d_0 v(\mathrm{t})}{[d_0 + x(\mathrm{t})]^2}, \tag{4}$$

where $x(\mathrm{t})$ is the time-dependence distance between the two triboelectric layers, ε_0 is the permittivity of free space, S is the surface of the electrode, $v(\mathrm{t})$ the speed of the relative mechanical movement and d_0 is the effective dielectric thickness. We then

obtained the TENG performance in a methane gas atmosphere at a constant pressure of 120 bar over a temperature from 25 up to 80 ºC to understand how is energy generation influenced by temperature at high pressures. The open-circuit output voltages of the TENG is shown in Figure 4.9(c), denoting a decrease with increasing temperature by 37% in the studied range. Figure 4.9(d) shows that the output voltage, current and the maximum power density generated by the TENG decrease with increasing temperature, up to 80 ºC. This temperature-dependence of the electrical outputs is related with competing effects between changes of the mechanical properties of the triboelectric materials (that affect the contact area between them) and thermal fluctuations that influence triboelectrification [172,176]. Previous studies have shown that the PTFE surface becomes softer with increasing temperature, which facilitates more deformations at the nanoscale [172,176]. Thus, one would expect that such increase of the contact area would lead to an increase of the charge transfer, improving the electrical outputs. However, Wen *et al.* demonstrated that thermal fluctuations have a dominant effect over the mechanical properties for temperatures above − 13 ºC, leading to a decrease of the electrical outputs [176] as here also observed. With increasing temperature, thermal fluctuations cause large charge transfer in the backward direction, i.e. there will be an increase in the negative charge transfer from the PTFE surface to the Nylon surface, as opposed to the desired forward direction from Nylon to PTFE. This then leads to the degradation of the TENG performance with increasing temperature [Figure 4.9(b)]. The temperature-dependence can also be attributed to electron thermionic emission, where the electrons are emitted from the material once they gain enough thermal energy to overcome the work function due to the heating of the material. Considering the thermionic emission current density [177], one as:

$$\mathrm{J} = \lambda A_0 T^2 e^{\frac{W}{kT}} \left[e^{\frac{\Delta W}{kT}} - 1 \right], \tag{5}$$

where λ is the material-specific correction factor, A_0 is the Richardson constant of a free electron, T is the temperature, W is the height of the potential barrier, k is the Boltzmann constant, and ΔW is the potential barrier height variation due to the surface electric field. The previous equation shows that the thermionic emission current density increases with increasing temperature. As a consequence, the triboelectric surface charge density decreases, as does V_{OC} and I_{SC}, as confirmed by the corresponding ruling equations (3) and (4) [68,88].

4.3.3.2. Energy generation in crude environment

To further test triboelectric energy generation in harsh environments, experiments were also performed in crude oil. For this study, our triboelectric device was placed inside the same high pressure container but now filled with crude. The composition of crude used during the studies is shown in Table 4.3. The experimental tests were performed up to pressures of 830 bar, with the pressure being gradually increased by the increase of the temperature (up to 120 ºC), as shown in Figure 4.10(a). In fact, and contrarily to the methane experiments, in this case, temperature and pressure cannot be changed independently.

Table 4.3 – Elements composition of crude used during the performance studies.

Component	Requested Concentration	Final Concentation	Relative Uncertainty	Calibration Method
C_6H_{14}-N	500 PPM	492.5 PPM	5.00 %	ANALYTIC
C_5H_{12}-N	1000 PPM	999.1 PPM	5.00 %	ANALYTIC
C_5H_{12}-ISSO	1000 PPM	979.1 PPM	5.00 %	ANALYTIC
C_5H_{12}-NEO	100 PPM	100.1 PPM	5.00 %	ANALYTIC
C_4H_{10}-N	2500 PPM	2384.8 PPM	3.50 %	ANALYTIC
C_4H_{10}-ISSO	2500 PPM	2387.7 PPM	3.50 %	ANALYTIC
% N_2	0.75 %	0.75 %	2.00 %	ANALYTIC
% C_3H_8	1.50 %	1.50 %	2.00 %	PONDERAL
% C_2H_6	3.00 %	3.00 %	2.00 %	PONDERAL
%CO_2	1.50 %	1.51 %	2.00 %	PONDERAL
% CH_4	REST	REST	–	–

Figure 4.10(a) shows that the voltage generated by our triboelectric device gradually decreases with increasing crude pressure and temperature. Even so, the assembled energy harvesting device continued to generate electrical power up to pressures of 830 bar (120 ºC). For such condition, the maximum generated voltage, charge, current and power density were 0.2 V, 4.3 μC, 132 nA and 51 μW/m^2, respectively [Figure 4.10(b)].

Comparing the electrical outputs generated in crude environment with those generated in methane at 25 ºC we observed a drastic decrease of ~ 90%. The output voltage generated by the TENG for different pressures is shown in Figure 4.10(b), evidencing a steady decrease with increasing pressure/temperature.

Finally, we analyzed the capacity of our assembled triboelectric device to charge a load capacitor of 10 μF in crude oil environment with different temperatures and pressures (Figure 4.11). For that, a full-bridge diode rectifier was implemented to prevent the charge from leaking back from the load capacitor (C_L) to the TENG. Figure 4.11

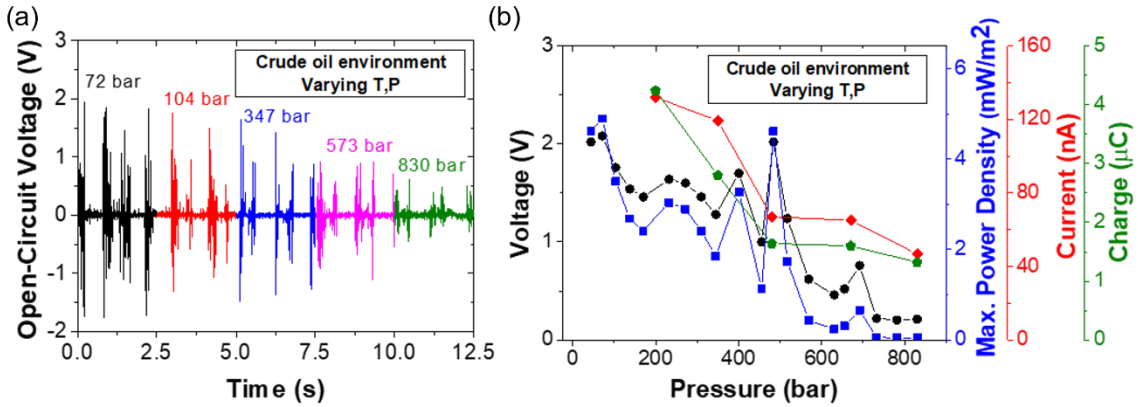


Figure 4.10 – (a) Open-circuit voltage of the TENG as a function of pressure in crude. (b) Output voltage, maximum power density generated in crude by the assembled triboelectric device up to 830 bar and 120 ºC.

shows a maximum stored electrical voltage of 0.3 V at 200 bar and 65 ºC after just 20 s of energy generation. The stored electrical energy tends to decrease with increasing temperature and pressure due to the reduction of the generated electrical power. Nevertheless, it was still possible to charge the capacitor up to 0.1 V at 830 bar and 120 ºC.

Before the previous experimental tests, we also evaluated fire and explosion hazards because static electricity discharges of the triboelectric device could be a potential ignition source. In this case, the Minimum Ignition Energy (MIE) is the parameter evaluating the smallest amount of energy needed to create a spark that can ignite a flammable environment. MIE is affected by several factors, such as fuel concentration, volatility and the presence of any fuel vapor. We calculated the maximum static energy of a typical TENG to verify if the accumulated density of charges on the

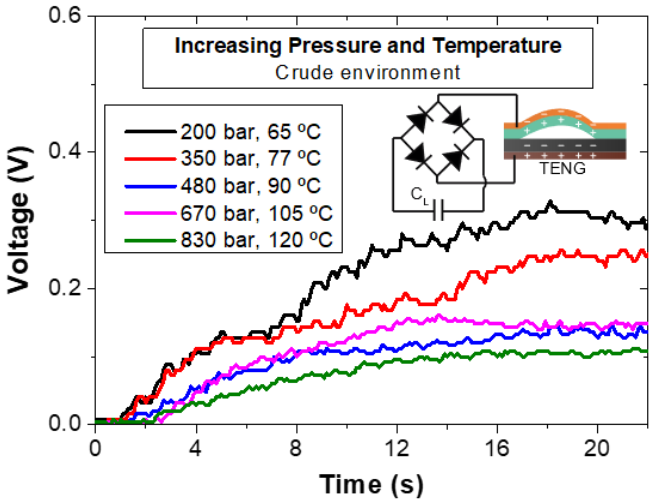


Figure 4.11 – Charging voltage over time for a 10 µF capacitor, using the assembled triboelectric device in crude environment for different temperatures and pressures.

dielectrics surfaces would be enough to create a spark in hazardous environments. One of the several reported works of Z. L. Wang and co-authors showed a spherical TENG based on spring-assisted multilayered structure to collect multidirectional water wave energy [124]. This device generated a transferred charge and output voltage of 1.0 μC, and 280 V, respectively. Calculating the maximum static energy stored $\left(E = \frac{QV}{2}\right)$, we obtain ~ 140 μJ which is much lower than the MIE of crude oil (~ 5 mJ) [204]. Therefore, the order of magnitude of the electrostatic charges generated on the triboelectric surfaces of typical TENGs is not enough to cause a fire or explosion hazard. Considering the electrical outputs generated in crude environment using our TENG, the maximum accumulated charge was ~ 4.3 μC, giving a maximum stored static energy of ~ 0.9 μJ, which is much smaller than the MIE of crude oil, as previously mentioned.

4.3.4. TENGs energy generation under closed-loop oil flux: a proof-of-concept

The previous study investigated temperature (up to 120 ºC) and pressure (up to 830 bar) effects on the performance of a triboelectric energy harvesting device in direct contact with methane and crude oil. However, the used high-pressure container available at Repsol Technology Lab does not allow testing TENGs under oil flows similar to those found in actual oil extraction wells. In order to demonstrate the ability of TENGs to generate energy under a continuous oil flux, simplified tests were performed using two closed loop oil flux systems, the first developed by inanoEnergy [89] and the second available at the company Xrig AS (Norway) [205].

4.3.4.1. Triboelectric prototype and working mechanism

To generate energy in extreme condition under a continuous fluid flow, a new prototype device was developed (Figure 4.12) to be placed inside a closed-loop setup. This triboelectric device is composed by the same triboelectric materials (Nylon 6,6 and PTFE) and has a similar design as the device developed in section 4.3.1. However, the gold electrode was replaced by silver ink in order to increase the device flexibility to the passage of an oil flow. The triboelectric prototype has an effective contact area of 50 × 80 mm^2 for this proof-of-concept experiment. Therefore, with this solution, it would be

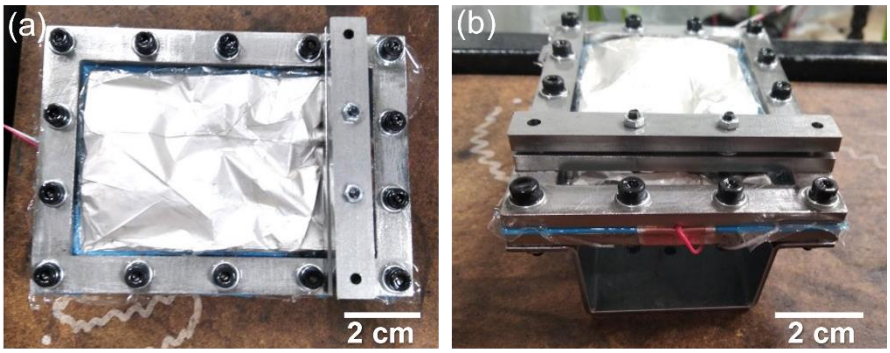


Figure 4.12 – Photographs of the triboelectric prototype: (a) top and (b) lateral perspectives.

possible to use the turbulent oil flow to produce energy in a very low flow-restriction implementation.

The working mechanism is similar to the previous one described in section 4.3.2; however, in this case, it is the turbulence of the oil flow that will promote contact and separation between the triboelectric pairs (Nylon 6,6/Ag and PTFE/Cu). The oil flow inside the pipe induces a vibration/turbulence to make the triboelectric materials come into contact, resulting in their triboelectrification. Thus, Nylon becomes positively charged while PTFE becomes negatively charged (Figure 4.13-I and II). Due to the turbulence caused by the oil flow, the triboelectric pairs separate (Figure 4.13-III) and an electrical potential difference is induced between the electrodes (silver and copper). Electrons then flow between the electrodes through an external load (Figure 4.13-III and IV). Therefore, it was possible to use the turbulent oil flow to produce energy in a very low flow-restriction implementation.

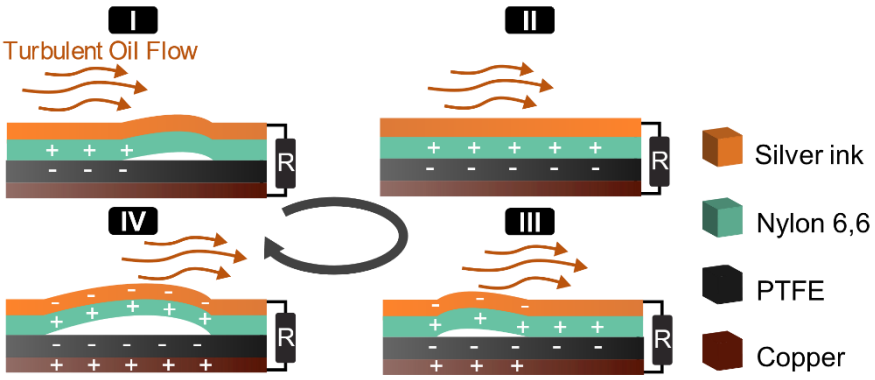


Figure 4.13 – Working mechanism of the triboelectric prototype based on the contact-separation mode.

4.3.4.2. Closed loop oil flux test systems

To demonstrate the potential of TENGs to harvest energy in harsh conditions, inanoEnergy designed and assembled a test bench system, as shown in Figure 4.14. This test bench system allows systematic tests at room temperature under a flow of oil of 55 L/min and a pressure of 1.013 bar. Thus, initial tests were carried out in this system to verify *a priori* the feasibility of TENGs to operate in continuous flows as a flexible membrane to generate energy. This system is composed by a tank where oil is stored to be pumped along a closed circuit using an electric pump (Figure 4.14). In this closed circuit, the oil pressure is controlled through two pressure gauges placed at the inlet and outlet of the testing chamber. This test chamber allows to fix the triboelectric prototype inside and monitor its power generation through a feedthrough connector.

The second experimental phase was performed at Xrig's facilities using a closed loop oil flux systems enabling pressures up to 100 bar under constant flux (of ~ 50 L/min), as shown is Figure 4.15. The main difference between the two systems is that Xrig's allows the pressure inside the test chamber to be controlled and safely changed.

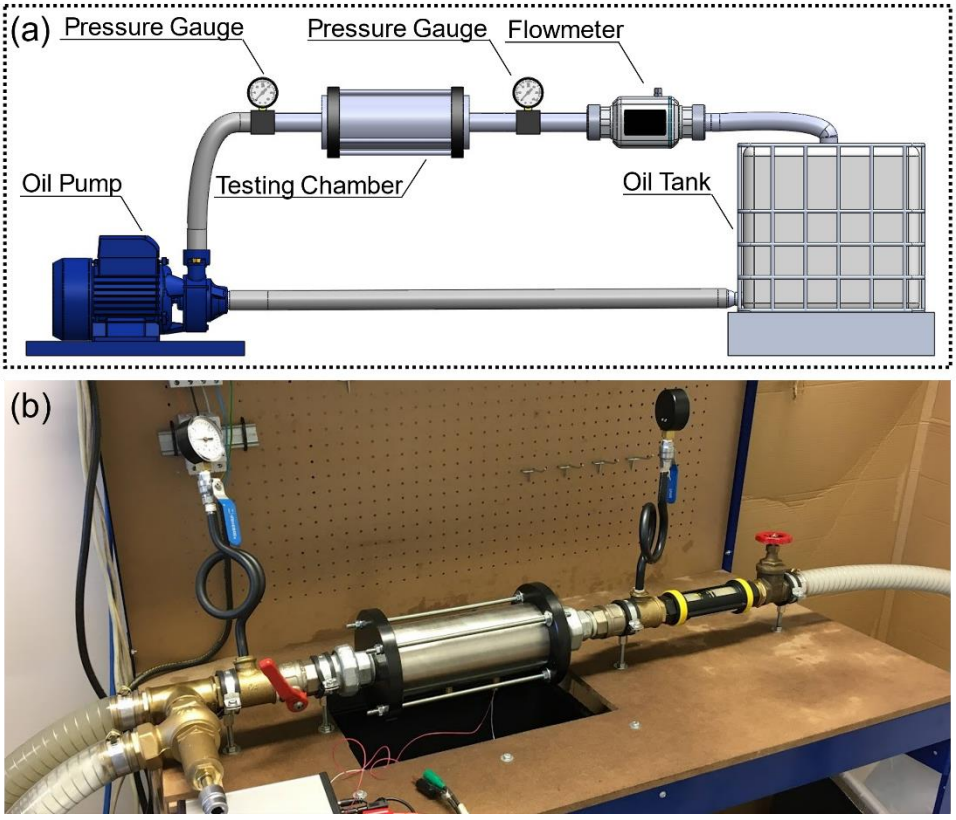


Figure 4.14 – (a) Schematic of the oil flux testing bench developed and available at inanoEnergy. (b) Photograph of the continuous oil flux test chamber.

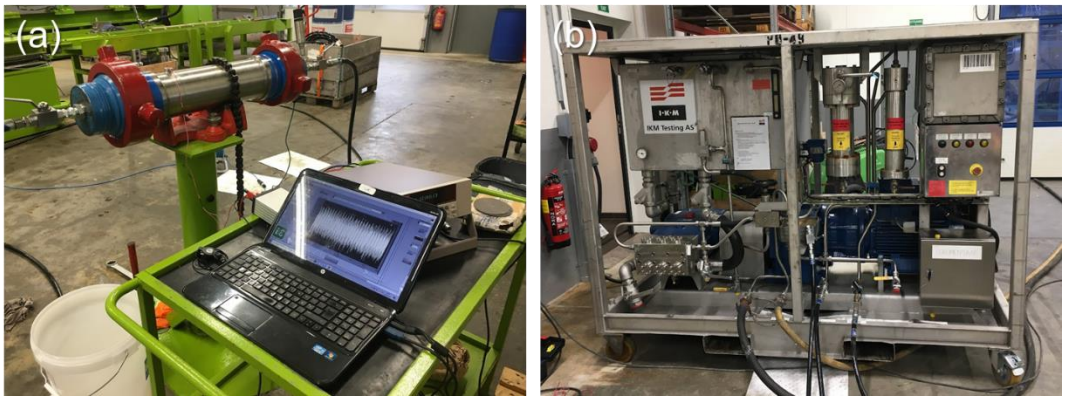


Figure 4.15 – (a) Photograph of the high pressure pipe with the triboelectric prototype assembled inside. (b) Photograph of the high pressure control system responsible for the closed circuit of the oil flow.

However, the working mechanism and operation mode are similar. In both test systems (at inanoEnergy and Xrig AS), Shell Morlina S2 BL 10 [206] was used as oil.

4.3.5. Experimental results

Figure 4.16 shows the open-circuit voltage and short-circuit current profile before and after oil starts circulating using the oil flux testing bench of inanoEnergy, where it is possible to observe the difference between the steady and dynamic stages with a fluid flux of 55 L/min, at 20 ºC and pressure of approximately 1 bar. As shown, the signal generated has a spiky random profile, representing the vibration of the triboelectric pairs caused by the turbulent motion of the fluid. For such conditions, a maximum V_{OC} and I_{SC} of 4.4 V and 589 nA were reached, respectively. To electrically characterize the developed triboelectric prototype, the generated voltage, current and power density were measured when connected to variable external load resistances from 100 Ω to 470 MΩ for the same flow conditions (Figure 4.16), giving a maximum power density value of 313 μW/m^2 for an external load of 10 MΩ. These results confirm that the assembled TENG is able to generate electrical energy from a continuous oil flow at low pressures.

The second experimental phase was then performed using the closed loop oil system available at Xrig facilities that enables us to validate the triboelectric energy generation under various pressures. To study the dependence of the pressure on the energy generation, the pressure inside the chamber was varied from 10 to 100 bar at 20 ºC using an oil flux of 50 L/min. Figure 4.17(a) shows that the open-circuit voltage decreases as a function of pressure, with a maximum generated value of ~ 0.6 V at the lowest achieved pressure (10 bar) and a decrease of 90% for the highest pressure (100

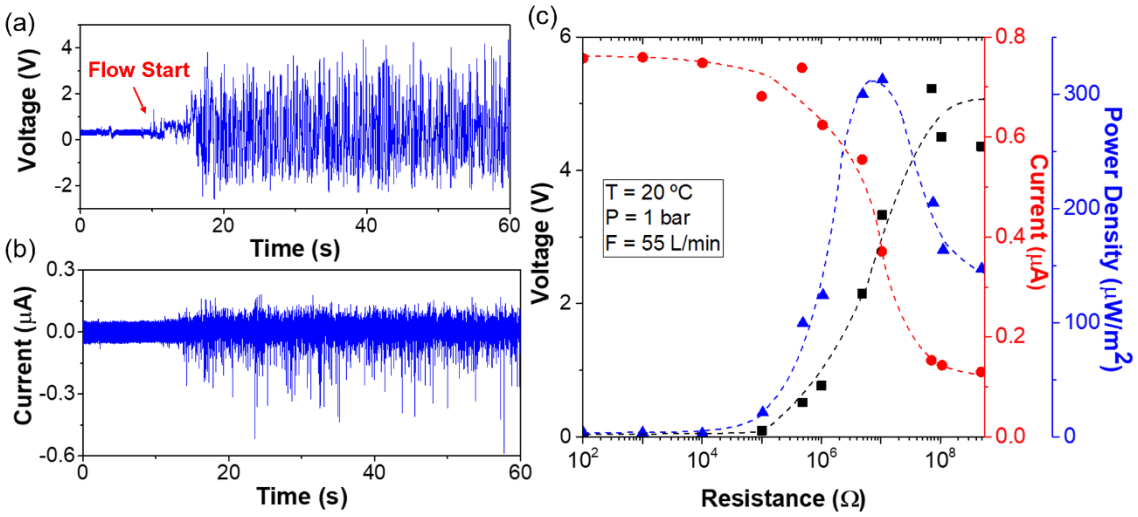


Figure 4.16 – (a) Open-circuit voltage and (b) short-circuit current under constant oil flow. (c) Dependence of the voltage, current and power density output on the external load resistance using the oil flux testing bench.

bar). The short-circuit current also decreases with increasing pressure, having a maximum value of ~ 69.9 nA at 10 bar, as shown in Figure 4.17(b). The power density generated by the triboelectric prototype also decreases with increasing pressure, giving a maximum value of ~ 5.8 μW/m^2 for P = 10 bar [Figure 4.17(c)]. The inset of Figure 4.17(c) shows that power density generated by the triboelectric device has an exponential decreasing trend with increasing pressure.

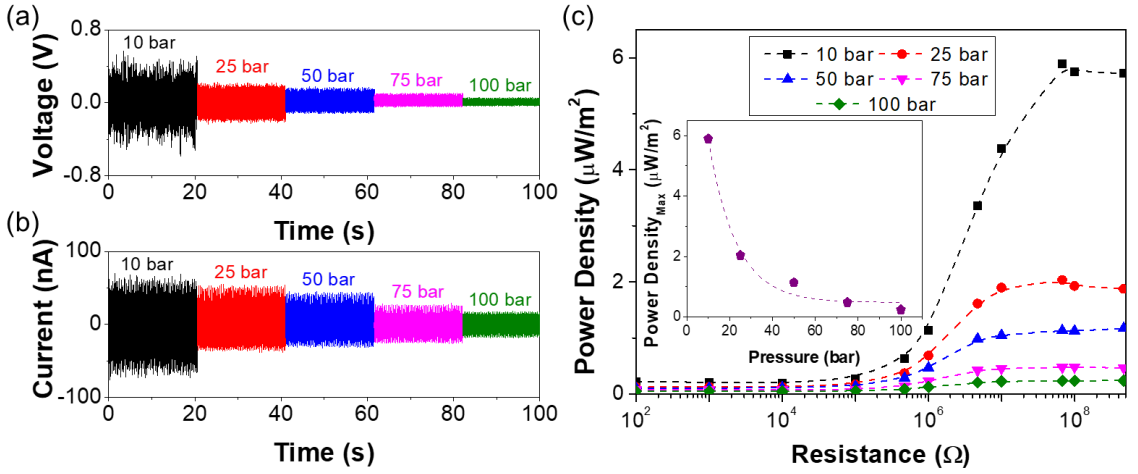


Figure 4.17 – (a) Open-circuit voltage and (b) short-circuit current of the TENG as a function of pressure. (c) Power density generated by the triboelectric device with inset showing its exponential decrease trend under different pressures.

4.3.6. Conclusions

In conclusion, triboelectric energy harvesting devices were developed to investigate the temperature and pressure effects in methane, crude and lubricant oil environments. Our results show that temperature is the most critical parameter affecting the electrical output performance (such as open-circuit voltage and power density) of TENGs. In fact, while a small increase of V_{OC} and P_{max} was observed between 28 and 119 bar in a methane atmosphere at T = 90 ºC, the TENG performance decreased significantly when the temperature varied from 25 up to 80 ºC at a constant pressure (P = 120 bar). The triboelectric device was also tested in contact with crude oil and the pressure was increased by steadily increasing the crude temperature. We found that both the voltage and maximum power density gradually decreased with increasing temperature and pressure. Finally, we demonstrated the possibility of storing the generated electrical power under various pressures/temperatures in crude oil.

The triboelectric device developed to study continuous energy harvesting under oil flows in high pressures showed a maximum power density of 5.8 $\mu W/m^2$ for 10 bar. The developed prototype followed the contact-separation working mode capable of converting the mechanical energy of a continuous flux into electricity. These proof-of-concept tests confirmed the potential of this technology as a solution to feed monitoring devices using downhole power generation in drilling and oil exploration platforms. The main advantage of this technology is the minimum flux obstruction created due to its flexibility and reduced thickness. With such solution, the safety and reliability on extraction wells can be improved, since it is not necessary to use batteries or cables (from the surface) to supply energy to monitoring systems or stop oil extraction to replace batteries or perform maintenance tasks.

The superior versatility of TENGs both in terms of materials and device configurations further ensures that these results can be generalized into different structures that can take advantage of the linear flow of fluids. Furthermore, besides increasing the application range of TENGs into the oil and gas sector, this study also opens new horizons to apply TENGs in deep underwater environments where pressures as high as 1000 bar (for a water column of 11 km) are present.

4.4. Triboelectric and thermomagnetic effects: a novel low-grade thermal energy harvesting technology

As we have seen, several reports have shown that TENGs can operate in harsh working environments, such as high/low temperatures, pressures or humidity. However, being a mechanical energy transducer, TENGs have never before been considered as candidates to harvest one of the most ubiquitous energy sources that surrounds us: heat. In this section we challenge this assumption and demonstrate, a triboelectric nanogenerator able to generate electrical power from small temperature gradients. Using the thermomagnetic effect, we were able to induce the periodic and sustained motion of a second-order phase transition magnetic material in temperature gradients below 30°C.

Thermomagnetic (TM) generators are an alternative thermal energy harvesting technology already proposed in the 19th century [207–211], whose development was hindered until ferromagnetic materials with Curie points near room temperature (such as Gd, $Gd_5Si_2Ge_2$, NiMnGa or LaFeSi) were applied [212–214]. Thermomagnetic generators rely on the temperature-driven phase transition of ferromagnetic (FM) materials and associated large magnetization variation (ΔM) at their Curie temperature (T_C) [214,215]. By periodically varying the temperature of the thermomagnetic material around T_C, these generators can convert thermal energy into electricity either directly (active devices) or indirectly via a mechanical motion (passive devices) [216–219]. Active thermomagnetic devices convert the T-driven magnetization change of the FM material into electrical energy directly through Faraday's law [220,221]. However, they require a cyclic variation of the temperature, usually through circulating heating/cooling fluids, making them low efficient and expensive. Figure 4.18(a) shows a schematic diagram of an active thermomagnetic device composed by a C-shaped permanent magnet, a FM material placed between the poles of the permanent magnet and a winding around the FM material. In this device, the FM is alternately heated and cooled through T_C using a heat source and a heat sink. Thus, increasing the FM temperature leads to a decrease of the magnetization which consequently results in a decreasing of the magnetic flux through the FM material. Decreasing the temperature of the FM materials has the opposite effect.

On the contrary, a passive thermomagnetic device operates with heat and cold sources at constant temperatures, does not require fluids or pumps, making it a much simpler and cost-effective alternative. Figure 4.18(b) shows a typical working mechanism of a passive thermomagnetic device where a FM material is placed between a hot magnetic reservoir and a cold non-magnetic reservoir. When the temperature of the FM

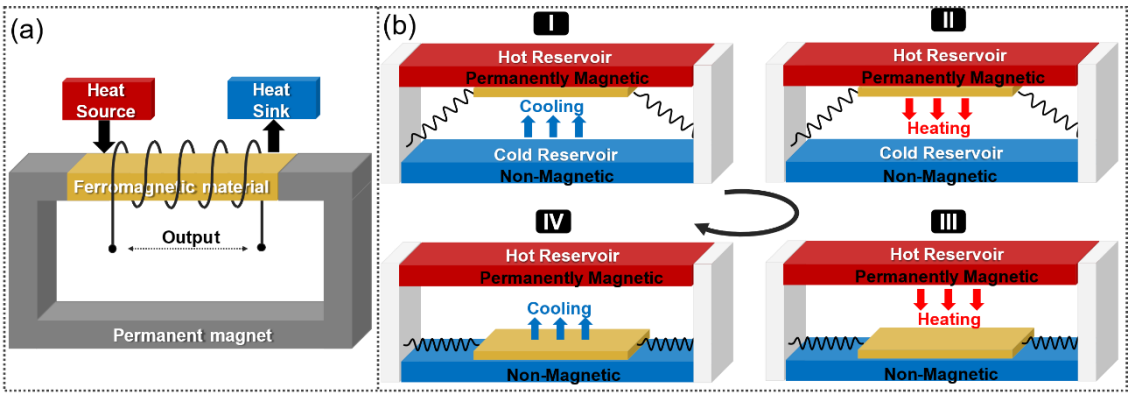


Figure 4.18 – Schematic diagram of (a) an active and (b) a passive thermomagnetic generator (adapted from Refs. [217,227]).

material is below T_C, it is attracted to the hot magnetic reservoir [Figure 4.18(b)-I]. Then, the FM material heats up [Figure 4.18(b)-II], losing magnetization, changing to the paramagnetic (PM) phase and falling into the cold reservoir [Figure 4.18(b)-III]. The consequent temperature decrease leads to a PM to FM transition, an increase of the magnetization [Figure 4.18(b)-IV] and consequently, the FM material is attracted back to the hot reservoir, completing the cycle [Figure 4.18(b)-I]. These generators then rely on an intermediate step in which ΔM is first converted into mechanical energy and then into electricity through magnetic induction, piezoelectric effect or other mechanical energy transducer.

Here, we demonstrate that TENGs, when combined with the thermomagnetic effect, can generate considerable electrical power by harvesting small temperature differences near room temperature.

4.4.1. Structural design of thermo-magnetic TENG demonstrator

The thermo-magnetic triboelectric nanogenerator (TM-TENG; Figure 4.19) is composed by four main parts: (i) the hot-side with a Peltier element (TEC1-12706; 40 × 40 × 3.5 mm^3) with a block-type hard magnet (Nd-Fe-B; 12 × 19 × 7 mm^3) on top; (ii) the cold-side with two Peltier elements connected in parallel mounted onto an aluminum heat sink; (iii) an TENG in contact with the Peltier coolers; and (iv) a freely moving ferromagnetic material [bulk gadolinium (Gd), 8 × 29 × 4 mm^3; 7.6 g] with a low Curie temperature (18.7 ± 0.5 ºC), with a copper plate (30 × 20 × 0.6 mm^3; 4 g) fixed to its bottom side, placed between the TENG and the hot side. The hot and cold sides were separated by a fixed distance of ~1 cm) and the temperature gradient was controlled by a TC-08 Thermocouple datalogger (Pico Technology) using *k*-type thermocouples The

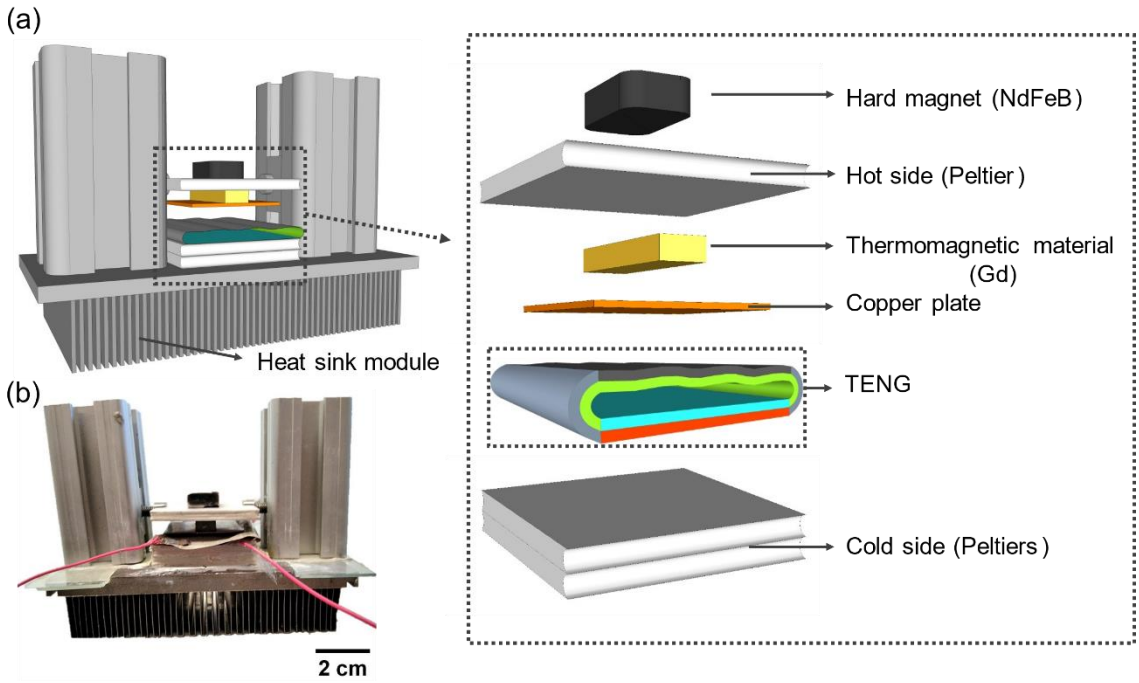


Figure 4.19 – (a) Detailed schematic illustration and (b) photograph of the fabricated TM-TENG with heat sink module.

developed system had a total dimension of 11 × 8 × 6 cm^3. The triboelectric generator is composed by Nylon 6,6 and PTFE films (~17 and 50 µm of thickness, respectively) with an area of 40 × 50 mm^2. A thin layer of silver was deposited on top of the Nylon film using screen printing, while the PTFE electrode consisted in a copper foil tape. To increase the contact area between the two triboelectric materials, a copper plate was attached to the Gd block.

4.4.2. Working mechanism of the TM-TENG and electrical signal generation

The main objective of this work is to demonstrate that triboelectric nanogenerators can harvest low-grade thermal energy in an efficient manner when integrated in a passive thermomagnetic device. For this, a Nd-Fe-B hard magnet was placed on top of a heat source (Peltier element) whose temperature is fixed at 65 ºC. As functional TM material, we used Gd that presents a broad second-order ferromagnetic-paramagnetic (PM) phase transition at a Curie temperature of 18.6 ºC (Figure 4.20). When in the FM state, the magnetic field produced by the hard magnet attracts the thermomagnetic material that comes into contact with the hot source and starts to increase its temperature. The consequent transition to the PM state leads to a severe decrease of

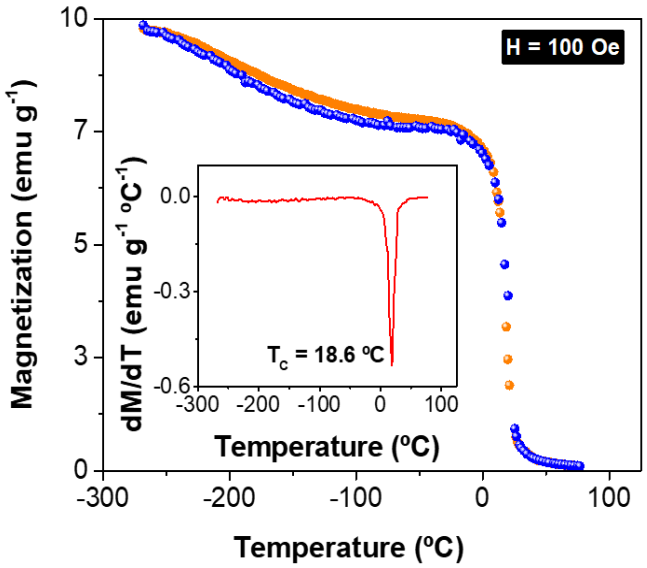


Figure 4.20 – Temperature dependence of the magnetization curve for Gd under a magnetic field of 100 Oe under heating (orange) and cooling temperature (blue). Inset: Temperature derivative of magnetization curve

the attractive magnetic force. Gravity then makes the Gd block (with an attached Cu plate to increase the contact area) fall on a triboelectric nanogenerator in contact with a cold source (at a constant temperature of 15 ºC). The TENG is based on Nylon 6,6 and PTFE films as opposite triboelectric materials (with Ag and Cu electrodes, respectively) assembled in an arc-shape to maximize energy generation. As the Nylon film comes into contact with the PTFE sheet, triboelectric charges are generated due to contact electrification [Figure 4.21(c)-I]. An equal amount of positive and negative charges is generated at the surfaces of the Nylon and PTFE films, respectively, due to the difference between the electron affinities of these two triboelectric materials. Being in contact with the cold source, the temperature of the Gd block decreases. As the thermomagnetic material changes into the FM state, the resulting magnetization increase again leads to a sizable attraction by the permanent magnet and the Gd block moves back to the hot side [Figure 4.21(c)-II]. Consequently, the PTFE and Nylon 6,6 triboelectric layers separate from each other so that positive (negative) charges appear at the bottom (top) electrode resulting from the electrical current that flows through the external circuit [Figure 4.21(c)-III]. This results in periodic electric output signals, with electrons flowing from the top to the bottom electrode when the triboelectric layers come into contact [Figure 4.21(c)-IV] and in the opposite direction upon separation, due to the conjugation of the triboelectric effect and electrostatic induction. As long as the stationary thermal gradient is maintained, the described back-and-forth process is cyclically driven by the

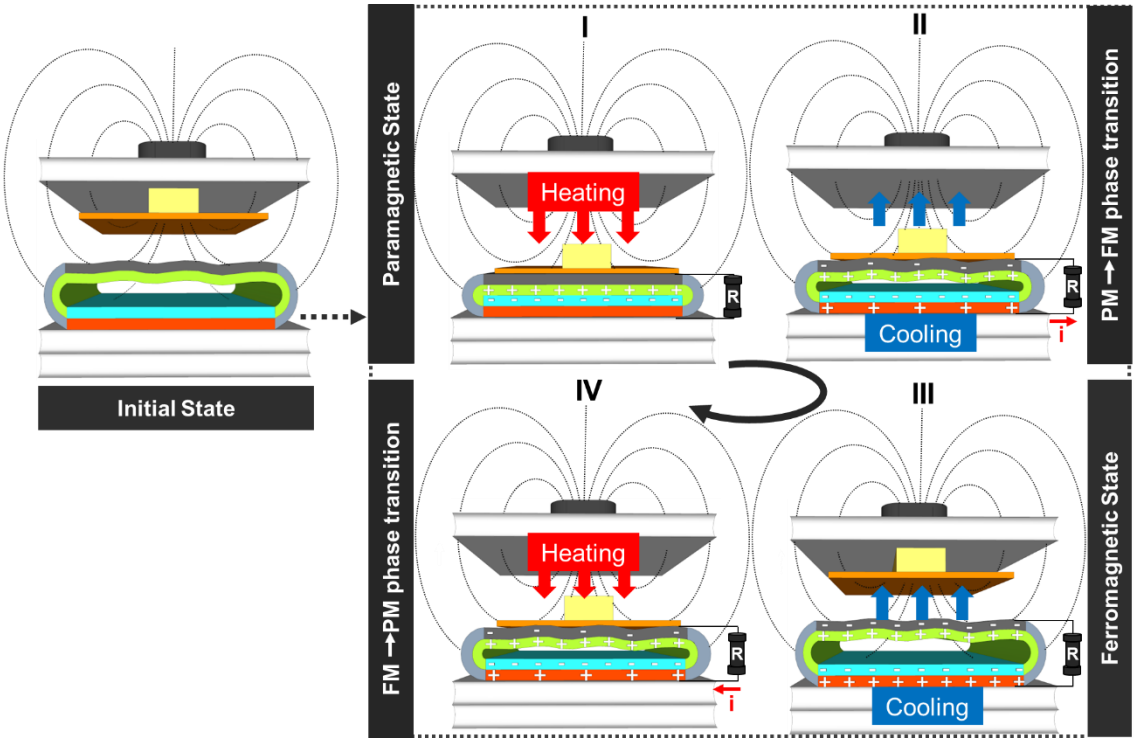


Figure 4.21 – Schematic representation of the working mechanism of TM-TENG.

gravitational field and steady temperature gradient without the necessity of an alternating temperature field or any other input from an alternative energy source.

Figure 4.22 shows the characterization of the TM-TENG operation under a fixed thermal gradient. The consecutive FM↔PM phase transitions of the Gd block are clearly evidenced by the temperature behavior of the hot- and cold-surfaces [Figure 4.22(a)]. The average thermal gradient (∇T) reached a stationary value of ~50 ºC (for cold- and hot-temperatures of ~15 and 65 ºC, respectively) after approximately 15 minutes of periodic Gd-vertical movement. Heat transfer numerical simulations allowed us to obtain the temperature distribution within the Gd block [Figure 4.22(b)] revealing the existence of a temperature gradient of approximately 4.5 and 1.5 ºC along the thickness of the sample when in the hot and cold side, respectively. Considering the previous thermal conditions, the arc-shaped TENG generated a maximum open circuit peak voltage of ~ 65.2 V at a self-governed motion frequency of ~11 mHz [Figure 4.22(c)]. Note the opposite voltage signs generated by the different motion directions of the thermomagnetic material. As the Gd temperature increases and its magnetization decreases, gravity takes over and the Gd block falls on top of the triboelectric nanogenerator due to gravity, generating a positive peak voltage [as shown Figure 4.22(c)]. These results are further confirmed by numerical simulations of the electrical

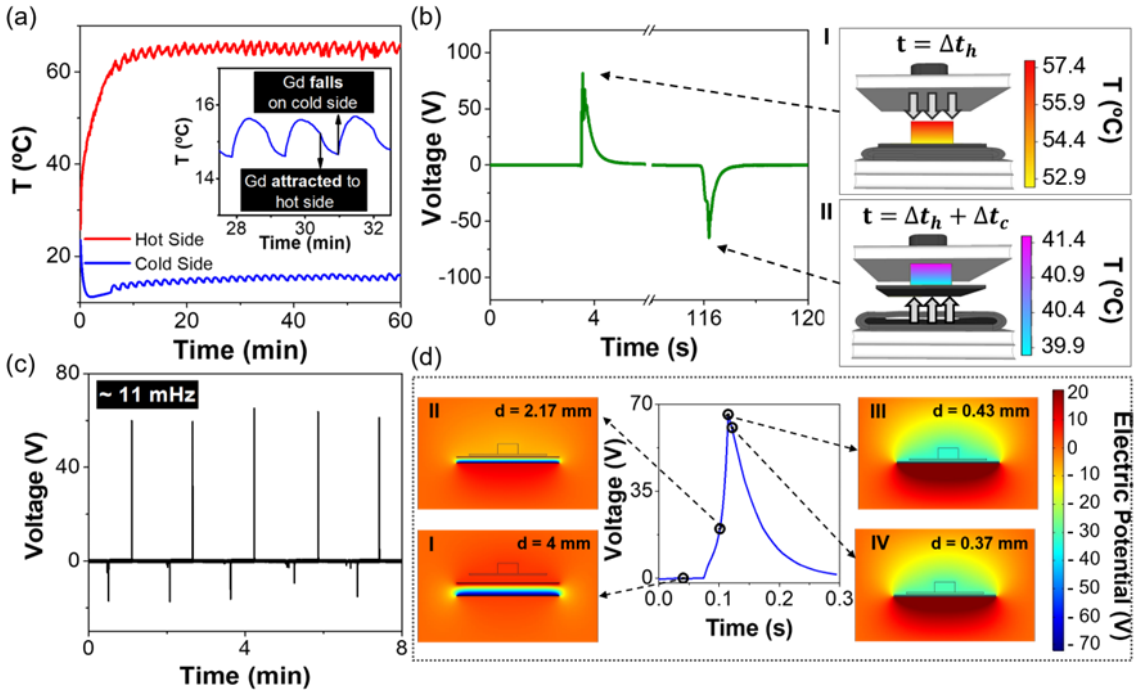


Figure 4.22 – (a) Measured temperature on the surfaces of cold-side and hot-side during TENG operation under a thermal gradient of ~50 ºC and the consecutive Gd FM↔PM phase transitions evidenced by the temperature behavior of the hot- and cold-surfaces. (b) Open-circuit voltage generated by arc-shaped TENG at frequency of ~11 mHz, and extended output voltage during heating and cooling with the different positions of Gd and Cu plate. (c) Voltage peak generated by TENG correlated with Spatial temperature of the Gd block obtained with the numerical simulations: I, initial state, II, before falling, III, after falling, and IV, before jumping. (d) Finite-element simulation of the electrical potential distribution in the device in a contact cycle.

potential distribution of the triboelectric device using COMSOL Multiphysics [222] [Figure 4.22(d)]. As the Gd/Cu set falls and the two triboelectric layers come together, the electrical potential varies [Figure 4.22(e)-I-IV] and a positive voltage is gradually generated between the top and bottom electrodes [Figure 4.22(d)]. At this point, the Gd block comes in contact with the cold source, so that its magnetization steadily increases until the attractive force of the hard magnet becomes strong enough to overcome gravity. The consequent separation of the triboelectric-pairs leads to a negative voltage peak.

To estimate the magnetic force (F_m) acting on the Gd block at the top and bottom positions, we use [223]:

$$F_m = \int_{\Omega} \nabla (\mu_0 H.M) dV, \tag{6}$$

where μ_0 is the permeability of vacuum, H is the magnetic field vector generated by the permanent magnet and M is the Gd-magnetization and the integral is performed over the volume Ω occupied by the Gd block. Note that M depends both on H and on temperature T, $M(H,T)$ so that one must take into account not only the position dependence of the magnetic field generated by the permanent magnet, but also and the time and space evolution of the temperature of the Gd block [as simulated in Figure 4.22(b) and (c)]. To estimate $M(H)$, we measured the magnetic field at the center of the Gd block at the top (444 Oe) and bottom (230 Oe) of the thermomagnetic device. Using the measured Gd-magnetization for the obtained temperature and magnetic field combinations one obtains $F_m \approx 50$ mN, thus of the same order of magnitude of the gravitational force (116 mN). It should be noted that these magnetization forces obtained are lower than the gravitational force, which does not reflect the oscillatory movement of the Gd block observed experimentally. This may be related to the approximations used in the model to calculate the magnetic forces as well as the fact that point measurements of the magnetic field are taken.

4.4.3. Optimization of the triboelectric device structure

Taking advantage of the available height, three different TENG structures with the triboelectric layers occupying the same area (4 × 5 cm^2) were built: arc-, zigzag- and parallel-shaped TENGs [Figure 4.23(a)-(c)]. The arc-shaped TENG has polypropylene tapes placed between the triboelectric pairs (Nylon/Ag and PTFE/Cu) to increase the overall stiffness and to main the distance of ~0.4 cm between the triboelectric materials after each mechanical cycle. The zigzag-shaped TENG is composed by the same tribo-pairs and by two plastic substrates (~4 × 5.5 cm^2). The angle between the two triboelectric layers is limited by the available height between the bottom surface of the copper plate and the top surface of the Peltier coolers and has a value of 8º. The parallel-shaped TENG is composed by two plastic plate assembled with the tribo-pairs in a parallel configuration, where PTFE/Cu is fixed on the surface of the Peltier cooler and Nylon/Ag is fixed on the bottom surface of the Cu plate. In this structure the distance between tribo-pairs is ~0.54 cm.

To study the performance of three different TENG structures and determine the optimum assembling, the maximum output voltage, current and power density were measured under a constant thermal gradient (41 ºC, giving an operation frequency of ~10 mHz). Figure 4.23(d) shows that the arc-shaped structure achieves the highest electrical outputs, reaching a maximum voltage, current and power density of ~67 V, 2.5

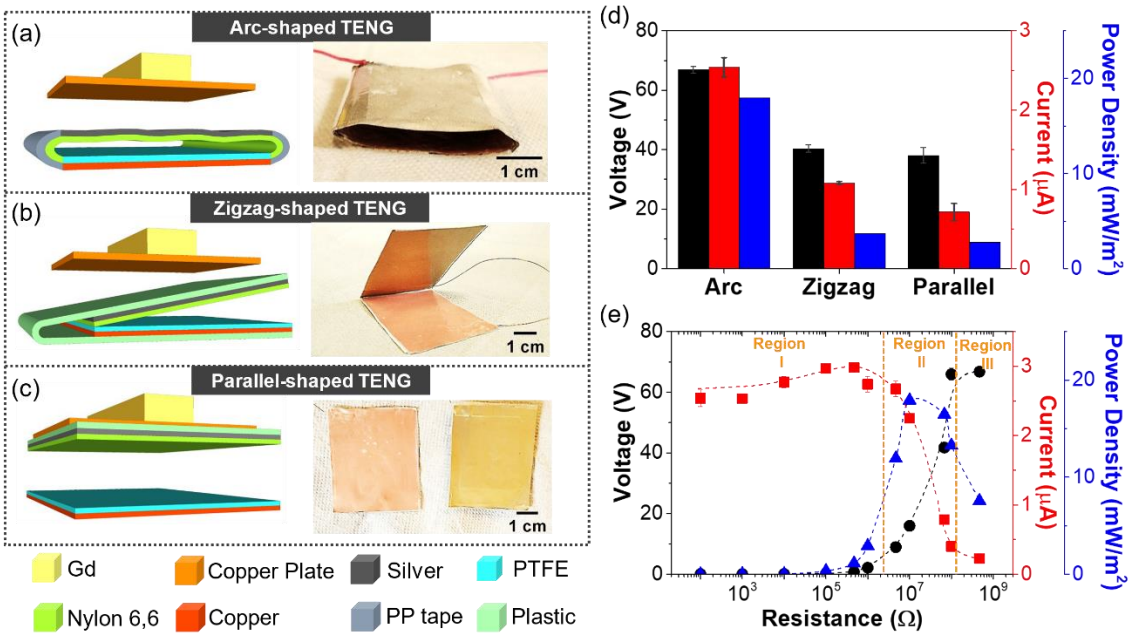


Figure 4.23 - Illustration (left) and photography (right) of the three different structures: (a) arc- (b) zigzag- and (c) parallel-shaped TENG. (d) Maximum open-circuit voltage, current and power density generated by the three different structures under a thermal gradient of ~41 ºC and frequency of ~10 mHz. (e) Electrical characterization of the arc-shaped TENG under a thermal gradient of ~41 ºC and ~10 mHz.

μA and 17.9 mW/m^2, respectively. On the other hand, the zigzag-shaped (parallel-shaped) TENG generated approximately 40 V (38 V), 1.1 μA (0.7 μA) and 3.7 mW/m^2 (2.8 mW/m^2) of maximum output voltage, current and power density, respectively. Although generating similar electrical outputs, these are significantly lower than the ones obtained in the arc-shaped TENG. This trend is attributed to the flexibility of the Nylon/Ag tribo-pair in the arc-shaped TENG, since in the case of zigzag- and parallel-shaped TENGs, the tribo-pairs are assembled in two rigid substrates. In this case, when the two rigid surfaces come into contact, the surface areas are not fully utilized. In the arc-shaped TENG, the flexible Nylon/Ag tribo-pair allows a more effective interfacial contact with the PTFE sheet for a more effective contact electrification [224]. This flexibility is beneficial to improve the output performance of TENG because it increases the effective contact area between triboelectric layers when the Gd/Cu set falls on the Nylon/Ag pair. Based on these results, the electrical outputs of the arc-shaped TENG were fully characterized when connected to variable external load resistances. Analyzing Figure 4.23(e), a typical three working-regions behavior is observed, where the output voltage increases with load resistance, while the current has the reverse trend. In the first region (Region I), the electrical charge transferred between electrodes is maximum because of the low resistance (100-1 MΩ; short-circuit-like conditions). Increasing the load resistance

(Region II; 1-100 MΩ range), the output current drops drastically while the generated voltage rises, leading to a maximum power density of ~17.9 mW/m^2 at a load resistance of 10 MΩ. For resistances larger than 100 MΩ (Region III), charge transfer between the electrodes is minimized, resulting in a high output voltage (~67 V; open-circuit-like conditions). Finally, note that the performance of a typical thermomagnetic generator driven by the induction of a moving magnetic material inside a coil under fixed cold and hot temperatures was also studied for comparison, generating much smaller maximum powers (~35×) when compared with the arc-shaped TENG (Figure 4.24).

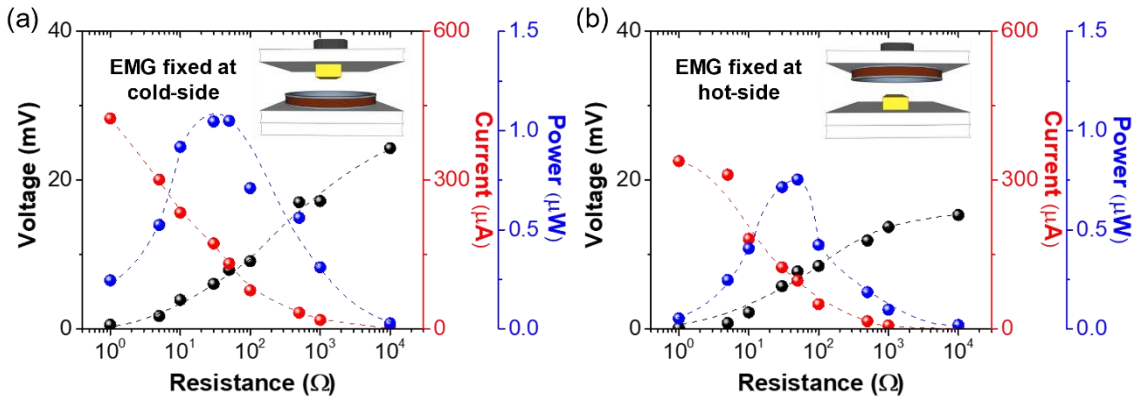


Figure 4.24 - Output voltage, current and power of the EMG fixed on surface of (a) Peltier coolers and (b) Peltier heater.

4.4.4. TM-TENG electrical performance

The thermal energy harvesting properties of the arc-shaped TENG were then systematically characterized in different low-grade temperature environments, as shown in Figure 4.25. With the arc-shaped TENG assembled in the cold-side, the thermal gradient between hot- and cold-sides was varied by systematically changing the cold-side temperature from 15 to 37 ºC and fixing the hot-side temperature at 65 ºC. Figure 4.25(a) shows that the electrical outputs increase from 62 to 79 V, 1.6 to 2.6 μA and 0.8 to 18 mW/m^2 with increasing cold-side temperature up to 30 ºC. However, further rising the cold-side temperature to 37 ºC, decreases the generated voltage, current and power density by 38%, 67% and 84%, respectively. Nevertheless, the proposed thermomagnetic generator can generate electrical energy over a fairly broad temperature range near room temperature (from 15 up to 30 ºC), including well above the Curie temperature of the thermomagnetic material due to the second-order nature of the magnetic transition.

For the lowest cold-side temperature, a thin water layer can condense on the surfaces of triboelectric materials. In fact, although PTFE is a hydrophobic material,

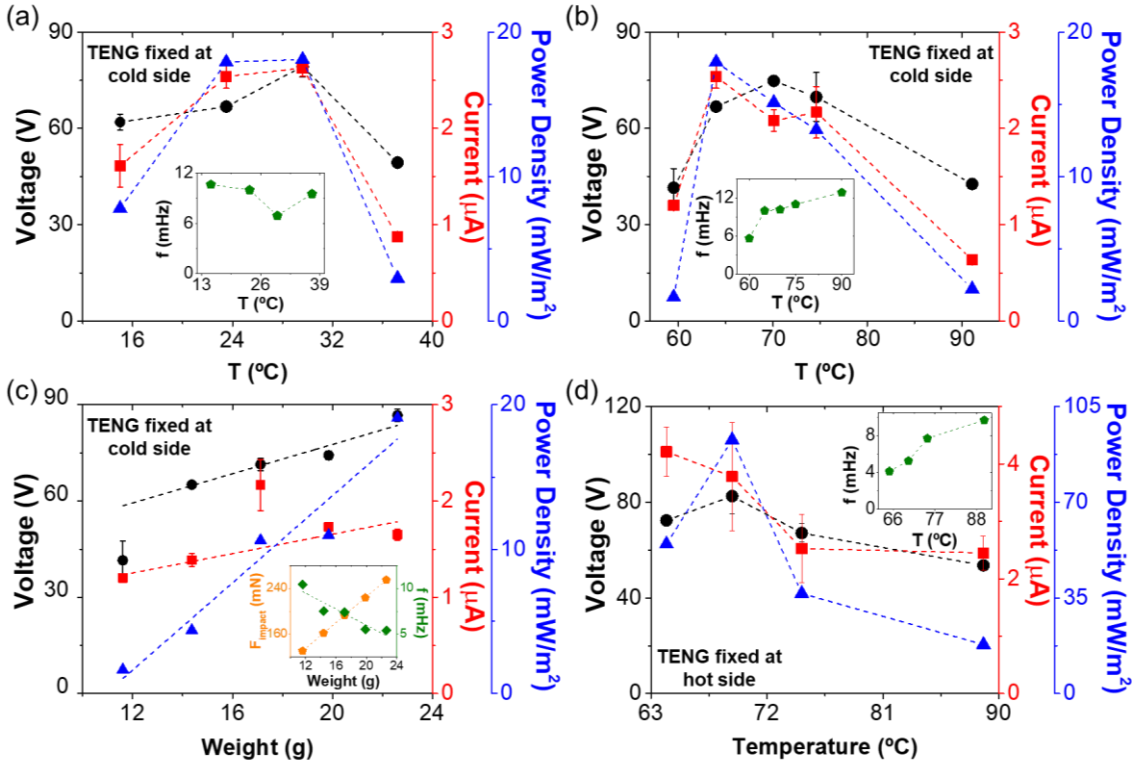


Figure 4.25 – Dependence of electrical outputs generated by the arc-shaped TENG when assembled on the cold-side surface under a range of: (a) cold-side temperatures from 15 to 37 ºC and fixed hot-side temperature of ~65 ºC; (b) hot-side temperature from ~60 to 90 ºC and fixed cold-side temperature of ~20º C. (c) Voltage, current and power density as function of the weight of the Gd/Cu set at fixed cold- and hot-side temperatures of ~20 and 60 ºC. (d) Performance-dependence of TENG assembled on hot-side surface under various hot-side temperatures.

Nylon is hydrophilic, having thus the tendency to retain water. This water layer will shield the surface charges and prevent their transfer between the two triboelectric materials, degrading the output of the thermomagnetic TENG. Increasing the cold side temperature will prevent the formation of this thin water layer resulting in the observed increase of the TENG performance. Nevertheless, note that the use of other triboelectric materials could further prevent this issue. On the other hand, for the highest temperatures, the generated electrical outputs decrease due to a competition between triboelectrification and electron thermionic emission, which leads to a decrease of the amount of static tribo-charges at the dielectric surfaces [45,177].

The operation frequency (f) of the thermomagnetic material has a slight downward trend with increasing cold-side temperature [inset of Figure 4.25(a)]. This dependence is likely related with the power used to feed the Peltier coolers, since higher power are necessary to achieve lower temperatures. Then, the thermomagnetic material takes longer to cool and transition to the ferromagnetic phase with increasing cold-side

temperature, leading a slight downward trend of the operation frequency. However, this frequency decrease is not significant to affect the performance of the arc-shaped TENG.

Using the same configuration, the TENG performance was also studied for different thermal gradients but using a fixed cold-side temperature of ~ 20 ºC and varying the hot-side temperature from ~ 60 to 90 ºC. Figure 4.25(b) shows that the electrical outputs rise with temperature due to the increase of the electron energy levels in Nylon and consequent enhancement of the charges transferred between the tribo-materials during the triboelectric effect. A maximum open-circuit voltage, short-circuit current and power density of 75 V, 2.5 μA and 18 mW/m^2, respectively, were reached using hot-side temperatures between 64 and 68 ºC. After 68 ºC, there is a competition between the previous phenomena and thermionic emission due the increase of the hot-side temperature. Then, some electrons can return to the Nylon surface or can be released into the air after contact between the tribo materials, resulting in a decrease in the electrical outputs. The oscillation frequency of the thermomagnetic material rises with increasing hot-side temperature, as shown the inset of Figure 4.25(b), related with the faster heating (and thus more rapid FM→PM transition) of the Gd block.

The effect of the weight of the Gd/Cu set on the performance of the arc-shaped TENG was also investigated by adding small copper plates (with an area of 1×3 cm^2 and ~1.4 g of weight) on the main Cu slab to minimize any interference on the heating and cooling processes. Figure 4.25(c) shows that the TENG output performance increases approximately linearly with increasing weight. Maximum open-circuit voltage, short-circuit current and power density of 86.7 V, 1.7 μA and 19.1 mW/m^2 were obtained for a Gd/Cu set weight of 22.6 g, a remarkable eleven-fold increase in the generated power when compared with the results obtained for the 11.6 g set (1.7 mW/m^2).

Combining energy conservation with the work-energy theorem under conservative conditions (neglecting air friction), when Gd transitions into the PM state and falls due to gravity, one has[224]:

$$F_{impact} = \frac{\frac{1}{2}mv^2}{d} = \frac{mgh}{d}, \tag{7}$$

where m is the mass of the Gd/Cu set, g the acceleration of gravity, h the fall height, v the impact velocity and d the distance covered after the impact event (equal to 0.4 cm in the arc-shaped TENG; the distance between the two tribo-pairs). Equation (7) confirms that the impact force increases linearly with the mass of the Gd/Cu set [inset of Figure

4.25(c)], which leads to an increase of the effective contact between the triboelectric-pairs and to the experimentally observed enhancement of the TENG outputs.

The inset of Figure 4.25(c) also shows that the motion frequency decreases linearly with increasing weight. For the Gd/Cu set to be attracted by the permanent magnet, the magnetic force has to surpass gravity, so that, with increasing Gd/Cu weight, the magnetic force must also increase. This is only possible by a further enhancement of the Gd magnetization, which in turn mandates reaching lower temperatures. Ultimately, this leads to the decrease of the motion frequency of the Gd/Cu set, as experimentally observed.

Finally, the arc-shaped TENG was assembled on the surface of the Peltier heater, fixing the cold-side temperature at ~20 ºC and varying the hot-side temperature from 65 to 90 ºC. Figure 4.25(d) shows that the output performance of the TENG decreases when the temperature of the hot-side increases. At 90 ºC (65 ºC), one obtains output voltage, current and power density of 54.6 V (72.4 V), 2.4 μA (4.2 μA) and 17.9 mW/m^2 (54.7 mW/m^2), a drop of 26, 42 and 67%, respectively. The TENG performance with the hot-side temperature can again be attributed to enhanced electron thermionic emission. With increasing temperature, electrons accumulated at the PTFE surface escape easily out of the potential well where they are trapped, thus decreasing the triboelectric charge density and the TENG performance. Nevertheless, it is remarkable that the developed thermomagnetic triboelectric nanogenerator operates in broad temperature ranges, both at the cold- and hot-sides, clearly demonstrating its versatility in harvesting low-grade temperature gradients.

4.4.5. Conclusions

In summary, we demonstrated that TENGs, when combined with the thermomagnetic effect, can generate considerable electrical power by harvesting small temperature differences near room temperature. Three different structures of TENGs (arc, zigzag and parallel shapes) were developed and studied and the arc-shaped structure achieved the highest voltage, current and power density (~67 V, 2.5 μA and 17.9 mW/m^2, respectively) under a constant thermal gradient of 41 ºC. Varying the low-grade temperature gradients with the arc-shaped TENG assembled in the cold-side, a maximum voltage, current and power density of to 79 V, 2.6 μA and 18 mW/m^2, respectively, was reached using a cold- and hot-sides temperature of 30 and 65 ºC. On the other hand, when the arc-shaped TENG was assembled on the surface of the Peltier heater, a maximum power density of 54.7 mW/m^2 was generated at a fixed cold-side

temperature of ~20 ºC and a hot-side temperature of 65 ºC. The presented results demonstrate that triboelectric nanogenerators offer a unique option for low-grade thermal energy harvesting when coupled with the thermomagnetic effect. This work clearly shows that TENGs is a high-efficient harvesting device to use the temperature difference and vibration mechanical energy to convert into electrical energy, when compared with conventional EMGs.

Chapter 5

Conclusions and Outlook

Chapter 5

Conclusions and Outlook

In this chapter, the main conclusions and achievements accomplished during this thesis are addressed. In the first part, the main results obtained are presented. In the second part, the main future perspectives opened by this thesis are described.

5.1. Main conclusions

In this thesis, different TENGs were developed with the main objective of understanding the ability and dependence of TENGs to harvest mechanical movements from blue energy and under harsh environments. The document can be divided in two main parts: Chapter 3 relating to triboelectric energy harvesting from ocean waves and Chapter 4 concerning the dependence of TENG performance under extreme conditions.

Harvesting blue energy

The developed TENGs designs based on rolling spheres to harvest energy from multidirectional water waves showed to be a good strategy to understand the impact of the hydrodynamic response of the buoy, due to the degrees of freedom of the spheres. Output performance tests using a “dry” bench testing system allowed to obtain preliminary results on the correlation of triboelectric energy generation with the main characteristics (frequency and amplitude) of realistic sea-states. The TENGs electrical outputs tended to increase with increasing pitch amplitudes and decreasing period due to the increase of the spheres’ velocity. Then, a realistic assessment of TENGs performance within a scaled commercial navigation buoy was carried using a wave basin facility capable of reproducing realistic sea-states. This integrated study in a large-scale wave basin showed the importance of the degrees of freedom of the movement of the floating bodies under the wave action on the excitation of the installed TENGs. The maximum voltage generated by the three different developed TENGs was achieved for periods close to the natural period of our scaled buoy. Furthermore. different floating platform geometries, when subjected to the same sea states, display different energy generation trends. Consequently, there was a dependence on the performance of the

couple lateral-based TENG for the different geometries of the floating platform, although no clear correlation was obtained between the generated electrical outputs and the hydrodynamic response of these platforms. This study showed how important it is to consider the hull geometry of the floating platforms where TENGs are incorporated.

Harvesting energy in harsh conditions

The TENG that we developed to operate under extreme conditions was crucial to demonstrate the ability of this technology to generate energy in methane and crude oil up to temperatures and pressures of 180 °C and 830 bar, respectively. Studies carried out under methane shows that temperature is the most critical parameter for TENG performance, showing a decrease of 37% in V_{OC} when the temperature increases from 25 to 80 °C. This temperature-dependence of the electrical outputs was explained by competing effects between changes of the mechanical properties of the triboelectric materials and thermal fluctuations that influence contact triboelectrification. The performance of the assembled triboelectric device in direct contact with crude oil also showed a gradually decrease with increasing pressure and temperature. Despite this, our device still continued to generate electrical energy up to pressures of 830 bar and temperatures of 120 °C. Finally, experimental tests performed using closed loop oil flux systems under conditions closer to those found in current oil extraction wells allowed us to establish a crucial proof-of-concept for actual application. These tests confirmed the potential of this technology as a solution to feed monitoring devices using downhole power generation in drilling and oil exploration platforms.

Lastly, a hybrid triboelectric/thermomagnetic device was proposed to harvest energy from small temperature gradients near room temperature. Using the periodic movement induced by the thermomagnetic effect, an arc-shaped TENG generated the highest electrical outputs under a broad range of operating temperatures in both the cold (15 to 37 °C) and hot (60 to 90 °C) sides. This work showed the potential of TENGs to use temperature gradients and oscillating mechanical motions to generate electric energy, leading to a power maximum ~35× higher than that generated by conventional EMGs.

5.2. Future perspectives

From the promising results obtained throughout this PhD work, one can now propose some of the most interesting future works that can be developed following this thesis.

Ocean wave harvesting

In this thesis, a realist assessment of TENGs performance within a scaled commercial navigation buoy was carried using a wave basin facility capable of reproducing realistic sea-states. This work opens new opportunities/challenges and shows new paths that TENGs can take for their implementation in the ocean. Based on our developed work, one should:

- optimize the UL-TENG by varying the length of the trough where spheres move freely, as well as the spheres number;
- develop a new TENG capable of taking advantage of the movement of the different degrees of freedom, taking into account the obtained correlation between the generated electrical outputs and the DoFs of the floating bodies;
- develop a novel TENG capable of adapting to generate maximum electrical signals for all realistic sea states, in order to guarantee the powering of sensors for real-time monitoring.
- hybridized triboelectric-electromagnetic device to increase the energy storage capacity in order to ensure enough power to feed sensors and electronic systems incorporated within a buoy.

Harsh conditions

Despite the studies carried out to demonstrate the applicability of our triboelectric energy harvesting device for continuous harvesting under oil flows under high pressures, a more detailed study is necessary for an optimization of this device by:

- improving the TENG design to increase the flux turbulence and induce enhanced movement between the triboelectric pairs;
- studying in detail the effect of different crude oil compositions on TENG performance;
- studying the encapsulation effect on the performance of the triboelectric prototype and performing endurance tests.

In the study on energy harvesting at low gradient temperatures combining the thermomagnetic effect and a low cost TENG, an optimization of this device can be made by:

- studying the dependence of the thermomagnetic TENG performance by varying the distance between the hot and cold side.

- studying in detail the triboelectric energy generation using hydrophobic materials on TENG to avoid water layers on their surfaces that degrades the output of the thermomagnetic TENG.
- developing an integrated study to fabricate a flexible membrane/film doped with ferromagnetic nanoparticles to be incorporated into a TENG in order to combine the triboelectric and thermomagnetic effects.

Since the emergence of TENGs in 2012, there has been an improvement in its fundamental theory, which has resulted in a significant increase in the performance of new devices. However, this technology still has a lot of room for improvement in research areas such as efficiency enhancement, hybridization, multifunctionality and power management systems. Synthesis and development of new triboelectric materials by physical, chemical, biological, and hybrid methods can be essential to enhance the output power and current generated by TENGs. This approach will not only improve the performance of TENGs for vast energy harvesting applications but will also allow designing new TENGs with longer lifetimes to work in a variety of practical environments. Applications of TENGs have diversified, from its use as a sustainable micro-scale power source for small electronic devices or to work as a self-powered active sensor focused on areas of human-machine interface, security systems and intelligent sensing, etc. This growing number of applications has made room for this emerging technology to be commercialized in the near future.

List of Publications

Several contributions were made to the scientific community, directly related to the work developed in the present thesis, including 4 oral communications, 4 poster presentations and the following publications:

- ***Articles in international scientific journals:***

Cátia Rodrigues, Ana Pires, Isabel Gonçalves, Daniel Silva, Joana OIiveira, André Pereira, and João Ventura, Hybridizing Triboelectric and Thermomagnetic Effects: A Novel Low-Grade Thermal Energy Harvesting Technology, Advanced Functional Materials, 32 (2022), 2110288. URL: https://doi.org/10.1002/adfm.202110288

C. Rodrigues, M. Ramos, R. Esteves, J. Correia, D. Clemente, F. Gonçalves, N. Mathias, M. Gomes, J. Silva, C. Duarte, T. Morais, P. Rosa-Santos, F. Taveira-Pinto, A. Pereira, J. Ventura, Integrated study of triboelectric nanogenerator for ocean wave energy harvesting: Performance assessment in realistic sea conditions, Nano Energy, 84 (2021), 105890. URL: http://dx.doi.org/10.1016/j.nanoen.2021.105890C. Rodrigues, D. Nunes, D. Clemente, N. Mathias, J. M. Correia, P. Rosa-Santos, F. Taveira-Pinto, T. Morais, A. Pereira and J. Ventura, Emerging triboelectric nanogenerators for ocean wave energy harvesting: state of the art and future perspectives, Energy & Environmental Science, 13 (2020). URL: https://doi.org/10.1039/D0EE01258K

C. Rodrigues, M. Kumar, M. P. Proenca, J. Gutierrez, R. Melo, A. Pereira, J. Ventura, Triboelectric energy harvesting in harsh conditions: Temperature and pressure effects in methane and crude oil environments, Nano Energy, 72 (2020), 105890. URL: https://doi.org/10.1016/j.nanoen.2020.104682

- ***International and national conferences with oral presentations***

C. Rodrigues, M. Ramos, R. Esteves, J. Correia, D. Clemente, F. Gonçalves, N. Mathias, M. Gomes, J. Silva, C. Duarte, T. Morais, P. Rosa-Santos, F. Taveira-Pinto, A. Pereira, J. Ventura, “Performance assessment of triboelectric nanogenerators based on rolling spheres motion in realistic sea states”, 6th International Conference on Nanogenerators and Piezotronics - NGPT2022 conference (Virtual), Mid Sweden University, Sundsvall (Sweden), 22 June 2022.

C. Rodrigues, M. Ramos, R. Esteves, J. Correia, D. Clemente, F. Gonçalves, N. Mathias, M. Gomes, J. Silva, C. Duarte, T. Morais, P. Rosa-Santos, F. Taveira-Pinto, A. Pereira, J. Ventura, “Navigational Buoy-Based Triboelectric Nanogenerators for Blue Energy Harvesting”, ANM2021 conference (virtual and in-person participating), University of Aveiro (Portugal), 24 July 2021.

C. Rodrigues, A. Pereira, J. Ventura, “Triboelectric energy harvesting in remote and harsh environments: performance characterization and novel applications”; MAP-Fis Conference, University of Porto; University of Aveiro; University of Minho (Portugal), 9 July 2021.

C. Rodrigues, M. Ramos, R. Esteves, J. Correia, D. Clemente, F. Gonçalves, N. Mathias, M. Gomes, J. Silva, C. Duarte, T. Morais, P. Rosa-Santos, F. Taveira-Pinto, A. Pereira, J. Ventura, “Performance analysis of a triboelectric nanogenerator in ocean-like conditions”, 4th Doctoral Congress in Engineering - DCE2021 (Virtual), Faculdade de Engenharia da Universidade do Porto (Porto, Portugal), 28 June 2021.

- ***International and national conferences with poster presentations***

C. Rodrigues, A. Pereira, J. Ventura, “Novel applications of triboelectric energy harvesting in remote and harsh environments”, FÍSICA 2022 – 23ª Conferência Nacional de Física, 7-10 September 2022, Porto (Portugal)

C. Rodrigues, M. Ramos, R. Esteves, J. Correia, D. Clemente, F. Gonçalves, N. Mathias, M. Gomes, J. Silva, C. Duarte, T. Morais, P. Rosa Santos, F. Taveira Pinto, A. Pereira, J. Ventura, “Integrated study of triboelectric nanogenerators for ocean wave energy harvesting: Assessing their behavior in model buoys and real sea conditions", First Workshop of the Laboratory for Physics of Materials and Emerging Technologies (LaPMET; Virtual), 24 September 2021, Porto (Portugal)

C. Rodrigues, M. Ramos, R. Esteves, J. Correia, D. Clemente, F. Gonçalves, N. Mathias, M. Gomes, J. Silva, C. Duarte, T. Morais, P. Rosa-Santos, F. Taveira-Pinto, A. Pereira, J. Ventura, “Performance of triboelectric nanogenerators based on rolling spheres motion under realistic water waves conditions”, AIP Publishing Horizons - Energy Storage and Conversion Conference Sponsored by Applied Physics Reviews, 4-6 August 2021

C. Rodrigues, M. Ramos, R. Esteves, J. Correia, D. Clemente, F. Gonçalves, N. Mathias, M. Gomes, J. Silva, C. Duarte, T. Morais, P. Rosa-Santos, F. Taveira-Pinto, A. Pereira,

J. Ventura, “Integrated study of triboelectric nanogenerator for ocean wave energy harvesting: Performance assessment in realistic sea conditions”, E-MRS Spring Meeting 2021 (Virtual), European Materials Research Society (E-MRS), 31 May 2021.

- ***Others***

Frontispiece. Cátia Rodrigues, Ana Pires, Isabel Gonçalves, Daniel Silva, Joana OIiveira ,André Pereira, João Ventura, Hybridizing Triboelectric and Thermomagnetic Effects: A Novel Low-Grade Thermal Energy Harvesting Technology (Adv. Funct. Mater. 21/2022) –; URL: https://doi.org/10.1002/adfm.202270121

Back Cover. C. Rodrigues, M. Kumar, M. P. Proença, J. Gutierrez, R. Melo, A. Pereira, J. Ventura, Triboelectric energy harvesting in harsh conditions: Temperature and pressure effects in methane and crude oil environments, Nano Energy, 72 (2020), 105890, ISSN: 2211-2855.

- ***Award***

2021 - Best oral communication (EX aequo) - Symposium on Engineering Physics, DCE2021 4th Doctoral Congress in Engineering, Universidade do Porto - Faculdade de Engenharia, Portugal.

Furthermore, several collaborations also took place, resulting in 10 oral presentations, 6 poster presentations and the following publications:

- ***Articles in international scientific journals***

Carolina Silva, Pedro M. Resende, Cátia Rodrigues, João Ventura, Marisol Martín-González, André Pereira, Boosted triboelectric generation in biodegradable PLA three-dimensional metamaterials, under preparation.

I. Gonçalves, C. Rodrigues, J. Ventura, Sea State Adaptation Enhances Power Output of Triboelectric Nanogenerators for Tailored Ocean Wave Energy Harvesting. Submitted to Advanced Energy Materials.

Andreia T. Pereira*, Cátia R. S. Rodrigues*, Ana C. Silva, Ricardo Vidal, João O. Ventura, Inês C. Gonçalves, Tailoring the electron trapping effect of a biocompatible triboelectric hydrogel by graphene oxide incorporation towards self-powered medical

electronics, ACS Biomaterials Science & Engineering, 9 (2023). *The authors contributed equally to this work. URL: https://doi.org/10.1021/acsbiomaterials.2c01513

T. Alves, C. Callaty, C. Rodrigues, C. Duarte, J. Ventura, Airflow-driven triboelectric-electromagnetic hybridized nanogenerator for biomechanical energy harvesting, Advanced Functional Materials (2023). URL: https://doi.org/10.1002/admt.202300689

Carlos Callaty, Isabel Goncalves, Catia Rodrigues, J. Ventura, Modeling the performance of contact-separation triboelectric nanogenerators, Current Applied Physics, 50 (2023), 100-106. URL: https://doi.org/10.1016/j.cap.2023.03.013

D. Clemente, C. Rodrigues, R. Esteves, J. Correia, A. Pereira, J. Ventura, P. Rosa-Santos, F. Taveira-Pinto and P. Martin, Experimental performance analysis of a hybrid wave energy harvesting system combining E-Motions with triboelectric nanogenerators. Journal of Marine Science and Engineering, 10 (2022). URL: https://doi.org/10.3390/jmse10121924

C. Rodrigues, M. M. Dias, L. Martins, D. J. Silva, J. P. Araújo, J.C.R.E. Oliveira, A. M. Pereira, J. Ventura, An Electromagnet-Based Magnetically-Activated Thermal Switch Without Moving Parts, Energy Conversion and Management 197 (2019). URL: https://doi.org/10.1016/j.enconman.2019.111881

C. Rodrigues, A. Gomes, A. Ghosh, A. Pereira, J. Ventura, Power-generating footwear based on a triboelectric-electromagnetic-piezoelectric hybrid nanogenerator, Nano Energy 62 (2019). URL: https://doi.org/10.1016/j.nanoen.2019.05.063

C. Rodrigues, T. Machado, A. L. Pires, B. Chaves, F. Carpinteiro, A. Pereira, Recovery of Thermal Energy Released in the Composting Process and their Conversion into Electricity Utilizing Thermoelectric Generators, Applied Thermal Energy, 138 (2018), 319-324. URL: https://doi.org/10.1016/j.applthermaleng.2018.04.046

- ***Book chapter***

D. Clemente, T. Cabral, P. Rosa-Santos, F. Taveira-Pinto, C. Rodrigues, J.M. Correia, A. Pereira, J. Ventura, N. Mathias, R. Marini, T. Morais, Experimental study of a navigational buoy powered by wave energy through triboelectric nanogenerators, Developments in Renewable Energies Offshore, 67-73, 1st Edition, CRC Press, 2020. URL: https://doi.org/10.1201/9781003134572-09

- ***International and national conferences with oral presentations***

C. Rodrigues, M. M. Dias, L. Martins, D. J. Silva, J. P. Araújo, J.C.R.E. Oliveira, A. M. Pereira, J. Ventura, “Magnetically-activated thermal switch without moving parts for fully solid-state magnetic refrigeration”, 9th IIR International Conference on Caloric Cooling and Applications of Caloric Materials (Virtual), University of Maryland (United States), 07 June 2021.

C. Rodrigues, R. Esteves, C. Duarte, L. Pessoa, A. Pereira, J. Ventura, “A multi-grating triboelectric nanogenerator for maritime applications”, 3rd Doctoral Congress in Engineering - DCE2019, Faculdade de Engenharia da Universidade do Porto (Porto, Portugal), 27 June 2019.

C. Rodrigues, A. Gomes, A. Pereira, J. Ventura, “Triboelectric-piezoelectric-electromagnetic hybrid nanogenerator built inside a footwear for harvesting walking energy”, 2019 Spring Meeting of the E-MRS, Nice (France) 29 May 2019

C. Rodrigues, R. Esteves, C. Duarte, L. Pessoa, A. Pereira, J. Ventura, “A floating buoy-based triboelectric nanogenerator for maritime applications”, CMPNC 2019, Faculty of Sciences of University of Porto (Porto, Portugal), 10 May 2019

Bibliography

[1] X. Zhao, H. Askari, J. Chen, Nanogenerators for smart cities in the era of 5G and Internet of Things, Joule. 5 (2021) 1391–1431. https://doi.org/10.1016/j.joule.2021.03.013.

[2] IoT Analytics, State of IoT 2023: Number of connected IoT devices growing 16% to 16.7 billion globally, (2023). https://iot-analytics.com/number-connected-iot-devices/ (accessed June 15, 2023).

[3] A. Ahmed, I. Hassan, M.F. El-Kady, A. Radhi, C.K. Jeong, P.R. Selvaganapathy, J. Zu, S. Ren, Q. Wang, R.B. Kaner, Integrated Triboelectric Nanogenerators in the Era of the Internet of Things, Adv. Sci. 6 (2019). https://doi.org/10.1002/advs.201802230.

[4] F.-R.R. Fan, Z.-Q.Q. Tian, Z. Lin Wang, Z.L. Wang, Z. Lin Wang, Flexible triboelectric generator, Nano Energy. 1 (2012) 328–334. https://doi.org/10.1016/j.nanoen.2012.01.004.

[5] C. Rodrigues, M. Ramos, R. Esteves, J. Correia, D. Clemente, F. Gonçalves, N. Mathias, M. Gomes, J. Silva, C. Duarte, T. Morais, P. Rosa-Santos, F. Taveira-Pinto, A. Pereira, J. Ventura, Integrated study of triboelectric nanogenerator for ocean wave energy harvesting: Performance assessment in realistic sea conditions, Nano Energy. 84 (2021) 105890. https://doi.org/10.1016/j.nanoen.2021.105890.

[6] Z. Saadatnia, E. Asadi, H. Askari, E. Esmailzadeh, H.E. Naguib, A heaving point absorber-based triboelectric-electromagnetic wave energy harvester: An efficient approach toward blue energy, Int. J. Energy Res. 42 (2018) 2431–2447. https://doi.org/10.1002/er.4024.

[7] H. Shao, P. Cheng, R. Chen, L. Xie, N. Sun, Q. Shen, X. Chen, Q. Zhu, Y. Zhang, Y. Liu, Z. Wen, X. Sun, Triboelectric–Electromagnetic Hybrid Generator for Harvesting Blue Energy, Nano-Micro Lett. 10 (2018) 1–9. https://doi.org/10.1007/s40820-018-0207-3.

[8] C. Hou, T. Chen, Y. Li, M. Huang, Q. Shi, H. Liu, L. Sun, C. Lee, A rotational pendulum based electromagnetic/triboelectric hybrid-generator for ultra-low-frequency vibrations aiming at human motion and blue energy applications, Nano

Energy. 63 (2019) 103871. https://doi.org/10.1016/j.nanoen.2019.103871.

[9] L. biao Huang, W. Xu, G. Bai, M.C. Wong, Z. Yang, J. Hao, Wind energy and blue energy harvesting based on magnetic-assisted noncontact triboelectric nanogenerator, Nano Energy. 30 (2016) 36–42. https://doi.org/10.1016/j.nanoen.2016.09.032.

[10] G. Zhu, Y.S. Zhou, P. Bai, X.S. Meng, Q. Jing, J. Chen, Z.L. Wang, A Shape-Adaptive Thin-Film-Based Approach for 50% High-Efficiency Energy Generation Through Micro-Grating Sliding Electrification, Adv. Mater. 26 (2014) 3788–3796. https://doi.org/10.1002/adma.201400021.

[11] Y. Xie, S. Wang, S. Niu, L. Lin, Q. Jing, J. Yang, Z. Wu, Z.L. Wang, Grating-Structured Freestanding Triboelectric-Layer Nanogenerator for Harvesting Mechanical Energy at 85% Total Conversion Efficiency, Adv. Mater. 26 (2014) 6599–6607. https://doi.org/10.1002/adma.201402428.

[12] P.-K.K. Yang, Z.-H.H. Lin, K.C. Pradel, L. Lin, X. Li, X. Wen, J.-H.H. He, Z.L. Wang, Paper-based origami triboelectric nanogenerators and self-powered pressure sensors, ACS Nano. 9 (2015) 901–907. https://doi.org/10.1021/nn506631t.

[13] S. Wang, X. Mu, Y. Yang, C. Sun, A.Y. Gu, Z.L. Wang, Flow-Driven Triboelectric Generator for Directly Powering a Wireless Sensor Node, Adv. Mater. (2015). https://doi.org/10.1002/adma.201403944.

[14] G. Zhu, W.Q. Yang, T. Zhang, Q. Jing, J. Chen, Y.S. Zhou, P. Bai, Z.L. Wang, Self-powered, ultrasensitive, flexible tactile sensors based on contact electrification, Nano Lett. 14 (2014) 3208–3213. https://doi.org/10.1021/nl5005652.

[15] Y.T. Jao, P.K. Yang, C.M. Chiu, Y.J. Lin, S.W. Chen, D. Choi, Z.H. Lin, A textile-based triboelectric nanogenerator with humidity-resistant output characteristic and its applications in self-powered healthcare sensors, Nano Energy. 50 (2018) 513–520. https://doi.org/10.1016/j.nanoen.2018.05.071.

[16] C. Zhang, L. Liu, L. Zhou, X. Yin, X. Wei, Y. Hu, Y. Liu, S. Chen, J. Wang, Z.L. Wang, Self-Powered Sensor for Quantifying Ocean Surface Water Waves Based on Triboelectric Nanogenerator, ACS Nano. 14 (2020) 7092–7100. https://doi.org/10.1021/acsnano.0c01827.

[17] Y. Su, G. Xie, H. Tai, S. Li, B. Yang, S. Wang, Q. Zhang, H. Du, H. Zhang, X. Du, Y. Jiang, Self-powered room temperature NO2 detection driven by triboelectric

nanogenerator under UV illumination, Nano Energy. 47 (2018) 316–324. https://doi.org/10.1016/j.nanoen.2018.02.031.

[18] X. Liang, T. Jiang, G. Liu, T. Xiao, L. Xu, W. Li, F. Xi, C. Zhang, Z.L. Wang, Triboelectric Nanogenerator Networks Integrated with Power Management Module for Water Wave Energy Harvesting, Adv. Funct. Mater. 29 (2019) 1–8. https://doi.org/10.1002/adfm.201807241.

[19] Z. Wu, H. Guo, W. Ding, Y.C. Wang, L. Zhang, Z.L. Wang, A Hybridized Triboelectric-Electromagnetic Water Wave Energy Harvester Based on a Magnetic Sphere, ACS Nano. (2019). https://doi.org/10.1021/acsnano.8b09088.

[20] A. Chang, C. Uy, X. Xiao, J. Chen, Self-powered environmental monitoring via a triboelectric nanogenerator, Nano Energy. 98 (2022) 107282. https://doi.org/10.1016/j.nanoen.2022.107282.

[21] M.T. Rahman, M. Salauddin, P. Maharjan, M.S. Rasel, H. Cho, J.Y. Park, Natural wind-driven ultra-compact and highly efficient hybridized nanogenerator for self-sustained wireless environmental monitoring system, Nano Energy. 57 (2019) 256–268. https://doi.org/10.1016/j.nanoen.2018.12.052.

[22] M. Xu, Y.C. Wang, S.L. Zhang, W. Ding, J. Cheng, X. He, P. Zhang, Z. Wang, X. Pan, Z.L. Wang, An aeroelastic flutter based triboelectric nanogenerator as a self-powered active wind speed sensor in harsh environment, Extrem. Mech. Lett. 15 (2017) 122–129. https://doi.org/10.1016/j.eml.2017.07.005.

[23] B. Bhushan, Introduction to Tribology, Second Edition, Wiley, New York, Chapter 1, 2013. https://doi.org/10.1002/9781118403259.

[24] Z.L. Wang, J. Chen, L. Lin, Progress in triboelectric nanogenerators as a new energy technology and self-powered sensors, Energy Environ. Sci. 8 (2015) 2250–2282. https://doi.org/10.1039/c5ee01532d.

[25] Z.L. Wang, A.C. Wang, On the origin of contact-electrification, Mater. Today. 30 (2019) 34–51. https://doi.org/https://doi.org/10.1016/j.mattod.2019.05.016.

[26] D.M. Gooding, G.K. Kaufman, Tribocharging and the Triboelectric Series, Encycl. Inorg. Bioinorg. Chem. (2014) 1–9. https://doi.org/10.1002/9781119951438.eibc2239.

[27] D.J. Lacks, R. Mohan Sankaran, Contact electrification of insulating materials, J. Phys. D. Appl. Phys. 44 (2011). https://doi.org/10.1088/0022-3727/44/45/453001.

[28] X. Shen, A.E. Wang, R.M. Sankaran, D.J. Lacks, First-principles calculation of

contact electrification and validation by experiment, J. Electrostat. 82 (2016) 11–16. https://doi.org/10.1016/j.elstat.2016.04.006.

[29] C. Xu, Y. Zi, A.C. Wang, H. Zou, Y. Dai, X. He, P. Wang, Y.C. Wang, P. Feng, D. Li, Z.L. Wang, On the Electron-Transfer Mechanism in the Contact-Electrification Effect, Adv. Mater. 30 (2018) 1–9. https://doi.org/10.1002/adma.201706790.

[30] H. Zou, Y. Zhang, L. Guo, P. Wang, X. He, G. Dai, H. Zheng, C. Chen, A.C. Wang, C. Xu, Z.L. Wang, Quantifying the triboelectric series, Nat. Commun. 10 (2019) 1427. https://doi.org/10.1038/s41467-019-09461-x.

[31] J. Lowell, A.C. Rose-Innes, Contact electrification, Adv. Phys. 29 (1980) 947–1023. https://doi.org/10.1080/00018738000101466.

[32] S. Huang, R.T. Atanasoski, R.A. Oriani, Detection of Effects of Low Electric Fields with the Kelvin Probe, J. Electrochem. Soc. 140 (1993) 1065–1067. https://doi.org/10.1149/1.2056198.

[33] A. Verdaguer, M. Cardellach, J.J. Segura, G.M. Sacha, J. Moser, M. Zdrojek, A. Bachtold, J. Fraxedas, Charging and discharging of graphene in ambient conditions studied with scanning probe microscopy, Appl. Phys. Lett. 94 (2009) 1–4. https://doi.org/10.1063/1.3149770.

[34] M.T. Nguyen, K.K. Kanazawa, P. Brock, A.F. Diaz, S. Yee, Surface Potential Map of Charged Ionomer-Polymer Blends Studied with a Scanning Kelvin Probe, Langmuir. 10 (1994) 597–601.

[35] H. Sun, H. Chu, J. Wang, L. Ding, Y. Li, Kelvin probe force microscopy study on nanotriboelectrification, Appl. Phys. Lett. 96 (2010) 10–13. https://doi.org/10.1063/1.3330866.

[36] J. Liu, A. Goswami, K. Jiang, F. Khan, S. Kim, R. McGee, Z. Li, Z. Hu, J. Lee, T. Thundat, Direct-current triboelectricity generation by a sliding Schottky nanocontact on MoS2 multilayers, Nat. Nanotechnol. 13 (2018) 112–116. https://doi.org/10.1038/s41565-017-0019-5.

[37] H. Zou, L. Guo, H. Xue, Y. Zhang, X. Shen, X. Liu, P. Wang, X. He, G. Dai, P. Jiang, H. Zheng, B. Zhang, C. Xu, Z.L. Wang, Quantifying and understanding the triboelectric series of inorganic non-metallic materials, Nat. Commun. 11 (2020) 2093. https://doi.org/10.1038/s41467-020-15926-1.

[38] S. Li, Y. Zhou, Y. Zi, G. Zhang, Z.L. Wang, Excluding Contact Electrification in Surface Potential Measurement Using Kelvin Probe Force Microscopy, ACS Nano. 10 (2016) 2528–2535. https://doi.org/10.1021/acsnano.5b07418.

[39] Y. Wang, Y. Yang, Z.L. Wang, Triboelectric nanogenerators as flexible power sources, Npj Flex. Electron. 1 (2017) 10. https://doi.org/10.1038/s41528-017-0007-8.

[40] Z.L. Wang, Triboelectric nanogenerators as new energy technology and self-powered sensors - Principles, problems and perspectives, Faraday Discuss. 176 (2014) 447–458. https://doi.org/10.1039/c4fd00159a.

[41] Z.L. Wang, Triboelectric nanogenerators as new energy technology for self-powered systems and as active mechanical and chemical sensors, ACS Nano. 7 (2013) 9533–9557. https://doi.org/10.1021/nn404614z.

[42] R.D.I.G.I.G. Dharmasena, K.D.G.I.G.I. Jayawardena, C.A. Mills, J.H.B.B. Deane, J. V. Anguita, R.A. Dorey, S.R.P.P. Silva, Triboelectric nanogenerators: Providing a fundamental framework, Energy Environ. Sci. 10 (2017) 1801–1811. https://doi.org/10.1039/c7ee01139c.

[43] Y. Chen, Y. Cheng, Y. Jie, X. Cao, N. Wang, Z.L. Wang, Energy harvesting and wireless power transmission by a hybridized electromagnetic–triboelectric nanogenerator, Energy \& Environ. Sci. 12 (2019) 2678–2684. https://doi.org/10.1039/C9EE01245A.

[44] T. Nanogenerator, G. Cheng, Z.H. Lin, Z.L. Du, Z.L. Wang, Electrostatic and Mechanical Energies from Flowing Water by a Hybridized, ACS Nano. 8 (2014) 1932–1939. https://doi.org/10.1021/nn406565k.

[45] C. Rodrigues, M. Kumar, M. Proença, J. Gutierrez, R. Melo, A. Pereira, J. Ventura, M.P. Proenca, J. Gutierrez, R. Melo, A. Pereira, J. Ventura, M. Proença, J. Gutierrez, R. Melo, A. Pereira, J. Ventura, Triboelectric energy harvesting in harsh conditions: temperature and pressure effects in methane and crude oil environments, Nano Energy. 72 (2020) 104682. https://doi.org/10.1016/j.nanoen.2020.104682.

[46] A. Šutka, K. Mālnieks, L. Lapčinskis, P. Kaufelde, A. Linarts, A. Bērziņa, R. Zābels, V. Jurķāns, I. Gorņevs, J. Blūms, M. Knite, The role of intermolecular forces in contact electrification on polymer surfaces and triboelectric nanogenerators, Energy \& Environ. Sci. 12 (2019) 2417–2421. https://doi.org/10.1039/C9EE01078E.

[47] C. Zhang, W. Tang, C. Han, F. Fan, Z.L. Wang, Theoretical Comparison, Equivalent Transformation, and Conjunction Operations of Electromagnetic Induction Generator and Triboelectric Nanogenerator for Harvesting Mechanical

Energy, Adv. Mater. 26 (n.d.) 3580–3591.

[48] Y.S. Choi, Q. Jing, A. Datta, C. Boughey, S. Kar-Narayan, A triboelectric generator based on self-poled Nylon-11 nanowires fabricated by gas-flow assisted template wetting, Energy \& Environ. Sci. 10 (2017) 2180–2189. https://doi.org/10.1039/C7EE01292F.

[49] S.-H. Shin, Y.H. Kwon, Y.-H. Kim, J.-Y. Jung, M.H. Lee, J. Nah, Triboelectric Charging Sequence Induced by Surface Functionalization as a Method To Fabricate High Performance Triboelectric Generators, ACS Nano. 9 (n.d.) 4621–4627. https://doi.org/10.1021/acsnano.5b01340.

[50] W. Liu, Z. Wang, G. Wang, G. Liu, J. Chen, X. Pu, Y. Xi, X. Wang, H. Guo, C. Hu, Z.L. Wang, Integrated charge excitation triboelectric nanogenerator, Nat. Commun. 10 (2019) 1426. https://doi.org/10.1038/s41467-019-09464-8.

[51] Z.H. Lin, G. Zhu, Y.S. Zhou, Y. Yang, P. Bai, J. Chen, Z.L. Wang, A Self-Powered Triboelectric Nanosensor for Mercury Ion Detection, Angew. Chemie - Int. Ed. 52 (2013) 5065–5069. https://doi.org/10.1002/anie.201300437.

[52] P. Bai, G. Zhu, Q. Jing, J. Yang, J. Chen, Y. Su, J. Ma, G. Zhang, Z.L. Wang, Membrane-Based Self-Powered Triboelectric Sensors for Pressure Change Detection and its Uses in Security Surveillance and Healthcare Monitoring, Adv. Funct. Mater. 24 (2014) 5807–5813. https://doi.org/10.1002/adfm.201401267.

[53] X.-S. Zhang, M.-D. Han, B. Meng, H.-X. Zhang, High performance triboelectric nanogenerators based on large-scale mass-fabrication technologies, Nano Energy. 11 (2015) 304–322. https://doi.org/10.1016/j.nanoen.2014.11.012.

[54] C.K. Jeong, K.M. Baek, S. Niu, T.W. Nam, Y.H. Hur, D.Y. Park, G.-T. Hwang, M. Byun, Z.L. Wang, Y.S. Jung, K.J. Lee, Topographically-Designed Triboelectric Nanogenerator via Block Copolymer Self-Assembly, Nano Lett. 14 (2014) 7031–7038. https://doi.org/10.1021/nl503402c.

[55] J. Huang, X. Fu, G. Liu, S. Xu, X. Li, C. Zhang, L. Jiang, Micro/nano-structures-enhanced triboelectric nanogenerators by femtosecond laser direct writing, Nano Energy. 62 (2019) 638–644. https://doi.org/10.1016/j.nanoen.2019.05.081.

[56] J. Chen, H. Guo, X. He, G. Liu, Y. Xi, H. Shi, C. Hu, Enhancing Performance of Triboelectric Nanogenerator by Filling High Dielectric Nanoparticles into Sponge PDMS Film, ACS Appl. Mater. Interfaces. 8 (2016) 736–744. https://doi.org/10.1021/acsami.5b09907.

[57] F.-R.R. Fan, L. Lin, G. Zhu, W.Z. Wu, R. Zhang, Z.L. Wang, Transparent

Triboelectric Nanogenerators and Self-Powered Pressure Sensors Based on Micropatterned Plastic Films, Nano Lett. 12 (2012) 3109–3114. https://doi.org/10.1021/nl300988z.

[58] X. He, H. Guo, X. Yue, J. Gao, Y. Xi, C. Hu, Improving energy conversion efficiency for triboelectric nanogenerator with capacitor structure by maximizing surface charge density, Nanoscale. 7 (2015) 1896–1903. https://doi.org/10.1039/c4nr05512h.

[59] N. Cui, L. Gu, Y. Lei, J. Liu, Y. Qin, X. Ma, Y. Hao, Z.L. Wang, Dynamic Behavior of the Triboelectric Charges and Structural Optimization of the Friction Layer for a Triboelectric Nanogenerator, ACS Nano. 10 (2016) 6131–6138. https://doi.org/10.1021/acsnano.6b02076.

[60] S. Shin, Y.E. Bae, H.K. Moon, J. Kim, S. Choi, Y. Kim, Formation of Triboelectric Series via Atomic- Level Surface Functionalization for Triboelectric Energy Harvesting, (2017). https://doi.org/10.1021/acsnano.7b02156.

[61] S. Wang, Y. Zi, Y.S. Zhou, S. Li, F. Fan, L. Lin, Z.L. Wang, Molecular surface functionalization to enhance the power output of triboelectric nanogenerators, J. Mater. Chem. A. 4 (2016) 3728–3734. https://doi.org/10.1039/c5ta10239a.

[62] G. Song, Y. Kim, S. Yu, M.O. Kim, S.H. Park, S.M. Cho, D.B. Velusamy, S.H. Cho, K.L. Kim, J. Kim, E. Kim, C. Park, Molecularly Engineered Surface Triboelectric Nanogenerator by Self-Assembled Monolayers (METS), Chem. Mater. 27 (2015) 4749–4755. https://doi.org/10.1021/acs.chemmater.5b01507.

[63] S. Wang, L. Lin, Z.L. Wang, Z. Lin, Triboelectric nanogenerators as self-powered active sensors, Nano Energy. 11 (2015) 436–462. https://doi.org/10.1016/j.nanoen.2014.10.034.

[64] S. Niu, Z.L. Wang, Theoretical systems of triboelectric nanogenerators, Nano Energy. 14 (2014) 161–192. https://doi.org/10.1016/j.nanoen.2014.11.034.

[65] F. Yi, L. Lin, S. Niu, P.K. Yang, Z. Wang, J. Chen, Y. Zhou, Y. Zi, J. Wang, Q. Liao, Y. Zhang, Z.L. Wang, Stretchable-Rubber-Based Triboelectric Nanogenerator and Its Application as Self-Powered Body Motion Sensors, Adv. Funct. Mater. 25 (n.d.) 3688–3696.

[66] S. Li, S. Wang, Y. Zi, Z. Wen, L. Lin, G. Zhang, Z.L. Wang, Largely Improving the Robustness and Lifetime of Triboelectric Nanogenerators Through Automatic Transition Between Contact and Noncontact Working States, ACS Nano. 9 (n.d.) 7479–7487. https://doi.org/10.1021/acsnano.5b02575.

[67] S. Niu, Y. Liu, S. Wang, L. Lin, Y.S. Zhou, Y. Hu, Z.L. Wang, Theory of sliding-mode triboelectric nanogenerators, Adv. Mater. 25 (2013) 6184–6193. https://doi.org/10.1002/adma.201302808.

[68] S. Niu, Y. Liu, X. Chen, S. Wang, Y.S. Zhou, L. Lin, Y. Xie, Z.L. Wang, Theory of freestanding triboelectric-layer-based nanogenerators, Nano Energy. 12 (2015) 760–774. https://doi.org/10.1016/j.nanoen.2015.01.013.

[69] S. Niu, Y.S. Zhou, S. Wang, Y. Liu, L. Lin, Y. Bando, Z.L. Wang, Simulation method for optimizing the performance of an integrated triboelectric nanogenerator energy harvesting system, Nano Energy. 8 (2014) 150–156. https://doi.org/10.1016/j.nanoen.2014.05.018.

[70] L. Lin, Y. Xie, S. Niu, S. Wang, P.-K.K. Yang, Z.L. Wang, Robust triboelectric nanogenerator based on rolling electrification and electrostatic induction at an instantaneous energy conversion efficiency of ~55%, ACS Nano. 9 (2015) 922–930. https://doi.org/10.1021/nn506673x.

[71] S. Niu, Y. Liu, S. Wang, L. Lin, Y.S. Zhou, Y. Hu, Z.L. Wang, Theoretical investigation and structural optimization of single-electrode triboelectric nanogenerators, Adv. Funct. Mater. 24 (2014) 3332–3340. https://doi.org/10.1002/adfm.201303799.

[72] Z.L. Wang, L. Lin, J. Chen, S. Niu, Y. Zi, Triboelectric Nanogenerator: Single-Electrode Mode, in: Triboelectric Nanogenerators, Springer International Publishing, Cham, 2016: pp. 91–107. https://doi.org/10.1007/978-3-319-40039-6_4.

[73] S. Wang, S. Niu, J. Yang, L. Lin, Z.L. Wang, Quantitative measurements of vibration amplitude using a contact-mode freestanding triboelectric nanogenerator, ACS Nano. 8 (2014) 12004–12013. https://doi.org/10.1021/nn5054365.

[74] Z.L. Wang, On Maxwell's displacement current for energy and sensors: the origin of nanogenerators, Mater. Today. 20 (2017) 74–82. https://doi.org/10.1016/j.mattod.2016.12.001.

[75] S. Wang, L. Lin, Z.L. Wang, Nanoscale-Triboelectric-Effect Enabled Energy Conversion for Sustainable Powering of Portable Electronics, Nano Lett. 12 (2012) 6339–6346. https://doi.org/10.1021/nl303573d.

[76] H. Zhang, Y. Yang, T.C. Hou, Y. Su, C. Hu, Z.L. Wang, Triboelectric nanogenerator built inside clothes for self-powered glucose biosensors, Nano

Energy. 2 (2013) 1019–1024. https://doi.org/10.1016/j.nanoen.2013.03.024.

[77] G. Zhu, P. Bai, J. Chen, Z. Lin Wang, Power-generating shoe insole based on triboelectric nanogenerators for self-powered consumer electronics, Nano Energy. 2 (2013) 688–692. https://doi.org/10.1016/j.nanoen.2013.08.002.

[78] X. Pu, L. Li, H. Song, C. Du, Z. Zhao, C. Jiang, G. Cao, W. Hu, Z.L. Wang, A self-charging power unit by integration of a textile triboelectric nanogenerator and a flexible lithium-ion battery for wearable electronics, Adv. Mater. 27 (2015) 2472–2478. https://doi.org/10.1002/adma.201500311.

[79] X. Li, J. Tao, W. Guo, X. Zhang, J. Luo, M. Chen, J. Zhu, C. Pan, A self-powered system based on triboelectric nanogenerators and supercapacitors for metal corrosion prevention, J. Mater. Chem. A. 3 (2015) 22663–22668. https://doi.org/10.1039/C5TA07053H.

[80] Y. Wu, Y. Su, J. Bai, G. Zhu, X. Zhang, Z. Li, Y. Xiang, J. Shi, A Self-Powered Triboelectric Nanosensor for PH Detection, J. Nanomater. 2016 (2016). https://doi.org/10.1155/2016/5121572.

[81] A. Ahmed, I. Hassan, T. Ibn-Mohammed, H. Mostafa, I.M. Reaney, L.S.C. Koh, J. Zu, Z.L. Wang, Environmental life cycle assessment and techno-economic analysis of triboelectric nanogenerators, Energy \& Environ. Sci. 10 (2017) 653–671. https://doi.org/10.1039/C7EE00158D.

[82] X. Cheng, W. Tang, Y. Song, H. Chen, H. Zhang, Z.L. Wang, Power management and effective energy storage of pulsed output from triboelectric nanogenerator, Nano Energy. 61 (2019) 517–532. https://doi.org/10.1016/j.nanoen.2019.04.096.

[83] H. Ryu, H. moon Park, M.K. Kim, B. Kim, H.S. Myoung, T.Y. Kim, H.J. Yoon, S.S. Kwak, J. Kim, T.H. Hwang, E.K. Choi, S.W. Kim, Self-rechargeable cardiac pacemaker system with triboelectric nanogenerators, Nat. Commun. 12 (2021) 1–9. https://doi.org/10.1038/s41467-021-24417-w.

[84] H. Guo, X. Pu, J. Chen, Y. Meng, M. Yeh, G. Liu, Q. Tang, B. Chen, D. Liu, S. Qi, C. Wu, C. Hu, J. Wang, Z.L. Wang, A highly sensitive, self-powered triboelectric auditory sensor for social robotics and hearing aids, Sci. Robot. 2516 (2018) 1–10.

[85] J. Huang, Y. Hao, M. Zhao, W. Li, F. Huang, Q. Wei, All-Fiber-Structured Triboelectric Nanogenerator via One-Pot Electrospinning for Self-Powered Wearable Sensors, ACS Appl. Mater. Interfaces. (2021). https://doi.org/10.1021/acsami.1c03894.

[86] X. Pu, H. Guo, J. Chen, X. Wang, Y. Xi, C. Hu, Z.L. Wang, Eye motion triggered self-powered mechnosensational communication system using triboelectric nanogenerator, Sci. Adv. 3 (2017) 1–8. https://doi.org/10.1126/sciadv.1700694.

[87] VFP Ink Technologies, Silver electron - VFP Ink Technologies, (n.d.) 92390. https://vfp-ink-technologies.com/products/printed-electronics/attachment/silver-electron-ink-2/ (accessed October 10, 2019).

[88] S. Niu, S. Wang, L. Lin, Y. Liu, Y.S. Zhou, Y. Hu, Z.L. Wang, Theoretical study of contact-mode triboelectric nanogenerators as an effective power source, Energy Environ. Sci. 6 (2013) 3576–3583. https://doi.org/10.1039/c3ee42571a.

[89] inanoEnergy, (n.d.). https://inanoe.com/ (accessed August 10, 2020).

[90] M. Ramos, Triboelectric nanogenerators for blue energy harvesting: Automated characterization and applicability studies, Faculdade de Ciências da Universidade do Porto, 2020. https://sigarra.up.pt/fcup/pt/pub_geral.pub_view?pi_pub_base_id=427326.

[91] J. Heidemann, M. Stojanovic, M. Zorzi, Underwater sensor networks: Applications, advances and challenges, Philos. Trans. R. Soc. A Math. Phys. Eng. Sci. 370 (2012) 158–175. https://doi.org/10.1098/rsta.2011.0214.

[92] S.B. Williams, O.R. Pizarro, M. V Jakuba, C.R. Johnson, N.S. Barrett, R.C. Babcock, G.A. Kendrick, P.D. Steinberg, A.J. Heyward, P.J. Doherty, I. Mahon, M. Johnson-Roberson, D. Steinberg, A. Friedman, Monitoring of Benthic Reference Sites: Using an Autonomous Underwater Vehicle, IEEE Robot. Autom. Mag. 19 (2012) 73–84. https://doi.org/10.1109/MRA.2011.2181772.

[93] U.K. Verfuss, A.S. Aniceto, D. V. Harris, D. Gillespie, S. Fielding, G. Jiménez, P. Johnston, R.R. Sinclair, A. Sivertsen, S.A. Solbø, R. Storvold, M. Biuw, R. Wyatt, A review of unmanned vehicles for the detection and monitoring of marine fauna, Mar. Pollut. Bull. 140 (2019) 17–29. https://doi.org/10.1016/j.marpolbul.2019.01.009.

[94] L. Centurioni, A. Horányi, C. Cardinali, E. Charpentier, R. Lumpkin, A global ocean observing system for measuring sea level atmospheric pressure : Effects and impacts on numerical weather prediction, Bull. Am. Meteorol. Soc. 98 (2017) 231–238. https://doi.org/10.1175/BAMS-D-15-00080.1.

[95] B. Reed, F. Hover, Oceanographic pursuit: Networked control of multiple vehicles tracking dynamic ocean features, Methods Oceanogr. 10 (2014) 21–43. https://doi.org/10.1016/j.mio.2014.05.001.

[96] M. Menicou, V. Vassiliou, Prospective energy needs in Mediterranean offshore aquaculture: Renewable and sustainable energy solutions, Renew. Sustain. Energy Rev. 14 (2010) 3084–3091. https://doi.org/10.1016/j.rser.2010.06.013.

[97] C. Rillahan, M. Chambers, W.H. Howell, W.H. Watson, A self-contained system for observing and quantifying the behavior of Atlantic cod, Gadus morhua, in an offshore aquaculture cage, Aquaculture. 293 (2009) 49–56. https://doi.org/10.1016/j.aquaculture.2009.04.003.

[98] M. Christiansen, K. Fagerholt, B. Nygreen, D. Ronen, Chapter 4 Maritime Transportation, Handbooks Oper. Res. Manag. Sci. 14 (2007) 189–284. https://doi.org/10.1016/S0927-0507(06)14004-9.

[99] M. Postacchini, L.R. Centurioni, L. Braasch, M. Brocchini, D. Vicinanza, Lagrangian Observations of Waves and Currents From the River Drifter, IEEE J. Ocean. Eng. 41 (2016) 94–104. https://doi.org/10.1109/JOE.2015.2418171.

[100] R. Hostache, P. Matgen, L. Giustarini, F.N. Teferle, C. Tailliez, J.F. Iffly, G. Corato, A drifting GPS buoy for retrieving effective riverbed bathymetry, J. Hydrol. 520 (2015) 397–406. https://doi.org/10.1016/j.jhydrol.2014.11.018.

[101] P. Wang, X. Tian, T. Peng, Y. Luo, A review of the state-of-the-art developments in the field monitoring of offshore structures, Ocean Eng. 147 (2018) 148–164. https://doi.org/10.1016/j.oceaneng.2017.10.014.

[102] J. Mendler de Suarez, B. Cicin-Sain, K. Wowk, R. Payet, O. Hoegh-Guldberg, Ensuring survival: Oceans, climate and security, Ocean Coast. Manag. 90 (2014) 27–37. https://doi.org/10.1016/j.ocecoaman.2013.08.007.

[103] E. Nyman, Techno-optimism and ocean governance: New trends in maritime monitoring, Mar. Policy. 99 (2019) 30–33. https://doi.org/10.1016/j.marpol.2018.10.027.

[104] D.O.B. Jones, J.M. Durden, K. Murphy, K.M. Gjerde, A. Gebicka, A. Colaço, T. Morato, D. Cuvelier, D.S.M. Billett, Existing environmental management approaches relevant to deep-sea mining, Mar. Policy. 103 (2019) 172–181. https://doi.org/10.1016/j.marpol.2019.01.006.

[105] T. Katz, Y. Weinstein, R. Alkalay, E. Biton, Y. Toledo, A. Lazar, O. Zlatkin, R. Soffer, E. Rahav, G. Sisma-Ventura, T. Bar, T. Ozer, H. Gildor, A. Almogi-Labin, M. Kanari, I. Berman-Frank, B. Herut, The first deep-sea mooring station in the eastern Levantine basin (DeepLev), outline and insights into regional sedimentological processes, Deep. Res. Part II Top. Stud. Oceanogr. 171 (2020)

104663. https://doi.org/10.1016/j.dsr2.2019.104663.

[106] S. Oliveira-Pinto, P. Rosa-Santos, F. Taveira-Pinto, Electricity supply to offshore oil and gas platforms from renewable ocean wave energy: Overview and case study analysis, Energy Convers. Manag. 186 (2019) 556–569. https://doi.org/10.1016/j.enconman.2019.02.050.

[107] R. Zhao, S. Hynes, G. Shun He, Defining and quantifying China's ocean economy, Mar. Policy. 43 (2014) 164–173. https://doi.org/10.1016/j.marpol.2013.05.008.

[108] IEA, World Energy Outlook: Offshore Energy Outlook, (2018) 80.

[109] E. Kabir, P. Kumar, S. Kumar, A.A. Adelodun, K.H. Kim, Solar energy: Potential and future prospects, Renew. Sustain. Energy Rev. 82 (2018) 894–900. https://doi.org/10.1016/j.rser.2017.09.094.

[110] A. Ajitha, N.M. Kumar, X.X. Jiang, G.R. Reddy, A. Jayakumar, K. Praveen, T. Anil Kumar, Underwater performance of thin-film photovoltaic module immersed in shallow and deep waters along with possible applications, Results Phys. 15 (2019) 102768. https://doi.org/10.1016/j.rinp.2019.102768.

[111] World Energy Resources: Solar World Energy, World Energy Council, Survey, 2013.

[112] T.K. Løken, V. Neshaug, L.R. Sætran, Energy Systems on an Autonomous Offshore Measurement Station, Energy Procedia. 94 (2016) 218–226. https://doi.org/10.1016/j.egypro.2016.09.227.

[113] J. Falnes, A review of wave-energy extraction, Mar. Struct. 20 (2007) 185–201. https://doi.org/10.1016/j.marstruc.2007.09.001.

[114] F. Taveira-Pinto, G. Iglesias, P. Rosa-Santos, Z.D. Deng, Preface to Special Topic: Marine Renewable Energy, J. Renew. Sustain. Energy. 7 (2015). https://doi.org/10.1063/1.4939086.

[115] K. Gunn, C. Stock-Williams, Quantifying the global wave power resource, Renew. Energy. 44 (2012) 296–304. https://doi.org/10.1016/j.renene.2012.01.101.

[116] A.F. d. O. Falcão, Wave energy utilization: A review of the technologies, Renew. Sustain. Energy Rev. 14 (2010) 899–918. https://doi.org/10.1016/j.rser.2009.11.003.

[117] I. López, J. Andreu, S. Ceballos, I. Martínez De Alegría, I. Kortabarria, Review of wave energy technologies and the necessary power-equipment, Renew. Sustain. Energy Rev. 27 (2013) 413–434. https://doi.org/10.1016/j.rser.2013.07.009.

[118] J. Portilla, J. Sosa, L. Cavaleri, Wave energy resources: Wave climate and exploitation, Renew. Energy. 57 (2013) 594–605. https://doi.org/10.1016/j.renene.2013.02.032.

[119] J.C.C. Henriques, J.C.C. Portillo, L.M.C. Gato, R.P.F. Gomes, D.N. Ferreira, A.F.O. Falcão, Design of oscillating-water-column wave energy converters with an application to self-powered sensor buoys, Energy. 112 (2016) 852–867. https://doi.org/10.1016/j.energy.2016.06.054.

[120] Q. Xie, T. Zhang, Y. Pan, Z. Zhang, Y. Yuan, Y. Liu, A novel oscillating buoy wave energy harvester based on a spatial double X-shaped mechanism for self-powered sensors in sea-crossing bridges, Energy Convers. Manag. 204 (2020) 112286. https://doi.org/10.1016/j.enconman.2019.112286.

[121] U. Khan, S.-W.W. Kim, Triboelectric Nanogenerators for Blue Energy Harvesting, ACS Nano. 10 (2016) 6429–6432. https://doi.org/10.1021/acsnano.6b04213.

[122] R. Li, Y. Li, Y. Zhao, Y. Li, Y. Li, Harvest of ocean energy by triboelectric generator technology, Appl. Phys. Rev. 5 (2018). https://doi.org/10.1063/1.5008606.

[123] Y. Zi, H. Guo, Z. Wen, M.-H. Yeh, C. Hu, Z.L. Wang, Harvesting Low-Frequency (<5 Hz) Irregular Mechanical Energy: A Possible Killer Application of Triboelectric Nanogenerator, ACS Nano. 10 (2016) 4797–4805. https://doi.org/10.1021/acsnano.6b01569.

[124] X. Liang, T. Jiang, G. Liu, Y. Feng, C. Zhang, Z.L. Wang, Spherical triboelectric nanogenerator integrated with power management module for harvesting multidirectional water wave energy, Energy \& Environ. Sci. 13 (2020) 277–285. https://doi.org/10.1039/C9EE03258D.

[125] Z.L. Wang, T. Jiang, L. Xu, Toward the blue energy dream by triboelectric nanogenerator networks, Nano Energy. 39 (2017) 9–23. https://doi.org/10.1016/j.nanoen.2017.06.035.

[126] J. Chen, J. Yang, Z. Li, X. Fan, Y. Zi, Q. Jing, H. Guo, Z. Wen, K.C. Pradel, S. Niu, Z.L. Wang, Networks of Triboelectric Nanogenerators for Harvesting Water Wave Energy: A Potential Approach toward Blue Energy, ACS Nano. 9 (n.d.) 3324–3331. https://doi.org/10.1021/acsnano.5b00534.

[127] Y. Su, X. Wen, G. Zhu, J. Yang, J. Chen, P. Bai, Z. Wu, Y. Jiang, Z. Lin Wang, Hybrid triboelectric nanogenerator for harvesting water wave energy and as a self-powered distress signal emitter, Nano Energy. 9 (2014) 186–195. https://doi.org/10.1016/j.nanoen.2014.07.006.

[128] Y. Zi, J. Wang, S. Wang, S. Li, Z. Wen, H. Guo, Z.L. Wang, Effective energy storage from a triboelectric nanogenerator, Nat. Commun. 7 (2016) 1–8. https://doi.org/10.1038/ncomms10987.

[129] R.D.I.G. Dharmasena, K.D.G.I. Jayawardena, C.A. Mills, R.A. Dorey, S.R.P. Silva, A unified theoretical model for Triboelectric Nanogenerators, Nano Energy. 48 (2018) 391–400. https://doi.org/10.1016/j.nanoen.2018.03.073.

[130] Y. Yang, G. Zhu, H. Zhang, J. Chen, X. Zhong, Z.H. Lin, Y. Su, P. Bai, X. Wen, Z.L. Wang, Triboelectric Nanogenerator for Harvesting Wind Energy and as Self-Powered Wind Vector Sensor System, ACS Nano. 7 (2013) 9461–9468. https://doi.org/10.1021/nn4043157.

[131] IALA AISM, Maritime Buoyage System and Other Aids to Navigation, (2010) 1–24. https://www.iala-aism.org/product/r1001/.

[132] LDL, Lagrangian Drifter Lab, Lagrangian Drifter Lab. (2018). http://gdp.ucsd.edu/ldl_drifter/index.html (accessed December 26, 2018).

[133] J.D. Irish, S.J. Boduch, Aquaculture feed buoy control - Part 2: Telemetry, data handling and shore-based control, Ocean. 2006. (2006). https://doi.org/10.1109/OCEANS.2006.307133.

[134] Z. Saadatnia, E. Esmailzadeh, H.E. Naguib, Design , simulation , and experimental characterization of a heaving triboelectric-electromagnetic wave energy harvester, Nano Energy. 50 (2018) 281–290. https://doi.org/10.1016/j.nanoen.2018.05.059.

[135] X. Wang, Z. Wen, H. Guo, C. Wu, X. He, L. Lin, X. Cao, Z.L. Wang, Fully Packaged Blue Energy Harvester by Hybridizing a Rolling Triboelectric Nanogenerator and an Electromagnetic Generator, ACS Nano. 10 (2016) 11369–11376. https://doi.org/10.1021/acsnano.6b06622.

[136] S.L. Zhang, M. Xu, C. Zhang, Y.-C.C. Wang, H. Zou, X. He, Z.Z.L. Wang, Z.Z.L. Wang, Rationally designed sea snake structure based triboelectric nanogenerators for effectively and efficiently harvesting ocean wave energy with minimized water screening effect, Nano Energy. 48 (2018) 421–429. https://doi.org/10.1016/j.nanoen.2018.03.062.

[137] P. Cheng, H. Guo, Z. Wen, C. Zhang, X. Yin, X. Li, D. Liu, W. Song, X. Sun, J. Wang, Z.L. Wang, Largely enhanced triboelectric nanogenerator for efficient harvesting of water wave energy by soft contacted structure, Nano Energy. 57 (2019) 432–439. https://doi.org/10.1016/j.nanoen.2018.12.054.

[138] W. Liu, L. Xu, T. Bu, H. Yang, G. Liu, W. Li, Y. Pang, C. Hu, C. Zhang, T. Cheng, Torus structured triboelectric nanogenerator array for water wave energy harvesting, Nano Energy. 58 (2019) 499–507. https://doi.org/10.1016/j.nanoen.2019.01.088.

[139] M. Xu, T. Zhao, C. Wang, S.L. Zhang, Z. Li, X. Pan, Z.L. Wang, High Power Density Tower-like Triboelectric Nanogenerator for Harvesting Arbitrary Directional Water Wave Energy, ACS Nano. 13 (2019) 1932–1939. https://doi.org/10.1021/acsnano.8b08274.

[140] J. An, Z.M. Wang, T. Jiang, X. Liang, Z.L. Wang, Whirling-Folded Triboelectric Nanogenerator with High Average Power for Water Wave Energy Harvesting, Adv. Funct. Mater. 29 (2019) 1–10. https://doi.org/10.1002/adfm.201904867.

[141] W. Zhong, L. Xu, X. Yang, W. Tang, J. Shao, B. Chen, Z.L. Wang, Open-book-like triboelectric nanogenerators based on low-frequency roll-swing oscillators for wave energy harvesting, Nanoscale. 11 (2019) 7199–7208. https://doi.org/10.1039/c8nr09978b.

[142] F. Xi, Y. Pang, G. Liu, S. Wang, W. Li, C. Zhang, Z.L. Wang, Self-powered intelligent buoy system by water wave energy for sustainable and autonomous wireless sensing and data transmission, Nano Energy. 61 (2019) 1–9. https://doi.org/10.1016/j.nanoen.2019.04.026.

[143] X. Li, J. Tao, J. Zhu, C. Pan, A nanowire based triboelectric nanogenerator for harvesting water wave energy and its applications, APL Mater. 5 (2017) 74104. https://doi.org/10.1063/1.4977216.

[144] Q. Shi, H. Wang, H. Wu, C. Lee, Self-powered triboelectric nanogenerator buoy ball for applications ranging from environment monitoring to water wave energy farm, Nano Energy. 40 (2017) 203–213. https://doi.org/10.1016/j.nanoen.2017.08.018.

[145] L. Xu, Y. Pang, C. Zhang, T. Jiang, X. Chen, J. Luo, W. Tang, X. Cao, Z.L. Wang, Integrated triboelectric nanogenerator array based on air-driven membrane structures for water wave energy harvesting, Nano Energy. 31 (2017) 351–358. https://doi.org/10.1016/j.nanoen.2016.11.037.

[146] D.Y. Kim, H.S.H.B. Kim, D.S. Kong, M. Choi, H.S.H.B. Kim, J.-H.H. Lee, G. Murillo, M. Lee, S.S. Kim, J.H. Jung, Floating buoy-based triboelectric nanogenerator for an effective vibrational energy harvesting from irregular and random water waves in wild sea, Nano Energy. 45 (2018) 247–254.

https://doi.org/10.1016/j.nanoen.2017.12.052.

[147] Z. Lin, B. Zhang, H. Guo, Z. Wu, H. Zou, J. Yang, Z.L. Wang, Super-robust and frequency-multiplied triboelectric nanogenerator for efficient harvesting water and wind energy, Nano Energy. 64 (2019) 103908. https://doi.org/10.1016/j.nanoen.2019.103908.

[148] G. Liu, H. Guo, S. Xu, C. Hu, Z.L. Wang, Oblate Spheroidal Triboelectric Nanogenerator for All-Weather Blue Energy Harvesting, Adv. Energy Mater. (2019) 1900801. https://doi.org/10.1002/aenm.201900801.

[149] L. Feng, G. Liu, H. Guo, Q. Tang, X. Pu, J. Chen, X. Wang, Y. Xi, C. Hu, Hybridized nanogenerator based on honeycomb-like three electrodes for efficient ocean wave energy harvesting, Nano Energy. 47 (2018) 217–223. https://doi.org/10.1016/j.nanoen.2018.02.042.

[150] H. Wang, Q. Zhu, Z. Ding, Z. Li, H. Zheng, J. Fu, C. Diao, X. Zhang, J. Tian, Y. Zi, A fully-packaged ship-shaped hybrid nanogenerator for blue energy harvesting toward seawater self-desalination and self-powered positioning, Nano Energy. 57 (2019) 616–624. https://doi.org/10.1016/j.nanoen.2018.12.078.

[151] Z. Saadatnia, E. Asadi, H. Askari, J. Zu, E. Esmailzadeh, Modeling and performance analysis of duck-shaped triboelectric and electromagnetic generators for water wave energy harvesting, Int. J. Energy Res. 41 (2017) 2392–2404. https://doi.org/10.1002/er.3811.

[152] X. Chen, L. Gao, J. Chen, S. Lu, H. Zhou, T. Wang, A. Wang, Z. Zhang, S. Guo, X. Mu, Z.L. Wang, Y. Yang, A chaotic pendulum triboelectric-electromagnetic hybridized nanogenerator for wave energy scavenging and self-powered wireless sensing system, Nano Energy. 69 (2020) 104440. https://doi.org/10.1016/j.nanoen.2019.104440.

[153] H. Díaz, S.A. Sannasiraj, C.G. Soares, Experimental study of behaviour and efficiency on a backward bent duct buoy, Adv. Renew. Energies Offshore - Proc. 3rd Int. Conf. Renew. Energies Offshore, RENEW 2018. (2019) 409–419.

[154] G. Bracco, A. Cagninei, E. Giorcelli, G. Mattiazzo, D. Poggi, M. Raffero, Experimental validation of the ISWEC wave to PTO model, Ocean Eng. 120 (2016) 40–51. https://doi.org/10.1016/j.oceaneng.2016.05.006.

[155] S. Huang, H. Shi, F. Cao, J. Tan, H. Cheng, D. Li, S. Liu, H. Gong, J. Tao, Experimental Study on Interaction Between Degrees of Freedom in a Wave Buoy, J. Ocean Univ. China. 18 (2019) 1256–1264. https://doi.org/10.1007/s11802-019-

4175-0.

[156] S. Fu, Y. Xu, K. Hu, Y. Zhang, Experimental investigation on hydrodynamics of floating cylinder in oscillatory and steady flows by forced oscillation test, Mar. Struct. 34 (2013) 41–55. https://doi.org/10.1016/j.marstruc.2013.08.005.

[157] M. Kamarlouei, J.F. Gaspar, M. Calvario, T.S. Hallak, M.J.G.C. Mendes, F. Thiebaut, C. Guedes Soares, Experimental analysis of wave energy converters concentrically attached on a floating offshore platform, Renew. Energy. 152 (2020) 1171–1185. https://doi.org/10.1016/j.renene.2020.01.078.

[158] P. Rosa-Santos, F. Taveira-Pinto, D. Clemente, T. Cabral, F. Fiorentin, F. Belga, T. Morais, Experimental study of a hybrid wave energy converter integrated in a harbor breakwater, J. Mar. Sci. Eng. 7 (2019) 1–18. https://doi.org/10.3390/jmse7020033.

[159] P. Rosa-Santos, F. Taveira-Pinto, L. Teixeira, J. Ribeiro, CECO wave energy converter: Experimental proof of concept, J. Renew. Sustain. Energy. 7 (2015). https://doi.org/10.1063/1.4938179.

[160] M. Wu, V. Stratigaki, T. Verbrugghe, P. Troch, C. Altomare, A. Crespo, D. Kisacik, L. Cappietti, J. Domínguez, M. Hall, M. Gómez-Gesteira, P. Stansby, R.B. Canelas, R. Ferreira, Experimental Study of Motion and Mooring Behavior of a Floating Oscillating Water Column Wave Energy Convert, Proc. 7th Int. Conf. Appl. Phys. Model. Coast. Port Eng. Sci. (2018) 1–8.

[161] C.A. Rodríguez, F. Taveira-Pinto, P. Rosa-Santos, Experimental assessment of the performance of ceco wave energy converter in irregular waves, Proc. Int. Conf. Offshore Mech. Arct. Eng. - OMAE. 10 (2018) 1–10. https://doi.org/10.1115/OMAE2018-77686.

[162] N. Pozzi, G. Bracco, B. Passione, S.A. Sirigu, G. Mattiazzo, PeWEC: Experimental validation of wave to PTO numerical model, Ocean Eng. 167 (2018) 114–129. https://doi.org/10.1016/j.oceaneng.2018.08.028.

[163] A. Pecher, J. Kofoed, Handbook of Ocean Wave Energy, 1st ed., Springer Cham, 2017. https://doi.org/https://doi.org/10.1007/978-3-319-39889-1.

[164] Sealite, Ocean Buoy Atlantic-2600, 2600mm Diameter Ocean Buoy (Atlantic SLB2600), (2019). https://www.sealite.com/large-ocean-buoy-2600mm-diameter/ (accessed October 3, 2019).

[165] J.H. Lee, I. Yu, S. Hyun, J.K. Kim, U. Jeong, Remarkable increase in triboelectrification by enhancing the conformable contact and adhesion energy

with a film-covered pillar structure, Nano Energy. 34 (2017) 233–241. https://doi.org/10.1016/j.nanoen.2017.02.032.

[166] W. Yang, X. Wang, H. Li, J. Wu, Y. Hu, Z. Li, H. Liu, Fundamental research on the effective contact area of micro-/nano-textured surface in triboelectric nanogenerator, Nano Energy. 57 (2019) 41–47. https://doi.org/10.1016/j.nanoen.2018.12.029.

[167] C.K. Chung, K.H. Ke, High contact surface area enhanced Al/PDMS triboelectric nanogenerator using novel overlapped microneedle arrays and its application to lighting and self-powered devices, Appl. Surf. Sci. 508 (2020). https://doi.org/10.1016/j.apsusc.2020.145310.

[168] D. Clemente, Energy Production from the Motions of Offshore Floating Platforms, Faculty of Engineering - University of Porto, 2022. https://hdl.handle.net/10216/141542.

[169] D. Clemente, P. Rosa-Santos, F. Taveira-Pinto, P. Martins, Influence of platform design and power take-off characteristics on the performance of the E-Motions wave energy converter, Energy Convers. Manag. 244 (2021) 114481. https://doi.org/10.1016/j.enconman.2021.114481.

[170] D. Silva, P. Martinho, C. Guedes Soares, Wave energy distribution along the Portuguese continental coast based on a thirty three years hindcast, Renew. Energy. 127 (2018) 1064–1075. https://doi.org/10.1016/j.renene.2018.05.037.

[171] D. Clemente, P. Rosa-Santos, F. Taveira-Pinto, P.T. Martins, Preliminary numerical optimization of the E-Motions wave energy converter, Trends Marit. Technol. Eng. Vol. 2. (2022) 361–372. https://doi.org/10.1201/9781003320289-38.

[172] V. Nguyen, R. Zhu, R. Yang, Environmental effects on nanogenerators, Nano Energy. 14 (2015) 49–61. https://doi.org/10.1016/j.nanoen.2014.11.049.

[173] C. Wu, A.C. Wang, W. Ding, H. Guo, Z.L. Wang, Triboelectric Nanogenerator: A Foundation of the Energy for the New Era, Adv. Energy Mater. 9 (2019) 1802906. https://doi.org/10.1002/aenm.201802906.

[174] M.-L.L. Seol, J.-W.W. Han, D.-I. Il Moon, M. Meyyappan, Triboelectric nanogenerator for Mars environment, Nano Energy. 39 (2017) 238–244. https://doi.org/10.1016/j.nanoen.2017.07.004.

[175] C.X. Lu, C.B. Han, G.Q. Gu, J. Chen, Z.W. Yang, T. Jiang, C. He, Z.L. Wang, Temperature Effect on Performance of Triboelectric Nanogenerator, Adv. Eng.

Mater. 19 (2017) 1700275. https://doi.org/10.1002/adem.201700275.

[176] X. Wen, Y. Su, Y. Yang, H. Zhang, Z.L. Wang, Applicability of triboelectric generator over a wide range of temperature, Nano Energy. 4 (2014) 150–156. https://doi.org/10.1016/j.nanoen.2014.01.001.

[177] C. Xu, A.C. Wang, H. Zou, B. Zhang, C. Zhang, Y. Zi, L. Pan, P. Wang, P. Feng, Z. Lin, Z.L. Wang, Raising the Working Temperature of a Triboelectric Nanogenerator by Quenching Down Electron Thermionic Emission in Contact-Electrification, Adv. Mater. 30 (2018) 1803968. https://doi.org/10.1002/adma.201803968.

[178] Y. Su, J. Chen, Z. Wu, Y. Jiang, Low temperature dependence of triboelectric effect for energy harvesting and self-powered active sensing, Appl. Phys. Lett. 106 (2015) 13114. https://doi.org/10.1063/1.4905553.

[179] V. Nguyen, R. Yang, Effect of Humidity and Pressure on the Triboelectric Nanogenerator, Nano Energy. 2 (2013) 604–608. https://doi.org/10.1016/j.nanoen.2013.07.012.

[180] K.Y. Lee, J. Chun, J.-H.H. Lee, K.N. Kim, N.-R.R. Kang, J.-Y.Y. Kim, M.H. Kim, K.-S.S. Shin, M.K. Gupta, J.M. Baik, S.-W.W. Kim, Hydrophobic Sponge Structure-Based Triboelectric Nanogenerator, Adv. Mater. 26 (2014) 5037–5042. https://doi.org/https://doi.org/10.1002/adma.201401184.

[181] A.S.M.I.S.M.I. Uddin, P.S. Kumar, K. Hassan, H.C. Kim, Enhanced sensing performance of bimetallic Al/Ag-CNF network and porous PDMS-based triboelectric acetylene gas sensors in a high humidity atmosphere, Sens. Actuators B Chem. 258 (2018) 857–869. https://doi.org/10.1016/j.snb.2017.11.160.

[182] S. Wang, Y. Jiang, H. Tai, B. Liu, Z. Duan, Z. Yuan, H. Pan, G. Xie, X. Du, Y. Su, An integrated flexible self-powered wearable respiration sensor, Nano Energy. 63 (2019) 103829. https://doi.org/10.1016/j.nanoen.2019.06.025.

[183] H. Zhang, Y. Yang, Y. Su, J. Chen, C. Hu, Z. Wu, Y. Liu, C. Ping Wong, Y. Bando, Z.L. Wang, C.P. Wong, Y. Bando, Z.L. Wang, Triboelectric nanogenerator as self-powered active sensors for detecting liquid/gaseous water/ethanol, Nano Energy. 2 (2013) 693–701. https://doi.org/10.1016/j.nanoen.2013.08.004.

[184] K. Han, W. Tang, J. Chen, J. Luo, L. Xu, Z.L. Wang, Atmosphere on the Performance of Contact–Separation Mode TENG, Adv. Mater. Technol. 4 (2019) 1800569. https://doi.org/10.1002/admt.201800569.

[185] H. Wang, T. Huang, H. Yu, M. Zhu, S. Lv, B. Yu, Q. Zhang, Gas-enhanced triboelectric nanogenerator based on fully-enclosed structure for energy harvesting and sensing, Nano Energy. 55 (2018) 463–469. https://doi.org/10.1016/j.nanoen.2018.11.022.

[186] T. Zhao, J. Li, H. Zeng, Y. Fu, H. He, L. Xing, Y. Zhang, X. Xue, Self-powered wearable sensing-textiles for real-time detecting environmental atmosphere and body motion based on surface-triboelectric coupling effect, Nanotechnology. 29 (2018) 405504. https://doi.org/10.1088/1361-6528/aad3fc.

[187] R.I. Haque, D. Briand, Triboelectric freestanding flapping film generator for energy harvesting from gas flow in pipes, Smart Mater. Struct. 28 (2019) 085002. https://doi.org/10.1088/1361-665X/ab0840.

[188] H. He, M. Zhang, T. Zhao, H. Zeng, L. Xing, X. Xue, A self-powered gas sensor based on PDMS/Ppy triboelectric-gas-sensing arrays for the real-time monitoring of automotive exhaust gas at room temperature, Sci. China Mater. 62 (2019) 1433–1444. https://doi.org/10.1007/s40843-019-9445-9.

[189] M. Wang, J. Zhang, Y. Tang, J. Li, B. Zhang, E. Liang, Y. Mao, X. Wang, Air-Flow-Driven Triboelectric Nanogenerators for Self-Powered Real-Time Respiratory Monitoring, ACS Nano. 12 (2018) 6156–6162. https://doi.org/10.1021/acsnano.8b02562.

[190] M. Ma, Z.Z.Z. Zhang, Q. Liao, G. Zhang, F. Gao, X. Zhao, Q. Zhang, X. Xun, Z.Z.Z. Zhang, Y. Zhang, Integrated hybrid nanogenerator for gas energy recycle and purification, Nano Energy. 39 (2017) 524–531. https://doi.org/10.1016/j.nanoen.2017.07.003.

[191] S. Cui, Y. Zheng, T. Zhang, D. Wang, F. Zhou, W. Liu, Self-powered ammonia nanosensor based on the integration of the gas sensor and triboelectric nanogenerator, Nano Energy. 49 (2018) 31–39. https://doi.org/10.1016/j.nanoen.2018.04.033.

[192] C. Xu, B. Zhang, A.C. Wang, W. Cai, Y. Zi, P. Feng, Z.L. Wang, Effects of Metal Work Function and Contact Potential Difference on Electron Thermionic Emission in Contact Electrification, Adv. Funct. Mater. 29 (2019) 1–8. https://doi.org/10.1002/adfm.201903142.

[193] D. Liu, L. Zhou, S. Li, Z. Zhao, X. Yin, Z. Yi, C. Zhang, X. Li, J. Wang, Z.L. Wang, Hugely Enhanced Output Power of Direct-Current Triboelectric Nanogenerators by Using Electrostatic Breakdown Effect, Adv. Mater. Technol. 5 (2020) 1–8.

https://doi.org/10.1002/admt.202000289.

[194] X. Tao, S. Li, Y. Shi, X. Wang, J. Tian, Z. Liu, P. Yang, X. Chen, Z.L. Wang, Triboelectric Polymer with High Thermal Charge Stability for Harvesting Energy from 200 °C Flowing Air, Adv. Funct. Mater. 31 (2021) 1–9. https://doi.org/10.1002/adfm.202106082.

[195] J. Wang, C. Wu, Y. Dai, Z. Zhao, A. Wang, T. Zhang, Z.L. Wang, Achieving ultrahigh triboelectric charge density for efficient energy harvesting, Nat. Commun. 8 (2017) 1–7. https://doi.org/10.1038/s41467-017-00131-4.

[196] J. Fu, G. Xu, C. Li, X. Xia, D. Guan, J. Li, Z. Huang, Y. Zi, Achieving Ultrahigh Output Energy Density of Triboelectric Nanogenerators in High-Pressure Gas Environment, Adv. Sci. 7 (2020) 1–8. https://doi.org/10.1002/advs.202001757.

[197] S. Lv, B. Yu, T. Huang, H. Yu, H. Wang, Q. Zhang, M. Zhu, Gas-enhanced triboelectric nanogenerator based on fully-enclosed structure for energy harvesting and sensing, Nano Energy. 55 (2019) 463–469. https://doi.org/10.1016/j.nanoen.2018.11.022.

[198] K. Han, W. Tang, J. Chen, J. Luo, L. Xu, Z.L. Wang, Effects of Environmental Atmosphere on the Performance of Contact–Separation Mode TENG, Adv. Mater. Technol. 4 (2019) 1–8. https://doi.org/10.1002/admt.201800569.

[199] Z.L. Wang, Entropy theory of distributed energy for internet of things, Nano Energy. 58 (2019) 669–672. https://doi.org/10.1016/j.nanoen.2019.02.012.

[200] X. Yang, L. Xu, P. Lin, W. Zhong, Y. Bai, J. Luo, J. Chen, Z.L. Wang, Macroscopic self-assembly network of encapsulated high-performance triboelectric nanogenerators for water wave energy harvesting, Nano Energy. 60 (2019) 404–412. https://doi.org/10.1016/j.nanoen.2019.03.054.

[201] H. Yong, J. Chung, D. Choi, D. Jung, M. Cho, S. Lee, Highly reliable wind-rolling triboelectric nanogenerator operating in a wide wind speed range, Sci. Rep. 6 (2016) 33977. https://doi.org/10.1038/srep33977.

[202] K. Lee, J. Lee, K. Kim, D. Yoo, D. Kim, W. Hwang, I. Song, J.-Y. Sim, A Spherical Hybrid Triboelectric Nanogenerator for Enhanced Water Wave Energy Harvesting, Micromachines. 9 (2018) 598. https://doi.org/10.3390/mi9110598.

[203] M.D.D. Hogue, C.R.R. Buhler, C.I.I. Calle, T. Matsuyama, W. Luo, E.E.E. Groop, Insulator-insulator contact charging and its relationship to atmospheric pressure, J. Electrostat. 61 (2004) 259–268. https://doi.org/10.1016/j.elstat.2004.03.002.

[204] S. Gant, Generation of flammable mists from high flashpoint fluids : Literature review, HSE Books, 2013.

[205] Xrig AS, (n.d.). www.xrig.com (accessed August 31, 2020).

[206] Shell, Shell Morlina S2 BL 10, Technical data sheet, 2016. http://tdc.ge/wp-content/uploads/2014/03/3_Morlina_S2_BL_10.pdf.

[207] N. Tesla, Thermo-Magnetic Motor, N. Tesla, 1889.

[208] J. Stefan, Ueber thermomagnetische Motoren, Ann. Phys. 274 (1889) 427–440. https://doi.org/10.1002/andp.18892741107.

[209] D. Solomon, Design of a thermomagnetic generator, Energy Convers. Manag. 31 (1991) 157–173. https://doi.org/10.1016/0196-8904(91)90068-T.

[210] T.A. Edison, Pyromagnetic Generator, T. A. Edison, 1892.

[211] H.E. Stauss, Efficiency of thermomagnetic generator, J. Appl. Phys. 30 (1959) 1622–1623. https://doi.org/10.1063/1.1735020.

[212] S. Ahmim, M. Almanza, V. Loyau, A. Pasko, F. Mazaleyrat, M. Lobue, A Thermal Energy Harvester Using LaFeSi Magnetocaloric Materials, IEEE Trans. Magn. 57 (2021) 1–5. https://doi.org/10.1109/TMAG.2020.3008753.

[213] V. Srivastava, Y. Song, K. Bhatti, R.D. James, The direct conversion of heat to electricity using multiferroic alloys, Adv. Energy Mater. 1 (2011) 97–104. https://doi.org/10.1002/aenm.201000048.

[214] M. Ujihara, G.P. Carman, D.G. Lee, Thermal energy harvesting device using ferromagnetic materials, Appl. Phys. Lett. 91 (2007) 093508. https://doi.org/10.1063/1.2775096.

[215] C.J. Hsu, S.M. Sandoval, K.P. Wetzlar, G.P. Carman, Thermomagnetic conversion efficiencies for ferromagnetic materials, J. Appl. Phys. 110 (2011) 123923. https://doi.org/10.1063/1.3672844.

[216] J. Chun, H.C. Song, M.G. Kang, H.B. Kang, R.A. Kishore, S. Priya, Thermo-Magneto-Electric Generator Arrays for Active Heat Recovery System, Sci. Rep. 7 (2017) 41383. https://doi.org/10.1038/srep41383.

[217] R.A. Kishore, S. Priya, A review on design and performance of thermomagnetic devices, Renew. Sustain. Energy Rev. 81 (2018) 33–44. https://doi.org/10.1016/j.rser.2017.07.035.

[218] R.A. Kishore, D. Singh, R. Sriramdas, A.J. Garcia, M. Sanghadasa, S. Priya,

Linear thermomagnetic energy harvester for low-grade thermal energy harvesting, J. Appl. Phys. 127 (2020) 044501. https://doi.org/10.1063/1.5124312.

[219] A. Waske, D. Dzekan, K. Sellschopp, D. Berger, A. Stork, K. Nielsch, S. Fähler, Energy harvesting near room temperature using a thermomagnetic generator with a pretzel-like magnetic flux topology, Nat. Energy. 4 (2019) 68–74. https://doi.org/10.1038/s41560-018-0306-x.

[220] M. Gueltig, F. Wendler, H. Ossmer, M. Ohtsuka, H. Miki, T. Takagi, M. Kohl, High-Performance Thermomagnetic Generators Based on Heusler Alloy Films, Adv. Energy Mater. 7 (2017) 1601879. https://doi.org/10.1002/aenm.201601879.

[221] R.A. Kishore, S. Priya, A Review on low-grade thermal energy harvesting: Materials, methods and devices, Materials (Basel). 11 (2018) 1433. https://doi.org/10.3390/ma11081433.

[222] J. Chen, J. Wang, W. Xuan, S. Dong, J. Luo, Universal triboelectric nanogenerator simulation based on dynamic finite element method model, Sensors. 20 (2020) 4838. https://doi.org/10.3390/s20174838.

[223] J.M.D. Coey, Magnetism and magnetic materials, Cambridge University Press, 2010. https://www.cambridge.org/core/product/identifier/9780511845000/type/book (accessed June 8, 2021).

[224] A. Khan, J. Khan, M. Uddin, M. Bokhari, Triboelectric nanogenerator as self-powered impact force sensor for falling object, Curr. Appl. Phys. 20 (2020) 137–144. https://doi.org/10.1016/j.cap.2019.10.016.

[225] C. Rodrigues, D. Nunes, D. Clemente, N. Mathias, J.M. Correia, P. Rosa-Santos, F. Taveira-Pinto, T. Morais, A. Pereira, J. Ventura, Emerging triboelectric nanogenerators for ocean wave energy harvesting: state of the art and future perspectives, Energy Environ. Sci. 13 (2020) 2657–2683. https://doi.org/10.1039/D0EE01258K.

[226] V. Ramos, M. López, F. Taveira-Pinto, P. Rosa-Santos, Influence of the wave climate seasonality on the performance of a wave energy converter: A case study, Energy. 135 (2017) 303–316. https://doi.org/10.1016/j.energy.2017.06.080.

[227] A. Post, C. Knight, E. Kisi, Thermomagnetic energy harvesting with first order phase change materials, J. Appl. Phys. 114 (2013). https://doi.org/10.1063/1.4815933.

Appendix

Appendix A

In this section, copyright information will be presented.

Figure nº	Publisher	License Number	Link
Figure 1.4	John Wiley and Sons	5426480802064	https://drive.google.com/file/d/1Hc-c0d0IHnkaldDOWa5FW-F2qfd7wJ_u/view?usp=share_link
Figure 1.12	Elsevier	N/A	https://drive.google.com/file/d/1nNmuwdeyI2xtqodgSv-0tvTR9u8PrUn5/view?usp=share_link
Figure 1.14(a)-(d)	Springer Nature	N/A	https://drive.google.com/file/d/1KmInGcUVcPbjOhUJiHImgSj8sq-iH8xv/view?usp=share_link
Figure 1.14(e)-(j)	AAAS	N/A	https://drive.google.com/file/d/15LEDa2H9eVjgQBSPd98Kupfs2E1lpEcc/view?usp=share_link
Figure 1.14(k)-(n)	American Chemical Society	N/A	https://drive.google.com/file/d/1TBWQSBCrWxdWm1sPRQraxXEwUYJAx60K/view?usp=share_link
Figure 1.14(o)-(q)	AAAS	N/A	https://drive.google.com/file/d/1t8oPO0IS_rSZ18drFiBX5j-ewtez8Ybq/view?usp=share_link
Chapter 3	Royal Society of Chemistry	N/A	https://drive.google.com/file/d/1C_RRVN-arlxAmfNJKpQE8QQwNNdUjY4Y/view?usp=share_link
	Elsevier	N/A	https://drive.google.com/file/d/1NeTMfWoqjcYEWykNyUqvRJc3I_s_QYAv/view?usp=share_link
Chapter 4	John Wiley and Sons	5426491443685	https://drive.google.com/file/d/1JM59OjoigL2gQbIk1HBDQuwxZ6ng6EhJ/view?usp=share_link

	Elsevier	N/A	https://drive.google.com/file/d/1Xe7GU_SilgIIU-R04WI4ByRwFI7IN1nh/view?usp=share_link
Figure 4.1(a)-(c)	John Wiley and Sons	5426530992283	https://drive.google.com/file/d/1obsnV89cRIsNGBBVP0R64i7at_Pkjbrp/view?usp=share_link
Figure 4.1(d)-(f)	John Wiley and Sons	5426531202895	https://drive.google.com/file/d/1Y0MiQJimyNg1ZtGJbSf_JoPBwo51cVEK/view?usp=share_link
Figure4.2(a)-(c)	John Wiley and Sons	N/A	https://drive.google.com/file/d/1h-HkN7cSbwHdhSMJg-1DuUqd5eF46or5/view?usp=share_link
Figure 4.2(d)-(f)	Springer Nature	N/A	https://drive.google.com/file/d/1EJ-bCMfbWRo0WIUej6Ty3QAmbHGZyzdU/view?usp=share_link
Figure 4.3	John Wiley and Sons	5426540596267	https://drive.google.com/file/d/1zvdEHx0a3UfD6SH8nP_uX7LB5ixaLjgb/view?usp=share_link
Figure 4.4(a)-(c)	Elsevier	5426540286724	https://drive.google.com/file/d/1w80duGTwrS75TXKO1ztkSRMGm0QqbziC/view?usp=share_link
Figure 4.4(d)-(g)	Elsevier	5426540381207	https://drive.google.com/file/d/1MOOGREvPbrRq-o3uTm99o62jgHsFKGq8/view?usp=share_link